U.PORTO

3º CICLO

DOUTORAMENTO EM BIOLOGIA MOLECULAR E CELULAR

# BIOPHYSICAL ANALYSIS OF ALZHEIMER'S AMYLOID-β PEPTIDE ASSEMBLY AND CLEARANCE PATHWAYS

José Pedro Santos Leite

D

2022

U.PORTO

José Pedro Leite. BIOPHYSICAL ANALYSIS OF ALZHEIMER'S AMYLOID-β PEPTIDE ASSEMBLY AND CLEARANCE PATHWAYS

BIOPHYSICAL ANALYSIS OF ALZHEIMER'S AMYLOID -β PEPTIDE ASSEMBLY AND CLEARANCE PATHWAYS

José Pedro Santos Leite

D.ICBAS 2022

SEDE ADMINISTRATIVA

INSTITUTO DE CIÊNCIAS BIOMÉDICAS ABEL SALAZAR

FACULDADE DE CIÊNCIAS

JOSÉ PEDRO SANTOS LEITE

# BIOPHYSICAL ANALYSIS OF ALZHEIMER'S AMYLOID-β PEPTIDE ASSEMBLY AND CLEARANCE PATHWAYS

Tese de Candidatura ao grau de Doutor em
Biologia Molecular e Celular;
Programa Doutoral da Universidade do Porto
(Instituto de Ciências Biomédicas Abel Salazar e
Faculdade de Ciências)

Orientador – Doutor Luís Miguel Gales Pereira Pinto
Categoria – Professor Associado
Afiliação – Instituto de Ciências Biomédicas Abel Salazar (ICBAS) e
Instituto de Investigação e Inovação em Saúde (i3S), Universidade do Porto

Co-orientador – Doutor Filipe Alexandre Almeida Paz
Categoria – Investigador Principal
Afiliação – Instituto de Materiais de Aveiro (CICECO), Universidade de Aveiro

*À minha avó*

*“But it ain't about how hard you hit.*
*It's about how hard you can get hit and keep moving forward;*
*how much you can take and keep moving forward.*
*That's how winning is done!”*

- Rocky,
*in Rocky Balboa (2006)*

José Pedro Santos Leite was the recipient of PhD fellowship SFRH/BD/129921/2017 and the COVID-related extension fellowship COVID/BD/151890/2021 from Fundação para a Ciência e a Tecnologia (FCT).

This work was funded by Norte-01-0145-FEDER-000008 - Porto Neurosciences and Neurologic Disease Research Initiative at I3S, supported by Norte Portugal Regional Operational Programme (NORTE2020), under the PORTUGAL 2020 Partnership Agreement; by COMPETE 2020 - Operational Programme for Competitiveness and Internationalization (POCI), Portugal 2020, through the European Regional Development Fund (FEDER); by Portuguese funds through FCT - Fundação para a Ciência e Tecnologia/ Ministério da Ciência, Tecnologia e Ensino Superior in the framework of the project "Institute for Research and Innovation in Health Sciences" (POCI-01-0145-FEDER-007274); by Fundació La Marató de TV3, Spain (neurodegenerative diseases call, project reference: 20140330-31-32-33-34); and, by the project CICECO - Aveiro Institute of Materials, POCI-01-0145-FEDER-007679 (FCT ref. UID/CTM/50011/2013), financed by national funds through the FCT/MEC and when appropriate co-financed by FEDER under the PORTUGAL 2020 Partnership Agreement.

# Table of Contents

## Agradecimentos

Apesar de ser o meu nome a figurar na capa desta tese de doutoramento, este trabalho nunca teria sido possível sem o contributo, direto ou indireto, de um conjunto de pessoas, às quais deixo aqui o meu agradecimento.

Ao Professor Luís Gales, meu orientador nesta tese, mas sobretudo o mentor do meu percurso científico. Cruzei-me por acaso com a cristalografia em 2013 quando o Professor me acolheu no seu laboratório para desenvolver a minha dissertação de mestrado em Bioengenharia. Nos 8 anos seguintes, não só acreditou nas minhas capacidades como me providenciou todas as ferramentas, nomeadamente excelente supervisão científica, condições materiais e um elevado grau de autonomia, aliados a muita paciência para tolerar os meus erros. Abriu-me todas as portas e permitiu que eu me tornasse no investigador que agora finaliza esta tese. Por tudo isto, deixo aqui o meu profundo obrigado.

Ao Doutor Filipe Paz, meu co-orientador, pela disponibilidade e aconselhamento científico, abrindo-me horizontes no domínio dos MOFs. Aos colaboradores nacionais e internacionais que permitiram enriquecer este trabalho.

No i3S, à Professora Paula Tamagnini, por me acolher para a realização deste trabalho no seu grupo: Bioengineering & Synthetic Microbiology (BSM). Aos meus colegas BSM: Paulo Oliveira, Pedro Albuquerque, Ângela Brito, Rita Mota, Sara Pereira, Steeve Lima, Eunice Ferreira, Marina Santos, Rute Oliveira, Delfim Cardoso, Frederico Lourenço, João Rodrigues, Cátia Gonçalves e Dona Helena. Obrigado por todos os momentos, desde as grandes discussões científicas aos momentos mais disparatados que ocorreram no nosso *"guetto* do PhD*"*, nos almoços, nos lanches e, claro, nas *voltinhas*. Ao "pessoal da cristalografia", sobretudo à Tatiana Cereija, a quem deixo um obrigado especial por toda a ajuda e companheirismo. Ao Frederico Silva pelas grandes discussões "proteicas". Aos elementos das plataformas científicas i3S e ciclotrões ESRF, SOLEIL e ALBA, pela assistência técnica.

Um agradecimento ao Professor Doutor Cláudio Sunkel por me ter aceite no programa doutoral em Biologia Molecular e Celular; à minha comissão de acompanhamento, Doutor João Cabral e Doutora Isabel Cardoso, pelos conselhos dados; e, aos meus colegas da 5ª Edição, 2ª Fase do programa doutoral, "Os miseráveis".

Por fim, quero agradecer à minha família e amigos. Em particular à minha avó e aos meus pais: esta tese é também vossa.

Zé Pedro

## Abstract

Alzheimer's disease (AD) is the most widely known human amyloid disease. Despite two major players being associated with it - tau protein and the amyloid-β (Aβ) peptide, responsible for intracellular deposition of neurofibrillary tangles or extracellular deposition of senile plaques, respectively - AD is largely a multifactorial, complex and puzzling disease. As such, intense research efforts over the past half-century only yielded 6 approved disease-modulating drugs, with the last one, antibody aducanumab in June 2021, ending a near twenty-year gap of drug approval. This stresses the importance of better understanding every aspect of AD. In this thesis, we focused on the biophysical *in vitro* analysis of Aβ clearance and assembly.

Aβ peptides can be enzymatically degraded. Here, Aβ interaction with transthyretin (TTR), which is one of the most abundant cerebrospinal fluid (CSF) proteins, and neprilysin (NEP), the most prominent amyloid-degrading enzyme (ADE), was investigated. Extensive X-ray crystallography trials of TTR-Aβ were performed, as well as of TTR-drug complexes that may facilitate TTR/drug/Aβ ternary interactions aiming at Aβ clearance. Regarding NEP-Aβ, we found that the reaction is partially inhibited by a reaction product. Crystal structures of a NEP structural surrogate model (*i.e.* bacterial protein thermolysin) showed that an Aβ degradation C-terminal product (*i.e.* $A\beta_{31\text{-}X}$) remained abnormally bound to the enzyme's active site. This Aβ fragment bound similarly to the NEP active site, reducing $A\beta_{1\text{-}40}$ proteolytic activity. Together with other studies, this pointed to $A\beta_{31\text{-}35}$ as being a critical sequence recognized by different target proteins, possibly mediating mechanisms that may be toxic to neurons.

Next, an alternative approach to obtain Aβ structural models through the crystallization of Aβ, namely $A\beta_{1\text{-}40}$ or $A\beta_{17\text{-}40}$, fused to a protein partner was also attempted. Three different constructs were designed, of which two were successfully expressed, purified and crystallized. However, X-Ray data diffraction only yielded a few N-terminal Aβ residues that, unfortunately, did not add novel physiological nor disease relevant conformations to the existing knowledge.

$A\beta_{1\text{-}40}$ aggregation kinetics were then investigated using a synergistic approach by nuclear magnetic resonance, thioflavin-T fluorescence, transmission electron microscopy and dynamic light scattering. We were able to disclose the formation of high molecular weight oligomers (HMWO) that convert to fibrils nuclei in the assembly pathway.

Finally, unconventional methods that made use of metal-organic frameworks (MOFs) were applied. MOFs - crystalline porous materials resulting from the combination of a metal cluster with a multidentate organic linker - proved very useful as scaffolds to investigate the photophysical properties of the widely used amyloid dye Thioflavin-T (ThT). They were also

found to be good seeding agents for protein crystallization, though not particularly successful for the crystallization of Aβ peptides.

Overall, the synergetic combination of conventional and innovative approaches led us to contribute to a better understanding of the highly complex Aβ clearance and assembly pathways.

## Resumo

A doença de Alzheimer é a doença amilóide humana mais conhecida. Apesar de estar intimamente associada a dois componentes de natureza proteica – proteína tau e péptidos amilóide-β (Aβ), responsáveis pela deposição intracelular de emaranhados neurofibrilares ou deposição extracelular de placas amilóides, respectivamente –, é uma patologia altamente multi-factorial, complexa e intrigante. Como consequência, os extensos esforços na sua investigação nos últimos cinquenta anos apenas resultaram em 6 fármacos aprovados para uso humano com capacidade para de alguma forma atrasar a progressão da doença. Prova desta dificuldade é a controversa aprovação em junho de 2021 de um novo fármaco, o anticorpo aducanumab, terminando um hiato de cerca de duas décadas desde a última aprovação. Perante este cenário, é evidente a necessidade de conhecer cada aspecto fisio-patológico da doença de Alzheimer. A presente tese foca-se na análise biofísica *in vitro* de processos de eliminação do péptido amilóide-β, bem como da formação de fibras amilóides.

Os péptidos amilóide-β podem ser degradados enzimaticamente. Neste trabalho, investigou-se a sua interação com transtirretina (TTR), uma das proteínas mais abundantes no líquido cefalorraquidiano, e com neprilisina (NEP), a principal enzima que catalisa a degradação de Aβ. Em relação à TTR, foram realizados ensaios exaustivos de co-cristalização com fragmentos de péptidos Aβ e respectiva análise por diffracção de Raio-X, assim como o estudo cristalográfico de complexos TTR com compostos mediadores da interacção ternária TTR/composto/Aβ tendo em vista a eliminação de Aβ. Por outro lado, ensaios com neprilisina revelaram que a enzima é parcialmente inibida por um produto da reação NEP-Aβ. Estruturas cristalográficas de um substituto estrutural de NEP (*i.e.* termolisina, uma proteína de origem bacteriana) evidenciaram que um produto C-terminal da degradação de Aβ (*i.e.* $A\beta_{31-X}$) se mantém anormalmente ligado ao local ativo da enzima. Este efeito foi igualmente observado no local ativo de NEP, através da quantificação de uma redução na proteólise de $A\beta_{1-40}$ por esta enzima na presença de $A\beta_{31-35}$. Em linha com estudos prévios, isto sugere que $A\beta_{31-35}$ é uma sequência aminoacídica reconhecida por diferentes proteínas, possivelmente com envolvimento em mecanismos neurotóxicos.

Em seguida, foi empregue uma abordagem alternativa para o estudo cristalográfico do péptido Aβ, nomeadamente $A\beta_{1-40}$ ou $A\beta_{17-40}$, através da técnica de proteínas de fusão. Foram preparadas três construções, das quais duas foram expressas, purificadas e cristalizadas com sucesso. Contudo, análise por difração de Raio-X apenas revelou alguns aminoácidos em N-terminal de Aβ, não constituindo informação nova na sua conformação fisiológica ou patológica.

A agregação de $A\beta_{1-40}$ foi igualmente estudada usando uma sinergia entre ressonância magnética nuclear, fluorescência do corante amilóide Tioflavina T, microscopia electrónica de transmissão e dispersão dinâmica de luz. Com esta abordagem, identificámos no processo de formação de fibras de Aβ o aparecimento de oligómeros de elevado peso molecular que, por sua vez, se convertem em núcleos de fibrilas no processo de agregação.

Por fim, recorremos ao uso de estruturas metalo-orgânicas - materiais cristalinos altamente porosos resultantes da combinação entre núcelos metálicos e moléculas orgânicas. Estes materiais permitiram-nos estudar as propriedades fotofísicas da Tioflavina T, assim como se mostraram eficazes como agentes de nucleação na cristalização de proteínas. No entanto, não contribuíram para a cristalização de péptidos Aβ.

Em suma, a combinação das técnicas biofísicas aplicadas nesta tese permitiu contribuir para um melhor conhecimento sobre os processos de eliminação ou agregação de péptidos Aβ.

## List of Publications

Some of the work presented in this doctoral thesis consists of articles published in international peer-reviewed scientific journals. I declare that I participated extensively in the conception and execution of the works, from lab work to data analysis and manuscript writing, unless stated otherwise. Publications are reproduced with the permission from the copyright holders.

Publications included in the main body of this thesis:

**Paper I** *Original research article*

**Leite, J. P.**, & Gales, L. (2019). *Alzheimer's Abeta1-40 peptide degradation by thermolysin: evidence of inhibition by a C-terminal Abeta product.* FEBS Lett, 593(1), 128-137. doi:10.1002/1873-3468.13285

**Paper II** *Original research article*

**Leite, J.P.**; Lete, M.G.; Fowler, S.B.; Gimeno, A.; Rocha, J.F.; Sousa, S.F.; Webster, C.I.; Jiménez-Barbero, J.J.; Gales, L. (2021) *$A\beta_{31-35}$ decreases Neprilysin-mediated Alzheimer's Amyloid-β peptide degradation*. ACS Chemical Neuroscience, 12(19), 3708-3718. doi:10.1021/acschemneuro.1c00432.

**Paper III** *Original research article*

**Leite, J. P.**, Gimeno, A., Taboada, P., Jiménez-Barbero, J. J., & Gales, L. (2020). *Dissection of the key steps of amyloid-β peptide 1–40 fibrillogenesis.* International Journal of Biological Macromolecules, 164, 2240-2246. doi: 10.1016/j.ijbiomac.2020.08.023

**Paper IV** *Original research article*

**Leite, J. P.**, & Gales, L. (2019). *Fluorescence properties of the amyloid indicator dye thioflavin T in constrained environments.* Dyes and Pigments, 160, 64-70. doi: 10.1016/j.dyepig.2018.07.049

**Paper V** *Original research article*

**Leite, J. P.**, Rodrigues, D., Ferreira, S., Figueira, F., Almeida Paz, F. A., & Gales, L. (2019). *Mesoporous Metal–Organic Frameworks as Effective Nucleating Agents in Protein Crystallography.* Crystal Growth & Design, 19(3), 1610-1615. doi: 10.1021/acs.cgd.8b01444

Publications to which I contributed within the scope of this thesis:

*Original research article*

Cotrina, E.Y.; Santos, L.M.; Rivas, J.; Blasi, D.; **Leite, J.P.**; Liz, M.A.; Busquets, M.A.; Planas, A.; Prohens, R.; Gimeno, A.; Jiménez-Barbero, J.J.; Gales, L.; Llop, J.; Quintana, J.; Cardoso, I.; Arsequell, G. (2021). *Targeting transthyretin in Alzheimer's disease: drug discovery of small-molecule chaperones as disease-modifying drug candidates for Alzheimer's disease.* European Journal of Medicinal Chemistry, 226, 113847. doi: https://doi.org/10.1016/j.ejmech.2021.113847

*Review article*

Mendes, R. F., Figueira, F., **Leite, J. P.**, Gales, L., & Almeida Paz, F. A. (2020). Metal–organic frameworks: a future toolbox for biomedicine? Chemical Society Reviews, 49(24), 9121-9153. doi:10.1039/D0CS00883D

*Review article*

**Leite, J.P.**; Figueira, F.; Mendes, R.F.; Almeida Paz, F.A.; Gales, L. (2022). *Metal-Organic Frameworks as Sensors for Human Amyloid Diseases*. Manuscript in preparation.

## List of Abbreviations

| | |
|---|---|
| **α7nAChRs** | α7 nicotinic acetylcholine receptors |
| **ABAD** | Aβ-binding alcohol dehydrogenase |
| **Abz** | Ortho-aminobenzoic acid |
| **ACE** | Angiotensin-1-converting enzyme |
| **Ach** | Acetylcholine |
| **ACN** | Acetonitrile |
| **AD** | Alzheimer's disease |
| **ADE** | Amyloid-degrading enzymes |
| **AFM** | Atomic force microscopy |
| **apoE** | Apolipoprotein E |
| **APP** | Amyloid precursor protein |
| **aTLN** | Active thermolysin |
| **Aβ** | Amyloid-β peptide |
| **BACE1/2** | β-site APP cleavage enzyme 1/2 |
| **BBB** | Blood-brain barrier |
| **BSA** | Bovine serum albumin |
| **CAC** | Critical aggregation concentration |
| **CCDC** | Cambridge Crystallographic Data Centre |
| **CD** | Circular dichroism |
| **CDR** | Complementarity-determining regions |
| **CNP** | C-type natriuretic peptide |
| **CNS** | Central nervous system |
| **cryoEM** | Cryogenic electron microscopy |
| **CSF** | Cerebrospinal fluid |
| **DEF** | N,N-Diethylformamide |
| **D.I.T.** | Data integration time |
| **DLS** | Dynamic light scattering |
| **DMF** | N,N-Dimethylformamide |
| **DMSO** | Dimethyl sulfoxide |
| **DOSY** | Diffusion ordered spectroscopy |
| **DSF** | Differential scanning fluorimetry |
| **E** | Enzyme concentration |
| ***E. coli*** | *Escherichia coli* |
| **ECM** | Extracellular matrix |

| | |
|---|---|
| **EDDnp** | N-(ethylenediamine)-2,4-dinitrophenyl amide |
| **EDTA** | Ethylenediaminetetraacetic acid |
| **ELISA** | Enzyme-Linked Immunosorbent Assay |
| **ERAB** | Endoplasmic reticulum-associated Aβ peptide binding protein |
| **ERK** | Extracellular-signal-regulated kinase |
| **ESRF** | European Synchrotron Radiation Facility |
| **FA** | Formic acid |
| **fAD** | Early-onset familial Alzheimer's disease |
| **FAP** | Familial amyloidotic polyneuropathy |
| **FCS** | Fluorescence correlation spectroscopy |
| **GST** | Glutathione S-transferase |
| **$H_2$BDC** | Benzene-1,4-dicarboxylic acid |
| **$H_3$BTB** | 1,3,5-Tris(4-carboxyphenyl)benzene |
| **$H_3$TATB** | 4,4',4''-s-triazine-2,4,6-triyltribenzoic acid |
| **HEPES** | 4-(2-hydroxyethyl)-1-piperazineethanesulfonic acid |
| **HFIP** | 1,1,1,3,3,3-hexafluoro-2-propanol |
| **hIAPP** | Human islet amyloid polypeptide |
| **HMWO** | High molecular weight oligomers |
| **HPLC** | High Performance Liquid Cromatography |
| **hPreP** | Human presequence protease |
| **HRV3C** | Human rhinovirus 3C protease |
| **HSA** | Human serum albumin |
| **IDE** | Insulin-degrading enzyme |
| **IDIF** | Iododiflunisal |
| **IDP** | Intrinsically disordered protein |
| **IGF-IR** | Type 1 insulin-like growth factor receptor |
| **IgNAR** | Immunoglobulin from sharks |
| **IMAC** | Immobilized metal affinity chromatography |
| **IM-MS** | Ion-mobility spectrometry–mass spectrometry |
| **IPTG** | Isopropyl β-d-1-thiogalactopyranoside |
| **iTLN** | Inactive thermolysin |
| **JNK** | c-Jun N-terminal kinase |
| $k_{cat}$ | Turnover number |
| $K_I$ | Inhibition constant |
| $K_M$ | Michaelis-Menten constant |
| **LC-MS-MS** | Liquid Chromatography with tandem mass spectrometry |

| | |
|---|---|
| **LRP** | Low-density lipoprotein receptor-related protein |
| $\boldsymbol{m_0}$ | Initial monomer concentration |
| **MAPK** | Mitogen-activated protein kinase |
| **MASSIF** | Massively Automated Sample Selection Integrated Facility |
| **MBP** | Maltose-binding protein |
| **MD** | Molecular dynamics simulations |
| **MES** | 2-(N-morpholino) ethanesulfonic acid |
| **microED** | Micro electron diffraction |
| **MM-GBSA** | Molecular Mechanics - Generalized Born Surface Area |
| **MMP-9** | Matrix metalloprotease 9 |
| **MOFs** | Metal-organic frameworks |
| **mPTP** | Mitochondrial permeability transition pore |
| **MRI** | Magnetic Ressonance Imaging |
| **MS** | Mass spectrometry |
| **MW** | Molecular weight |
| **NEP** | Neprilysin |
| **NFTs** | Neurofibrillary tangles |
| **NIR** | Near-infrared |
| **NLN** | Neurolysin |
| **NMDA** | N-methyl-D-aspartic acid |
| **NMR** | Nuclear magnetic resonance |
| $\mathbf{N_R}$ | Number of residues |
| ***P*** | Concentration of product |
| **P3 peptide** | $A\beta_{17\text{-}40/42}$ peptide |
| **PAC3** | Proteasome assembly chaperone 3 |
| **PAGE** | Polyacrylamide gel electrophoresis |
| **PCMT1** | L-isoaspartate (D-aspartate) O-methyltransferase |
| **PD** | Parkinson's diasease |
| **PDB** | Protein Data Bank |
| **PE-FRET** | Probe enhancement FRET |
| **PEG** | Polyethylene glycol |
| **PI3K** | Phosphatidylinositol 3 kinase |
| **PMSF** | Phenylmethylsulfonyl fluoride |
| **PSEN1/2 or PS1/2** | Presenilin 1/2 |
| **PTMs** | Post-translational modifications |
| **RAGE** | Receptor for advanced glycation end products |

| | |
|---|---|
| **$R_g$** | Radius of gyration |
| **$R_h$** | Hydrodynamic radius |
| **RMSD** | Root-mean-square deviation |
| **RMSF** | Root Mean Square Fluctuation |
| **ROS** | Reactive oxygen species |
| **$S_0$** | Initial concentration of substrate |
| **sAD** | Late-onset sporadic Alzheimer's disease |
| **sAPPα/β** | Soluble APPα/β domain |
| **SDS** | Sodium dodecyl sulfate |
| **SDS-PAGE** | Sodium dodecyl sulfate–polyacrylamide gel electrophoresis |
| **SEC** | (context sensitive) serpin-enzyme complex or size-exclusion chromatography |
| **SF** | Soluble fraction |
| **SMCs** | Small-molecule chaperones |
| **smFRET** | Single-molecule Förster resonance energy transfer |
| **SN** | Supernatant |
| **ssNMR** | Solid state NMR |
| **STD-NMR** | Saturation-transfer difference nuclear magnetic resonance |
| $t$ | Time |
| $t_{1/2}$ | Characteristic half-time of protein aggregation |
| **T4** | Thyroxine hormone |
| **T4 Lysozyme** | Lysozyme from phage T4 |
| **Tb-mesoMOF** | Meso porous terbium-based MOF |
| **TEM** | Transmission electron microscopy |
| **TF** | Total fraction |
| **TFA** | Trifluoroacetic acid |
| **TGA** | Thermogravimetric analysis |
| **ThT** | Thioflavin-T |
| **TLN** | Thermolysin |
| **TLR** | Toll-like receptor |
| $t_M^*$ | HMWO formation kinetics |
| $t_{MN}^*$ | Characteristic time for the formation of fibrils nuclei |
| **TM** | Transmembrane region |
| **$T_m$** | Melting temperature |
| $t_N^*$ | Time of conversion of HMWO into nuclei |
| **TTR** | Transthyretin |

**VDAC** Voltage-dependent anion channels

$\boldsymbol{\nu}$ Scaling factor

# CHAPTER I. Introduction

## 1.1 The amyloid state

The denaturation and aggregation of proteins and peptides, resulting in the loss of their structural and functional properties and the formation of amyloid-like fibrous deposits, are associated with more than 20 diseases, like familial amyloidotic polyneuropathy (FAP), Parkinson's or Alzheimer's disease (AD). The term "amyloid" was first introduced in medical science by German pathologist Rudolf Virchow in 1854 to describe abnormal tissue formations that reacted positive to a iodine-staining protocol, something typical of starch-based materials ("amyloid" derives from the Latin word for starch, *amylum*)(Sipe *et al.*, 2000). Initially, pathologists defined amyloids exclusively as the disease-associated fibrils that deposited extracellularly in body tissues and could be detected by using specific dyes, such as Congo Red, yielding a green birefringence under polarized light. Later, *in vitro* identification started to be performed, for example, through fluorescence spectroscopy with dye Thioflavin-T (Biancalana *et al.*, 2010). However, amyloids may also be attributed a functional role, from bacteria to animals. For example, in *Escherichia coli*, curli protein-derived amyloid fibers are involved in host invasion and cell aggregation/biofilm formation, while, in humans, several functional amyloids have been identified, such as the protein Pmel17 playing a role in the synthesis of the UV-radiation protective pigment melanin and proteins involved in programmed necrosis (Barnhart *et al.*, 2006; Brown *et al.*, 2021).

To accommodate these findings, amyloids are currently defined from a molecular-based biophysical point of view as all structures characterized by a "cross-β-sheet" motif (*i.e.* not only deposited in tissues). This motif is defined by a unique X-ray fiber diffraction pattern, first described by William Astbury, consisting of particularly arranged β-sheets, with 4.8 Å spacing between strands along the fibril axis and about 10 Å between sheets, perpendicular to the fibril axis (Astbury *et al.*, 1935). This is common to all amyloids independently of the monomeric species, and, unlike normal occurring β-sheets, cross-β-sheets are virtually infinite and much more resilient to cleavage (Sunde *et al.*, 1997). Amyloids form when the backbone segments of certain proteins/peptides expose their amide groups and their concentration exceeds the entropy for fiber formation. Therefore, amyloid aggregation is a concentration-dependent phenomenon. The catalyst of this process might be denaturation, overexpression or cleavage of a normally folded protein, as well as production of an intrinsically disordered protein (Eisenberg *et al.*, 2012).

## 1.2 Alzheimer's disease

According to the World Alzheimer's Disease Report by the Alzheimer's Disease International organization (https://www.alz.co.uk/), there are currently about 20 to 30 million

diagnosed Alzheimer's disease patients. Clinically, the first striking symptom of the disease is the progressive loss of short-term memory. As disease advances, more debilitating symptoms appear, such as loss of orientation, language impairment and lack of judgment (J. Xie *et al.*, 2020). Despite the sheer scale of AD, and decades of intensive research, the disease is very far from being completely understood. A complete pathophysiological knowledge of AD is therefore of the utmost importance to minimize human and economic costs of the disease.

Alzheimer's disease was first described by the German doctor Alois Alzheimer in 1906, through the histological identification of its two defining pathological features in brain tissue: intracellular deposition of neurofibrillary tangles (NFTs) and extracellular deposition of amyloid plaques (Alzheimer *et al.*, 1995). The "culprits" for both structures were identified during the 1980s, being the tau protein and the amyloid-β peptide (Aβ), respectively (Glenner *et al.*, 1984; Wood *et al.*, 1986). AD can be classified under two categories: early-onset familial AD (fAD) or late-onset sporadic AD (sAD). Both have associated genetic factors, such as mutations of the genes of amyloid precursor protein (APP) and presenilin 1/2 (PSEN1, PSEN2) in fAD (Cruts *et al.*, 1996; St George-Hyslop *et al.*, 1987) or of the cholesterol-associated apolipoprotein E (apoE) in sAD (Saunders *et al.*, 1993). However, the incidence of both forms is disproportionate, with around 95% of the cases being of sAD. Furthermore, despite similar pathological features, they present distinct disease progressions (Ricciarelli *et al.*, 2017).

Over the years, a few hypotheses have been put forward by researchers as the single, most important cause of Alzheimer's disease, with the first being the cholinergic hypothesis (Perry, 1986). The evidence linking a cholinergic synaptic dysfunction to neurodegeneration is, for example, a decrease in acetylcholine synthesis in the AD brain, cognitive and behavioral dysfunction caused by decrease in brain cholinergic markers and the finding that cholinergic agonists can rescue cognitive dysfunction (Blokland, 1995; Terry *et al.*, 2003). Based on these findings, 4 of the 6 approved clinical drugs for Alzheimer's disease are cholinesterase inhibitors (Francis *et al.*, 1999). However, these drugs do not cure AD. Their action regulates the levels of ACh at the neuronal synapsis, delaying disease progression. Thus, the cholinergic dysfunction alone does not account for AD, likely acting in synergy with other players (*i.e.,* tau and Aβ). A second hypothesis to explain AD is the tau hypothesis (Goedert *et al.*, 1991). Tau is an intrinsically disordered protein (IDP) formed by alternative splicing of the microtubule-associated protein tau gene and is present throughout the nervous system. Under normal conditions, tau is phosphorylated and binds microtubules within central nervous system axons, promoting their formation, stability and avoiding depolymerization. In addition, it may help in neurite growth and axoplasm transport by acting as an enzyme anchor in the cytoskeleton and plasma membrane (J. Xie *et al.*, 2020; Zhao

*et al.*, 2014). However, when tau is abnormally phosphorylated (*i.e.,* hyperphosphorylated) or suffers other modifications, like glycosylation, it changes its conformation and leads to the formation of straight filaments, paired helical filaments and, ultimately, intracellular neurofibrillary tangles. This results in loss of its physiological function, leading to impairment in neuronal communication, neurodegeneration and loss of memory (Avila *et al.*, 2004). In AD patients' brains, these effects occur due to kinase overactivation (*e.g.,* glycogen synthase kinase-3β) and the inactivation of protein phosphatases (*e.g.,* protein tyrosine phosphatase-A). Finally, the most spotlighted hypothesis for AD has been arguably the amyloid hypothesis, in which the extracellular Aβ senile plaques are the main cause of the disease (Hardy *et al.*, 1992). This hypothesis has been evolving throughout the years, from the main culprit being the mature plaques to a more recent approach in which soluble intermediate Aβ oligomers are the cause for neurodegeneration. In addition, AD has also been linked with other pathological features, such as mitochondrial or insulin signaling dysfunction, inflammation, calcium transport dysregulation or cell damage by cell cycle interference.

Alzheimer's disease diagnosis remained virtually unchanged for a long time since its identification by Alois Alzheimer, being performed by searching NFTs and/or Aβ plaques during autopsy (McKhann *et al.*, 1984). The introduction of biomarkers allowed refining disease confirmation when compared to other dementias, and, more importantly, identifying the disease at different stages during the patient's life, not only when dementia presented itself, but also in pre-symptomatic or mild cognitive impairment stages (Chrem Mendez *et al.*, 2019). This is particularly useful for known early-onset fAD cases. The biomarkers can be divided in the invasive collection of cerebrospinal fluid (CSF) levels of $A\beta_{1-42}$ (subscript numbers indicate amino acid number), total tau levels or phosphorylated tau or structural/functional neuroimaging (*i.e.,* hippocampus brain volume, brain metabolic activity or even Aβ plaques detected through imaging *in vivo*)(Chrem Mendez *et al.*, 2019). Despite Aβ and tau have not been single-handedly and undisputedly attributed blame for AD (for example, 30% of not cognitively impaired people present amyloid deposits), they are its defining feature, and hence their combined use as biomarkers.

## 1.3 The Amyloid-β and P3 (or amyloid-α) peptides

Aβ is produced by the cleavage of the amyloid precursor protein (APP). The main form of APP in neurons is a 695 amino acid transmembrane protein with a short C-terminal cytoplasmic domain and a larger glycosylated N-terminal domain, belonging to the transmembrane type-1 protein family. It can be found in glial cells (*i.e.,* oligodendrocytes) and, particularly, in neuronal synapses (Chen *et al.*, 2017; Copani, 2017; Ricciarelli *et al.*,

2017; J. Xie *et al.*, 2020; Zhao *et al.*, 2014). Regarding a physiological role, APP has been implicated in functions such as regulation of synaptic transmission/formation, neuronal transport and metal homeostasis (Duce *et al.*, 2010; Priller *et al.*, 2006; Turner *et al.*, 2003).

APP can be cleaved in one of two ways: “amyloidogenic” or “non-amyloidogenic”, resulting in the formation of either Aβ or P3 peptide, respectively. Both pathways are a two-step process (Figure 1.1). In the “amyloidogenic” pathway, APP is first cleaved by β-secretase, also known as β-site APP cleavage enzyme 1 (BACE1), generating a 99 residue C-terminal fragment (CTFβ/C99) and releasing sAPPβ. The CTFβ/C99 is then cleaved by γ-secretase at possible multiple sites yielding different fragments that are, finally, processed within endocytic compartments to yield Aβ isoforms (from 37 to 49 residues), of which the two most commonly occurring forms are $Aβ_{1-40}$ and $Aβ_{1-42}$ (in basal conditions, 90% $Aβ_{1-40}$ and 10% of other forms). Besides, other N-terminal truncated post-translationally modified forms of Aβ have been identified *in vivo* and attributed significant role in cytotoxicity, such as $Aβ_{2-x}$ and $Aβ_{pE3-x}$ (pyroglutamate modification) (Wildburger *et al.*, 2017). One possible explanation for the overlook of these forms over the decades in AD research might reside in the fact that a broadly used *in* vivo model relies on the so-called Swedish mutation of APP, a mutation that greatly increases Aβ production through the action of BACE1 (Cai *et al.*, 1993). However, Aβ truncated forms are likely the result of post-synthetic proteolytic cleavage.

On the other hand, in the “non-amyloidogenic” pathway, APP is first cleaved by α-secretase, releasing a soluble APPα domain (sAPPα) and leaving a membrane-bound 83 residue C-terminal fragment (CTFα/C83). CTFα/C83 is then cleaved by γ-secretase, resulting in the formation of the P3 peptide. Curiously, the P3 peptide is, in fact, $Aβ_{17-40/42}$. P3 has been found to be released twice as much as Aβ from cultured neurons, while amyloid plaques encompassing this peptide have been found in AD brains (Kuhn & Raskatov, 2020; Moghekar *et al.*, 2011). However, P3 remains largely understudied in the context of AD, which may be explained by: exclusive use of antibodies against N-terminal Aβ do not detect P3, while antibodies against C-terminal do not distinguish both forms; extraction and handling of both peptides should be tailored, as the lack of the hydrophilic N-terminal affects peptide solubility and stability; without tyrosines, UV-Vis detection is a challenge (Kuhn & Raskatov, 2020). These difficulties explain why only a single study relates CSF P3 peptide levels with AD (Abraham *et al.*, 2013) and, crucially, there are no reports of Aβ/P3 interactions. Nevertheless, P3 has been identified with amyloid characteristics. It forms cross-β sheet containing fibrils (as detected by green birefringence and circular dichroism), its transmission electron microscopy analyzed fibrils closely resemble Aβ quiescent fibrils, it can be detected by the anti-amyloid fibril OC antibody and it aggregates faster than Aβ (Ali *et al.*, 2000; Kuhn, Abrams*, et al.*, 2020). Furthermore, oligomer induced cell-toxicity is

greater for hydrophobic species, and thus P3 likely plays a role in AD toxicity, despite *in vitro* showing a higher cell viability (Bolognesi *et al.*, 2010; Kuhn, Abrams*, et al.*, 2020). In this context, a renaming of P3 peptide to “amyloid-α peptide” has been proposed (Kuhn, Abrams*, et al.*, 2020).

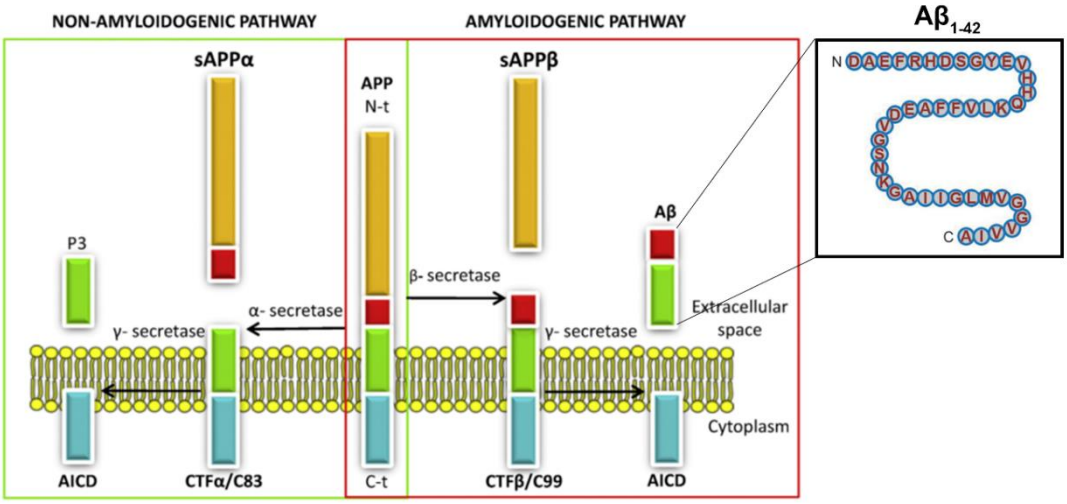


**Figure 1.1.** Amyloid precursor protein (APP) two-step cleavage, by either α- and γ-secretase (non-amyloidogenic pathway) or β- and γ-secretase (amyloidogenic pathway), yielding P3 or Aβ peptides, respectively. (inset) $A\beta_{1-42}$ amino acid sequence. The peptide has two predominantly hydrophilic regions ($A\beta_{1-16}$ and $A\beta_{22-29}$) and two hydrophobic cores ($A\beta_{17-21}$ and $A\beta_{30-40/42}$). Adapted from (Chen *et al.*, 2017; Montoliu-Gaya *et al.*, 2015).

The “amyloidogenic” APP cleavage provides strong evidence for the AD amyloid hypothesis, particularly the hereditary familial form. BACE1 is a transmembrane aspartyl protease and constitutes the limiting step in Aβ formation. γ-secretase, on the other hand, is a multicomponent protease complex, composed by presenilin 1 or 2 (PSEN1/2), nicastrin, presenilin enhancer 2 and anterior pharynx defective 1, that together exert endopeptidase and carboxypeptidase activity. As mentioned before, mutations of the genes of amyloid precursor protein (APP) or presenilin 1/2 (PSEN1, PSEN2) correlate with fAD (Cruts *et al.*, 1996; St George-Hyslop *et al.*, 1987). People with Down’s syndrome have an extra copy for the APP gene (present in chromosome 21) and invariantly develop AD, showing overproduction of Aβ and P3 peptides, the latter of which are also a major component of diffuse amyloid plaques in these patients (Kuhn & Raskatov, 2020). Curiously, people with chromosome duplication excluding the APP gene exhibit Down’s syndrome pathology, but not AD; on the other hand, people with rare micro-duplication of the APP gene develop AD, but not Down’s syndrome (Prasher *et al.*, 1998; Rovelet-Lecrux *et al.*, 2006). Missense mutations (*i.e.,* single nucleotide change that results in a different amino acid) are also critical. Regarding PSEN1/2, missense mutations lead to the preferential formation of

longer, more aggregation prone Aβ forms (like $A\beta_{1-42}$ and $A\beta_{1-43}$), such as the well-documented E280A in PSEN1 (Fuller *et al.*, 2019). On the other hand, an A673T APP mutation changes the second residue of Aβ (Figure 1.1, inset), resulting in less amyloidogenic cleavage and, when this pathway does occur, the resulting Aβ is less aggregation prone (Zheng *et al.*, 2015). Other APP mutations result in a variety of Aβ mutations (numbers refer to Aβ residues): A2V (increases Aβ production and aggregation (Di Fede *et al.*, 2009)); H6R and D7N (English and Tottori mutation, respectively; more prone to fibril seeding and increased oligomeric toxicity (Ono *et al.*, 2010)); A21G (Flemish mutation; favors APP amyloidogenic pathway (Tang *et al.*, 2014)); D23N (Iowa mutation; increased fibrillation (Grabowski *et al.*, 2001)); finally, several mutations affect residue E22, namely E22Δ (Osaka mutation, a deletion that reduces Aβ secretion, favoring intracellular aggregation (Ovchinnikova *et al.*, 2011)), E22G (Arctic mutation, results in increased protofibril formation and lower Aβ circulating levels (Nilsberth *et al.*, 2001)), E22Q (Dutch mutation, increased Aβ aggregation (Davis *et al.*, 1996)) and E22K (Italian mutation, potentiates aggregation of stable oligomers (Masuda *et al.*, 2008)).

### 1.3.1 The Amyloid-β peptide: physiological roles

Traditionally, the Aβ peptide had been defined as exclusively disease-associated when in fibril form. However, one might wonder that if evolution maintained it virtually intact (particularly, its amyloidogenic core of residues $A\beta_{16-21}$, KLVFFA, Figure 1.1, inset) across different species, it is unlikely to be a simple evolutionary byproduct (Copani, 2017). In fact, the Aβ monomer is, like tau, an intrinsically disordered protein (IDP). This confers it the ability to bind a multitude of targets. The amyloidogenic APP cleavage pathway is present in healthy brain tissue, where numerous proteases, such as neprilysin and endothelin converting enzymes, can handle Aβ clearance. As amyloid aggregation is concentration-dependent, the balance between basal state and pathology seems to be dependent on the Aβ production/degradation ratio. The current knowledge of the physiological function of the Aβ monomer is limited and comes mostly from indirect observations. Aβ has been attributed two tightly interconnected roles: neuronal homeostasis and synaptic activity.

Aβ in complex with components of extracellular matrix (ECM), like fibronectin, was shown to promote neuron growth (Koo *et al.*, 1993). *In vitro*, in neuron cell lines, absence of Aβ (for example, by immuno-depletion) led to cell death, a phenotype reverted by addition of physiological concentrations of exogenous $A\beta_{1-40}$. This effect might occur due to the control of neuron excitability, as Aβ levels appear also to be related to the expression of potassium channels (Plant *et al.*, 2006). Furthermore, Aβ may modulate neurite outgrowth, for example, by increasing tau concentrations, essential for microtubule formation (C. Wang

*et al.*, 2000). Interestingly, given the most known symptom of AD, a counter-intuitive function of Aβ is that, at physiological levels, it presented a memory enhancing function. Aβ administered to mice where APP/Aβ had been previously depleted improved memory tests scores (Puzzo *et al.*, 2011). This memory enhancing role may be related to the ability of Aβ to increase acetylcholine production and promote neuron growth by activation of protein kinases, such as phosphatidylinositol 3 kinase (PI3K) or mitogen-activated protein kinase (MAPK), possibly providing a link between Aβ and NFT formation by tau hyperphosphorylation if this process becomes deregulated (Luo *et al.*, 1996; Morley *et al.*, 2012; Sui *et al.*, 2008). Another neuronal homeostatic effect of Aβ is related to brain glucose metabolism. Binding the insulin receptor IGF-IR promotes glucose uptake in depolarized neurons (Giuffrida *et al.*, 2015). Both Aβ and insulin are able to bind the insulin receptor, while type 2 diabetes (insulin-resistant, with occurrence of hyperinsulinemia and hyperglycemia) is a known risk factor for Alzheimer's disease (Sims-Robinson *et al.*, 2010; L. Xie *et al.*, 2002). In fact, Aβ inhibits the action of insulin by competing for the receptor. Concomitantly, insulin-degrading enzyme (IDE) is also able to cleave Aβ but has higher affinity towards insulin (Qiu *et al.*, 1998). In hyperinsulinemia, IDE-mediated Aβ clearance is hindered by excess insulin, resulting in elevation of peptide concentration and subsequent neurotoxic effects. Interestingly, in other neurodegenerative diseases that do not present amyloid plaques, such as amyotrophic lateral sclerosis, CSF Aβ levels are also decreased, hinting that this peptide may indeed be important for neuronal function (Sjogren *et al.*, 2002).

Regarding synaptic activity, Aβ was attributed a role as a repressor of excitotoxicity by avoiding excess release of the neurotransmitter glutamate and consequent synaptic activity. In APP KO mice, seizures were potentiated; when a γ-secretase inhibitor was used, increased excitatory postsynaptic potential was detected, likely due to changes in potassium channel expression (Kamenetz *et al.*, 2003; Steinbach *et al.*, 1998). There is also proof that excessive N-methyl-D-aspartic acid receptor (NMDA) receptor activation by glutamate results in a feedback loop that increases Aβ production as a counter-measure (Lesne *et al.*, 2005). Aβ was also found to be a modulator of synaptic vesicle release at the pre-synaptic junction in the hippocampus (Abramov *et al.*, 2009). Finally, Aβ was found to act similarly to an innate immune response anti-microbial peptide (Kumar *et al.*, 2016).

### 1.3.2 The Amyloid-β peptide: interactions and pathological roles

#### 1.3.2.1 Circulating proteins

As examples of Aβ interactions with circulating proteins we have apolipoprotein E (apoE), human serum albumin (HSA) and transthyretin (TTR). As mentioned before, the most undisputed genetic link associated with sAD so far is an apoE mutation (Saunders *et*

*al.*, 1993). ApoE is involved in lipid metabolism, is present in the brain and blood with different isoforms (E2, E3 or E4) and binds Aβ ($Aβ_{12-28}$) for its clearance with different affinities according to the isoform; ApoE4 binds Aβ with less affinity and thus the increased propensity for developing AD in individuals where this isoform is more prevalent (Tokuda *et al.*, 2000). HSA is the most prevalent protein in the serum, with extremely high binding capacities to a plethora of circulating proteins/peptides, including monomeric Aβ (Kuo *et al.*, 2000). HSA is much more prevalent in the serum than the CSF, which possibly accounts for the significant difference between CSF and blood Aβ levels, also explaining why amyloid plaques deposit in the brain, but not in peripheral tissues (Stanyon *et al.*, 2012). A decrease of HSA levels correlates with the onset of AD (Kim *et al.*, 2006), likely because HSA is able to delay or inhibit Aβ fibrillation by sequestering free monomer and, thus, also impacting the occurrence of the formation of toxic oligomeric species in the fibrillation pathway (Stanyon *et al.*, 2012). Similarly, TTR is also present in the CSF and serum and its levels correlate with AD (Ribeiro *et al.*, 2012), being able to inhibit fibrillation and promote Aβ clearance (Ribeiro *et al.*, 2014).

#### 1.3.2.2 Cell receptors

Aβ also binds cell receptors, triggering downstream signaling effects. These include the insulin-receptor, NMDA receptor, α7nAChR (α7 nicotinic acetylcholine receptors), RAGE (receptor for advanced glycation end products) or LRP (low-density lipoprotein receptor-related protein). RAGE acts as a receptor activating different signaling cascades, but also as an Aβ transporter across the BBB, from blood to brain. The latter function leads to an increase in cerebral Aβ levels, influencing AD pathology (Deane *et al.*, 2003). Regarding the signaling cascade, effects include inflammation, oxidative stress and synaptic dysfunction by a positive loop effect of RAGE/Aβ expression (Cho *et al.*, 2009; Herold *et al.*, 2007). Contrarily to RAGE, LRP is involved in the clearance of Aβ from the brain across the BBB by endocytosis or transcytosis; its levels are reduced in AD, while RAGE is overexpressed, constituting yet another candidate mechanism for AD amyloid plaque formation initiation (Donahue *et al.*, 2006). Aβ interaction with NMDA and α7nACh receptors may also trigger deleterious consequences. In pathologic conditions, Aβ overproduction is detrimental as Aβ oligomers disrupt calcium levels and cause cell death by binding to the NMDA receptor (Alberdi *et al.*, 2010). This constitutes the background for the action of the NMDA blocker memantine, the only approved AD drug that is not a cholinesterase inhibitor (Matsunaga *et al.*, 2015). In addition, Aβ may induce tau hyperphosphorylation by binding the α7nACh receptors and triggering the extracellular-signal-regulated kinase (ERK) and c-Jun N-terminal kinase (JNK) signaling pathways (H.

Y. Wang *et al.*, 2003). Aβ may also interact with multiple immunity-related cell receptors, triggering cell-mediated and inflammatory responses. For example, interaction of Aβ fibrillar forms with toll-like receptors (TLR), such as TLR-2, leads to microglia activation and consequent inflammatory response (Jana *et al.*, 2008). Peripheric deposits of the peptide can also trigger central nervous system (CNS) deposition. These deposits were already observed in AD patients. Recently, it was found that intra-gastrointestinal injection of Aβ oligomers affect cognitive function and resulted in weight changes, something also linked to AD dementia (Ikeda *et al.*, 2002; Sun *et al.*, 2020). This indicates that Aβ oligomers can migrate from the periphery to the brain via, for example, axonal transport in vagal nerves, after internalization in the enteric nervous system (Sun *et al.*, 2020). A similar periphery to brain transport through monocytes has also been described (Cintron *et al.*, 2015).

#### 1.3.2.3 Intracellular proteins

Besides with circulating proteins and cell-receptors, intracellular Aβ interactions is also an early event in AD, including with mitochondrial components (LaFerla *et al.*, 2007). Intracellular targets include the endoplasmic reticulum-associated Aβ peptide binding protein (ERAB; extracellular Aβ upregulates ERAB and their intracellular interaction causes apoptosis (Yan *et al.*, 1997)) and chaperone proteins (*i.e.,* heat-shock proteins (Fonte *et al.*, 2002)). Mitochondrial dysfunction and accompanying oxidative stress are a key early event in AD pathogenesis. For example, Aβ can bind a subunit of cytochrome C oxidase, which aggregates the peptide and causes, for instance, respiratory chain impairment (Hernandez-Zimbron *et al.*, 2012). Similar deleterious effects can also be caused by Aβ interactions with voltage-dependent anion channels (VDAC), a component of the mitochondrial permeability transition pore (mPTP). Interaction with VDAC-1 leads to mitochondria failure and cell death; notably, VDAC-1 is upregulated in AD brains (Manczak *et al.*, 2012). Lastly, mitochondrial impairment can also be caused by interaction of Aβ with some of its enzymes, such as the mitochondrial peptidasome human presequence protease (hPreP) or Aβ-binding alcohol dehydrogenase (ABAD). ABAD is an enzyme present in the mitochondrial matrix of neurons; Aβ/ABAD interaction causes memory impairment through oxidative stress and cell death (Lustbader *et al.*, 2004). In addition, hPreP is an enzyme able to degrade $A\beta_{1-40}$ and $A\beta_{1-42}$, but its activity is lowered in AD brains. Thus, Aβ accumulation and negative effects on mitochondria may inactivate hPreP, further aggravating Aβ aggregation (Alikhani *et al.*, 2011; Falkevall *et al.*, 2006).

### 1.3.2.4 Metal ions

Finally, several studies suggest that dyshomeostasis of transient metal cations and their interactions with Aβ play an important role in AD pathogenesis. Copper (Cu) and zinc (Zn) both localize extracellularly in the brain, showing elevated levels in AD patients and being present in amyloid plaques (Brewer *et al.*, 2010; Religa *et al.*, 2006). Zn binds the N-terminal of Aβ ($A\beta_{1-16}$)(Zirah *et al.*, 2006), promoting its aggregation to an amorphous state (Rezaei-Ghaleh *et al.*, 2011). In an animal model, Cu was found to induce neurotoxicity by increasing Aβ levels (Singh *et al.*, 2013). An increase in neurotoxicity has also been linked to oxidative stress caused by the reduction of Cu to a more toxic state when bound to Aβ (Hureau *et al.*, 2009). Another interesting observation points to the fact that the negative effect of the metal might depend on the metal/Aβ molar ratio and the Aβ form in question, with the metal directly influencing the peptide's oligomeric state. Sub-equimolar Cu/Aβ ratios resulted in the formation of somewhat stable protofibrils ($A\beta_{1-40}$ aggregates and $A\beta_{1-42}$ in monodisperse cylindrical form), while at supra-equimolecular Cu/Aβ ratios led to the formation of toxic oligomeric species, specially of the more toxic/aggregation prone $A\beta_{1-42}$ (Ryan *et al.*, 2015). Curiously, both Zn and Cu have a dichotomic effect on Aβ. On the one hand, they produce neurotoxic effects by inducing production of reactive oxygen species (ROS) and oxidative stress when bound to Aβ (Hureau *et al.*, 2009). On the other hand, by promoting Aβ aggregation to an amorphous state, they prevent the formation of highly toxic intermediate oligomeric species. In addition, in a monomeric state, Aβ sequesters metal ions, avoiding the oxidative stress induced by them (Hou *et al.*, 2006). However, a strategy to inhibit metal-associated plaque formation or, in particular, promote plaque disaggregation does not appear to be particularly interesting, as it resulted in increased neurotoxicity by the formation of toxic oligomers, in a reversal of the fibril formation pathway (Sharma *et al.*, 2012). In addition, iron (Fe) also interacts with Aβ, binding at the N-terminal of the peptide (Bousejra-ElGarah *et al.*, 2011), accumulates intracellularly and causes toxicity by generation of ROS and lipid oxidation (Rottkamp *et al.*, 2001). Accumulation of Fe and Zn, intra and extracellularly, respectively, appears to be interconnected, as Zn inhibits the transporter of Fe (Duce *et al.*, 2010). Finally, Al is also a potential Aβ aggregation enhancer, leading to the formation of β-sheets and neurotoxicity, as well as inhibiting Aβ clearance by the serine protease plasmin (Exley, 2006; Korchazhkina *et al.*, 2002).

## 1.4 The Amyloid Hypothesis

Following the discovery of Aβ as the component of the amyloid plaques (Glenner *et al.*, 1984), a landmark paper by Hardy and Higgins established the amyloid cascade

hypothesis, stating that the “deposition of amyloid β protein, the main component of the plaques, is the causative agent of Alzheimer's pathology and that the neurofibrillary tangles, cell loss, vascular damage, and dementia follow as a direct result of this deposition” (Hardy *et al.*, 1992). As reviewed by one of the authors of this hypothesis a quarter of century later, several cumulative observations support an Aβ-centric AD pathology (Selkoe *et al.*, 2016), including the previously mentioned genetic factors (*i.e.,* mutations to the APP, PSEN or ApoE genes), neurodegenerative effects and tau hyperphosphorylation. Furthermore, neuronal synapse dysfunction appears to inversely correlate to the neuronal distance to amyloid plaques, while low Aβ CSF levels as well as plaques detected *in vivo* by imaging techniques precede, by decades, the onset of other metabolic dysfunctions (*e.g.,* glucose metabolism) (Selkoe *et al.*, 2016).

Nevertheless, the amyloid hypothesis has also been put under scrutiny as the cause for AD. Some state that the observed oligomeric states of Aβ samples isolated from AD brains that cause *in vitro* cell death are artifacts from purification procedures and do not occur *in vivo* (*i.e.,* the mouse models of AD do not exhibit such neurotoxicity)(Ricciarelli *et al.*, 2017). Furthermore, people not clinically diagnosed with dementia present *post mortem* amyloid brain deposits, some studies suggest that NFTs precede amyloid plaques and amyloid plaque does not correlate as strongly with cognitive impairment as other features, like NFTs (Schonheit *et al.*, 2004). The counter-arguments for these observations are, respectively, that such plaques have a lower Aβ oligomer content than in AD cases, APP mutations resulting in increased Aβ production can lead to tau hyperphosphorylation (but not the other way around) and, finally, amyloid dysfunction may be the first event in the pathologic cascade, triggering, for example, NFTs formation and mitochondrial dysfunction, themselves the cause for cognitive impairment (Selkoe *et al.*, 2016). In fact, “Aβ may be the trigger, but tau the bullet” in the AD cascade and neurodegeneration (Bloom, 2014). If so, Aβ would trigger the “tau hypothesis”. Finally, the existing doubts about the “amyloid hypothesis” may stem from the existing *in vivo* models, resulting in studies that do not translate well to the human pathology. Adding to the previously mentioned fact that they do not represent the multiple isoforms of Aβ observed in human AD brains, they also model fAD (based on known genetic mutations, namely in the APP gene), while sAD accounts for the majority of AD cases. Current models show critical features very distinct from human AD, namely they do not present extensive neuronal death or NFTs formation and they over express APP (which only occurs in a minority of cases, like Down’s syndrome patients). In short, they are essentially designed to study APP processing and Aβ formation and not to mimic AD in its entirety (accounting, for example, for risk factors associated with sAD). Therefore, the development of more accurate models is of the utmost importance (Onos *et al.*, 2016; Ricciarelli *et al.*, 2017).

In addition, some voices against the amyloid hypothesis claim that the multiple failed Aβ targeting drugs under trial over the years prove Aβ is not the main culprit for AD. Regarding this, besides the abovementioned lack of appropriate animal models or Aβ triggering tau hyperphosporylation as the causative agent of cell death, Doig and colleagues proposed an interesting set of reasons for such clinical trial failure, including: a large discrepancy between physiological and *in vitro* concentrations of Aβ (observed oligomeric species to which drugs are developed for may never occur *in vivo*); lack of reproducibility of *in vitro* tests (due to the inherently unstable nature of Aβ preparations); drugs are highly specific for a particular Aβ form; small molecules bind much more tightly to aggregates than to monomeric Aβ (if aggregates are indeed an AD endpoint, the designed drugs are of little effect); proposed targets are not ideal, because they have many substrates (*i.e.,* γ-secretase inhibitors); clinical trials rely on clearly diagnosed patients, which could be too late in disease progression to observe any reverting effect; finally, there is a lack of high resolution structural models of Aβ (by themselves or interacting with one of the many players mentioned before)(Doig *et al.*, 2017).

In this context, new amyloid hypotheses are being put forward, explaining the observed "failures" of the amyloid cascade hypothesis, while keeping Aβ as the key player in AD. Over the years, the amyloid hypothesis has been evolving, from the idea that Aβ mature plaques are the cause of dementia to a more contemporary view where Aβ exerts its toxicity through soluble and toxic oligomeric species, that not only act directly on several cell processes, but also deplete a physiological pool of Aβ monomer, itself critical for neuronal homeostasis. This originates the "Aβ dysfunction" hypothesis (Hillen, 2019). Contrary to the amyloid cascade hypothesis, where Aβ is regarded as a disease-only component, the amyloid dysfunction hypothesis gives great relevance to the discussed physiological role of Aβ as modulator for the synaptic vesicle cycle: disruption of the Aβ production/clearance balance by yet unknown factors hinders its neurotrophic effects. In addition, formation of different forms, ratios and/or oligomeric species not only inhibit Aβ's physiological effect, but also interact with multiple cell components to cause, or at least indirectly induce, neurodegeneration. This hypothesis allows to address some of the criticisms to the amyloid cascade hypothesis, such as amyloid plaques not correlating with cognitive impairment. Furthermore, it gives some explanations (beyond key issues, like drug delivery and bioavailability) to previous failures in AD amyloid clinical trials: secretase modulators should be more efficacious than inhibitors and tested immunotherapies against the monomer or mature fibrils do not work, because the true culprits are oligomers (Hillen, 2019). In conclusion, an amyloid hypothesis, whatever form it may assume, still lives on.

## 1.5 Structural biology applied to the Amyloid-β peptide

In this section, current structural information will be discussed, with emphasis on single crystal analysis by X-Ray diffraction, including isolated fragments and protein-Aβ crystal complexes. The few available cases of protein-fusion constructs encompassing Aβ regions will be discussed in the context of CHAPTER III. In addition, data from the recently advanced cryogenic electron microscopy (cryoEM) technique and fibril models obtained with nuclear magnetic resonance (NMR) and cryoEM is also briefly discussed.

### 1.5.1 Amyloid-β peptide isolated fragments

Until now, no crystal structures of the full isolated Aβ peptide are available. However, Aβ fragments have been crystallized, disclosing some structural features of Aβ aggregates, presumably in disease-relevant conformations. Eisenberg and collaborators determined 7 distinct Aβ fragment structures, that together comprise the segment $A\beta_{16-42,}$ and coined the term “steric zipper” (Colletier *et al.*, 2011; Nelson *et al.*, 2005; Sawaya *et al.*, 2007). This consists of complementary interconnected sidechains of amino acids in adjacent sheets, physically resembling the teeth of a zipper, and constitutes the core binding motif of the amyloid cross-β motif. Crystallographic data suggests features that confer the cross-β motif its robustness (Figure 1.2). First, the zipper interface is dry, which potentiates the strength of the hydrophobic interaction, in combination with hydrogen bonds. Next, it is formed by self-complementary, interdigitating amino acid sequences, independent of their nature (*e.g.,* size, electrostatic nature). It is, however, worth noting that some amyloids might be formed by heterosteric zippers (Luhrs *et al.*, 2005). Finally, their typical in-register conformation allows not only strong hydrogen bonds, but also stacking, particularly for glutamine, tyrosine and asparagine residues. A second striking feature extrapolated from Eisenberg’s work is that Aβ assemblies are structurally polymorphic in nature, meaning that for the same environmental conditions (temperature, pH, etc) different structural arrangements are possible for the same fragments, as is the case of $A\beta_{16-21}$ (Figure 1.2A-C). This polymorphism presents three variations. The fact that different regions of the Aβ peptide can interdigitate results in segmental polymorphism; the same fragment can stack in different conformations, which is termed packing polymorphism; finally, despite typically amyloid fibrils being homotypic (same segment constitutes the cross-β-sheet spine), heterotypic polymorphism has been observed (binary mixtures of Aβ yield fibrils with distinct morphologies) (Colletier *et al.*, 2011). Overall, polymorphism is one of the possible explanations for the difficulties in obtaining high resolution atomic crystallographic models and the multitude of different fibril arrangements obtained through NMR. The

crystallographic data, however, only confirms segmental and packing polymorphism of Aβ fragments suggesting that, for Aβ, each molecule has multiple interaction sites capable of being the backbone of the cross-β-spine of the fibril. This might further explain why amyloid fibrils of the same Aβ peptide present different degrees of toxicity in neuronal cells (A T Petkova *et al.*, 2005). Two observations point to the fact that the segments presented in Figure 1.2 are very similar to the structure of the core of the full fibrils. Firstly, the X-ray diffraction patterns of the microcrystals and of fully formed protein fibrils are closely related, namely regarding the inter-sheet and inter-strand distances (Sawaya *et al.*, 2007). Secondly, if single amino acid mutations within the identified steric zipper forming fragments are generated, the formation of the full fibrils is impacted. For instance, mutations M35L, G37D and G38F slow or even disrupt the fibril formation process (Kanski *et al.*, 2002; Luhrs *et al.*, 2005).

Cross-seeding fibril formation properties of distal Aβ segments that alone do not fibrillate were also investigated (Do *et al.*, 2018). The selected fragments were the mutants $A\beta_{19-24}$ F19I (named I6V by the authors) and $A\beta_{27-32}$ I32F (named N6F by the authors) and were selected based on the following criteria: contain pairs of hydrophobic residues that facilitate nucleation, opposite net charges to promote cross aggregation and a Rosetta energy of around -20 $kcal.mol^{-1}$ (this energy function uses small molecule and protein crystallographic data to estimate the energy of each biomolecule conformation; the lower the value, the more stable it is (Alford *et al.*, 2017)). The native selected fragments contain residues described to be essential for fibril structure formation, such as F19, D23, K28 and I32. Therefore, the introduced mutations (F19I and I32F) aimed at reducing the aggregation propensity of each fragment (Do *et al.*, 2018). Using a combination of atomic force microscopy (AFM) and Ion-mobility spectrometry–mass spectrometry (IM-MS), it was shown that the peptides by themselves did not aggregate to mature fibril (with I6V being less aggregation prone than N6F). However, when combined, they did form hetero-oligomers and full fibrils, with I6V also forming homo-oligomers. When alone, the I6V fragment formed a class 7 steric zipper without a dry interface (Figure 1.2L), meaning that the interactions are not as stable and explaining the formation of globular aggregates rather than full fibrils. On the other hand, the N6F crystals form a class 1, tightly hydrophobic steric zipper (Figure 1.2M) with two possible interfaces (packing polymorphism), very similar to the ones by the native peptide fragment (Figure 1.2D), and thus is more prone to aggregation than I6V, as assessed by AFM (Do *et al.*, 2018). When crystallized in an equimolar condition, only crystals of the I6V fragment were obtained. However, these were in a different packing than before, now showing a class 8 steric zipper with anti-parallel β-sheets (Figure 1.2N). The authors proposed a catalysis mechanism in which N6F induces I6V to form homo or hetero oligomers more readily and even full fibrils. Together, these

results suggest that distal Aβ fragments that by themselves do not aggregate are able to do so when mixed together (Do *et al.*, 2018).

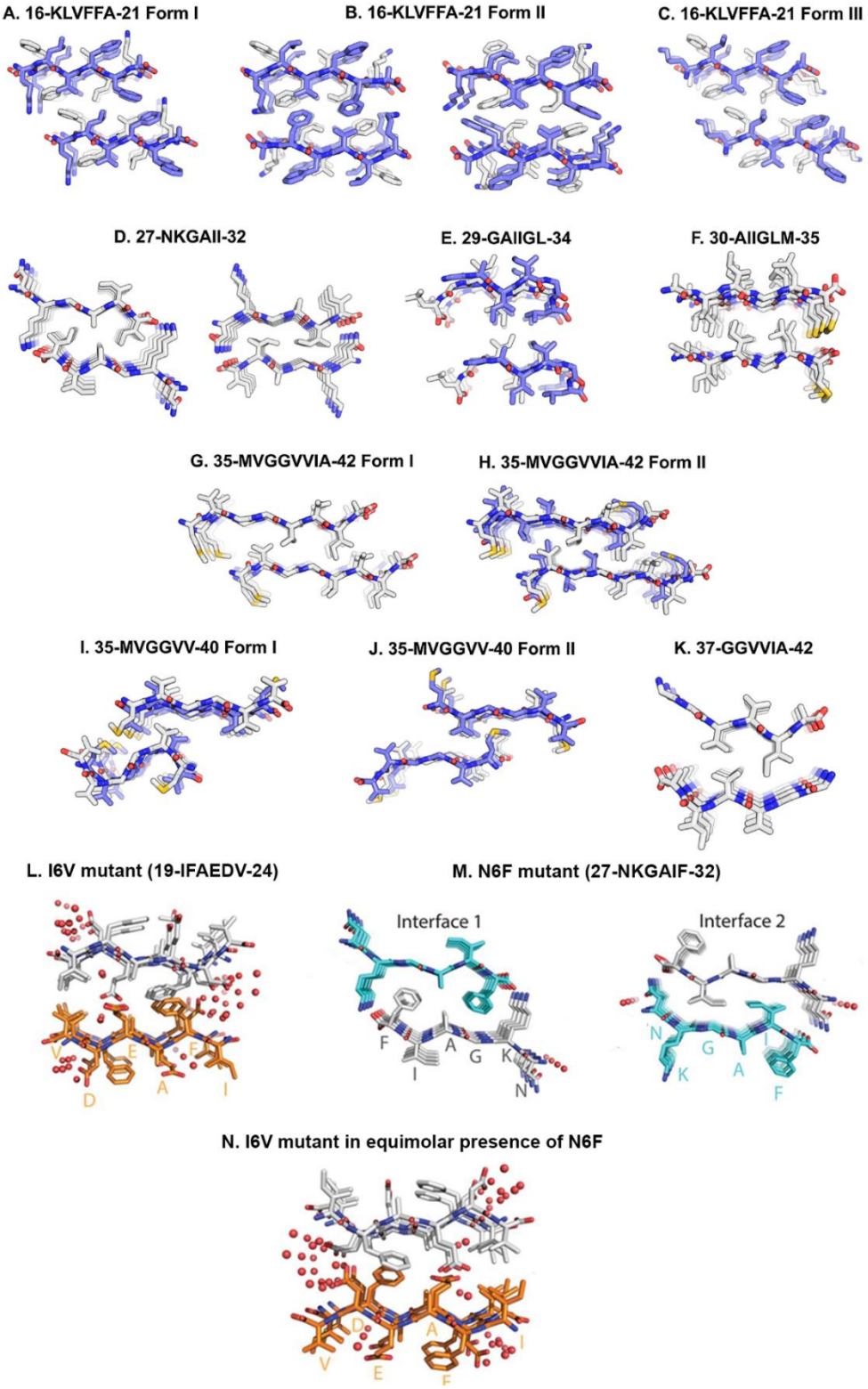


**Figure 1.2.** X-ray diffraction crystal structures of Aβ peptide fragments. Images represent a top view on the fibril axis. (A-C) $A\beta_{16-21}$ polymorphs; (D) $A\beta_{27-32}$; (E) $A\beta_{29-34}$; (F) $A\beta_{30-35}$; (G-H) $A\beta_{35-42}$ polymorphs; (I-J) $A\beta_{35-40}$ polymorphs; (K) $A\beta_{37-42}$. (L) $A\beta_{19-24}$ F19I (named I6V by the authors). (M)

$A\beta_{27-32}$ I32F (named N6F by the authors). (N) I6V crystals when crystallized in the equimolar presence of N6F. Water molecules as red spheres. Adapted from (Colletier *et al.*, 2011; Do *et al.*, 2018; Sawaya *et al.*, 2007).

In X-ray crystallography, a diffraction pattern is obtained by the diffraction of X-ray photons upon interacting with a relatively large and robust macromolecule crystal. For IDPs like Aβ, crystal growth has been a very difficult hurdle to overcome. As such, some recent works have been employing a cryo-EM derived technique called micro electron diffraction (microED), in which data can be collected from crystals up to six orders of magnitude smaller than for X-ray crystallography (*i.e.,* microcrystals) (Shi *et al.*, 2013). First, a microED study of $A\beta_{24-34}$ and its crossing seeding with a fragment from human islet amyloid polypeptide (hIAPP) may provide a structural link between AD and type II diabetes (Krotee *et al.*, 2018). This cross seeding was observed *in* vivo, with hIAPP or Aβ seed injection in hIAPP transgenic mice inducing amyloid deposition (Oskarsson *et al.*, 2015)), and thought to occur because fibrils of one peptide lower the energy barrier for nucleation of the other. The microED structure reveals a class I steric zipper of in-register antiparallel β-sheets, with dry interface in two possible arrangements (Figure 1.3A). Of the two interfaces, the diffraction pattern of interface A closely relates to the diffraction pattern of $A\beta_{1-42}$ fibrils, leading the authors to propose this as the spine of those fibrils (Krotee *et al.*, 2018). To further support this, $A\beta_{24-34}$ also evidenced cytotoxicity, particularly in fibrillar form. Interestingly, the $A\beta_{24-34}$ structure is very similar to $hIAPP_{19–29}$ S20G and cross-seeding appears to rely more on structural similarities than sequence homology (Krotee *et al.*, 2018). This work may provide an important link between AD and type II diabetes and new avenues for therapy of both diseases, as hIAPP fibril inhibitors also worked on $A\beta_{1-42}$ (Krotee *et al.*, 2018). Next, there is the microED structure of $A\beta_{20-34}$ and $A\beta_{20-34}$ L-isoaspartate D23 (Warmack *et al.*, 2019). Post-translational modifications (PTMs) on the Aβ peptide make aggregation more likely, such as isomerization of D23 (or N23 in the Iowa mutation) resulting in increased aggregation, despite the presence of a repair enzyme in the brain (L-isoaspartate (D-aspartate) O-methyltransferase, PCMT1) (Warmack *et al.*, 2019). Both structures form steric zippers, in two possible interfaces, with a β-helix-like turn topology (Figure 1.3B). Despite similarities with the previously discussed $A\beta_{24-34}$ structure, as well as with full fibril structures, $A\beta_{20-34}$ and $A\beta_{20-34}$ L-isoaspartate D23 show a previously unknown interface (Figure 1.3, interface B). In the native peptide, this interface contains water molecules and an important bond is established between D23 and K28 (Figure 1.3B). On the isomerized form, however, the interface is not only completely dry but also evidences higher surface complementarity, with D23 interacting with S26 (Figure 1.3B). This observation, or possibly the facilitation of a nucleus formation by the methylene group of L-

isoaspartate D23, may explain why the PTM peptide has increased fibrillation propensity and why such fibrils are more resistant and stable (for example, to SDS degradation). The same mechanism occurs in the Iowa mutation. Notably, despite being detected in low concentration *in vivo*, isomerized Aβ can seed fibrils of the native peptide and is resistant to PCMT1 action. The slow and gradual accumulation of PTM such as isomerization might, therefore, be at the stem of sporadic AD (Warmack *et al.*, 2019). Lastly, there is the microED structure of $A\beta_{16–26}$ D23N (Iowa mutation) (Griner *et al.*, 2019). As previously mentioned, tau hyperphosphorylation and/or aggregation may be triggered by Aβ dysregulation. The $A\beta_{16–26}$ D23N structure (Figure 1.3C) reveals an anti-parallel β-sheet with a C-terminal non-β extended conformation. The class VII steric zipper is formed by residues K16, V18, F20 and E22 of one strand interdigitating with L17, F19 and the N-terminus of another. Interestingly, the overall structure is similar to form I of $A\beta_{16\text{-}21}$ (Figure 1.2A), with a notable exception: the hydrogen bonds are out-of-register (*i.e.,* non-canonical cross-β motif). This feature, together with a comparison with elongated β strand also observable in residues K16-E22 in a cryo-EM $A\beta_{1\text{-}42}$ fibril model (Gremer *et al.*, 2017), led the authors to propose the structure as sharing both amyloid and toxic oligomeric features (Griner *et al.*, 2019). Using a rational design approach, Aβ inhibitors were designed based on this structure. The selected molecules inhibited $A\beta_{1\text{-}42}$ fibrillation, neutralized toxic oligomers and could dissociate pre-existing aggregates (both *in vitro* and in disease conformations, retrieved from brain samples). More importantly, these inhibitors allowed the study of Aβ-tau cross-seeding. Aβ was found to cross-seed tau, although to a lesser extent than tau to itself. Aβ aggregation inhibitors led to a decrease in tau seeding, hinting that Aβ oligomers/fibrils may indeed be a trigger for NFT formation. Through mutant analysis and comparison with previous structures (backbone alignment and residue complementarity), the interaction could be mapped to tau and Aβ segments (VQIINK/VQIVYK and $A\beta_{16\text{-}22}$, respectively) In addition, the inhibitors are specific for these AD players (they do not act, for example, on hIAPP). Overall, this structural analysis provided important clues linking Aβ and tau (Griner *et al.*, 2019), assuming extreme relevance under the previously discussed possible AD pathogenesis events: Aβ is critical to trigger NFT neurotoxicity but not the “bullet” itself.

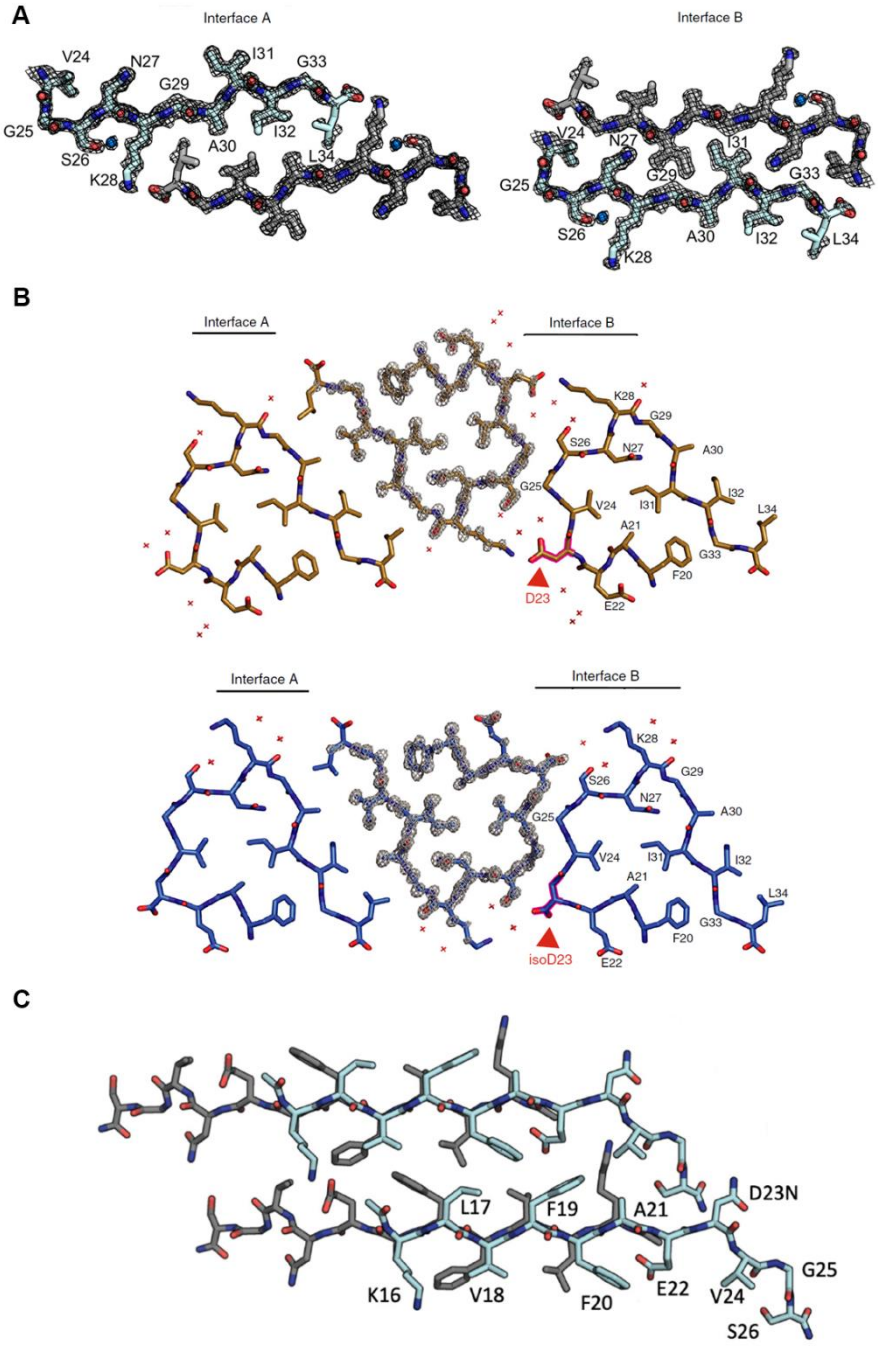


**Figure 1.3.** Micro electron diffraction crystal structures of Aβ peptide fragments, looking down on fibril axis. (A) $Aβ_{24-34}$, showing two possible class I steric zipper dry interface arrangements, with in-register antiparallel β-sheets. Black mesh represents $2F_o$-$F_c$ map at 1σ contour. (B) $Aβ_{20-34}$ (orange) and $Aβ_{20-34}$ L-isoaspartate D23 (blue) crystal structures. For each fragment, two possible interfaces are present. Black mesh represents $2F_o$-$F_c$ map at 2σ contour, red crosses are water molecules. Residue D23 (native or isomerized) highlighted by red arrow. (C) $Aβ_{16–26}$ D23N crystal structure, with a dry and out-of-register class VII steric zipper between K16, V18, F20 and E22 of one strand and L17, F19 and the N-terminus of another. Adapted from (Griner *et al.*, 2019; Krotee *et al.*, 2018; Warmack *et al.*, 2019).

### 1.5.2 Aβ-protein complexes: proteases

Aβ was found to be the proteolytic target of several proteases, including $Zn^{2+}$ dependent M16 metalloproteases, such as insulin-degrading enzyme (IDE; EC 3.4.24.56) and human presequence protease (hPreP; EC 3.4.24), the M3 peptidase neurolysin (NLN; EC 3.4.24.16) and the M2 peptidase family angiotensin-1-converting enzyme (ACE; EC 3.4.15.1). Over the years, Aβ-protein complexes with these enzymes have been crystallized. IDE, a M16A class zinc metalloprotease, is composed by homologous N and C-terminal subunits, connected by a 28 amino acid loop. In general terms, IDE-N is the catalytic subunit and IDE-C stabilizes the substrates for catalysis, containing an exosite that binds the N-terminal side of the substrate. The structures of IDE E111Q (inactive mutant) in complex with $Aβ_{1-40}$, as well as the cysteine free IDE E111Q (cysteines required a reducing agent for crystallization, which affected substrate conformation and subsequent recognition mechanisms) in complex with $Aβ_{1-42}$ were solved (Guo *et al.*, 2010; Shen *et al.*, 2006). Two segments of complexed $Aβ_{1-40}$ are visible: N-terminal residues D1-E3 and K16-D23; the binding of $Aβ_{1-42}$ was found to be identical (Figure 1.4A) (Guo *et al.*, 2010; Shen *et al.*, 2006). The Aβ N-terminal residues act as anchors to stabilize the peptide and allow IDE mediated cleavage. A few identified cleavage sites have been proposed: V18-F19, F19-F20 and F20-A21. IDE preferably cleaves, initially, around 10 or more residues away from the N-terminal of the substrate, in peptides that are no longer than 80 amino acids, due to steric limitations of the catalytic pocket. Furthermore, selectivity depends on the substrate conformation and charge complementarity. Other identified Aβ cleavage sites, like H14-Q15, are less frequent and likely occur as secondary cleavage events. The fact that $Aβ_{1-40}$ and $Aβ_{1-42}$ have identical binding modes suggests that IDE acts on the monomeric species. Thus, the disclosure of this catalytic mechanism can have important implications for AD as well as diabetes (Guo *et al.*, 2010; Shen *et al.*, 2006).

hPreP is a mitochondrial enzyme and has been linked to AD. Belonging to the M16C family, hPreP has an identical two-homologous subunits overall structure as IDE, with the difference being that they are connected by an extended helical linker rather than a loop region. The mechanism of Aβ cleavage by hPreP has been elucidated by solving the structure of the complex with $Aβ_{1-40}$, using hPreP E107Q to reduce catalytic activity while maintaining native protein folding for substrate recognition (Figure 1.4B) (King *et al.*, 2014). hPreP substrate recognition also depends on its size, shape, and charge distribution. However, in solution, hPreP is mainly monomeric and in closed conformation, while IDE is in dimeric open state. In addition, substrate recognition at the exosite and cleavage is distinct. IDE binds Aβ through hydrogen bonds, leading the peptide to maintain structure within the catalytic pocket. For cleavage to ensue, unfolding is necessary, and cleavage

occurs stochastically and sequentially at a few predefined sites. For hPreP, on the other hand, the peptide binds in an opposite direction when compared to IDE. Furthermore, the exosite recognizes hydrophobic patches of Aβ, constraining, along with the catalytic pocket, cleavage to specific sites, such as F20-A21. This cleaves Aβ exclusively at the amyloidogenic core and thus prevents Aβ aggregation in mitochondria. This "locking" mechanism is particularly relevant because the catalytic site of hPreP is negatively charged, as is Aβ peptide at mitochondrial pH. This way cleavage, otherwise impossible due to electrostatic repulsion, occurs (King *et al.*, 2014). In the context of AD, enhancing the activity of these enzymes would be beneficial. As an example, benzimidazole-based compounds were designed and demonstrated to improve Aβ degradation by hPreP (Vangavaragu *et al.*, 2014). However, hPreP mediated Aβ cleavage may generate fragments that are themselves hydrophobic and, thus, aggregation-prone, such as $Aβ_{35-40}$. Considering this, a second mitochondrial matrix peptidase, called neurolysin (NLN), was found to cleave Aβ, acting synergistically and downstream of hPreP (Teixeira *et al.*, 2018). PDB entry 5LV0 reports the complex of a less catalytically active NLN (E475Q) with $Aβ_{38-40}$ (Figure 1.4C). Neurolysin has two major domains surrounding a somewhat restrict catalytic pocket. Together with mass-spectrometry analysis, NLN alone could not degrade $Aβ_{1-40}$, degrading only peptides up to 20 amino acids. When the peptide was incubated with a mixture of hPreP and NLN, degradation fragments could be detected, particularly at the C-terminal (Teixeira *et al.*, 2018). Together, these results illustrate that Aβ degradation, in the mitochondria, is a complex pathway involving, at least, these two enzymes. Therefore, complete abrogation of amyloid formation through peptidase activity modulation should account for the multiple enzymes involved.

Next, there is the complex of Aβ with angiotensin converting enzyme (ACE), a M2 class zinc metallopeptidase. Its main function is the cleavage of vasopeptides, converting angiontensin I to angiotensin II, as well as bradykinin, therefore having an important role in blood pressure regulation. However, it can degrade a variety of other substrates, including Aβ (Larmuth *et al.*, 2016). The structural interaction of Aβ with the N-domain of ACE was investigated (Larmuth *et al.*, 2016). Contrary to the previous examples, an active form of the enzyme was used. Structure of the complexes showed that the overall protein structure is not changed by Aβ binding. For the tested fragments $Aβ_{1-16}$, $Aβ_{4-10}$, the fluorogenic $Aβ_{(4-10)}$Y and $Aβ_{35-42}$, two residues at the N-terminal ACE catalytic site are visible, while for $Aβ_{10-16}$ there are two pairs visible, with an identical binding mechanism for all (Figure 1.4D). Some Aβ cleavage sites of Aβ by ACE have been identified, mainly at the Aβ N-terminal side. Overall, the structures suggest a main proteolytic site at H14-Q15 (Larmuth *et al.*, 2016).

Finally, a brief mention to two Aβ-protein complexes deposited at the PDB. First, there are the coordinates of Aβ in complex with anticalins (PDB entries 4MVI, 4MVL and 4MVK).

Lipocalins are small circulating proteins (typically 150 to 180 amino acids) that bind and scavenge poorly soluble compounds, such as vitamins or hormones. Structurally, they are formed essentially by a β barrel that houses the ligand binding pocket, with the access restricted by a loop region. By engineering of this loop region, so-called anticalins able to bind and sequester Aβ have been developed, as a potential alternative to antibodies as an Aβ clearance therapy (Rauth *et al.*, 2016). Figure 1.4E shows an example of $A\beta_{1-40}$ in complex with anticalin US7, with region $A\beta_{16-28}$ visible at the anticalin binding pocket. Complementary assays showed that equimolar concentrations of Aβ and anticalins inhibited fibril formation (by monomer or prenuclear oligomeric intermediates sequestration) in a dose dependent manner. Furthermore, $A\beta_{42}$ cytotoxicity was also prevented by anticalins. In short, the authors propose anticalins as a potential form of AD treatment using the peripheral sink hypothesis: anticalin binding to Aβ in peripheral tissues would displace the equilibrium across the BBB, increasing Aβ brain clearance and, hopefully, reduce brain aggregates and their toxic effects (Rauth *et al.*, 2016). However, it should be mentioned that a previous study using the amyloid degrading enzyme neprilysin enhanced with albumin showed that decreasing peripheral Aβ levels in mice, rats and even monkeys did not alter the cerebral levels of the peptide, casting some doubts over the peripheral sink hypothesis (Henderson *et al.*, 2014). The complex of Aβ with phospholipase A2, in which $A\beta_{28-35}$ residues are visible (Figure 1.4F), is also available. Phospholipases A2 are a family of enzymes that catalyze the hydrolysis of membrane glycerophospholipids, releasing, for example, the precursor of prostaglandins. The interaction of phospholipase A2 with Aβ has been linked to toxicity from mitochondrial dysfunction, through disruption of membrane potential and ROS production (Zhu *et al.*, 2006).

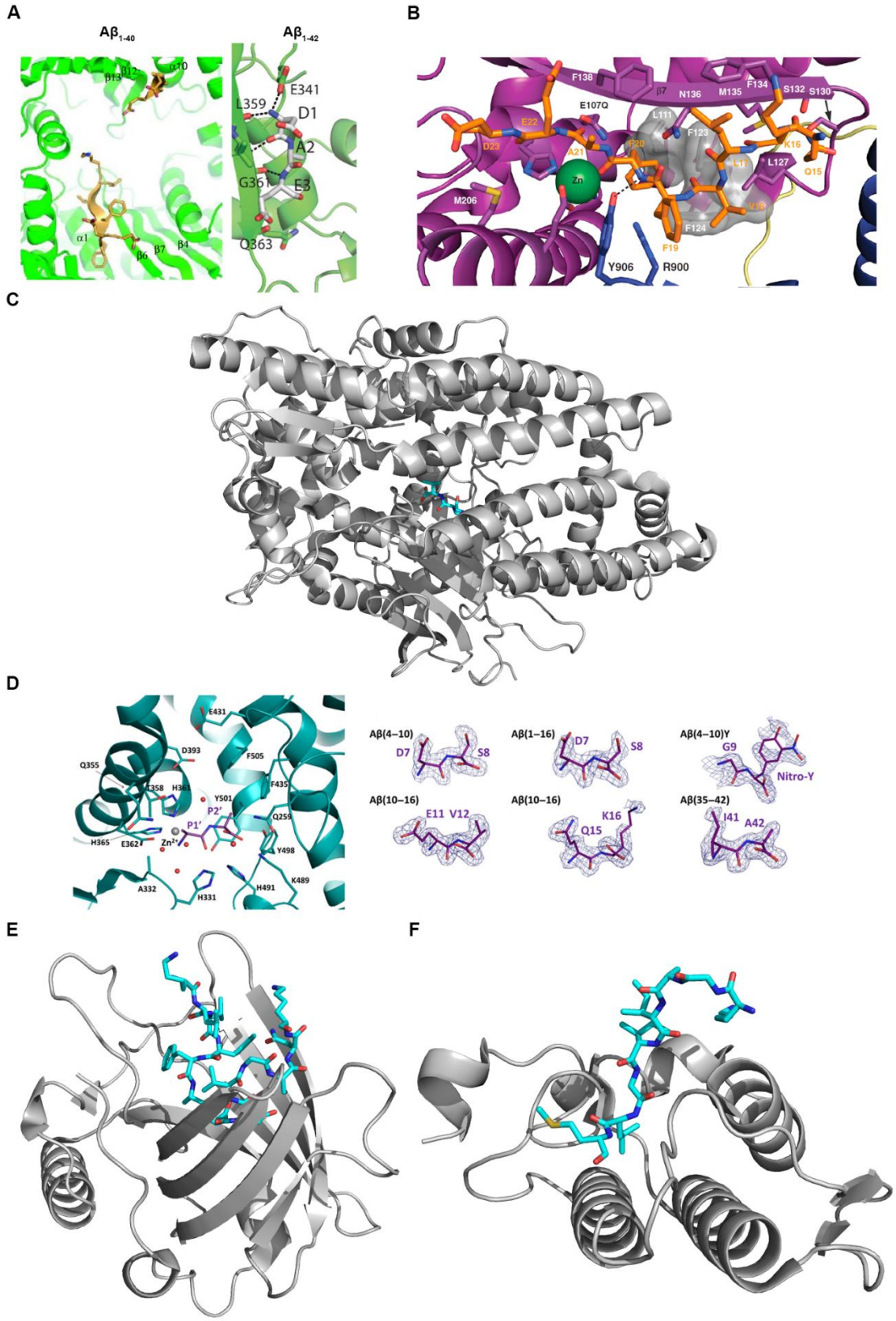


**Figure 1.4.** Aβ in complex with proteases. (A) (left) Close-up view of the $Aβ_{1-40}$ residues (orange) in complex with IDE E111Q (green). D1-E3 and K16-D23 from Aβ are visible. (right) Close-up view of the $Aβ_{1-42}$ residues D1-E3 (grey) in complex with the exosite of cysteine free IDE E111Q. (B) close-

up view of Aβ residues (orange) in complex with the catalytic site of hPreP (purple). (C) hNLN E475Q (grey) in complex with $A\beta_{38-40}$ (cyan), from PDB entry 5LV0. (D) (left) close view of the ACE-Aβ catalytic site (an AA dipeptide place-holds for all observed fragments; grey and red spheres represent water and zinc, respectively); (right) detailed view of observed Aβ fragments with $2F_o$-$F_c$ map contoured at 1 σ. (E) $A\beta_{1-40}$ (cyan) in complex with anticalin US7 (grey), from PDB entry 4MVI. Residues $A\beta_{16-28}$ are visible, binding within the anticalin β barrel. (F) Aβ (visible residues $A\beta_{28-35}$, in cyan) in complex with phospholipase A2 (grey), from PDB entry 3JTI. Panels C, E and F made in PyMol (Schrodinger, 2015) with indicated PDB entries. A, B and D adapted from (Guo *et al.*, 2010; King *et al.*, 2014; Larmuth *et al.*, 2016; Shen *et al.*, 2006)).

### 1.5.3 Aβ-protein complexes: antibodies

PFA1/PFA2, WO2, 12A11/10D5/12B4, Gantenerumab, C706 and Bapineuzumab/3D6 are antibodies that bind to the N-terminal region of Aβ in a closely related fashion, with the peptide devoid of typical α/β secondary structure (Figure 1.5A) (Basi *et al.*, 2010; Bohrmann *et al.*, 2012; Gardberg *et al.*, 2007; Miles *et al.*, 2013; Miles *et al.*, 2008; Teplyakov *et al.*, 2017). The antibodies establish hydrogen bonds, salt bridges and van der Waals interactions with Aβ, mainly through $A\beta_{2-8.}$ Gantenerumab binds segment $A\beta_{1-11}$ in an extended conformation (Bohrmann *et al.*, 2012). However, the peptide orientation is reversed 180° when compared to the previous antibodies (Figure 1.5B), which may be explained by primary structure differences of complementarity-determining regions (CDR) between the antibodies. The peptide binds gantenerumab through hydrogen bonds of the amino or carbonyl atoms. Interestingly, this antibody also binds the more central region $A\beta_{18-27}$ (no structure available), suggesting that it can bind different forms of Aβ, from monomers to fibrils. This was confirmed using transgenic mice and functional assays, which showed the potential of gantenerumab for clearing oligomers and plaques through activation of effector immune cells (Bohrmann *et al.*, 2012). C706, 3D6 and its humanized form, Bapineuzumab, are other available examples of antibody-Aβ complex structures targeting the N-terminal, with a major difference residing in the fact that Aβ is in an helical/coiled conformation, rather than an extended one, stabilized by intramolecular hydrogen bonds (Figure 1.5C,D) (Feinberg *et al.*, 2014; Miles *et al.*, 2013; Teplyakov *et al.*, 2017). Aducanumab also binds N-terminal Aβ in an extended conformation (Figure 1.5E) (Arndt *et al.*, 2018). The differences between CDRs determine that, despite being all in an extended conformation, Aβ interactions with PFA1, gantenerumab and aducanumab are all different. Aducanumab-Aβ have a shallow interaction (*i.e.,* not through deep binding pockets), and this antibody is highly selective for aggregated forms of Aβ, with this observation being a theoretical advantage in a potential treatment by not interfering with

monomeric Aβ and its physiological role (Arndt *et al.*, 2018). However, it does not show appreciable affinity for N-terminal post-translationally modified versions of Aβ, such as $Aβ_{pE3}$ (Arndt *et al.*, 2018), a prevalent isoform in AD amyloid deposits, that can convert $Aβ_{42}$ from stable fibrils to more toxic oligomeric species (Nussbaum *et al.*, 2012; Wu *et al.*, 2014). Immunotherapies targeting Aβ have been displaying disappointing results in clinical trials, likely because targeting the monomer disrupts its physiological effects; in that regard, oligomer/fibril targeting antibodies, such as gantenerumab or aducanumab, may be more promising (Panza *et al.*, 2019). In June 2021, aducanumab (under the commercial name of Aduhelm) became the six approved AD targeting drug, the first since 2003 (Cavazzoni, 2021). In addition, since $Aβ_{pE3}$ is a disease related isoform, targeting this form may be the best option of an AD immunotherapy. Piechotta and colleagues presented three antibodies (C#6, C#24 and C#17) against $Aβ_{pE3}$ (Piechotta *et al.*, 2017). These antibodies exhibit high affinity (in nM range) for epitopes in the region $Aβ_{pE3-18}$, as well as high specificity (*i.e.,* do not bind $Aβ_{42}$). $Aβ_{pE3}$ is more prone to aggregation due to the formation of a so-called “pEF head”, constituting a bulky hydrophobic core composed by superposition of residues pE3 and F4. Despite presenting slight variations in the $Aβ_{pE3}$ binding pockets, C#6/C#24/C#17 bind Aβ in similar conformations (Figure 1.5F) (Piechotta *et al.*, 2017). *In vitro*, C#6/C#24/C#17 bind $Aβ_{pE3}$ oligomers and prevent fibril formation; *in vivo*, C#6 showed memory improvement in mice pre-treated with Aβ oligomers (Piechotta *et al.*, 2017).

Then, crystal structures of two closely related antibodies bound to the mid region of Aβ are available. Solanezumab structure shows the binding of $Aβ_{16-26}$, while crenezumab binds $Aβ_{11-25}$ (Figure 1.5G/H). The mechanism is identical in both cases, with the Aβ β-hairpin disrupted and several intra- and intermolecular interactions, in particular F19 and F20, which bind to a hydrophobic pocket of the antibody (Crespi *et al.*, 2015; Ultsch *et al.*, 2016). An antibody bound to residues 16 to 28 of a conformation-restricted $Aβ_{1-42}$ was also reported, with possible implications, for example, in measuring peptide levels in CSF and blood (Kageyama *et al.*, 2021).

Lastly, there is the example of ponezumab, an antibody binding the C-terminal of $Aβ_{1-40}$ (Figure 1.8I)(La Porte *et al.*, 2012). $Aβ_{30-40}$ can be traced in the complex, presenting four β-turns conformation instead of pronounced α/β secondary structure. V40 is the residue with the most interaction with the peptide (La Porte *et al.*, 2012).

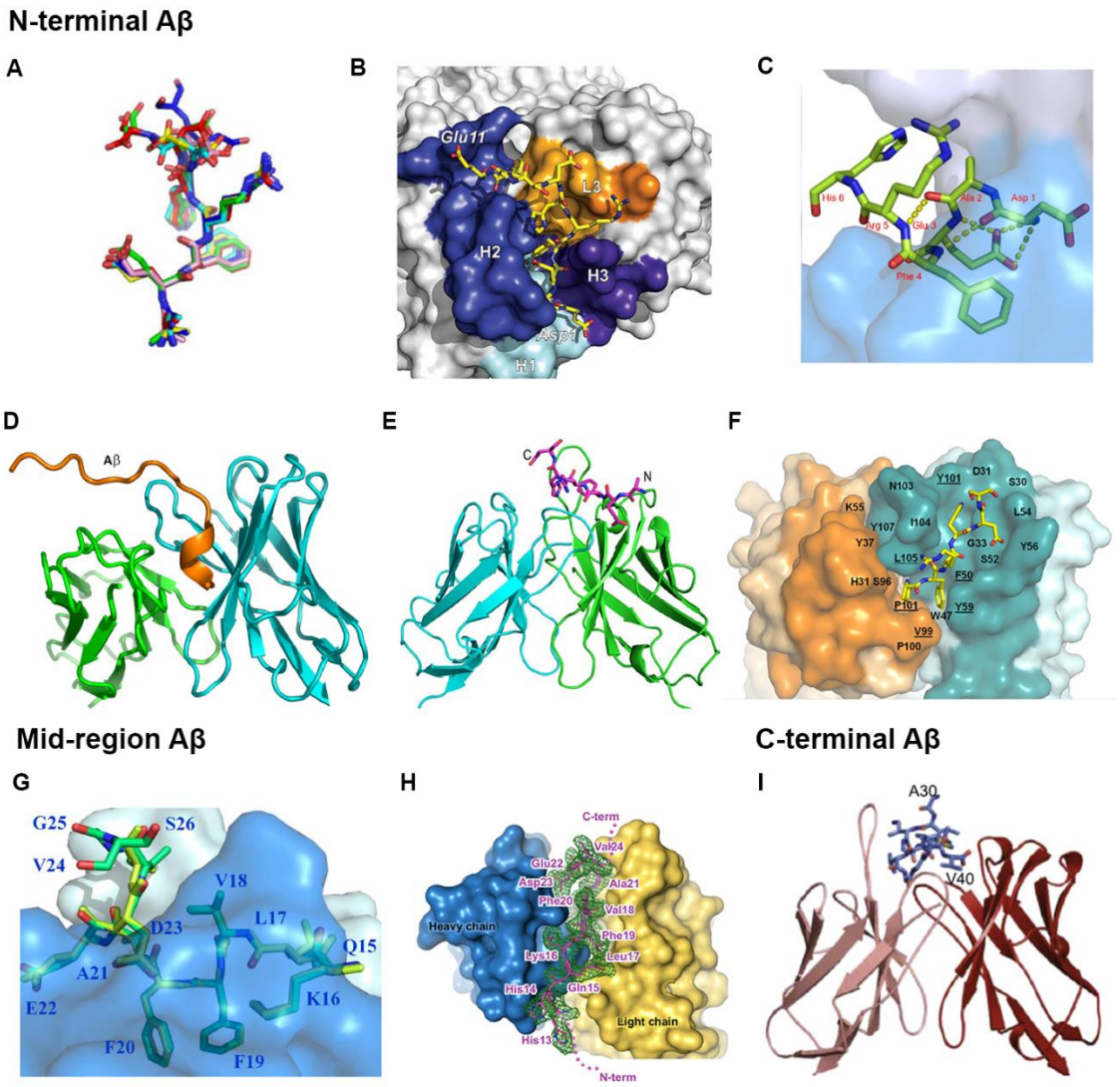


**Figure 1.5.** Crystallographic structures of antibodies binding N-terminal (A-F), mid-region (G,H) or C-terminal (I) Aβ fragments. (A) Superposition of $Aβ_{2-6}$ in complex with PFA1 (red), PFA2 (green), WO2 (blue), 12A11 (pink), 10D5 (yellow) and 12B4 (cyan). (B) Binding of $Aβ_{1-11}$ (stick representation) to Gantenerumab (surface representation. (C) Helical conformation of $Aβ_{1-6}$ in complex with Bapineuzumab. (D) C706 complexed with $Aβ_{1-16}$. (E) Aducanumab (cartoon representation, with heavy chain in green and light chain in cyan) in complex with $Aβ_{1-11}$ (stick representation, with carbon in magenta, nitrogen in blue and oxygen in red). (F) N-terminal $Aβ_{pE3}$ (yellow sticks) in complex with c#17 antibody (light chain in orange; heavy chain in cyan). (G) $Aβ_{15-26}$ (both copies of the asymmetric unit in stick representation) bound to solanezumab (in surface representation). (H) $Aβ_{11-25}$ in stick representation overlaid with $2F_o$-$F_c$ map at 1σ in complex with crenezumab. (I) Ponezumab (cartoon representation) binding C-terminal $Aβ_{30-40}$ (stick representation). Adapted from (Arndt *et al.*, 2018; Basi *et al.*, 2010; Bohrmann *et al.*, 2012; Crespi *et al.*, 2015; Gardberg *et al.*, 2007; La Porte *et al.*, 2012; Miles *et al.*, 2013; Miles *et al.*, 2008; Piechotta *et al.*, 2017; Teplyakov *et al.*, 2017; Ultsch *et al.*, 2016).

### 1.5.4 Amyloid-β fibrils: NMR and cryoEM

Given the difficulties in crystallizing Aβ, the structure of mature Aβ assemblies has been studied by solid-state NMR (ssNMR) and cryoEM. Here, some examples will be briefly addressed. Luhrs *et al.* presented the first full $A\beta_{1-42}$ fibril structure. The N-terminal $A\beta_{1-17}$ was disordered, with the remaining peptide adopting a U-shaped form of two parallel and in-register β-strands ($A\beta_{18-26}$ and $A\beta_{31-42}$), stabilized by intramolecular salt bridges, and a turn at $A\beta_{27-30}$. The fibril would grow by successive stacking of U-shaped monomers along the fibril axis (Figure 1.6A) (Luhrs *et al.*, 2005). More recently, three independent studies presented higher resolution and virtually identical S-shaped models for $A\beta_{1-42}$ fibrils, with the difference that, in two of them, the fibril building unit is dimeric rather than a monomer (Figure 1.6B exemplifies the monomeric assembly) (Colvin *et al.*, 2016; Wälti *et al.*, 2016; Xiao *et al.*, 2015). These models assume great importance, because hint to the S-shaped structure being a thermodynamically favorable fibril polymorph of $A\beta_{1-42}$, since these three samples were prepared in different conditions. Furthermore, bonds K28-A42 and G29-I41 may explain why $A\beta_{1-42}$ fibrils are different from $A\beta_{1-40}$ and why despite having virtually identical sequences, one peptide does not seed fibril growth of the other (Xiao *et al.*, 2015).

$A\beta_{1-40}$, on the other hand, appears to assume a U-shaped form, with the fibril packing seeming to be dependent on environmental conditions (Bertini *et al.*, 2011; Lu *et al.*, 2013; Paravastu *et al.*, 2008; A T Petkova *et al.*, 2006; Schütz *et al.*, 2015). As examples, Petkova and colleagues proposed a model of the monomer with two β-strands connected by a loop in region $A\beta_{25-29}$ (Figure 1.6C). Two monomers assemble and form the cross-β mature fibril (the steric zipper is proposed to be in the C-terminal region) (A T Petkova *et al.*, 2006). Bertini *et al.* proposed an identical model, with only minor changes in intermolecular bonds between cross-β sheet forming monomers (Bertini *et al.*, 2011). Then, a three-fold symmetry related fibril model was also found, where hydrophobic residues face the interior of the fibril, while polar residues face the outside (Paravastu *et al.*, 2008). A very interesting aspect is that fibrils obtained from an Alzheimer's patient's brain tissue present a similar three-fold symmetry (Figure 1.6D) (Lu *et al.*, 2013). In the same study, another patient's sample presented different inter-residue bonds; knowing that both patients had different clinical profiles, this suggests that polymorphism plays a role in disease progression/severity (Lu *et al.*, 2013). Aβ mutations or post translational modifications can also influence fibril structure. For example, in the case of the Osaka deletion mutation Glu22Δ, a rigid dimer with more than two β-sheets, connected by loops, constitute the fibril forming unit (Schütz *et al.*, 2015). $A\beta_{1-40}$ and $A\beta_{1-42}$ only form in-register parallel fibrils, with antiparallel amyloid sheets only typical of smaller fragments, such as $A\beta_{16-22}$ or $A\beta_{11-25}$ (A. T. Petkova *et al.*, 2004; Tycko *et al.*, 2003). However, the Iowa mutation (*i.e.,* $A\beta_{1-40}$ D23N) is known to form both parallel and

anti-parallel fibrils, with Qiang and co-workers providing a purely antiparallel fibril model (Qiang *et al.*, 2012). Despite showing equal toxicity to parallel structures, $A\beta_{1-40}$ D23N anti-parallel β-sheet structures were thought to trigger early-onset AD. Like wild type $A\beta_{1-40}$ (Paravastu *et al.*, 2008; A T Petkova *et al.*, 2006), $A\beta_{1-40}$ D23N fibrils show a U-shaped conformation with β-sheet from the N-terminal side contacting with opposing one from C-terminus. However, the structure is thermodynamically less favorable than parallel structures, slowly converting to this arrangement over time (Qiang *et al.*, 2012). Finally, post translational modifications, such as pyroglutamation, isomerization, nitration or phosphorylation lead to early fibril amyloid formation (compared to wild type form), with increased neuronal cytotoxicity and concentrating in mature plaques more easily. In this context, a fibril model for $A\beta_{1-40}$ phosphorylated at S8 (pS8-$A\beta_{40}$) was disclosed (Hu *et al.*, 2019). As with the Iowa mutant, these fibrils exhibit a similar arrangement to wild type $A\beta_{1-40}$ (Hu *et al.*, 2019). However, here the N-terminal is not disordered, showing strong inter-strand interaction with the amyloid core. This N-terminal conformation may serve as a docking point for monomers, catalyzing aggregation, and possibly accounting for the 5-fold increase in elongation rate constant for seeded fibrillation when compared to wild type $A\beta_{1-40}$. In addition, pS8-$A\beta_{40}$ can cross seed wild type $A\beta_{1-40}$, wild type $A\beta_{1-42}$ and pE3-$A\beta_{1-40}$ and pS8-$A\beta_{40}$ fibrils also show a more rigid fibrillar core and are thermodynamically more stable. Altogether, these observations hint at the structural importance of Aβ N-terminal residues and may explain how low abundance species, such as pS8-$A\beta_{40}$, can nonetheless dominate amyloid polymorphisms (Hu *et al.*, 2019).

Finally, cryoEM has also been recently employed to assess the supramolecular structure of mature fibrils. For example, Zhang *et al.* propose a model for $A\beta_{1-42}$ where two protofilaments of stacked U-shaped monomers assemble together with a hollow core to form the mature fibril, similar to an early NMR model (Luhrs *et al.*, 2005; Zhang *et al.*, 2009). For $A\beta_{1-40,}$ Sachse *et al.* found a U-shaped dimeric arrangement as well, but with no hollow core between monomers, a close packing through the C-terminal region and a disordered N-terminal (Sachse *et al.*, 2008). Schmidt *et al*. present a tilde-shaped dimeric conformation for $A\beta_{1-42}$ fibrils (Schmidt *et al.*, 2015). In this model, the monomers are in face-to-face conformation, with a steric zipper interface residing in the center region of the segment from E22/D23 to the C-terminus of the peptide. Another, higher resolution $A\beta_{1-42}$ fibril model suggests a LS-shaped fibril (Figure 1.6E) (Gremer *et al.*, 2017). The fibril is in a slightly tilted, helical conformation, with C-terminal of each monomer in S-shape and an L-shaped N-terminal. Here, the C-terminal is not exposed, constituting the protofilament steric zipper interface (reinforcing the region as a target for inhibition). Furthermore, the $A\beta_{20-25}$ segment might explain the pathological hereditary mutations A21G (Flemish), E22G (Arctic), E22K (Italian) and D23N (Iowa); in contrast, the arrangement for the N-terminal may explain why

mutation A2T (Icelandic) is possibly protective (disruption of the hydrophobic cluster comprised by A2/V36/F4/L34) (Gremer *et al.*, 2017). Lastly, we have an example of a cryo-EM model derived from purified Alzheimer's brain tissue (Figure 1.6F) (Kollmer *et al.*, 2019). The fibrils were isolated *post-mortem* from the meninges of three different patients. Interestingly, they not only proved more resistant to proteolytic cleavage than *in vitro* generated fibrils, but also showed good correlation between morphology and patient neuropathology (Kollmer *et al.*, 2019). In terms of composition, they exhibit a low $A\beta_{1-42}$ content, with the differences being mainly between peptide fragment length (as opposed to PTMs). Structure-wise, the cryo-EM data of one of the fibrils shows that they are right-handed fibrils (typically, fibrils are left-handed (Gremer *et al.*, 2017; Schmidt *et al.*, 2015)), composed by two C-shaped $A\beta_{1-40}$ molecules, with each one with four cross-β sheet motifs ($A\beta_{2-8}$; $A\beta_{10-13}$; $A\beta_{15-19}$; $A\beta_{32-34}$). Furthermore, major disordered regions are absent (Figure 1.6E)(Kollmer *et al.*, 2019). Despite a degree of uncertainty in the detailed geometry of the poly-peptide backbone and sidechains, an N-terminal arch and a central position of the fibril at $A\beta_{24-26}$ (rather than $A\beta_{30-42}$) are unique features of these fibrils (Kollmer *et al.*, 2019). The authors suggest that specific neuropathology may derive from specific fibril morphologies, instead of peptide composition (Kollmer *et al.*, 2019).

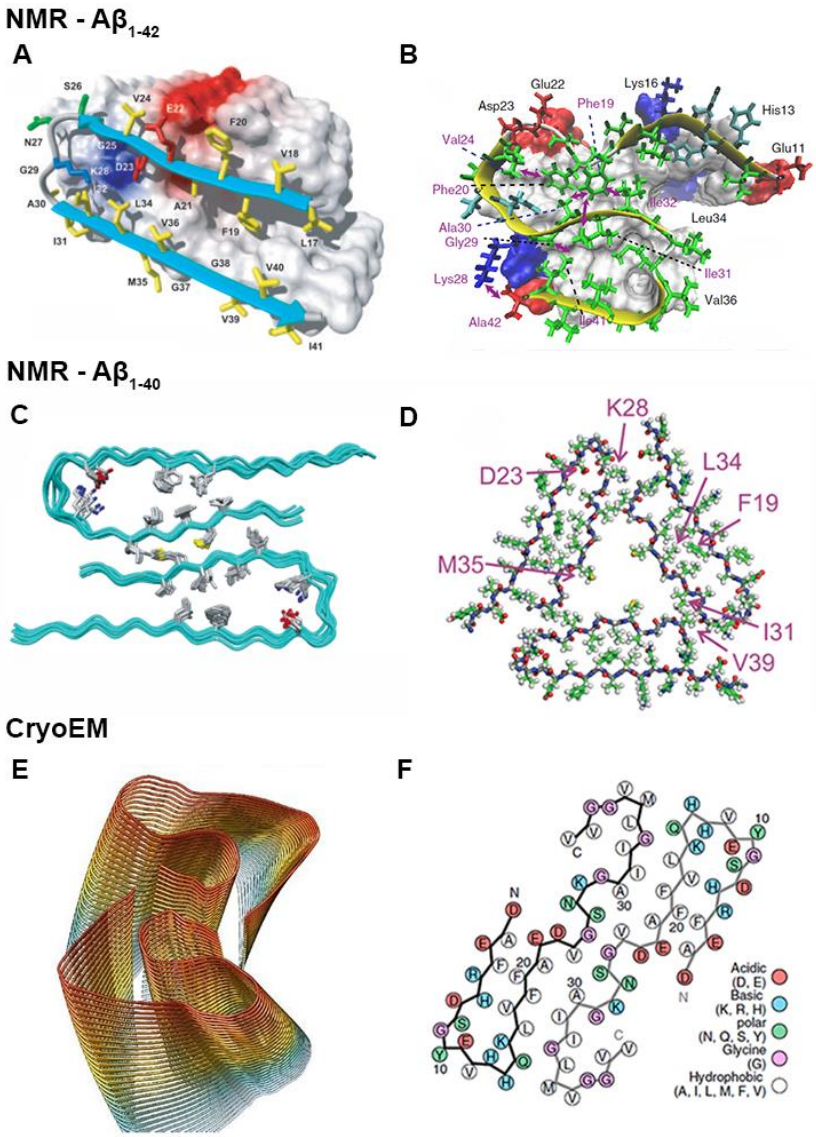


**Figure 1.6.** (A) U-shaped $A\beta_{1-42}$ fibril, with β-sheets in cyan and turn region in grey. (B) S-shaped $A\beta_{1-42}$ fibril, with view down the fibril axis. (C) Top view of $A\beta_{1-40}$ U-shaped wild type monomer forming a symmetric dimer fibril structure. (D) Fibril structure of $A\beta_{1-40}$ sample from an Alzheimer's patient. (E) LS shaped (L: N-terminal; S: C- terminal) conformation of mature $A\beta_{1-42}$ fibrils. (F) Cryo-EM structure of fibril extracted from an AD patient. Adapted from (Gremer *et al.*, 2017; Kollmer *et al.*, 2019; Lu *et al.*, 2013; Luhrs *et al.*, 2005; A T Petkova *et al.*, 2006; Xiao *et al.*, 2015).

## 1.6 Thesis: motivation and outline

Alzheimer's disease is associated with the presence of amyloid-β (Aβ) fibrils in the brain. Structural characterization of Aβ peptides, from monomers to higher order species (*i.e.* oligomers to fibrils), by themselves or with their multiple known interactors, is a key factor to a better understanding of the pathology. However, given the intrinsically disordered nature of Aβ, the use of single crystal X-ray diffraction has proved very difficult, as peptide crystallization is very elusive. Furthermore, due to the peptide's polymorphism, Nuclear Magnetic Resonance analysis of fibrils evidences the myriad of possible disease-relevant occurring forms, sometimes leading in the literature to the proposal of several conflicting models. Thus, a complete understanding of the molecular basis behind Aβ aggregation and physiological interactions is still lacking. With this PhD thesis, we aim at adding novel information to the overall understanding of the Aβ peptide role in one of the most puzzling and crippling diseases of our time. To do so, we resort to a plethora of *in vitro* biophysical and biochemical techniques to achieve novel structural elucidation of physio-pathological roles of Aβ peptides, as well as functional dissection of an Aβ assembly pathway.

In Chapter II, we study the interaction between Aβ and Aβ proteases: transthyretin, thermolysin and neprilsyin. Initially, we attempt to co-crystallize or perform crystal soaking of transthyretin with a myriad of Aβ fragments. Furthermore, taking advantage of the TTR crystallization expertise acquired, wild type TTR was co-crystallized with two small-molecules to explore the importance of these molecules in TTR tetramer stabilization for AD modulation. After a further screening for candidates for crystallographic interactions, we found that thermolysin (TLN), a bacterial metalloprotease, also cleaves Aβ (Zhang *et al.*, 2009). This protein is easily crystallizable and shares catalytic consensus with the amyloid-degrading enzyme neprilysin (NEP), making TLN a good template for NEP inhibitor design and kinetic analysis (Dion *et al.*, 1995; Roques *et al.*, 1993; Tiraboschi *et al.*, 1999). In this context, we used TLN as a template for the crystallographic study of the interaction with Aβ, resulting in Paper I - *Alzheimer's $A\beta_{1-40}$ peptide degradation by thermolysin: evidence of inhibition by a C-terminal Aβ product*. These findings are then assessed on NEP: Paper II - *$A\beta_{31-35}$ decreases Neprilysin-mediated Alzheimer's Amyloid-β peptide degradation*.

In Chapter III, we present the use of a fusion-protein approach with the goal of obtaining Aβ crystallographic information. Three constructs were designed. Two include the full $A\beta_{1-40}$ (T4 Lysozyme-$A\beta_{1-40}$ and PAC3-$A\beta_{1-40}$), while the third aimed at studying the P3 peptide (*i.e.* $A\beta_{17-40}$, in the construct T4 Lysozyme-$A\beta_{17-40}$). With this approach we intended to circumvent the major bottleneck in protein crystallization, which is crystal growth, using heterologous partners that potentiate polar contacts favorable to crystal growth.

It is widely accepted that higher order oligomeric species, which are next to impossible to follow by conventional structural techniques (*i.e.* X-Ray diffraction or NMR), are responsible for neurotoxic events. In this regard, the use of complementary biophysical techniques in combination with quantitative and theoretical modeling have emerged as a prime strategy to study amyloid oligomerization and fibril formation. In Chapter IV, this strategy is employed to study the aggregation behavior of $A\beta_{1-40}$: Paper III - *Dissection of the key steps of amyloid-β peptide 1-40 fibrillogenesis*.

Finally, Chapter V describes the application of metal-organic frameworks (MOFs) to the amyloid field. MOFs are a class of crystalline materials synthesized from the combination of metal ions (or a cluster thereof) and multidentate organic linkers. The multiplicity of combinations of these components confers MOFs their defining features: permanent porosity, high specific surface area and versatile pore geometry. Among the uses of MOF materials in research is the so-called crystalline sponge method. As defined by the authors, *"crystalline sponges are porous metal complexes that can absorb and orient common organic molecules in their pores and make them observable by conventional X-ray structure analysis"* (Hoshino *et al.*, 2016). The goal of this method is to obtain structural information of hard to crystallize guest molecules, typically small organic molecules, since there is no need to crystallize the guest molecule as long as it is embedded in the host porous material in a repetitive orientated way compatible with X-Ray diffraction analysis (Du *et al.*, 2018). In this context, we initially attempted to use the crystalline sponge method to study Aβ. Despite no peptide structural data could be obtained from diffraction at synchrotron facilities, we still employed MOFs to the amyloid field. First, we used MOFs to study the fluorescence properties of Thioflavin T (ThT). This benzothiazole dye was first described as an amyloid probe in 1959 (Vassar *et al.*, 1959). However, despite extensive use ever since, the exact binding mechanism to amyloids is poorly understood (Groenning, 2010). Due to the difficulties in obtaining crystal structures of amyloid structures, co-crystallization with ThT has been elusive. Nevertheless, understanding the ThT amyloid binding mechanism can have important implications, for example, in the design of small amyloid inhibiting molecules. As ThT binds to all amyloids independent of their monomeric components, the interaction is likely due to physical constraints imposed by the characteristic cross-β motif rather than binding to specific amino acids. We study this interaction in Paper IV: *Fluorescence properties of the amyloid indicator dye thioflavin T in constrained environments*. Finally, from our initial experiments with the crystalline sponge method using MOFs and Aβ, we disclosed a protein crystal seeding potential of the meso porous Tb-mesoMOF, resulting in Paper V - *Mesoporous Metal−Organic Frameworks as Effective Nucleating Agents in Protein Crystallography*.

## 1.7 References

Abraham, J. D., Promé, S., Salvetat, N., Rubrecht, L., Cobo, S., du Paty, E., Galéa, P., Mathieu-Dupas, E., Ranaldi, S., Caillava, C., Crémer, G. A., Rieunier, F., Robert, P., Molina, F., Laune, D., Checler, F., & Fareh, J. (2013). Cerebrospinal Aβ11-x and 17-x levels as indicators of mild cognitive impairment and patients' stratification in Alzheimer's disease. *Translational Psychiatry, 3*(7), e281-e281. doi:10.1038/tp.2013.58

Abramov, E., Dolev, I., Fogel, H., Ciccotosto, G. D., Ruff, E., & Slutsky, I. (2009). Amyloid-beta as a positive endogenous regulator of release probability at hippocampal synapses. *Nat Neurosci, 12*(12), 1567-1576. doi:10.1038/nn.2433

Alberdi, E., Sanchez-Gomez, M. V., Cavaliere, F., Perez-Samartin, A., Zugaza, J. L., Trullas, R., Domercq, M., & Matute, C. (2010). Amyloid beta oligomers induce Ca2+ dysregulation and neuronal death through activation of ionotropic glutamate receptors. *Cell Calcium, 47*(3), 264-272. doi:10.1016/j.ceca.2009.12.010

Alford, R. F., Leaver-Fay, A., Jeliazkov, J. R., O'Meara, M. J., DiMaio, F. P., Park, H., Shapovalov, M. V., Renfrew, P. D., Mulligan, V. K., Kappel, K., Labonte, J. W., Pacella, M. S., Bonneau, R., Bradley, P., Dunbrack, R. L., Jr., Das, R., Baker, D., Kuhlman, B., Kortemme, T., & Gray, J. J. (2017). The Rosetta All-Atom Energy Function for Macromolecular Modeling and Design. *J Chem Theory Comput, 13*(6), 3031-3048. doi:10.1021/acs.jctc.7b00125

Ali, F., Thompson, A. J., & Barrow, C. J. (2000). The p3 Peptide, a Naturally Occurring Fragment of the Amyloid-β Peptide (Aβ)Found in Alzheimer's Disease, Has a Greater Aggregation Propensity In Vitro Than Full-Length Aβ, But Does Not Bind Cu2+. *Australian Journal of Chemistry, 53*(4), 321-326. doi:10.1071/CH99169

Alikhani, N., Guo, L., Yan, S. Q., Du, H., Pinho, C. M., Chen, J. X., Glaser, E., & Yan, S. S. (2011). Decreased Proteolytic Activity of the Mitochondrial Amyloid-beta Degrading Enzyme, PreP Peptidasome, in Alzheimer's Disease Brain Mitochondria. *Journal of Alzheimers Disease, 27*, 75-87. doi: 10.3233/JAD-2011-101716

Alzheimer, A., Stelzmann, R. A., Schnitzlein, H. N., & Murtagh, F. R. (1995). An English translation of Alzheimer's 1907 paper, "Uber eine eigenartige Erkankung der Hirnrinde". *Clin Anat, 8*(6), 429-431. doi:10.1002/ca.980080612

Arndt, J. W., Qian, F., Smith, B. A., Quan, C., Kilambi, K. P., Bush, M. W., Walz, T., Pepinsky, R. B., Bussiere, T., Hamann, S., Cameron, T. O., & Weinreb, P. H. (2018). Structural and kinetic basis for the selectivity of aducanumab for aggregated forms of amyloid-beta. *Sci Rep, 8*(1), 6412. doi:10.1038/s41598-018-24501-0

Astbury, W. T., Dickinson, S., & Bailey, K. (1935). The X-ray interpretation of denaturation and the structure of the seed globulins. *Biochem J, 29*(10), 2351-2360 2351. doi:10.1042/bj0292351

Avila, J., Lucas, J. J., Perez, M., & Hernandez, F. (2004). Role of tau protein in both physiological and pathological conditions. *Physiol Rev, 84*(2), 361-384. doi:10.1152/physrev.00024.2003

Barnhart, M. M., & Chapman, M. R. (2006). Curli biogenesis and function. *Annu Rev Microbiol, 60*, 131-147. doi:10.1146/annurev.micro.60.080805.142106

Basi, G. S., Feinberg, H., Oshidari, F., Anderson, J., Barbour, R., Baker, J., Comery, T. A., Diep, L., Gill, D., Johnson-Wood, K., Goel, A., Grantcharova, K., Lee, M., Li, J., Partridge, A., Griswold-Prenner, I., Piot, N., Walker, D., Widom, A., Pangalos, M. N., Seubert, P., Jacobsen, J. S., Schenk, D., & Weis, W. I. (2010). Structural correlates of antibodies associated with acute reversal of amyloid beta-related behavioral deficits in a mouse model of Alzheimer disease. *J Biol Chem, 285*(5), 3417-3427. doi:10.1074/jbc.M109.045187

Bertini, I., Gonnelli, L., Luchinat, C., Mao, J., & Nesi, A. (2011). A new structural model of Aβ40 fibrils. *Journal of the American Chemical Society, 133*, 16013-16022. doi:10.1021/ja2035859

Biancalana, M., & Koide, S. (2010). Molecular mechanism of Thioflavin-T binding to amyloid fibrils. *Biochim Biophys Acta, 1804*(7), 1405-1412. doi:10.1016/j.bbapap.2010.04.001

Blokland, A. (1995). Acetylcholine: a neurotransmitter for learning and memory? *Brain Res Brain Res Rev, 21*(3), 285-300. doi:10.1016/0165-0173(95)00016-x

Bloom, G. S. (2014). Amyloid-beta and tau: the trigger and bullet in Alzheimer disease pathogenesis. *JAMA Neurol, 71*(4), 505-508. doi:10.1001/jamaneurol.2013.5847

Bohrmann, B., Baumann, K., Benz, J., Gerber, F., Huber, W., Knoflach, F., Messer, J., Oroszlan, K., Rauchenberger, R., Richter, W. F., Rothe, C., Urban, M., Bardroff, M., Winter, M., Nordstedt, C., & Loetscher, H. (2012). Gantenerumab: a novel human anti-Abeta antibody demonstrates sustained cerebral amyloid-beta binding and elicits cell-mediated removal of human amyloid-beta. *J Alzheimers Dis, 28*(1), 49-69. doi:10.3233/JAD-2011-110977

Bolognesi, B., Kumita, J. R., Barros, T. P., Esbjorner, E. K., Luheshi, L. M., Crowther, D. C., Wilson, M. R., Dobson, C. M., Favrin, G., & Yerbury, J. J. (2010). ANS Binding Reveals Common Features of Cytotoxic Amyloid Species. *ACS Chemical Biology, 5*(8), 735-740. doi:10.1021/cb1001203

Bousejra-ElGarah, F., Bijani, C., Coppel, Y., Faller, P., & Hureau, C. (2011). Iron(II) binding to amyloid-beta, the Alzheimer's peptide. *Inorg Chem, 50*(18), 9024-9030. doi:10.1021/ic201233b

Brewer, G. J., Kanzer, S. H., Zimmerman, E. A., Celmins, D. F., Heckman, S. M., & Dick, R. (2010). Copper and ceruloplasmin abnormalities in Alzheimer's disease. *Am J Alzheimers Dis Other Demen, 25*(6), 490-497. doi:10.1177/1533317510375083

Brown, A., & Török, M. (2021). Functional amyloids in the human body. *Bioorganic & Medicinal Chemistry Letters, 40*, 127914. doi:10.1016/j.bmcl.2021.127914

Cai, X. D., Golde, T. E., & Younkin, S. G. (1993). Release of excess amyloid beta protein from a mutant amyloid beta protein precursor. *Science, 259*(5094), 514-516. doi:10.1126/science.8424174

Cavazzoni, P. (2021). FDA’s Decision to Approve New Treatment for Alzheimer’s Disease.

Chen, G. F., Xu, T. H., Yan, Y., Zhou, Y. R., Jiang, Y., Melcher, K., & Xu, H. E. (2017). Amyloid beta: structure, biology and structure-based therapeutic development. *Acta Pharmacol Sin, 38*(9), 1205-1235. doi:10.1038/aps.2017.28

Cho, H. J., Son, S. M., Jin, S. M., Hong, H. S., Shin, D. H., Kim, S. J., Huh, K., & Mook-Jung, I. (2009). RAGE regulates BACE1 and Abeta generation via NFAT1 activation in Alzheimer's disease animal model. *FASEB J, 23*(8), 2639-2649. doi:10.1096/fj.08-126383

Chrem Mendez, P., Surace, E., Bérgamo, Y., Calandri, I., Vázquez, S., Sevlever, G., & Allegri, R. F. (2019). Biomarkers for Alzheimer's disease. Where we stand and where we are headed. *Medicina, 79*(Spec 6/1), 546-551.

Cintron, A. F., Dalal, N. V., Dooyema, J., Betarbet, R., & Walker, L. C. (2015). Transport of cargo from periphery to brain by circulating monocytes. *Brain Research, 1622*, 328-338. doi:10.1016/j.brainres.2015.06.047

Colletier, J. P., Laganowsky, A., Landau, M., Zhao, M., Soriaga, A. B., Goldschmidt, L., Flot, D., Cascio, D., Sawaya, M. R., & Eisenberg, D. (2011). Molecular basis for amyloid-beta polymorphism. *Proc Natl Acad Sci U S A, 108*(41), 16938-16943. doi:10.1073/pnas.1112600108

Colvin, M. T., Silvers, R., Ni, Q. Z., Can, T. V., Sergeyev, I., Rosay, M., Donovan, K. J., Michael, B., Wall, J., Linse, S., & Griffin, R. G. (2016). Atomic Resolution Structure of Monomorphic Aβ42 Amyloid Fibrils. *Journal of the American Chemical Society, 138*(30), 9663-9674. doi:10.1021/jacs.6b05129

Copani, A. (2017). The underexplored question of beta-amyloid monomers. *Eur J Pharmacol, 817*, 71-75. doi:10.1016/j.ejphar.2017.05.057

Crespi, G. A., Hermans, S. J., Parker, M. W., & Miles, L. A. (2015). Molecular basis for mid-region amyloid-beta capture by leading Alzheimer's disease immunotherapies. *Sci Rep, 5*, 9649. doi:10.1038/srep09649

Cruts, M., Hendriks, L., & Van Broeckhoven, C. (1996). The presenilin genes: a new gene family involved in Alzheimer disease pathology. *Hum Mol Genet, 5 Spec No*, 1449-1455. doi:10.1093/hmg/5.supplement_1.1449

Davis, J., & Van Nostrand, W. E. (1996). Enhanced pathologic properties of Dutch-type mutant amyloid beta-protein. *Proc Natl Acad Sci U S A, 93*(7), 2996-3000. doi:10.1073/pnas.93.7.2996

Deane, R., Du Yan, S., Submamaryan, R. K., LaRue, B., Jovanovic, S., Hogg, E., Welch, D., Manness, L., Lin, C., Yu, J., Zhu, H., Ghiso, J., Frangione, B., Stern, A., Schmidt, A. M., Armstrong, D. L., Arnold, B., Liliensiek, B., Nawroth, P., Hofman, F., Kindy, M., Stern, D., & Zlokovic, B. (2003). RAGE mediates amyloid-beta peptide transport across the blood-brain barrier and accumulation in brain. *Nat Med, 9*(7), 907-913. doi:10.1038/nm890

Di Fede, G., Catania, M., Morbin, M., Rossi, G., Suardi, S., Mazzoleni, G., Merlin, M., Giovagnoli, A. R., Prioni, S., Erbetta, A., Falcone, C., Gobbi, M., Colombo, L., Bastone, A., Beeg, M., Manzoni, C., Francescucci, B., Spagnoli, A., Cantu, L., Del Favero, E., Levy, E., Salmona, M., & Tagliavini, F. (2009). A recessive mutation in the APP gene with dominant-negative effect on amyloidogenesis. *Science, 323*(5920), 1473-1477. doi:10.1126/science.1168979

Dion, N., Le Moual, H., Fournié-Zaluski, M. C., Roques, B. P., Crine, P., & Boileau, G. (1995). Evidence that Asn542 of neprilysin (EC 3.4.24.11) is involved in binding of the P2′ residue of substrates and inhibitors. *Biochemical Journal, 311*(2), 623-627. doi:10.1042/bj3110623

Do, T. D., Sangwan, S., de Almeida, N. E. C., Ilitchev, A. I., Giammona, M., Sawaya, M. R., Buratto, S. K., Eisenberg, D. S., & Bowers, M. T. (2018). Distal amyloid beta-protein fragments template amyloid assembly. *Protein Sci, 27*(7), 1181-1190. doi:10.1002/pro.3375

Doig, A. J., Del Castillo-Frias, M. P., Berthoumieu, O., Tarus, B., Nasica-Labouze, J., Sterpone, F., Nguyen, P. H., Hooper, N. M., Faller, P., & Derreumaux, P. (2017). Why Is Research on Amyloid-beta Failing to Give New Drugs for Alzheimer's Disease? *ACS Chem Neurosci, 8*(7), 1435-1437. doi:10.1021/acschemneuro.7b00188

Donahue, J. E., Flaherty, S. L., Johanson, C. E., Duncan, J. A., 3rd, Silverberg, G. D., Miller, M. C., Tavares, R., Yang, W., Wu, Q., Sabo, E., Hovanesian, V., & Stopa, E. G. (2006). RAGE, LRP-1, and amyloid-beta protein in Alzheimer's disease. *Acta Neuropathol, 112*(4), 405-415. doi:10.1007/s00401-006-0115-3

Du, Q., Peng, J., Wu, P., & He, H. (2018). Review: Metal-organic framework based crystalline sponge method for structure analysis. *TrAC Trends in Analytical Chemistry, 102*, 290-310. doi:10.1016/j.trac.2018.02.014

Duce, J. A., Tsatsanis, A., Cater, M. A., James, S. A., Robb, E., Wikhe, K., Leong, S. L., Perez, K., Johanssen, T., Greenough, M. A., Cho, H. H., Galatis, D., Moir, R. D., Masters, C. L., McLean, C., Tanzi, R. E., Cappai, R., Barnham, K. J., Ciccotosto, G. D., Rogers, J. T., & Bush, A. I. (2010). Iron-export ferroxidase activity of beta-amyloid precursor protein is inhibited by zinc in Alzheimer's disease. *Cell, 142*(6), 857-867. doi:10.1016/j.cell.2010.08.014

Eisenberg, D., & Jucker, M. (2012). The amyloid state of proteins in human diseases. *Cell, 148*(6), 1188-1203. doi:10.1016/j.cell.2012.02.022

Exley, C. (2006). Aluminium and iron, but neither copper nor zinc, are key to the precipitation of beta-sheets of Abeta_{42} in senile plaque cores in Alzheimer's disease. *J Alzheimers Dis, 10*(2-3), 173-177. doi:10.3233/jad-2006-102-305

Falkevall, A., Alikhani, N., Bhushan, S., Pavlov, P. F., Busch, K., Johnson, K. A., Eneqvist, T., Tjernberg, L., Ankarcrona, M., & Glaser, E. (2006). Degradation of the amyloid β-protein by the novel mitochondrial peptidasome, PreP. *Journal of Biological Chemistry, 281*, 29096-29104. doi:10.1074/jbc.M602532200

Feinberg, H., Saldanha, J. W., Diep, L., Goel, A., Widom, A., Veldman, G. M., Weis, W. I., Schenk, D., & Basi, G. S. (2014). Crystal structure reveals conservation of amyloid-β conformation recognized by 3D6 following humanization to bapineuzumab. *Alzheimer's research & therapy, 6*, 31. doi:10.1186/alzrt261

Fonte, V., Kapulkin, W. J., Taft, A., Fluet, A., Friedman, D., & Link, C. D. (2002). Interaction of intracellular beta amyloid peptide with chaperone proteins. *Proc Natl Acad Sci U S A, 99*(14), 9439-9444. doi:10.1073/pnas.152313999

Francis, P. T., Palmer, A. M., Snape, M., & Wilcock, G. K. (1999). The cholinergic hypothesis of Alzheimer's disease: a review of progress. *J Neurol Neurosurg Psychiatry, 66*(2), 137-147. doi:10.1136/jnnp.66.2.137

Fuller, J. T., Cronin-Golomb, A., Gatchel, J. R., Norton, D. J., Guzman-Velez, E., Jacobs, H. I. L., Hanseeuw, B., Pardilla-Delgado, E., Artola, A., Baena, A., Bocanegra, Y., Kosik, K. S., Chen, K., Tariot, P. N., Johnson, K., Sperling, R. A., Reiman, E. M., Lopera, F., & Quiroz, Y. T. (2019). Biological and Cognitive Markers of Presenilin1 E280A Autosomal Dominant Alzheimer's Disease: A Comprehensive Review of the Colombian Kindred. *J Prev Alzheimers Dis, 6*(2), 112-120. doi:10.14283/jpad.2019.6

Gardberg, A. S., Dice, L. T., Ou, S., Rich, R. L., Helmbrecht, E., Ko, J., Wetzel, R., Myszka, D. G., Patterson, P. H., & Dealwis, C. (2007). Molecular basis for passive immunotherapy

of Alzheimer's disease. *Proc Natl Acad Sci U S A, 104*(40), 15659-15664. doi:10.1073/pnas.0705888104

Giuffrida, M. L., Tomasello, M. F., Pandini, G., Caraci, F., Battaglia, G., Busceti, C., Di Pietro, P., Pappalardo, G., Attanasio, F., Chiechio, S., Bagnoli, S., Nacmias, B., Sorbi, S., Vigneri, R., Rizzarelli, E., Nicoletti, F., & Copani, A. (2015). Monomeric ss-amyloid interacts with type-1 insulin-like growth factor receptors to provide energy supply to neurons. *Front Cell Neurosci, 9*, 297. doi:10.3389/fncel.2015.00297

Glenner, G. G., & Wong, C. W. (1984). Alzheimer's disease: initial report of the purification and characterization of a novel cerebrovascular amyloid protein. *Biochem Biophys Res Commun, 120*(3), 885-890. doi:10.1016/s0006-291x(84)80190-4

Goedert, M., Spillantini, M. G., & Crowther, R. A. (1991). Tau proteins and neurofibrillary degeneration. *Brain Pathol, 1*(4), 279-286. doi:10.1111/j.1750-3639.1991.tb00671.x

Grabowski, T. J., Cho, H. S., Vonsattel, J. P., Rebeck, G. W., & Greenberg, S. M. (2001). Novel amyloid precursor protein mutation in an Iowa family with dementia and severe cerebral amyloid angiopathy. *Ann Neurol, 49*(6), 697-705. doi:10.1002/ana.1009

Gremer, L., Scholzel, D., Schenk, C., Reinartz, E., Labahn, J., Ravelli, R. B. G., Tusche, M., Lopez-Iglesias, C., Hoyer, W., Heise, H., Willbold, D., & Schroder, G. F. (2017). Fibril structure of amyloid-beta(1-42) by cryo-electron microscopy. *Science, 358*(6359), 116-119. doi:10.1126/science.aao2825

Griner, S. L., Seidler, P., Bowler, J., Murray, K. A., Yang, T. P., Sahay, S., Sawaya, M. R., Cascio, D., Rodriguez, J. A., Philipp, S., Sosna, J., Glabe, C. G., Gonen, T., & Eisenberg, D. S. (2019). Structure-based inhibitors of amyloid beta core suggest a common interface with tau. *Elife, 8*. doi:10.7554/eLife.46924

Groenning, M. (2010). Binding mode of Thioflavin T and other molecular probes in the context of amyloid fibrils—current status. *Journal of Chemical Biology, 3*(1), 1-18. doi:10.1007/s12154-009-0027-5

Guo, Q., Manolopoulou, M., Bian, Y., Schilling, A. B., & Tang, W. J. (2010). Molecular basis for the recognition and cleavages of IGF-II, TGF-alpha, and amylin by human insulin-degrading enzyme. *J Mol Biol, 395*(2), 430-443. doi:10.1016/j.jmb.2009.10.072

Hardy, J. A., & Higgins, G. A. (1992). Alzheimer's disease: the amyloid cascade hypothesis. *Science, 256*(5054), 184. doi:10.1126/science.1566067

Henderson, S. J., Andersson, C., Narwal, R., Janson, J., Goldschmidt, T. J., Appelkvist, P., Bogstedt, A., Steffen, A.-C., Haupts, U., Tebbe, J., Freskgård, P. O., Jermutus, L., Burrell, M., Fowler, S. B., & Webster, C. I. (2014). Sustained peripheral depletion of amyloid-β with a novel form of neprilysin does not affect central levels of amyloid-β. *Brain, 137*(2), 553-564. doi:10.1093/brain/awt308

Hernandez-Zimbron, L. F., Luna-Munoz, J., Mena, R., Vazquez-Ramirez, R., Kubli-Garfias, C., Cribbs, D. H., Manoutcharian, K., & Gevorkian, G. (2012). Amyloid-beta peptide binds to cytochrome C oxidase subunit 1. *PLoS One, 7*(8), e42344. doi:10.1371/journal.pone.0042344

Herold, K., Moser, B., Chen, Y., Zeng, S., Yan, S. F., Ramasamy, R., Emond, J., Clynes, R., & Schmidt, A. M. (2007). Receptor for advanced glycation end products (RAGE) in a

dash to the rescue: inflammatory signals gone awry in the primal response to stress. *J Leukoc Biol, 82*(2), 204-212. doi:10.1189/jlb.1206751

Hillen, H. (2019). The Beta Amyloid Dysfunction (BAD) Hypothesis for Alzheimer's Disease. *Front Neurosci, 13*, 1154. doi:10.3389/fnins.2019.01154

Hoshino, M., Khutia, A., Xing, H., Inokuma, Y., & Fujita, M. (2016). The crystalline sponge method updated. *IUCrJ, 3*(2), 139-151. doi:10.1107/S2052252515024379

Hou, L., & Zagorski, M. G. (2006). NMR reveals anomalous copper(II) binding to the amyloid Abeta peptide of Alzheimer's disease. *J Am Chem Soc, 128*(29), 9260-9261. doi:10.1021/ja046032u

Hu, Z. W., Vugmeyster, L., Au, D. F., Ostrovsky, D., Sun, Y., & Qiang, W. (2019). Molecular structure of an N-terminal phosphorylated beta-amyloid fibril. *Proc Natl Acad Sci U S A, 116*(23), 11253-11258. doi:10.1073/pnas.1818530116

Hureau, C., & Faller, P. (2009). Abeta-mediated ROS production by Cu ions: structural insights, mechanisms and relevance to Alzheimer's disease. *Biochimie, 91*(10), 1212-1217. doi:10.1016/j.biochi.2009.03.013

Ikeda, M., Brown, J., Holland, A. J., Fukuhara, R., & Hodges, J. R. (2002). Changes in appetite, food preference, and eating habits in frontotemporal dementia and Alzheimer's disease. *J Neurol Neurosurg Psychiatry, 73*(4), 371. doi:10.1136/jnnp.73.4.371

Jana, M., Palencia, C. A., & Pahan, K. (2008). Fibrillar amyloid-beta peptides activate microglia via TLR2: implications for Alzheimer's disease. *J Immunol, 181*(10), 7254-7262. doi:10.4049/jimmunol.181.10.7254

Kageyama, Y., Irie, Y., Matsushima, Y., Segawa, T., Bellier, J.-P., Hidaka, K., Sugiyama, H., Kaneda, D., Hashizume, Y., Akatsu, H., Miki, K., Kita, A., Walker, D. G., Irie, K., & Tooyama, I. (2021). Characterization of a Conformation-Restricted Amyloid β Peptide and Immunoreactivity of Its Antibody in Human AD brain. *ACS Chemical Neuroscience*. doi:10.1021/acschemneuro.1c00416

Kamenetz, F., Tomita, T., Hsieh, H., Seabrook, G., Borchelt, D., Iwatsubo, T., Sisodia, S., & Malinow, R. (2003). APP processing and synaptic function. *Neuron, 37*(6), 925-937. doi:10.1016/s0896-6273(03)00124-7

Kanski, J., Aksenova, M., & Butterfield, D. A. (2002). The hydrophobic environment of Met35 of Alzheimer's Abeta(1-42) is important for the neurotoxic and oxidative properties of the peptide. *Neurotox Res, 4*(3), 219-223. doi:10.1080/10298420290023945

Kim, T. S., Pae, C. U., Yoon, S. J., Jang, W. Y., Lee, N. J., Kim, J. J., Lee, S. J., Lee, C., Paik, I. H., & Lee, C. U. (2006). Decreased plasma antioxidants in patients with Alzheimer's disease. *Int J Geriatr Psychiatry, 21*(4), 344-348. doi:10.1002/gps.1469

King, J. V., Liang, W. G., Scherpelz, K. P., Schilling, A. B., Meredith, S. C., & Tang, W. J. (2014). Molecular basis of substrate recognition and degradation by human presequence protease. *Structure, 22*(7), 996-1007. doi:10.1016/j.str.2014.05.003

Kollmer, M., Close, W., Funk, L., Rasmussen, J., Bsoul, A., Schierhorn, A., Schmidt, M., Sigurdson, C. J., Jucker, M., & Fandrich, M. (2019). Cryo-EM structure and polymorphism of Abeta amyloid fibrils purified from Alzheimer's brain tissue. *Nat Commun, 10*(1), 4760. doi:10.1038/s41467-019-12683-8

Koo, E. H., Park, L., & Selkoe, D. J. (1993). Amyloid beta-protein as a substrate interacts with extracellular matrix to promote neurite outgrowth. *Proc Natl Acad Sci U S A, 90*(10), 4748-4752. doi:10.1073/pnas.90.10.4748

Korchazhkina, O. V., Ashcroft, A. E., Kiss, T., & Exley, C. (2002). The degradation of Abeta(25-35) by the serine protease plasmin is inhibited by aluminium. *J Alzheimers Dis, 4*(5), 357-367. doi:10.3233/jad-2002-4503

Krotee, P., Griner, S. L., Sawaya, M. R., Cascio, D., Rodriguez, J. A., Shi, D., Philipp, S., Murray, K., Saelices, L., Lee, J., Seidler, P., Glabe, C. G., Jiang, L., Gonen, T., & Eisenberg, D. S. (2018). Common fibrillar spines of amyloid-beta and human islet amyloid polypeptide revealed by microelectron diffraction and structure-based inhibitors. *J Biol Chem, 293*(8), 2888-2902. doi:10.1074/jbc.M117.806109

Kuhn, A. J., Abrams, B. S., Knowlton, S., & Raskatov, J. A. (2020). Alzheimer's Disease "Non-amyloidogenic" p3 Peptide Revisited: A Case for Amyloid-α. *ACS Chemical Neuroscience, 11*(11), 1539-1544. doi:10.1021/acschemneuro.0c00160

Kuhn, A. J., & Raskatov, J. (2020). Is the p3 Peptide (Aβ17-40, Aβ17-42) Relevant to the Pathology of Alzheimer's Disease? *Journal of Alzheimer's Disease, 74*, 43-53. doi:10.3233/JAD-191201

Kumar, D. K., Choi, S. H., Washicosky, K. J., Eimer, W. A., Tucker, S., Ghofrani, J., Lefkowitz, A., McColl, G., Goldstein, L. E., Tanzi, R. E., & Moir, R. D. (2016). Amyloid-beta peptide protects against microbial infection in mouse and worm models of Alzheimer's disease. *Sci Transl Med, 8*(340), 340ra372. doi:10.1126/scitranslmed.aaf1059

Kuo, Y. M., Kokjohn, T. A., Kalback, W., Luehrs, D., Galasko, D. R., Chevallier, N., Koo, E. H., Emmerling, M. R., & Roher, A. E. (2000). Amyloid-beta peptides interact with plasma proteins and erythrocytes: implications for their quantitation in plasma. *Biochem Biophys Res Commun, 268*(3), 750-756. doi:10.1006/bbrc.2000.2222

La Porte, S. L., Bollini, S. S., Lanz, T. A., Abdiche, Y. N., Rusnak, A. S., Ho, W. H., Kobayashi, D., Harrabi, O., Pappas, D., Mina, E. W., Milici, A. J., Kawabe, T. T., Bales, K., Lin, J. C., & Pons, J. (2012). Structural basis of C-terminal beta-amyloid peptide binding by the antibody ponezumab for the treatment of Alzheimer's disease. *J Mol Biol, 421*(4-5), 525-536. doi:10.1016/j.jmb.2011.11.047

LaFerla, F. M., Green, K. N., & Oddo, S. (2007). Intracellular amyloid-beta in Alzheimer's disease. *Nat Rev Neurosci, 8*(7), 499-509. doi:10.1038/nrn2168

Larmuth, K. M., Masuyer, G., Douglas, R. G., Schwager, S. L., Acharya, K. R., & Sturrock, E. D. (2016). Kinetic and structural characterization of amyloid-beta peptide hydrolysis by human angiotensin-1-converting enzyme. *FEBS J, 283*(6), 1060-1076. doi:10.1111/febs.13647

Lesne, S., Ali, C., Gabriel, C., Croci, N., MacKenzie, E. T., Glabe, C. G., Plotkine, M., Marchand-Verrecchia, C., Vivien, D., & Buisson, A. (2005). NMDA receptor activation inhibits alpha-secretase and promotes neuronal amyloid-beta production. *J Neurosci, 25*(41), 9367-9377. doi:10.1523/JNEUROSCI.0849-05.2005

Lu, J. X., Qiang, W., Yau, W. M., Schwieters, C. D., Meredith, S. C., & Tycko, R. (2013). Molecular structure of β-amyloid fibrils in alzheimer's disease brain tissue. *Cell, 154*, X1257-1268. doi:10.1016/j.cell.2013.08.035

Luhrs, T., Ritter, C., Adrian, M., Riek-Loher, D., Bohrmann, B., Dobeli, H., Schubert, D., & Riek, R. (2005). 3D structure of Alzheimer's amyloid-beta(1-42) fibrils. *Proc Natl Acad Sci U S A, 102*(48), 17342-17347. doi:10.1073/pnas.0506723102

Luo, Y., Sunderland, T., & Wolozin, B. (1996). Physiologic levels of beta-amyloid activate phosphatidylinositol 3-kinase with the involvement of tyrosine phosphorylation. *J Neurochem, 67*(3), 978-987. doi:10.1046/j.1471-4159.1996.67030978.x

Lustbader, J. W., Cirilli, M., Lin, C., Xu, H. W., Takuma, K., Wang, N., Caspersen, C., Chen, X., Pollak, S., Chaney, M., Trinchese, F., Liu, S., Gunn-Moore, F., Lue, L. F., Walker, D. G., Kuppusamy, P., Zewier, Z. L., Arancio, O., Stern, D., Yan, S. S., & Wu, H. (2004). ABAD directly links Abeta to mitochondrial toxicity in Alzheimer's disease. *Science, 304*(5669), 448-452. doi:10.1126/science.1091230

Manczak, M., & Reddy, P. H. (2012). Abnormal interaction of VDAC1 with amyloid beta and phosphorylated tau causes mitochondrial dysfunction in Alzheimer's disease. *Hum Mol Genet, 21*(23), 5131-5146. doi:10.1093/hmg/dds360

Masuda, Y., Nakanishi, A., Ohashi, R., Takegoshi, K., Shimizu, T., Shirasawa, T., & Irie, K. (2008). Verification of the intermolecular parallel beta-sheet in E22K-Abeta42 aggregates by solid-state NMR using rotational resonance: implications for the supramolecular arrangement of the toxic conformer of Abeta42. *Biosci Biotechnol Biochem, 72*(8), 2170-2175. doi:10.1271/bbb.80250

Matsunaga, S., Kishi, T., & Iwata, N. (2015). Memantine monotherapy for Alzheimer's disease: a systematic review and meta-analysis. *PLoS One, 10*(4), e0123289. doi:10.1371/journal.pone.0123289

McKhann, G., Drachman, D., Folstein, M., Katzman, R., Price, D., & Stadlan, E. M. (1984). Clinical diagnosis of Alzheimer's disease: report of the NINCDS-ADRDA Work Group under the auspices of Department of Health and Human Services Task Force on Alzheimer's Disease. *Neurology, 34*(7), 939-944. doi:10.1212/wnl.34.7.939

Miles, L. A., Crespi, G. A., Doughty, L., & Parker, M. W. (2013). Bapineuzumab captures the N-terminus of the Alzheimer's disease amyloid-beta peptide in a helical conformation. *Sci Rep, 3*, 1302. doi:10.1038/srep01302

Miles, L. A., Wun, K. S., Crespi, G. A., Fodero-Tavoletti, M. T., Galatis, D., Bagley, C. J., Beyreuther, K., Masters, C. L., Cappai, R., McKinstry, W. J., Barnham, K. J., & Parker, M. W. (2008). Amyloid-beta-anti-amyloid-beta complex structure reveals an extended conformation in the immunodominant B-cell epitope. *J Mol Biol, 377*(1), 181-192. doi:10.1016/j.jmb.2007.12.036

Moghekar, A., Rao, S., Li, M., Ruben, D., Mammen, A., Tang, X., & O'Brien, R. J. (2011). Large Quantities of Aβ Peptide Are Constitutively Released during Amyloid Precursor Protein Metabolism in Vivo and in Vitro*. *Journal of Biological Chemistry, 286*(18), 15989-15997. doi:10.1074/jbc.M110.191262

Montoliu-Gaya, L., & Villegas, S. (2015). Protein structures in Alzheimer's disease: The basis for rationale therapeutic design. *Arch Biochem Biophys, 588*, 1-14. doi:10.1016/j.abb.2015.10.005

Morley, J. E., & Farr, S. A. (2012). Hormesis and amyloid-beta protein: physiology or pathology? *J Alzheimers Dis, 29*(3), 487-492. doi:10.3233/JAD-2011-111928

Nelson, R., Sawaya, M. R., Balbirnie, M., Madsen, A. Ø., Riekel, C., Grothe, R., & Eisenberg, D. (2005). Structure of the cross-β spine of amyloid-like fibrils. *Nature, 435*, 773-778. doi:10.1038/nature03680

Nilsberth, C., Westlind-Danielsson, A., Eckman, C. B., Condron, M. M., Axelman, K., Forsell, C., Stenh, C., Luthman, J., Teplow, D. B., Younkin, S. G., Naslund, J., & Lannfelt, L. (2001). The 'Arctic' APP mutation (E693G) causes Alzheimer's disease by enhanced Abeta protofibril formation. *Nat Neurosci, 4*(9), 887-893. doi:10.1038/nn0901-887

Nussbaum, J. M., Schilling, S., Cynis, H., Silva, A., Swanson, E., Wangsanut, T., Tayler, K., Wiltgen, B., Hatami, A., Rönicke, R., Reymann, K., Hutter-Paier, B., Alexandru, A., Jagla, W., Graubner, S., Glabe, C. G., Demuth, H.-U., & Bloom, G. S. (2012). Prion-like behaviour and tau-dependent cytotoxicity of pyroglutamylated amyloid-β. *Nature, 485*(7400), 651-655. doi:10.1038/nature11060

Ono, K., Condron, M. M., & Teplow, D. B. (2010). Effects of the English (H6R) and Tottori (D7N) familial Alzheimer disease mutations on amyloid beta-protein assembly and toxicity. *J Biol Chem, 285*(30), 23186-23197. doi:10.1074/jbc.M109.086496

Onos, K. D., Sukoff Rizzo, S. J., Howell, G. R., & Sasner, M. (2016). Toward more predictive genetic mouse models of Alzheimer's disease. *Brain Res Bull, 122*, 1-11. doi:10.1016/j.brainresbull.2015.12.003

Oskarsson, M. E., Paulsson, J. F., Schultz, S. W., Ingelsson, M., Westermark, P., & Westermark, G. T. (2015). In vivo seeding and cross-seeding of localized amyloidosis: a molecular link between type 2 diabetes and Alzheimer disease. *Am J Pathol, 185*(3), 834-846. doi:10.1016/j.ajpath.2014.11.016

Ovchinnikova, O. Y., Finder, V. H., Vodopivec, I., Nitsch, R. M., & Glockshuber, R. (2011). The Osaka FAD mutation E22Delta leads to the formation of a previously unknown type of amyloid beta fibrils and modulates Abeta neurotoxicity. *J Mol Biol, 408*(4), 780-791. doi:10.1016/j.jmb.2011.02.049

Panza, F., Lozupone, M., Seripa, D., & Imbimbo, B. P. (2019). Amyloid-β immunotherapy for alzheimer disease: Is it now a long shot? *Annals of Neurology, 85*(3), 303-315. doi:10.1002/ana.25410

Paravastu, A. K., Leapman, R. D., Yau, W. M., & Tycko, R. (2008). Molecular structural basis for polymorphism in Alzheimer's beta-amyloid fibrils. *Proc Natl Acad Sci U S A, 105*(47), 18349-18354. doi:10.1073/pnas.0806270105

Perry, E. K. (1986). The cholinergic hypothesis--ten years on. *Br Med Bull, 42*(1), 63-69. doi:10.1093/oxfordjournals.bmb.a072100

Petkova, A. T., Buntkowsky, G., Dyda, F., Leapman, R. D., Yau, W. M., & Tycko, R. (2004). Solid State NMR Reveals a pH-dependent Antiparallel β-Sheet Registry in Fibrils Formed by a β-Amyloid Peptide. *Journal of Molecular Biology, 335*(1), 247-260. doi:10.1016/j.jmb.2003.10.044

Petkova, A. T., Leapman, R. D., Guo, Z., Yau, W. M., Mattson, M. P., & Tycko, R. (2005). Self-propagating, molecular-level polymorphism in Alzheimer's β-amyloid fibrils. *Science, 307*, 262-265. doi:10.1126/science.1105850

Petkova, A. T., Yau, W. M., & Tycko, R. (2006). Experimental constraints on quaternary structure in Alzheimer's β-amyloid fibrils. *Biochemistry, 45*, 498-512. doi:10.1021/bi051952q

Piechotta, A., Parthier, C., Kleinschmidt, M., Gnoth, K., Pillot, T., Lues, I., Demuth, H. U., Schilling, S., Rahfeld, J. U., & Stubbs, M. T. (2017). Structural and functional analyses of pyroglutamate-amyloid-beta-specific antibodies as a basis for Alzheimer immunotherapy. *J Biol Chem, 292*(30), 12713-12724. doi:10.1074/jbc.M117.777839

Plant, L. D., Webster, N. J., Boyle, J. P., Ramsden, M., Freir, D. B., Peers, C., & Pearson, H. A. (2006). Amyloid beta peptide as a physiological modulator of neuronal 'A'-type K+ current. *Neurobiol Aging, 27*(11), 1673-1683. doi:10.1016/j.neurobiolaging.2005.09.038

Prasher, V. P., Farrer, M. J., Kessling, A. M., Fisher, E. M., West, R. J., Barber, P. C., & Butler, A. C. (1998). Molecular mapping of Alzheimer-type dementia in Down's syndrome. *Ann Neurol, 43*(3), 380-383. doi:10.1002/ana.410430316

Priller, C., Bauer, T., Mitteregger, G., Krebs, B., Kretzschmar, H. A., & Herms, J. (2006). Synapse formation and function is modulated by the amyloid precursor protein. *J Neurosci, 26*(27), 7212-7221. doi:10.1523/JNEUROSCI.1450-06.2006

Puzzo, D., Privitera, L., Fa, M., Staniszewski, A., Hashimoto, G., Aziz, F., Sakurai, M., Ribe, E. M., Troy, C. M., Mercken, M., Jung, S. S., Palmeri, A., & Arancio, O. (2011). Endogenous amyloid-beta is necessary for hippocampal synaptic plasticity and memory. *Ann Neurol, 69*(5), 819-830. doi:10.1002/ana.22313

Qiang, W., Yau, W. M., Luo, Y., Mattson, M. P., & Tycko, R. (2012). Antiparallel beta-sheet architecture in Iowa-mutant beta-amyloid fibrils. *Proc Natl Acad Sci U S A, 109*(12), 4443-4448. doi:10.1073/pnas.1111305109

Qiu, W. Q., Walsh, D. M., Ye, Z., Vekrellis, K., Zhang, J., Podlisny, M. B., Rosner, M. R., Safavi, A., Hersh, L. B., & Selkoe, D. J. (1998). Insulin-degrading enzyme regulates extracellular levels of amyloid beta-protein by degradation. *J Biol Chem, 273*(49), 32730-32738. doi:10.1074/jbc.273.49.32730

Rauth, S., Hinz, D., Borger, M., Uhrig, M., Mayhaus, M., Riemenschneider, M., & Skerra, A. (2016). High-affinity Anticalins with aggregation-blocking activity directed against the Alzheimer beta-amyloid peptide. *Biochem J, 473*(11), 1563-1578. doi:10.1042/BCJ20160114

Religa, D., Strozyk, D., Cherny, R. A., Volitakis, I., Haroutunian, V., Winblad, B., Naslund, J., & Bush, A. I. (2006). Elevated cortical zinc in Alzheimer disease. *Neurology, 67*(1), 69-75. doi:10.1212/01.wnl.0000223644.08653.b5

Rezaei-Ghaleh, N., Giller, K., Becker, S., & Zweckstetter, M. (2011). Effect of zinc binding on beta-amyloid structure and dynamics: implications for Abeta aggregation. *Biophys J, 101*(5), 1202-1211. doi:10.1016/j.bpj.2011.06.062

Ribeiro, C. A., Oliveira, S. M., Guido, L. F., Magalhaes, A., Valencia, G., Arsequell, G., Saraiva, M. J., & Cardoso, I. (2014). Transthyretin stabilization by iododiflunisal promotes amyloid-beta peptide clearance, decreases its deposition, and ameliorates cognitive deficits in an Alzheimer's disease mouse model. *J Alzheimers Dis, 39*(2), 357-370. doi:10.3233/JAD-131355

Ribeiro, C. A., Santana, I., Oliveira, C., Baldeiras, I., Moreira, J., Saraiva, M. J., & Cardoso, I. (2012). Transthyretin decrease in plasma of MCI and AD patients: investigation of mechanisms for disease modulation. *Curr Alzheimer Res, 9*(8), 881-889. doi:10.2174/156720512803251057

Ricciarelli, R., & Fedele, E. (2017). The Amyloid Cascade Hypothesis in Alzheimer's Disease: It's Time to Change Our Mind. *Curr Neuropharmacol, 15*(6), 926-935. doi:10.2174/1570159X15666170116143743

Roques, B. P., Noble, F., Daugé, V., Fournié-Zaluski, M. C., & Beaumont, A. (1993). Neutral endopeptidase 24.11: structure, inhibition, and experimental and clinical pharmacology. *Pharmacological Reviews, 45*(1), 87.

Rottkamp, C. A., Raina, A. K., Zhu, X., Gaier, E., Bush, A. I., Atwood, C. S., Chevion, M., Perry, G., & Smith, M. A. (2001). Redox-active iron mediates amyloid-beta toxicity. *Free Radic Biol Med, 30*(4), 447-450. doi:10.1016/s0891-5849(00)00494-9

Rovelet-Lecrux, A., Hannequin, D., Raux, G., Le Meur, N., Laquerriere, A., Vital, A., Dumanchin, C., Feuillette, S., Brice, A., Vercelletto, M., Dubas, F., Frebourg, T., & Campion, D. (2006). APP locus duplication causes autosomal dominant early-onset Alzheimer disease with cerebral amyloid angiopathy. *Nat Genet, 38*(1), 24-26. doi:10.1038/ng1718

Ryan, T. M., Kirby, N., Mertens, H. D., Roberts, B., Barnham, K. J., Cappai, R., Pham Cle, L., Masters, C. L., & Curtain, C. C. (2015). Small angle X-ray scattering analysis of Cu(2+)-induced oligomers of the Alzheimer's amyloid beta peptide. *Metallomics, 7*(3), 536-543. doi:10.1039/c4mt00323c

Sachse, C., Fändrich, M., & Grigorieff, N. (2008). Paired β-sheet structure of an Aβ(1-40) amyloid fibril revealed by electron microscopy. *Proceedings of the National Academy of Sciences of the United States of America, 105*, 7462-7466. doi:10.1073/pnas.0712290105

Saunders, A. M., Strittmatter, W. J., Schmechel, D., George-Hyslop, P. H., Pericak-Vance, M. A., Joo, S. H., Rosi, B. L., Gusella, J. F., Crapper-MacLachlan, D. R., Alberts, M. J., & et al. (1993). Association of apolipoprotein E allele epsilon 4 with late-onset familial and sporadic Alzheimer's disease. *Neurology, 43*(8), 1467-1472. doi:10.1212/wnl.43.8.1467

Sawaya, M. R., Sambashivan, S., Nelson, R., Ivanova, M. I., Sievers, S. A., Apostol, M. I., Thompson, M. J., Balbirnie, M., Wiltzius, J. J., McFarlane, H. T., Madsen, A. O., Riekel, C., & Eisenberg, D. (2007). Atomic structures of amyloid cross-beta spines reveal varied steric zippers. *Nature, 447*(7143), 453-457. doi:10.1038/nature05695

Schmidt, M., Rohou, A., Lasker, K., Yadav, J. K., Schiene-Fischer, C., Fandrich, M., & Grigorieff, N. (2015). Peptide dimer structure in an Abeta(1-42) fibril visualized with cryo-EM. *Proc Natl Acad Sci U S A, 112*(38), 11858-11863. doi:10.1073/pnas.1503455112

Schonheit, B., Zarski, R., & Ohm, T. G. (2004). Spatial and temporal relationships between plaques and tangles in Alzheimer-pathology. *Neurobiol Aging, 25*(6), 697-711. doi:10.1016/j.neurobiolaging.2003.09.009

Schrodinger, LLC. (2015). *The PyMOL Molecular Graphics System, Version 1.8*.

Schütz, A. K., Vagt, T., Huber, M., Ovchinnikova, O. Y., Cadalbert, R., Wall, J., Güntert, P., Bcöckmann, A., Glockshuber, R., & Meier, B. H. (2015). Atomic-resolution three-dimensional structure of amyloid b fibrils bearing the osaka mutation. *Angewandte Chemie - International Edition, 54*, 331-335. doi:10.1002/anie.201408598

Selkoe, D. J., & Hardy, J. (2016). The amyloid hypothesis of Alzheimer's disease at 25 years. *EMBO Mol Med, 8*(6), 595-608. doi:10.15252/emmm.201606210

Sharma, A. K., Pavlova, S. T., Kim, J., Finkelstein, D., Hawco, N. J., Rath, N. P., Kim, J., & Mirica, L. M. (2012). Bifunctional compounds for controlling metal-mediated aggregation of the abeta42 peptide. *J Am Chem Soc, 134*(15), 6625-6636. doi:10.1021/ja210588m

Shen, Y., Joachimiak, A., Rich Rosner, M., & Tang, W. J. (2006). Structures of human insulin-degrading enzyme reveal a new substrate recognition mechanism. *Nature, 443*, 870-874. doi:10.1038/nature05143

Shi, D., Nannenga, B. L., Iadanza, M. G., & Gonen, T. (2013). Three-dimensional electron crystallography of protein microcrystals. *Elife, 2*, e01345. doi:10.7554/eLife.01345

Sims-Robinson, C., Kim, B., Rosko, A., & Feldman, E. L. (2010). How does diabetes accelerate Alzheimer disease pathology? *Nat Rev Neurol, 6*(10), 551-559. doi:10.1038/nrneurol.2010.130

Singh, I., Sagare, A. P., Coma, M., Perlmutter, D., Gelein, R., Bell, R. D., Deane, R. J., Zhong, E., Parisi, M., Ciszewski, J., Kasper, R. T., & Deane, R. (2013). Low levels of copper disrupt brain amyloid-beta homeostasis by altering its production and clearance. *Proc Natl Acad Sci U S A, 110*(36), 14771-14776. doi:10.1073/pnas.1302212110

Sipe, J. D., & Cohen, A. S. (2000). Review: history of the amyloid fibril. *J Struct Biol, 130*(2-3), 88-98. doi:10.1006/jsbi.2000.4221

Sjogren, M., Davidsson, P., Wallin, A., Granerus, A. K., Grundstrom, E., Askmark, H., Vanmechelen, E., & Blennow, K. (2002). Decreased CSF-beta-amyloid 42 in Alzheimer's disease and amyotrophic lateral sclerosis may reflect mismetabolism of beta-amyloid induced by disparate mechanisms. *Dement Geriatr Cogn Disord, 13*(2), 112-118. doi:10.1159/000048642

St George-Hyslop, P. H., Tanzi, R. E., Polinsky, R. J., Haines, J. L., Nee, L., Watkins, P. C., Myers, R. H., Feldman, R. G., Pollen, D., Drachman, D., & et al. (1987). The genetic defect causing familial Alzheimer's disease maps on chromosome 21. *Science, 235*(4791), 885-890. doi:10.1126/science.2880399

Stanyon, H. F., & Viles, J. H. (2012). Human serum albumin can regulate amyloid-beta peptide fiber growth in the brain interstitium: implications for Alzheimer disease. *J Biol Chem, 287*(33), 28163-28168. doi:10.1074/jbc.C112.360800

Steinbach, J. P., Muller, U., Leist, M., Li, Z. W., Nicotera, P., & Aguzzi, A. (1998). Hypersensitivity to seizures in beta-amyloid precursor protein deficient mice. *Cell Death Differ, 5*(10), 858-866. doi:10.1038/sj.cdd.4400391

Sui, L., Wang, J., & Li, B. M. (2008). Role of the phosphoinositide 3-kinase-Akt-mammalian target of the rapamycin signaling pathway in long-term potentiation and trace fear conditioning memory in rat medial prefrontal cortex. *Learn Mem, 15*(10), 762-776. doi:10.1101/lm.1067808

Sun, Y., Sommerville, N. R., Liu, J. Y. H., Ngan, M. P., Poon, D., Ponomarev, E. D., Lu, Z., Kung, J. S. C., & Rudd, J. A. (2020). Intra-gastrointestinal amyloid-β1–42 oligomers perturb enteric function and induce Alzheimer's disease pathology. *The Journal of Physiology, 598*(19), 4209-4223. doi:10.1113/JP279919

Sunde, M., Serpell, L. C., Bartlam, M., Fraser, P. E., Pepys, M. B., & Blake, C. C. (1997). Common core structure of amyloid fibrils by synchrotron X-ray diffraction. *J Mol Biol, 273*(3), 729-739. doi:10.1006/jmbi.1997.1348

Tang, T. C., Hu, Y., Kienlen-Campard, P., El Haylani, L., Decock, M., Van Hees, J., Fu, Z., Octave, J. N., Constantinescu, S. N., & Smith, S. O. (2014). Conformational changes induced by the A21G Flemish mutation in the amyloid precursor protein lead to increased Abeta production. *Structure, 22*(3), 387-396. doi:10.1016/j.str.2013.12.012

Teixeira, P. F., Masuyer, G., Pinho, C. M., Branca, R. M. M., Kmiec, B., Wallin, C., Warmlander, S., Berntsson, R. P., Ankarcrona, M., Graslund, A., Lehtio, J., Stenmark, P., & Glaser, E. (2018). Mechanism of Peptide Binding and Cleavage by the Human Mitochondrial Peptidase Neurolysin. *J Mol Biol, 430*(3), 348-362. doi:10.1016/j.jmb.2017.11.011

Teplyakov, A., Obmolova, G., & Gilliland, G. L. (2017). A coiled conformation of amyloid-beta recognized by antibody C706. *Alzheimers Res Ther, 9*(1), 66. doi:10.1186/s13195-017-0296-0

Terry, A. V., Jr., & Buccafusco, J. J. (2003). The cholinergic hypothesis of age and Alzheimer's disease-related cognitive deficits: recent challenges and their implications for novel drug development. *J Pharmacol Exp Ther, 306*(3), 821-827. doi:10.1124/jpet.102.041616

Tiraboschi, G., Jullian, N., Thery, V., Antonczak, S., Fournie-Zaluski, M.-C., & Roques, B. P. (1999). A three-dimensional construction of the active site (region 507–749) of human neutral endopeptidase (EC.3.4.24.11). *Protein Engineering, Design and Selection, 12*(2), 141-149. doi:10.1093/protein/12.2.141

Tokuda, T., Calero, M., Matsubara, E., Vidal, R., Kumar, A., Permanne, B., Zlokovic, B., Smith, J. D., Ladu, M. J., Rostagno, A., Frangione, B., & Ghiso, J. (2000). Lipidation of apolipoprotein E influences its isoform-specific interaction with Alzheimer's amyloid beta peptides. *Biochem J, 348 Pt 2*, 359-365. doi:10.1042/bj3480359

Turner, P. R., O'Connor, K., Tate, W. P., & Abraham, W. C. (2003). Roles of amyloid precursor protein and its fragments in regulating neural activity, plasticity and memory. *Prog Neurobiol, 70*(1), 1-32. doi:10.1016/s0301-0082(03)00089-3

Tycko, R., & Ishii, Y. (2003). Constraints on Supramolecular Structure in Amyloid Fibrils from Two-Dimensional Solid-State NMR Spectroscopy with Uniform Isotopic Labeling. *Journal of the American Chemical Society, 125*(22), 6606-6607. doi:10.1021/ja0342042

Ultsch, M., Li, B., Maurer, T., Mathieu, M., Adolfsson, O., Muhs, A., Pfeifer, A., Pihlgren, M., Bainbridge, T. W., Reichelt, M., Ernst, J. A., Eigenbrot, C., Fuh, G., Atwal, J. K., Watts, R. J., & Wang, W. (2016). Structure of Crenezumab Complex with Abeta Shows Loss of beta-Hairpin. *Sci Rep, 6*, 39374. doi:10.1038/srep39374

Vangavaragu, J. R., Valasani, K. R., Gan, X., & Yan, S. S. (2014). Identification of human presequence protease (hPreP) agonists for the treatment of Alzheimer's disease. *Eur J Med Chem, 76*, 506-516. doi:10.1016/j.ejmech.2014.02.046

Vassar, P. S., & Culling, C. F. (1959). Fluorescent stains, with special reference to amyloid and connective tissues. *Arch Pathol, 68*, 487-498.

Wälti, M. A., Ravotti, F., Arai, H., Glabe, C. G., Wall, J. S., Böckmann, A., Güntert, P., Meier, B. H., & Riek, R. (2016). Atomic-resolution structure of a disease-relevant Aβ(1-42) amyloid fibril. *Proceedings of the National Academy of Sciences of the United States of America, 113*, E4976-4984. doi:10.1073/pnas.1600749113

Wang, C., Wurtman, R. J., & Lee, R. K. (2000). Amyloid precursor protein and membrane phospholipids in primary cortical neurons increase with development, or after exposure to nerve growth factor or Abeta(1-40). *Brain Res, 865*(2), 157-167. doi:10.1016/s0006-8993(00)02183-1

Wang, H. Y., Li, W., Benedetti, N. J., & Lee, D. H. (2003). Alpha 7 nicotinic acetylcholine receptors mediate beta-amyloid peptide-induced tau protein phosphorylation. *J Biol Chem, 278*(34), 31547-31553. doi:10.1074/jbc.M212532200

Warmack, R. A., Boyer, D. R., Zee, C. T., Richards, L. S., Sawaya, M. R., Cascio, D., Gonen, T., Eisenberg, D. S., & Clarke, S. G. (2019). Structure of amyloid-beta (20-34) with Alzheimer's-associated isomerization at Asp23 reveals a distinct protofilament interface. *Nat Commun, 10*(1), 3357. doi:10.1038/s41467-019-11183-z

Wildburger, N. C., Esparza, T. J., LeDuc, R. D., Fellers, R. T., Thomas, P. M., Cairns, N. J., Kelleher, N. L., Bateman, R. J., & Brody, D. L. (2017). Diversity of Amyloid-beta Proteoforms in the Alzheimer's Disease Brain. *Sci Rep, 7*(1), 9520. doi:10.1038/s41598-017-10422-x

Wood, J. G., Mirra, S. S., Pollock, N. J., & Binder, L. I. (1986). Neurofibrillary tangles of Alzheimer disease share antigenic determinants with the axonal microtubule-associated protein tau (tau). *Proc Natl Acad Sci U S A, 83*(11), 4040-4043. doi:10.1073/pnas.83.11.4040

Wu, G., Miller, R. A., Connolly, B., Marcus, J., Renger, J., & Savage, M. J. (2014). Pyroglutamate-Modified Amyloid-β Protein Demonstrates Similar Properties in an Alzheimer's Disease Familial Mutant Knock-In Mouse and Alzheimer's Disease Brain. *Neurodegenerative Diseases, 14*(2), 53-66. doi:10.1159/000353634

Xiao, Y., Ma, B., McElheny, D., Parthasarathy, S., Long, F., Hoshi, M., Nussinov, R., & Ishii, Y. (2015). Aβ(1-42) fibril structure illuminates self-recognition and replication of amyloid in Alzheimer's disease. *Nature structural & molecular biology, 22*, 499-505. doi:10.1038/nsmb.2991

Xie, J., Liang, R., Wang, Y., Huang, J., Cao, X., & Niu, B. (2020). Progress in Target Drug Molecules for Alzheimer's Disease. *Curr Top Med Chem, 20*(1), 4-36. doi:10.2174/1568026619666191203113745

Xie, L., Helmerhorst, E., Taddei, K., Plewright, B., Van Bronswijk, W., & Martins, R. (2002). Alzheimer's beta-amyloid peptides compete for insulin binding to the insulin receptor. *J Neurosci, 22*(10), RC221. doi:20026383

Yan, S. D., Fu, J., Soto, C., Chen, X., Zhu, H., Al-Mohanna, F., Collison, K., Zhu, A., Stern, E., Saido, T., Tohyama, M., Ogawa, S., Roher, A., & Stern, D. (1997). An intracellular protein that binds amyloid-beta peptide and mediates neurotoxicity in Alzheimer's disease. *Nature, 389*(6652), 689-695. doi:10.1038/39522

Zhang, R., Hu, X., Khant, H., Ludtke, S. J., Chiu, W., Schmid, M. F., Frieden, C., & Lee, J.-M. (2009). Interprotofilament interactions between Alzheimer's Abeta1-42 peptides in amyloid fibrils revealed by cryoEM. *Proceedings of the National Academy of Sciences of the United States of America, 106*, 4653-4658. doi:10.1073/pnas.0901085106

Zhao, L. N., Lu, L., Chew, L. Y., & Mu, Y. (2014). Alzheimer's disease--a panorama glimpse. *Int J Mol Sci, 15*(7), 12631-12650. doi:10.3390/ijms150712631

Zheng, X., Liu, D., Roychaudhuri, R., Teplow, D. B., & Bowers, M. T. (2015). Amyloid beta-Protein Assembly: Differential Effects of the Protective A2T Mutation and Recessive A2V Familial Alzheimer's Disease Mutation. *ACS Chem Neurosci, 6*(10), 1732-1740. doi:10.1021/acschemneuro.5b00171

Zhu, D., Lai, Y., Shelat, P. B., Hu, C., Sun, G. Y., & Lee, J. C. (2006). Phospholipases A2 mediate amyloid-beta peptide-induced mitochondrial dysfunction. *J Neurosci, 26*(43), 11111-11119. doi:10.1523/JNEUROSCI.3505-06.2006

Zirah, S., Kozin, S. A., Mazur, A. K., Blond, A., Cheminant, M., Segalas-Milazzo, I., Debey, P., & Rebuffat, S. (2006). Structural changes of region 1-16 of the Alzheimer disease amyloid beta-peptide upon zinc binding and in vitro aging. *J Biol Chem, 281*(4), 2151-2161. doi:10.1074/jbc.M504454200

# CHAPTER II. Amyloid-β peptide interaction with proteins

Work from this chapter has been published on:

**Leite, J. P.**, & Gales, L. (2019). Alzheimer's Abeta1-40 peptide degradation by thermolysin: evidence of inhibition by a C-terminal Abeta product. FEBS Lett, 593(1), 128-137. doi:10.1002/1873-3468.13285

**Leite, J.P.**; Lete, M. G.; Fowler, S.B.; Gimeno, A.; Rocha, J.F.; Sousa, S.F.; Webster, C.I.; Jiménez-Bàrbero, J.J.; Gales, L. (2021). $A\beta_{31-35}$ decreases Neprilysin-mediated Alzheimer's Amyloid-β peptide degradation. ACS Chemical Neuroscience, 12(19), 3708-3718. doi:10.1021/acschemneuro.1c00432.

# 2.1 Amyloid-β peptide interaction with transthyretin

Work contributions:

Transthyretin overexpression and purification was performed and kindly gifted by the Molecular Neurobiology group (i3S, Porto, Portugal).

### 2.1.1 Introduction

Transthyretin (TTR) is a transporter protein of the thyroid hormone thyroxine and of retinol (also known as vitamin A) bound to retinol-binding protein (hence its name, as indicated by underlined text segments), regulating the plasma levels of both molecules (Episkopou *et al.*, 1993). It is produced in the liver, choroid plexus and retinal pigment epithelium, being released to the bloodstream, cerebrospinal fluid and eye, respectively (Liz *et al.*, 2020). Structurally, it is a homo-tetrameric protein, composed by four identical 13.75 kDa, 127 amino acid monomers. It predominantly has β-chain structure, with the dimer stabilized mainly by hydrogen bonds, while the dimer-dimer interface mostly contains hydrophobic interactions (Hamilton *et al.*, 2001). The dissociation of the TTR tetramer leads to the generation of an amyloid aggregation prone monomer, causing senile systemic amyloidosis (Westermark *et al.*, 1990). In addition to wild type TTR, there are several single point mutations that increase the amyloidogenic potential of TTR, such as V30M, L55P, V122I, causing autosomal-dominant hereditary amyloidosis familial amyloid polyneuropathy (FAP, first described in Portugal by (Andrade, 1952)), familial amyloid cardiomyopathy or familial leptomeningeal amyloidosis. Currently, liver transplant is the main treatment for these diseases, with a more recent alternative use of tetramer kinetic stabilizers (*i.e.* small-molecules, typically halogenated, that bind the thyroxine binding pocket and halt tetramer dissociation) also being pursued. Tafamidis was the first approved drug for that purpose (Bulawa *et al.*, 2012).

Over the years, TTR has been associated with Alzheimer's disease and the amyloid-β peptide. TTR accounts for around 20% of the total CSF protein content (Schreiber *et al.*, 1990). The first *in vitro* TTR-Aβ interaction was confirmed by Schwartzman and colleagues, who observed by transmission electron microscope and using the amyloid dye thioflavin-T at a 300:1 Aβ:TTR molar ratio causing Aβ inhibition (Schwarzman *et al.*, 1994). This was later confirmed in a *C. elegans* AD animal model, where co-expression of TTR with Aβ significantly decreased amyloid deposits (Link, 1995). Then, significant negative correlation between TTR CSF levels and AD has been established and corroborated in different reports (Elovaara *et al.*, 1986; Gloeckner *et al.*, 2008; Serot *et al.*, 1997), as well as with TTR plasma levels (Han *et al.*, 2011). However, the role of TTR as an AD biomarker is still under debate, as other studies found no difference between CSF levels in AD and control groups (Schultz *et al.*, 2010). Nevertheless, several observations point to a role of TTR in AD, including a protective feedback loop found in an AD mouse model overexpressing Aβ in which TTR gene was up-regulated to cope with increased levels of the peptide (Stein *et al.*, 2002), suppression of TTR by an antibody results in Aβ overexpression and loss of protection against neuronal death (Stein *et al.*, 2004), expressing human wtTTR in mice halts Aβ

deposition (Buxbaum *et al.*, 2008) and thickening of basement membranes (an early hallmark of AD) is observed in mice with lower TTR expression (Ricardo Vieira *et al.*, 2019).

TTR-Aβ interaction seems at this point undeniable, although the exact mechanism of such interaction is still unknown. Possible mechanisms include TTR mediated inhibition and disruption of Aβ fibril formation (Costa *et al.*, 2008), TTR proteolytic action on Aβ (Silva *et al.*, 2017) and an increased effect of the TTR tetramer over Aβ inhibition (Alemi *et al.*, 2017). However, TTR-Aβ structural information has undoubtedly been elusive. Currently, most of the knowledge arises from computer modeling simulations or mass-spectrometry assisted assays. A few examples include modeling of Aβ binding sites in the TTR monomer surface, identification of TTR $_{38-42}$ as a critical segment for the interaction, Aβ binding to TTR residues from strands A and D located in or around the thyroxine binding pocket and possible binding to the TTR EF helix and loop (Du *et al.*, 2012; Du *et al.*, 2010; Schwarzman *et al.*, 1996; Schwarzman *et al.*, 1994; Schwarzman *et al.*, 2005). A study combining computer modeling and NMR also indicated that TTR-Aβ interaction occurs at the surface of the protein and that $A\beta_{18-20}$ is the critical peptide region for binding (Gimeno *et al.*, 2017). Here, we aimed at obtaining crystallographic information of the TTR-Aβ complex, by performing co-crystallization and crystal soaking experiments of wtTTR and mutant TTR L55P with a plethora of Aβ peptides and its fragments.

### 2.1.2 Materials and methods

#### 2.1.2.1. Aβ peptides

The following fragments were tested: $A\beta_{1-40}$, $A\beta_{1-42}$, $A\beta_{1-11}$, $A\beta_{1-16}$, $A\beta_{1-28}$, $A\beta_{1-37}$, $A\beta_{6-20}$, $A\beta_{10-20}$, $A\beta_{10-35}$, $A\beta_{12-28}$, $A\beta_{16-20}$, $A\beta_{19-20}$, $A\beta_{20-29}$, $A\beta_{25-35}$, $A\beta_{29-40}$, $A\beta_{31-35}$ and $A\beta_{33-42}$, purchased from Bachem (Switzerland); and, two iodinated $A\beta_{16-21}$ forms, KLVF(I)FA and KLVFF(I)A, here denominated IAβ1 and IAβ2, respectively (synthesized by IQAC - Institut de Química Avançada de Catalunya, Spain). Peptide samples were prepared based on (Broersen *et al.*, 2011). Briefly, lyophilized Aβ peptides were dissolved in 1,1,1,3,3,3-hexafluoro-2-propanol (HFIP) and incubated overnight at room temperature to disassemble possible pre-existing amyloid aggregates. The next day, HFIP was removed with a gentle stream of nitrogen, and further dried with a vacuum concentrator for 2.5 h to remove remaining traces. Dried peptide films were thoroughly resuspended in dimethyl sulfoxide (DMSO) and stored at -20˚C until further use.

### 2.1.2.2 Transthyretin co-crystallization or soaking with Aβ fragments and compounds 35 or 73

Transthyretin wild type (wtTTR) and TTR L55P amyloidogenic mutant (TTR55 for short) were produced as previously described (Furuya *et al.*, 1991) and kindly gifted by the Molecular Neurobiology group (i3S, Porto, Portugal). Both proteins were subsequently prepared for crystallographic studies by diafiltration and concentration in 10 mM HEPES pH 7.5 using a 3 kDa Amicon® Ultra-4 centrifugal filter unit (Merck, Germany). Concentration ranges were 4 - 8.5 $mg.ml^{-1}$ and 8 - 10 $mg.ml^{-1}$ for TTR55 and wtTTR, respectively. Protein concentration was determined by absorbance at 280 nm in a Nanodrop ND-1000 Spectrophotometer (Thermo Fisher Scientific, USA), using MW of 55 kDa and a $\varepsilon$ of 77 600 $M^{-1}$ $cm^{-1}$. For co-crystallization trials, Aβ peptides were incubated overnight at 4ºC with TTR, in a fragment/compound to protein molar ratio average of 10:1. In addition, co-crystallization with *in-drop* protein/Aβ peptide mixing also tested. For soaking experiments, pre-grown protein crystals were transferred to fresh drops containing each Aβ peptide and allowed to incubate for at least three days before crystal cryo-protection. Crystallization was performed by hanging-drop vapor diffusion at 293 K, with 500 µl reservoir and drops with a total volume of 4 µl, after a 5 minute, 4ºC sample spin. For wtTTR, crystallization conditions were selected based on (Gales *et al.*, 2005) (0.2 M sodium acetate buffer pH 5.2/5.4/5.6, 2 M ammonium sulphate, 7% glycerol) and (Lima *et al.*, 2010) (100 mM Tris-HCl pH 7.5, 100 mM KCl , 20-28% PEG 400). Crystals were transferred to reservoir solutions with glycerol (up to 20%) for cryo-protection and flash frozen in liquid nitrogen. For TTR55, crystallization conditions were based on (Castro-Rodrigues *et al.*, 2011) (3% PEG 8000, 0.1 M Cacodylate pH 6.5, 2-3 mM Zn acetate). For cryo-protection, crystals were submitted to a two-step sequential cryo-protectant (5% PEG 8000, 0.1 M Cacodylate pH 6.5, 3 mM Zn acetate, 20% glycerol and 5% PEG 8000, 0.1 M Cacodylate pH 6.5, 3 mM Zn acetate, 35% glycerol) or directly to 10% PEG 8000, 0.1 M Cacodylate pH 6.5, 3 mM Zn acetate, 25% glycerol, before flash freezing in liquid nitrogen. For co-crystallization with compounds 35 and 73, TTR (9.9 mg.ml-1) was incubated with each compound (molar ratios 35/TTR = 20 and 73/TTR=50) at 4 °C ON, in HEPES buffer 10mM pH 7.5. Crystals suitable for X-ray diffraction were obtained by hanging-drop vapour-diffusion techniques at 20 °C. Crystals were grown within 1 week by mixing 2 µl of the protein:compound solutions with 2 µl of reservoir solution. The reservoir solutions used in the crystallization trials contained acetate buffer 0.2 M pH 4.8-5.4, ammonium sulfate 1.8-2.2 M and 7% glycerol. Crystals were transferred to reservoir solutions containing increasing concentrations of glycerol (10 to 25%) and flash frozen in liquid nitrogen.

#### 2.1.2.3 X-Ray diffraction data, processing and refinement

High-resolution X-Ray diffraction data was collected from cryo-cooled single crystals at 100 K in synchrotron beamlines PROXIMA-1 and PROXIMA-2 of the French National Synchrotron Source (SOLEIL, Paris, France) (Coati *et al.*, 2017), at the XALOC beamline of the ALBA synchrotron center (Barcelona, Spain)(Juanhuix *et al.*, 2014) and ID29 and ID30B of European Synchrotron Radiation Facility (ESRF, Grenoble, France)(Gabadinho *et al.*, 2010). Images were processed with the XDS program package (Kabsch, 2010) with a random 5% sample of the reflection data flagged for R-free (Brunger, 1992). Diffraction intensities were converted to structure factors in the CCP4 format (Bailey, 1994) and unit cell content estimated with Matthew's coefficient (Matthews, 1968). Phases were generated by molecular replacement with Phaser MR using manually prepared models from PDB entries 1Y1D and 3SSG for wtTTR and TTR55, respectively (Castro-Rodrigues *et al.*, 2011; Gales *et al.*, 2005). Final models were obtained after iterative cycles of refinement and manual model building with Refmac/PHENIX and Coot, respectively (Adams *et al.*, 2010; Emsley *et al.*, 2010; Murshudov *et al.*, 1997).

### 2.1.3 Results and discussion

As mentioned before, disclosing the TTR-Aβ interaction at the molecular level has been elusive. In fact, some uncertainty and conflicting results exist regarding which protein and peptide species interact. While TTR tetramer stabilization is essential (Alemi *et al.*, 2017), some found that TTR monomer binds tighter to Aβ monomer and that the TTR tetramer binds preferably to Aβ aggregates (Du *et al.*, 2010). Others conclude that monomeric TTR does not bind monomeric Aβ in solution and that Aβ aggregation inhibition is caused by binding of TTR tetramer to Aβ monomer and of TTR monomer and tetramer to Aβ oligomers (Li *et al.*, 2013). Moreover, such Aβ aggregation inhibition effect may derive from co-aggregation of TTR and Aβ to amorphous non-amyloid deposits (Garai *et al.*, 2018). From a crystallographic point of view, until now only indirect observations have been reported. More precisely, TTR crystal structures indicate that the interaction occurs through copper ions (Ciccone *et al.*, 2018).

In our TTR-Aβ crystallization trials, we tested wtTTR and TTR55 with many Aβ fragments, in co-crystallization or crystal soaking experiments. The TTR potential to bind Aβ has been inversely correlated with the amyloidogenic potential of the TTR variant (Costa *et al.*, 2008), including a report that TTR55 is actually incapable of binding Aβ (Schwarzman *et al.*, 2004). Nevertheless, that variant can be crystallized in a reservoir condition containing zinc (Castro-Rodrigues *et al.*, 2011). In a long-shot attempt to capitalize on the

known affinity of Aβ for divalent metal cations (Zirah *et al.*, 2006), pre-grown TTR55 crystals in zinc-free reservoir solution were used for soaking experiments. Furthermore, given the observations that small-molecules, such as iododiflunisal (IDIF), stabilize the TTR tetramer and potentiate interaction with Aβ (Ribeiro *et al.*, 2014), TTR crystallization in a ternary complex with IDIF-IAB1 and IDIF-IAB2 was also attempted. Despite TTR crystals could be routinely obtained in a variety of conditions (Figure 2.1), X-Ray diffraction data was only obtained from wtTT and TTR55 co-crystallized and/or soaked with $A\beta_{1-40}$, $A\beta_{1-16}$, $A\beta_{12-28}$, IDIF-IAB1 or IDIF-IAB2. Sadly, no electron density corresponding to Aβ residues was found.

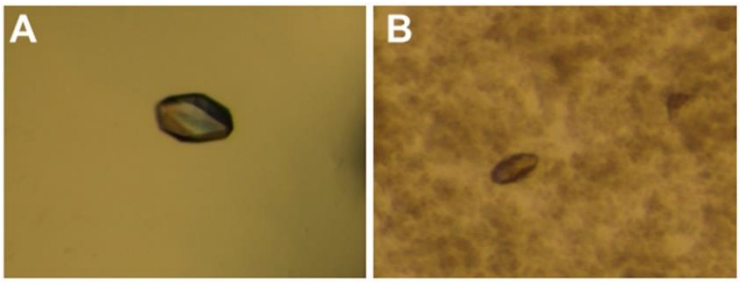


**Figure 2.1.** Examples of wild type transthyretin crystals co-crystallized with Aβ fragments. Fragments were incubated with the protein overnight at 4˚C, followed by vapor-diffusion crystallization: (A) $A\beta_{1-28}$, with TTR crystallized in 0.2 M sodium acetate buffer pH 5.4, 2 M ammonium sulfate, 7 % glycerol; (B) $A\beta_{29-40}$, with TTR crystallized in 100 mM tris pH 7.5, 100 mM KCl, 20 % PEG 400.

*The following portion of the work was extracted from Cotrina, E.Y.; Santos, L.M.; Rivas, J.; Blasi, D.;* ***Leite, J.P.****; Liz, M.A.; Busquets, M.A.; Planas, A.; Prohens, R.; Gimeno, A.; Jiménez-Barbero, J.J.; Gales, L.; Llop, J.; Quintana, J.; Cardoso, I.; Arsequell, G. (2021). Targeting transthyretin in Alzheimer's disease: drug discovery of small-molecule chaperones as disease-modifying drug candidates for Alzheimer's disease. European Journal of Medicinal Chemistry, 226, 113847. doi: https://doi.org/10.1016/j.ejmech.2021.113847*

Nevertheless, taking advantage of the established TTR crystallization pipeline, crystallization with compounds candidates as small-molecule chaperones (SMCs) was performed. Starting from a computational analysis of candidate molecules, the aim consists on repurposing currently approved drugs and direct them for AD treatment, circumventing the extremely expensive and time-consuming process of novel drug design, especially as the current pipeline for AD drugs in phase I is exhausted. In this case, by stabilizing the TTR tetramer, TTR/Aβ interaction could be potentiated. After a few rounds of selection, a set of compounds was chosen for a high-throughput screening ternary test (TTR/Aβ/compound), two of which, compound 35 (5-(4-nitrophenylazo)-3-iodosalicylic acid) and compound 73 (4-Benzothiazol-2-yl-2-methyl-phenylamine), were selected for the structure elucidation of the

TTR complexes by X-ray diffraction, because their TTR-ligand structures have not been previously analyzed. Both compounds bind in the so-called thyroxine binding sites (Figure 2.2; Table 2.1). Compound 35 (Figure 2.2, left panel) binds very deeply with the iodinated ring located at the outmost part of the $T_4$ channel. This binding induces the rotation of S117 side chains of the four monomers creating new strong intermonomer hydrogen bonds between these residues. The K15 residues, located at the entrance of the binding sites, establish interactions with the carboxylate substituents of the ligand. Compound 73 does not bind so deeply in the channel as 35 (Figure 2.2, right panel) and, consequently, it does not induce the formation of such strong interactions between the S117 residues of the TTR tetramer. The K15 residues, in the TTR: 73 complex, are not pointing to the center of the channel and are not involved in interactions with the compound. However, careful analysis should be considered, as good TTR tetramer stabilizers do not necessarily have good chaperone action.

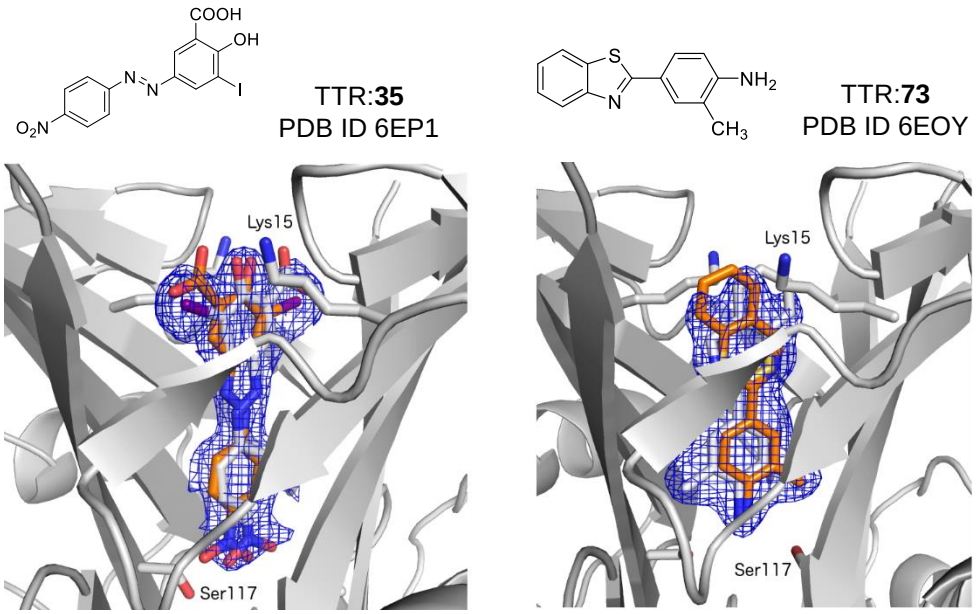


**Figure 2.2.** Close view of one binding site of the crystal structures of TTR:35 (left, PDB ID 6EP1) and TTR:73 (right, PDB ID 6EOY). The two-symmetry related positions of each compound are shown with carbon atoms in grey and orange. The $2F_o$-$F_c$ electron density maps at 1σ are drawn as a blue mesh around compounds 35 and 73 and residues K15 and S117 highlighted in stick representation.

**Table 2.1.** TTR-compound diffraction data collection, processing and refinement statistics.

| **Collection and processing** | | |
|---|---|---|
| Compound | 35 | 73 |
| Wavelength (Å) | 1.033 | 0.973 |
| Space Group | *P* $2_12_12$ | *P* $2_12_12$ |
| Unit-cell parameters (Å) | | |
| *a* | 42.96 | 42.97 |
| *b* | 84.87 | 85.64 |
| *c* | 64.75 | 64.24 |
| Resolution range (Å) | 84.866 - 1.299 (1.303 - 1.299) | 35.72 - 1.38 (1.43 - 1.38) |
| Observed reflections | 292370 (2710) | 196098 (18525) |
| Completeness (%) | 99.9 (61.5) | 98.4 (95.7) |
| Multiplicity | 5.0 (4.8) | 4.0 (4.0) |
| $<I/\sigma(I)>$ | 17.8 (1.5) | 11.2 (1.1) |
| $R_{merge}(\%)^{\#}$ | 3.8 (85.1) | 4.2 (125.7) |
| **Refinement** | | |
| $R_{cryst}(\%)$ | 16.3 | 18.6 |
| $R_{free}(\%)$ | 18.3 | 19.8 |
| RMSD for bonds (Å) | 0.006 | 0.006 |
| RMSD for angles (°) | 0.870 | 0.959 |
| Average main chain B-factor ($Å^2$) | 20.27 | 23.82 |
| Average side chain B-factor ($Å^2$) | 25.16 | 26.89 |
| Average compound B-factor ($Å^2$) | 34.33 | 42.94 |
| Average water B-factor ($Å^2$) | 38.30 | 39.34 |
| Ramachandran plot statistics (%) | | |
| Favoured regions | 99.10 | 96.36 |
| Allowed regions | 0.90 | 3.64 |

### 2.1.4. References

Adams, P. D., Afonine, P. V., Bunkoczi, G., Chen, V. B., Davis, I. W., Echols, N., Headd, J. J., Hung, L. W., Kapral, G. J., Grosse-Kunstleve, R. W., McCoy, A. J., Moriarty, N. W., Oeffner, R., Read, R. J., Richardson, D. C., Richardson, J. S., Terwilliger, T. C., & Zwart, P. H. (2010). PHENIX: a comprehensive Python-based system for macromolecular structure solution. *Acta Crystallogr D Biol Crystallogr, 66*(Pt 2), 213-221. doi:10.1107/S0907444909052925

Alemi, M., Silva, S. C., Santana, I., & Cardoso, I. (2017). Transthyretin stability is critical in assisting beta amyloid clearance– Relevance of transthyretin stabilization in Alzheimer's disease. *CNS Neuroscience & Therapeutics, 23*(7), 605-619. doi:10.1111/cns.12707

Andrade, C. (1952). A peculiar form of peripheral neuropathy; familiar atypical generalized amyloidosis with special involvement of the peripheral nerves. *Brain, 75*(3), 408-427. doi:10.1093/brain/75.3.408

Bailey, S. (1994). The CCP4 suit - programs for protein crystallography. *Acta Crystallographica Section D: Biological Crystallography, 58*, 760-763. doi:10.1107/S0907444994003112

Broersen, K., Jonckheere, W., Rozenski, J., Vandersteen, A., Pauwels, K., Pastore, A., Rousseau, F., & Schymkowitz, J. (2011). A standardized and biocompatible preparation of aggregate-free amyloid beta peptide for biophysical and biological studies of Alzheimer's disease. *Protein Engineering, Design and Selection, 24*(9), 743-750. doi:10.1093/protein/gzr020

Brunger, A. T. (1992). Free R value: a novel statistical quantity for assessing the accuracy of crystal structures. *Nature, 355*(6359), 472-475. doi:10.1038/355472a0

Bulawa, C. E., Connelly, S., DeVit, M., Wang, L., Weigel, C., Fleming, J. A., Packman, J., Powers, E. T., Wiseman, R. L., Foss, T. R., Wilson, I. A., Kelly, J. W., & Labaudinière, R. (2012). Tafamidis, a potent and selective transthyretin kinetic stabilizer that inhibits the amyloid cascade. *Proceedings of the National Academy of Sciences, 109*(24), 9629. doi:10.1073/pnas.1121005109

Buxbaum, J. N., Ye, Z., Reixach, N., Friske, L., Levy, C., Das, P., Golde, T., Masliah, E., Roberts, A. R., & Bartfai, T. (2008). Transthyretin protects Alzheimer's mice from the behavioral and biochemical effects of Abeta toxicity. *Proceedings of the National Academy of Sciences of the United States of America, 105*(7), 2681-2686. doi:10.1073/pnas.0712197105

Castro-Rodrigues, A. F., Gales, L., Saraiva, M. J., & Damas, A. M. (2011). Structural insights into a zinc-dependent pathway leading to Leu55Pro transthyretin amyloid fibrils. *Acta Crystallographica Section D, 67*(12), 1035-1044. doi:10.1107/S090744491104491X

Ciccone, L., Fruchart-Gaillard, C., Mourier, G., Savko, M., Nencetti, S., Orlandini, E., Servent, D., Stura, E. A., & Shepard, W. (2018). Copper mediated amyloid-β binding to Transthyretin. *Scientific Reports, 8*(1), 13744. doi:10.1038/s41598-018-31808-5

Coati, A., Chavas, L. M. G., Fontaine, P., Foos, N., Guimaraes, B., Gourhant, P., Legrand, P., Itie, J. P., Fertey, P., Shepard, W., Isabet, T., Sirigu, S., Solari, P. L., Thiaudiere, D., & Thompson, A. (2017). Status of the crystallography beamlines at synchrotron SOLEIL⋆. *The European Physical Journal Plus, 132*(4), 174. doi:10.1140/epjp/i2017-11403-3

Costa, R., Gonçalves, A., Saraiva, M. J., & Cardoso, I. (2008). Transthyretin binding to A-Beta peptide – Impact on A-Beta fibrillogenesis and toxicity. *FEBS Letters, 582*(6), 936-942. doi:10.1016/j.febslet.2008.02.034

Du, J., Cho, P. Y., Yang, D. T., & Murphy, R. M. (2012). Identification of beta-amyloid-binding sites on transthyretin. *Protein Eng Des Sel, 25*(7), 337-345. doi:10.1093/protein/gzs026

Du, J., & Murphy, R. M. (2010). Characterization of the interaction of β-amyloid with transthyretin monomers and tetramers. *Biochemistry, 49*(38), 8276-8289. doi:10.1021/bi101280t

Elovaara, I., Maury, C. P. J., & Palo, J. (1986). Serum amysoid A protein, albumin and prealbumin in Alzheimer's disease and in demented patients with Down's syndrome. *Acta Neurologica Scandinavica, 74*(3), 245-250. doi:10.1111/j.1600-0404.1986.tb07863.x

Emsley, P., Lohkamp, B., Scott, W. G., & Cowtan, K. (2010). Features and development of Coot. *Acta Crystallogr D Biol Crystallogr, 66*(Pt 4), 486-501. doi:10.1107/S0907444910007493

Episkopou, V., Maeda, S., Nishiguchi, S., Shimada, K., Gaitanaris, G. A., Gottesman, M. E., & Robertson, E. J. (1993). Disruption of the transthyretin gene results in mice with depressed levels of plasma retinol and thyroid hormone. *Proceedings of the National Academy of Sciences, 90*(6), 2375. doi:10.1073/pnas.90.6.2375

Furuya, H., Saraiva, M. J. M., Gawinowicz, M. A., Alves, I. L., Costa, P. P., Sasaki, H., Goto, I., & Sakaki, Y. (1991). Production of recombinant human transthyretin with biological activities toward the understanding of the molecular basis of familial amyloidotic polyneuropathy (FAP). *Biochemistry, 30*(9), 2415-2421. doi:10.1021/bi00223a017

Gabadinho, J., Beteva, A., Guijarro, M., Rey-Bakaikoa, V., Spruce, D., Bowler, M. W., Brockhauser, S., Flot, D., Gordon, E. J., Hall, D. R., Lavault, B., McCarthy, A. A., McCarthy, J., Mitchell, E., Monaco, S., Mueller-Dieckmann, C., Nurizzo, D., Ravelli, R. B. G., Thibault, X., Walsh, M. A., Leonard, G. A., & McSweeney, S. M. (2010). MxCuBE: a synchrotron beamline control environment customized for macromolecular crystallography experiments. *Journal of Synchrotron Radiation, 17*(5), 700-707. doi:10.1107/S0909049510020005

Gales, L., Macedo-Ribeiro, S., Arsequell, G., Valencia, G., Saraiva, Maria J., & Damas, Ana M. (2005). Human transthyretin in complex with iododiflunisal: structural features associated with a potent amyloid inhibitor. *Biochemical Journal, 388*(2), 615-621. doi:10.1042/BJ20042035

Garai, K., Posey, A. E., Li, X., Buxbaum, J. N., & Pappu, R. V. (2018). Inhibition of amyloid beta fibril formation by monomeric human transthyretin. *Protein Science, 27*(7), 1252-1261. doi:10.1002/pro.3396

Gimeno, A., Santos, L. M., Alemi, M., Rivas, J., Blasi, D., Cotrina, E. Y., Llop, J., Valencia, G., Cardoso, I., Quintana, J., Arsequell, G., & Jiménez-Barbero, J. (2017). Insights on the Interaction between Transthyretin and Aβ in Solution. A Saturation Transfer Difference (STD) NMR Analysis of the Role of Iododiflunisal. *Journal of Medicinal Chemistry, 60*(13), 5749-5758. doi:10.1021/acs.jmedchem.7b00428

Gloeckner, S. F., Meyne, F., Wagner, F., Heinemann, U., Krasnianski, A., Meissner, B., & Zerr, I. (2008). Quantitative Analysis of Transthyretin, Tau and Amyloid-β in Patients with Dementia. *Journal of Alzheimer's Disease, 14*, 17-25. doi:10.3233/JAD-2008-14102

Hamilton, J. A., & Benson, M. D. (2001). Transthyretin: a review from a structural perspective. *Cellular and Molecular Life Sciences CMLS, 58*(10), 1491-1521. doi:10.1007/PL00000791

Han, S.-H., Jung, E. S., Sohn, J.-H., Hong, H. J., Hong, H. S., Kim, J. W., Na, D. L., Kim, M., Kim, H., Ha, H. J., Kim, Y. H., Huh, N., Jung, M. W., & Mook-Jung, I. (2011). Human Serum Transthyretin Levels Correlate Inversely with Alzheimer's Disease. *Journal of Alzheimer's Disease, 25*, 77-84. doi:10.3233/JAD-2011-102145

Juanhuix, J., Gil-Ortiz, F., Cuni, G., Colldelram, C., Nicolas, J., Lidon, J., Boter, E., Ruget, C., Ferrer, S., & Benach, J. (2014). Developments in optics and performance at BL13-XALOC, the macromolecular crystallography beamline at the Alba Synchrotron. *Journal of Synchrotron Radiation, 21*(4), 679-689. doi:doi:10.1107/S160057751400825X

Kabsch, W. (2010). XDS. *Acta crystallographica. Section D, Biological crystallography, 66*(Pt 2), 125-132. doi:10.1107/S0907444909047337

Li, X., Zhang, X., Ladiwala, A. R. A., Du, D., Yadav, J. K., Tessier, P. M., Wright, P. E., Kelly, J. W., & Buxbaum, J. N. (2013). Mechanisms of transthyretin inhibition of β-amyloid aggregation in vitro *The Journal of Neuroscience, 33*(50), 19423. doi:10.1523/JNEUROSCI.2561-13.2013

Lima, L. M. T. R., Silva, V. d. A., Palmieri, L. d. C., Oliveira, M. C. B. R., Foguel, D., & Polikarpov, I. (2010). Identification of a novel ligand binding motif in the transthyretin channel. *Bioorganic & Medicinal Chemistry, 18*(1), 100-110. doi:10.1016/j.bmc.2009.11.025

Link, C. D. (1995). Expression of human beta-amyloid peptide in transgenic Caenorhabditis elegans. *Proceedings of the National Academy of Sciences, 92*(20), 9368. doi:10.1073/pnas.92.20.9368

Liz, M. A., Coelho, T., Bellotti, V., Fernandez-Arias, M. I., Mallaina, P., & Obici, L. (2020). A Narrative Review of the Role of Transthyretin in Health and Disease. *Neurology and Therapy, 9*(2), 395-402. doi:10.1007/s40120-020-00217-0

Matthews, B. W. (1968). Solvent content of protein crystals. *J Mol Biol, 33*(2), 491-497. doi:10.1016/0022-2836(68)90205-2

Murshudov, G. N., Vagin, A. A., & Dodson, E. J. (1997). Refinement of macromolecular structures by the maximum-likelihood method. *Acta Crystallogr D Biol Crystallogr, 53*(Pt 3), 240-255. doi:10.1107/S0907444996012255

Ribeiro, C. A., Oliveira, S. M., Guido, L. F., Magalhães, A., Valencia, G., Arsequell, G., Saraiva, M. J., & Cardoso, I. (2014). Transthyretin Stabilization by Iododiflunisal Promotes Amyloid-β Peptide Clearance, Decreases its Deposition, and Ameliorates Cognitive Deficits in an Alzheimer's Disease Mouse Model. *Journal of Alzheimer's Disease, 39*, 357-370. doi:10.3233/JAD-131355

Ricardo Vieira, J., Patrícia Moreira, A., Oliveira, Â., Alemi, M., & Cardoso, I. (2019). Collagen type IV in brain vessels of an AD mouse model: modulation by transthyretin? *Amyloid, 26*(sup1), 138-139. doi:10.1080/13506129.2019.1582489

Schreiber, G., Aldred, A. R., Jaworowski, A., Nilsson, C., Achen, M. G., & Segal, M. B. (1990). Thyroxine transport from blood to brain via transthyretin synthesis in choroid plexus. *American Journal of Physiology-Regulatory, Integrative and Comparative Physiology, 258*(2), R338-R345. doi:10.1152/ajpregu.1990.258.2.R338

Schultz, K., Nilsson, K., Nielsen, J. E., Lindquist, S. G., Hjermind, L. E., Andersen, B. B., Wallin, A., Nilsson, C., & Petersén, Å. (2010). Transthyretin as a potential CSF biomarker for Alzheimer's disease and dementia with Lewy bodies: effects of treatment with cholinesterase inhibitors. *European Journal of Neurology, 17*(3), 456-460. doi:10.1111/j.1468-1331.2009.02841.x

Schwarzman, A. L., & Goldgaber, D. (1996). Interaction of transthyretin with amyloid beta-protein: binding and inhibition of amyloid formation. *Ciba Found Symp, 199*, 146-160; discussion 160-144. doi:10.1002/9780470514924.ch10

Schwarzman, A. L., Gregori, L., Vitek, M. P., Lyubski, S., Strittmatter, W. J., Enghilde, J. J., Bhasin, R., Silverman, J., Weisgraber, K. H., & Coyle, P. K. (1994). Transthyretin sequesters amyloid beta protein and prevents amyloid formation. *Proceedings of the National Academy of Sciences, 91*(18), 8368. doi:10.1073/pnas.91.18.8368

Schwarzman, A. L., Tsiper, M., Gregori, L., Goldgaber, D., Frakowiak, J., Mazur-Kolecka, B., Taraskina, A., Pchelina, S., & Vitek, M. P. (2005). Selection of peptides binding to the amyloid b-protein reveals potential inhibitors of amyloid formation. *Amyloid, 12*(4), 199-209. doi:10.1080/13506120500350762

Schwarzman, A. L., Tsiper, M., Wente, H., Wang, A., Vitek, M. P., Vasiliev, V., & Goldgaber, D. (2004). Amyloidogenic and anti-amyloidogenic properties of recombinant transthyretin variants. *Amyloid, 11*(1), 1-10. doi:10.1080/13506120410001667458

Serot, J. M., Christmann, D., Dubost, T., & Couturier, M. (1997). Cerebrospinal fluid transthyretin: aging and late onset Alzheimer's disease. *Journal of Neurology, Neurosurgery & Psychiatry, 63*(4), 506. doi:10.1136/jnnp.63.4.506

Silva, C. S., Eira, J., Ribeiro, C. A., Oliveira, Â., Sousa, M. M., Cardoso, I., & Liz, M. A. (2017). Transthyretin neuroprotection in Alzheimer's disease is dependent on proteolysis. *Neurobiology of Aging, 59*, 10-14. doi:10.1016/j.neurobiolaging.2017.07.002

Stein, T. D., Anders, N. J., DeCarli, C., Chan, S. L., Mattson, M. P., & Johnson, J. A. (2004). Neutralization of transthyretin reverses the neuroprotective effects of secreted amyloid precursor protein (APP) in APPSW mice resulting in tau phosphorylation and loss of hippocampal neurons: support for the amyloid hypothesis. *The Journal of Neuroscience, 24*(35), 7707. doi:10.1523/JNEUROSCI.2211-04.2004

Stein, T. D., & Johnson, J. A. (2002). Lack of Neurodegeneration in Transgenic Mice Overexpressing Mutant Amyloid Precursor Protein Is Associated with Increased Levels of Transthyretin and the Activation of Cell Survival Pathways. *The Journal of Neuroscience, 22*(17), 7380. doi:10.1523/JNEUROSCI.22-17-07380.2002

Westermark, P., Sletten, K., Johansson, B., & Cornwell, G. G., 3rd. (1990). Fibril in senile systemic amyloidosis is derived from normal transthyretin. *Proceedings of the National Academy of Sciences of the United States of America, 87*(7), 2843-2845. doi:10.1073/pnas.87.7.2843

Zirah, S., Kozin, S. A., Mazur, A. K., Blond, A., Cheminant, M., Ségalas-Milazzo, I., Debey, P., & Rebuffat, S. (2006). Structural Changes of Region 1-16 of the Alzheimer Disease Amyloid β-Peptide upon Zinc Binding and in Vitro Aging *<sup></sup>. *Journal of Biological Chemistry, 281*(4), 2151-2161. doi:10.1074/jbc.M504454200

# 2.2 Paper I: Alzheimer's $A\beta_{1-40}$ peptide degradation by thermolysin: evidence of inhibition by a C-terminal Aβ product

Work contributions:

Mass spectrometry measurements and analysis was performed by Hugo Osório (i3S Proteomics Scientific Platform, Porto, Portugal).

FEBS Letters

FEBS PRESS science publishing by scientists

# Alzheimer's $A\beta_{1-40}$ peptide degradation by thermolysin: evidence of inhibition by a C-terminal Aβ product

José P. Leite[1,2,3] and Luís Gales[1,2,3]

1 i3S – Instituto de Investigação e Inovação em Saúde, Porto, Portugal
2 IBMC – Instituto de Biologia Molecular e Celular Universidade do Porto, Portugal
3 ICBAS – Instituto de Ciências Biomédicas Abel Salazar, Porto, Portugal

**Correspondence**
L. Gales, i3S – Instituto de Investigação e Inovação em Saúde, Rua Alfredo Allen, 208 Porto, Portugal
Fax: +351 220 428 091
Tel: +351 220 408 800
E-mail: lgales@ibmc.up.pt

(Received 1 June 2018, revised 18 September 2018, accepted 30 October 2018)

doi:10.1002/1873-3468.13285

Edited by Christian Griesinger

**The interaction of the amyloid-β peptide (Aβ) with thermolysin (TLN) was investigated by X-ray crystallography. Structural models of the complexes of TLN with several Aβ fragments show that, despite the numerous possible cleavage sites of the Aβ sequence, the C-terminal product of Ala30-Ile31 cleavage does not dissociate, thus inhibiting the enzyme. The high similarity between the TLN structural motif and neprilysin (NEP), the most extensively studied peptidase associated with Aβ clearance, suggests that NEP should be more efficient against Aβ polymorphs where Ala30-Ile31 is inaccessible, which is in agreement with studies in living mice that point to the limited role of NEP in degrading soluble Aβ and its higher ability to degrade insoluble and/or oligomeric Aβ forms, producing only the $A\beta_{10-37}$ intermediate.**

**Keywords:** β-turn-β conformation; amyloid-β peptide cleavage; amyloid-β peptide/thermolysin; thermolysin inhibition; X-ray crystallography

The "amyloid hypothesis" has been the cornerstone of Alzheimer's disease (AD) research for the past decades, placing the amyloid-β peptide (Aβ) at the heart of the pathology [1]. Aβ peptides are usually 36–43 residues in length, constituting the main component of amyloid aggregates found in the brains of Alzheimer's patients, with $A\beta_{1-40}$ and $A\beta_{1-42}$ (subscript numbers indicate residue number) being the two most common and studied forms. The peptides derive from the amyloid precursor protein (APP), which is present in neurons, oligodendrocytes, and neuronal synapses, and has attributed functions such as regulation of synaptic transmission and metal transport [2]. Aβ is generated when APP is cleaved in an amyloidogenic way, by a two-step β-secretase/γ-secretase cleavage [2].

Advances aim at modulating the elimination of Aβ, either in a monomeric, oligomeric, or fibrillary form, are underway. However, such action may be counterproductive, because several physiological roles are being linked to Aβ, such as blood clotting, neuronal cell survival, and even gene expression regulation [3–5]. The pathology might be, therefore, a result of an imbalance between the formation and the clearance of Aβ species by the so-called amyloid-degrading enzymes (ADE). In this regard, understanding Aβ-ADE interactions constitutes a promising therapeutic path. ADEs like plasmin and cathepsin B are serine and cysteine proteases, respectively, with intriguing roles in AD. Cathepsin B was reported to aggravate AD pathology as a type of β-secretase but, on the other hand, seems to assume a protective role by degrading $A\beta_{1-42}$ [6,7].

**Abbreviations**
ACE, angiotensin-converting enzyme; AD, Alzheimer's disease; ADE, amyloid-degrading enzymes; APP, amyloid precursor protein; Aβ, amyloid-β peptide; hPreP, human presequence protease; IDE, insulin-degrading enzyme; MMP-9, matrix metalloprotease 9; NEP, neprilysin; TLN, thermolysin (aTLN, active; iTLN, inactive).

In the case of plasmin, it was found to cleave monomeric and fibrillary Aβ, but no significant differences are detected in plasmin protein or plasmin activity in human postmortem AD brain tissues compared to control [8,9].

Nevertheless, most of the identified ADEs belong to the zinc-dependent metalloprotease superfamily, namely the M2 class (e.g., EC 3.4.15.1 angiotensin-converting enzyme, ACE), M13 class (e.g. EC 3.4.24.11 neprilysin, NEP), and the M16 class (e.g. EC 3.4.24.64 human presequence protease, hPreP; EC 3.4.24.56 insulin-degrading enzyme, IDE). X-ray crystallographic data for IDE, hPreP, and ACE in complex with Aβ fragments is available, allowing the identification of cleavage sites [10–12]. On the other hand, no data is available for NEP, which is the most extensively studied peptidase associated with Aβ clearance. Several neuroprotective effects have been reported for NEP. For example, coexpression of human $A\beta_{1-42}$ with NEP in *Drosophila* resulted in decreased amyloid plaque formation [13]; in mice brains, NEP expression reduced $A\beta_{1-40}/A\beta_{1-42}$ levels, as well as overall amyloid pathology [14,15]; overexpression of NEP in peripheral tissues has also had an impact in decreasing brain Aβ levels, given the fact that these are in equilibrium across the brain–blood barrier [16].

Interestingly, NEP shares active site structural identity with a widely studied zinc-dependent metalloprotease, TLN, with both proteins sharing substrates and inhibitors, such as phosphomaridon [17]. TLN is often used as a suitable structural surrogate model for NEP, because it yields diffraction-quality crystals and is readily accessible in large quantities. TLN (EC 3.4.24.27) is a 316 amino acid, M4 family, zinc-dependent thermostable metalloproteinase, originally from *Bacillus thermoproteolyticus* Rokko, with a β-rich N-terminus side and an α-helix rich C-terminus side, containing as cofactors four calcium ions which enhance thermostructural stability [18]. It catalyzes the hydrolysis of peptide bonds on the N-terminus side of hydrophobic amino acids isoleucine, leucine, phenylalanine, or valine, including monomeric and fibrillary forms of Aβ, as assessed *in vitro* [19]. Substitution of the zinc ion by cadmium induces structural shifts in TLN that greatly reduce enzymatic activity, while not disturbing the overall protein architecture [20].

Application of X-ray crystallography to Aβ samples has proved elusive, due to their hydrophobic and rapidly aggregating natures, which hamper the formation of crystals. Nonetheless, crystallization of short isolated peptide fragments led to identification of several fibril forming core segments, suggesting high structural polymorphism for Aβ [21]. Protein fusion techniques have also been adopted: the structure of fragment $A\beta_{28-42}$ fused to the C-terminal of *Tk*-RNase HII suggests a β-rich, U-shaped conformation, with the bend at Val36 [22]; fragment $A\beta_{18-41}$ fused to an immunoglobulin from sharks indicates a tetrameric conformation of the construct [23]; a ternary complex of $A\beta_{1-16}$ fused to the N terminus of Im7 (small immunity protein) and stabilized by WO2 (anti-Aβ monoclonal antibody) indicates that the structure of the Tyr10-Lys16 segment of Aβ has a PPII-helix conformation, closely related to β-strands, to which it can shift given the proper environmental conditions and possibly facilitating the aggregation process [24]. In addition, aiming to establish the molecular basis for immunotherapy, X-ray crystallographic models of Aβ with different antibodies, currently in various stages of clinical trials [25], have disclosed binding sites at the N-terminus (i.e. $A\beta_{1-11}$) [26–31], midregion (i.e. $A\beta_{16-26}$ and $A\beta_{11-25}$) [32,33], and C-terminus (i.e. $A\beta_{30-40}$) regions of the Aβ peptide [34].

Here, we use TLN in order to infer the physiologically relevant clearance mechanism of $A\beta_{1-40}$ by NEP in AD. Crystal soaking trials of peptide fragments $A\beta_{1-16}$, $A\beta_{20-29}$, $A\beta_{29-40}$, $A\beta_{31-35}$, and the full-length $A\beta_{1-40}$ with the active (aTLN, zinc-bound) and the inactive (iTLN, cadmium-substituted) forms of TLN were performed.

## Materials and methods

### Reagents

TLN from *Geobacillus stearothermophilus* was purchased from Sigma-Aldrich (St. Louis, MO, USA) and used without further purification. Amyloid-β peptide $A\beta_{1-40}$ and fragments $A\beta_{1-16}$, $A\beta_{20-29}$, $A\beta_{29-40}$, and $A\beta_{31-35}$ were purchased from Bachem (Switzerland). All other reagents were of analytical grade.

### Mass spectrometry

Peptide cleavage characterization was performed by nanoLC–MS/MS, with a Ultimate 3000 liquid chromatography system coupled to a Q-Exactive Hybrid Quadrupole-Orbitrap mass spectrometer (Thermo Scientific, Bremen, Germany). Samples were loaded onto a trapping cartridge in a mobile phase of 2% ACN, 0.1% FA at 10 $\mu L \cdot min^{-1}$. After 3 min loading, the trap column was switched in-line to a reverse phase column at 300 $nL \cdot min^{-1}$. Separation was performed with a gradient of 0.1% FA (A) 80% ACN, 0.1% FA (B). The mass spectrometer was operated in a Full MS positive acquisition mode. The ESI spray voltage was 1.9 kV. The global settings were use lock masses best ($m/z$ 445.12003), lock mass injection Full MS, chrom. peak width (FWHM) 30s. The full scan settings were 70k

resolution ($m/z$ 200), AGC target 3e6, maximum injection time 200 ms, scan range: 400–4000 $m/z$.

## TLN metal substitution

Metal substitution was performed based on [20]. Briefly, TLN was incubated with cadmium chloride for 11 days at room temperature and excess metal was removed through dialysis. Cd-substituted TLN putative activity was assessed by mass spectrometry after incubation with $A\beta_{1-40}$ in the crystallization buffer and approximately for 5 days, to replicate the crystal soaking trials. The full $A\beta_{1-40}$ peptide was not only identified but also traces of cleavage at Glu11-Val12 and Ala30-Ile31 were observed, meaning that the enzyme was not fully inactive.

## Crystallization conditions

Lyophilized peptide was suspended in 1,1,1,3,3,3-hexafluoro-2-propanol and incubated overnight at room temperature. In the following day, solvent was removed with a nitrogen stream and further dried in a speed-vac. The resulting

**Table 1.** Thermolysin/Aβ fragments data collection and refinement statistics.

| | Thermolysin: $A\beta_{1-40}$ (zinc) | Thermolysin: $A\beta_{1-40}$ (cadmium) | Thermolysin: $A\beta_{29-40}$ (cadmium) | Thermolysin: $A\beta_{31-35}$ (cadmium) | Thermolysin: $A\beta_{1-16}$ (cadmium) | Thermolysin: $A\beta_{20-29}$ (cadmium) |
|---|---|---|---|---|---|---|
| PDB ID | 5ONR | 5ONP | 5ONQ | 6GHX | N/A | N/A |
| Visible Aβ residues | Ile31-Gly33 | Gly29-Gly33 | Gly29-Gly33 | Ile31-Ile32 | None | None |
| Wavelength (Å) | 0.97265 | 0.97265 | 0.97265 | 1.07227 | 0.97264 | 0.97264 |
| Space group | *P $6_122$* | *P $6_122$* | *P $6_122$* | *P $6_122$* | *P $6_122$* | *P $6_122$* |
| Unit-cell parameters (Å) | | | | | | |
| *a* | 92.70 | 93.41 | 93.49 | 93.06 | 93.55 | 92.83 |
| *b* | 92.70 | 93.41 | 93.49 | 93.06 | 93.55 | 92.83 |
| *c* | 129.37 | 130.15 | 129.56 | 130.29 | 130.08 | 129.62 |
| Resolution range (Å) | 46.35–1.388 (1.438–1.388) | 38.23–1.340 (1.388–1.340) | 43.97–1.170 (1.212–1.170) | 46.53–1.156 (1.198–1.156) | 44.02–1.428 (1.479–1.428) | 43.7–1.059 (1.097–1.059) |
| Observed reflections | 65 845 | 73 752 | 111 609 | 115 213 | 61 700 | 146 488 |
| No. of unique reflections | 6372 | 7144 | 10 829 | 10 704 | 5887 | 12 864 |
| Completeness (%) | 98.78 (97.24) | 97.66 (96.36) | 99.36 (97.65) | 99.25 (93.75) | 98.31 (95.52) | 98.50 (87.92) |
| Multiplicity | 9.69 (8.22) | 9.40 (9.30) | 8.85 (7.88) | 17.3 (16.4) | 7.96 (7.6) | 5.4 (2.1) |
| $\langle I/\sigma(I)\rangle$ | 12.7 (1.7) | 12.5 (2.0) | 14.6 (2.1) | 17.2 (0.8) | 13.53 (1.6) | 9.8 (0.7) |
| $R_{merge}$(%)# | 8.4 (114.5) | 8.6 (98.8) | 7.3 (81.0) | 6.8 (269.9) | 8.8 (139.0) | 5.9 (102.9) |
| Refinement | | | | | | |
| $R_{cryst}$(%) | 0.1789 (0.2888) | 0.1610 (0.2361) | 0.1625 (0.2358) | 0.2016 (0.3510) | 0.1622 (0.3279) | 0.1767 (0.3524) |
| $R_{free}$(%) | 0.2004 (0.3117) | 0.1799 (0.2587) | 0.1716 (0.2415) | 0.2198 (0.3654) | 0.1835 (0.3551) | 0.1913 (0.3490) |
| RMSD for bonds (Å) | 0.005 | 0.005 | 0.005 | 0.007 | 0.015 | 0.012 |
| RMSD for angles (°) | 0.76 | 0.84 | 0.82 | 0.87 | 1.35 | 1.21 |
| Average main chain B-factor (Å$^2$) | 17.38 | 15.84 | 12.91 | 21.82 | 17.54 | 15.77 |
| Average Aβ fragment B-factor (Å$^2$) | 24.90 | 32.34 | 26.10 | 26.1 | – | – |
| Average ligand B-factor (Å$^2$) | 30.32 | 29.45 | 26.12 | 28.60 | 18.76 | 14.73 |
| Average water B-factor (Å$^2$) | 32.04 | 31.45 | 25.29 | 36.96 | 29.86 | 29.20 |
| Ramachandran plot statistics (%) | | | | | | |
| Favored regions | 96.51 | 96.53 | 96.53 | 96.82 | 96.50 | 96.18 |
| Allowed regions | 3.49 | 3.47 | 3.15 | 3.18 | 3.50 | 3.82 |

#Rmerge = $\Sigma_{hkl}\ \Sigma_i\ |Ii(hkl) - (I(hkl))|/\Sigma_{hkl}\ \Sigma_i\ Ii(hkl)$, where Ii(hkl) is the $i^{th}$ observation of reflection hkl and $\langle I(hkl)\rangle$ is the weighted average intensity for all observations of reflection hkl.

peptide film was stored at −20 °C; immediately before TLN crystal soaking trials, it was suspended in dimethyl sulfoxide (DMSO). TLN samples were prepared as previously described [18]. In short, lyophilized protein was dissolved in 45% DMSO, 50 mM 2-(*N*-morpholino) ethanesulfonic acid hydrate (MES) buffer pH 6.0, kindly agitated for 1 h at room temperature, followed by centrifugation, and the pellet discarded. Protein crystals were grown by a hanging-drop vapor diffusion technique at 20 °C. Equal volumes of TLN at 100 mg·mL$^{-1}$ and mixing solution (50 mM MES pH 6.0; 45% DMSO; 0.7–0.9 M NaCl; 0 or 0.4 M $CdCl_2$) were equilibrated against reservoir solution containing 30–40% ammonium sulfate. Full-grown crystals were soaked for 5 days in freshly prepared drops containing 50 mM MES pH 6.0, 45%

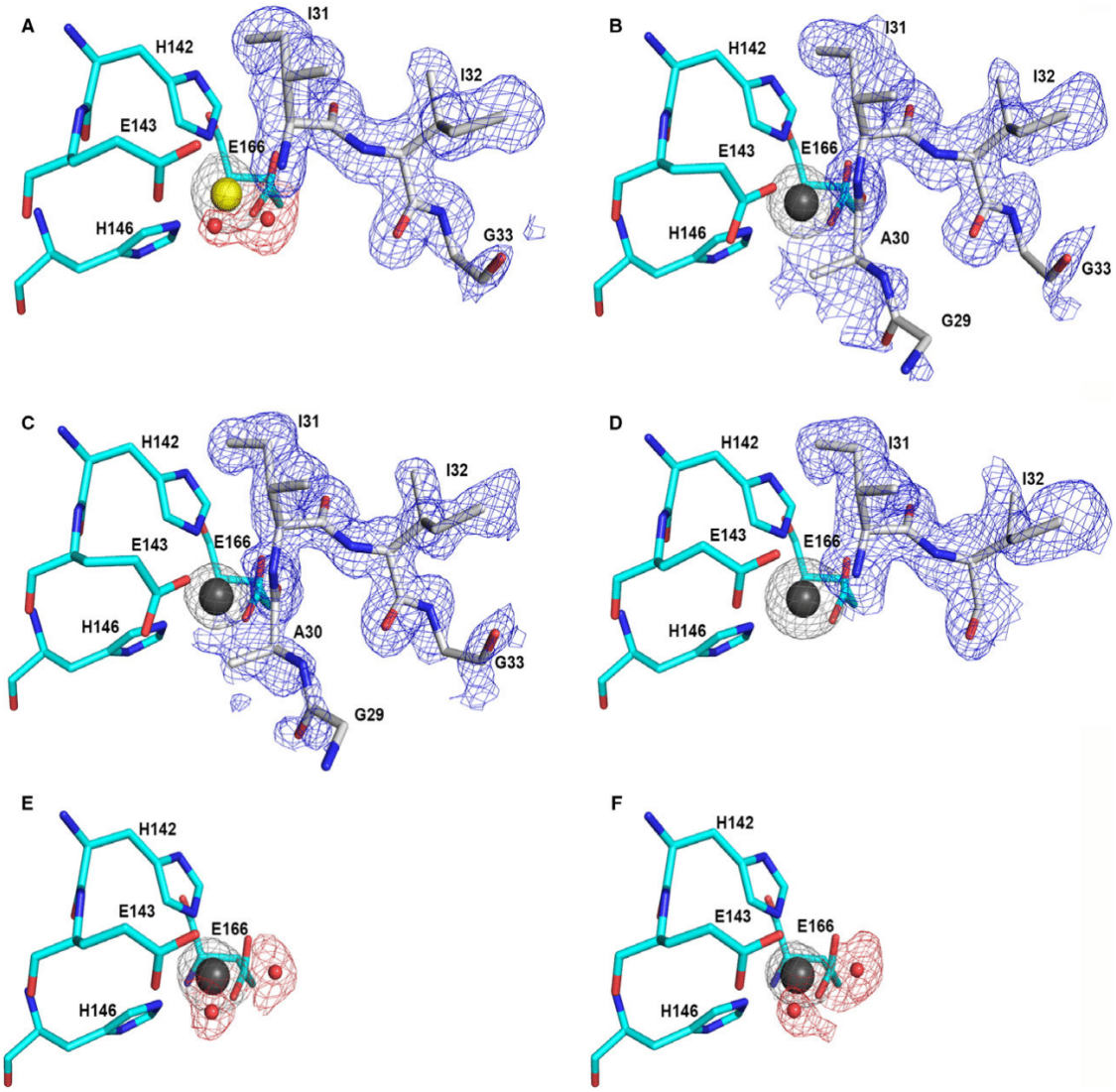


**Fig. 1.** X-ray diffraction co-crystal structures of TLN (aTLN, active form; iTLN, inactive form) with Aβ peptides: aTLN:$Aβ_{1–40}$ (A), iTLN:$Aβ_{1–40}$ (B), iTLN:$Aβ_{29–40}$ (C), iTLN:$Aβ_{31–35}$ (D), iTLN:$Aβ_{1–16}$ (E), and iTLN:$Aβ_{20–29}$ (F). Cadmium, zinc, and water molecules represented as gray, yellow, and red spheres, respectively. Fo-Fc omit maps as follows: metals at 3 σ; peptide fragments at 2 σ; water at 3 σ. The position of the Aβ sequence Gly-Ala-Ile-Ile-Gly was clearly observed in the electron density maps of (B) and (C) in a close turn conformation; cross-analysis of structures A–C shows that TLN cleaves Aβ at the Ala30-Ile31 bond. Aβ Ile31 and Ile32 are the key residues for binding to TLN (D). $Aβ_{20–29}$ and $Aβ_{1–16}$ could not be found in the crystal structures (E, F).

DMSO, and supplemented with an Aβ peptide fragment. Crystals were subjected to a glycerol gradient up to 20% prior to being flash frozen in liquid nitrogen.

### Data collection and processing

Data sets of TLN: peptide complexes were collected at ID30B and ID29 beamlines of the European Synchrotron Radiation Facility (Grenoble, France). Data collection and refinement statistics are presented in Table 1. Diffraction images were processed with the XDS PROGRAM Package [35] and the diffraction intensities converted to structure factors in the CCP4 format [36]. A random 5% sample of the reflection data was flagged for R-free calculations during model building and refinement [37]. The crystals belonged to the hexagonal group P $6_1$ 2 2. Matthew's coefficient calculations suggested the presence of one molecule in the asymmetric unit (MW of 34 600 Da) [38]. Molecular replacement phases were generated with Phaser MR, using as initial model substrate-free TLN (PDB entry 1KEI [39]). The final models were obtained after further cycles of refinement and manual model building, carried out with PHENIX and Coot, respectively [40,41]. Protein structure figures were generated with PyMol [42].

## Results and Discussion

A total of six TLN crystal structures soaked with various Aβ fragments were determined: aTLN:$A\beta_{1–40}$, iTLN:$A\beta_{1–40}$, iTLN:$A\beta_{29–40}$, iTLN:$A\beta_{31–35}$, iTLN:$A\beta_{1–16}$, and iTLN:$A\beta_{20–29}$ (Fig. 1). No significant differences, either induced by the binding of the Aβ peptides or by metal substitution, were observed between the TLN models, with RMSD of the structures superimposed to aTLN:$A\beta_{1–40}$ being 0.1313 Å (iTLN:$A\beta_{1–40}$), 0.1586 Å (iTLN:$A\beta_{29–40}$), 0.1227 Å (iTLN:$A\beta_{31–35}$), 0.1468 Å (iTLN:$A\beta_{1–16}$), and 0.1003 Å (iTLN:$A\beta_{20–29}$). Despite the several possible Aβ cleavage sites, aTLN crystal structure provided the interactions with the C-terminal product of Ala30-Ile31 cleavage while the iTLN models, despite the residual activity maintained by the enzyme (checked by mass spectrometry), provided the interactions with the substrate aligned for the same reaction. Only the few residues of Aβ peptides which are bound to TLN are observed.

For the iTLN models, the electron density peaks suggest that the $Zn^{2+}$ to $Cd^{2+}$ metal substitution protocol also induces a partial substitution of $Ca^{2+}$ by $Cd^{2+}$, with the nature of these cofactors assigned according to their most plausible temperature factor. $Ca^{2+}$ by $Cd^{2+}$ partial substitution has already been reported [20]. A close view of the active sites of TLN for the six crystal structures is shown in Fig. 1. In the catalytically active form of TLN (Fig. 1A), the zinc ion is coordinated by two histidines (His142 and His146) and by one glutamate (Glu 166) in a bidentate fashion. The positions for two water molecules

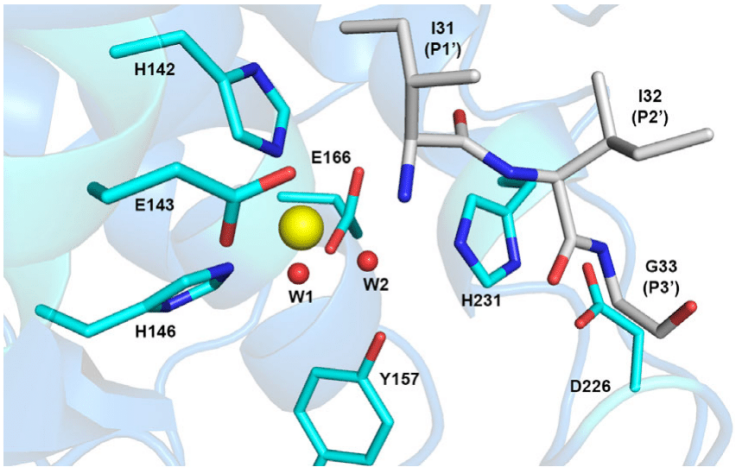


**Fig. 2.** Close-up view of the active site of aTLN in complex with $A\beta_{1–40}$, evidencing their structure and interaction. TLN catalytically relevant residues His142, Glu143, His146, Glu166, along with Tyr157, Asp226, and His231 in cyan (side chains in stick representation). Zinc (yellow sphere) is pentacoordinated by His142, Glu143, His146, Glu166, and a water molecule (red spheres; W1, W2 represent alternative positions for the water molecule, with W2 being the most favorable according to *B*-value). $A\beta_{31–33}$ (gray sticks) results from the hydrolytic action of TLN over $A\beta_{1–40}$. Remaining TLN residues in faded cartoon representation, with some portions in the foreground omitted for clarity. This active site architecture closely resembles the one from neprilysin.

(hereafter referred as W1 and W2) at a distance of 2.5 and 2.1 Å, respectively, from the zinc ion are observed. W1 establishes a strong hydrogen bond with Glu143, while W2 interacts with His231. Previous structural studies suggest that W1 and W2 are two alternative positions of a water molecule at the active site, as usually W1 and W2 display above average B factors [20]. In our model, B factors of W1 and W2 are 40.7 and 13.4 $Å^2$, respectively, which indicates that the water molecule occupies preferentially position W2. In the vicinity of the active site, an electron density corresponding to a short fragment of the Aβ peptide was observed. The good quality of the map enabled the unambiguous assignment of that electron density to the Aβ residues sequence Ile-Ile-Gly, which correspond to fragment $Aβ_{31–33}$ of the full peptide (Fig. 1A). Regarding the inactive form of TLN, the crystal structure of the iTLN:$Aβ_{1–40}$ complex shows a displacement in Glu143 to interact with the cadmium ion when compared to the aTLN model, presumably deviating it from optimum alignment for catalysis (Fig. 1B). As previously described, this structural shift results in the reduction of TLN catalytic activity [20]. Moreover, the interaction of TLN residues His142, His146, and Glu166 with cadmium mimics the one observed with zinc. The sixfold coordination for $Cd^{2+}$ in the structure of the complex is completed by the interaction of the carbonyl of Ala30 of the Aβ fragment bound to the enzyme, replacing the interaction with the water molecule (Fig. 1B–D). With this inactive form of the enzyme in complex with $Aβ_{1–40}$, the position of five residues of the Aβ peptide, Gly-Ala-Ile-Ile-Gly, corresponding to fragment $Aβ_{29–33}$, could be clearly assigned to electron density (Fig. 1B). Additional crystal structures of iTLN with shorter Aβ peptides were obtained. The model of the iTLN:$Aβ_{29–40}$ complex (Fig. 1C) was very similar to the iTLN:$Aβ_{1–40}$, namely in the structure of the Aβ fragment bound to the enzyme. In the case of iTLN:$Aβ_{31–35}$ (Fig. 1D), Ile-Ile residues were unambiguously observed (fragment $Aβ_{31–32}$). Finally, for iTLN:$Aβ_{1–16}$ (Fig. 1E) and iTLN:$Aβ_{20–29}$ (Fig. 1F), the electron density maps did not reveal the presence of fragments of $Aβ_{1–16}$ and $Aβ_{20–29}$.

The crystal models suggest that the carbonyl oxygen from Aβ's Ala30 (P1 residue, Fig. 2), displaces the zinc bound water molecule toward Glu143, which is the key active site residue, as shown by enzymatic inactivation upon single amino acid substitution [43]. The zinc ion potentiates deprotonation of the water nucleophile (in our case, likely W2) and polarizes the carbonyl of Ala30. The combined influence of Glu143 and the zinc ion on the water molecule increase its nucleophilicity, triggering the attack on the carbonyl of Ala30. Asp226 has a stabilizing role in intermediate steps by bonding a protonated His231. Therefore, the motif $H_{142}E_{143}XXH_{146}$ plus $E_{166}$ make up the critical core for catalysis in TLN (in other zinc

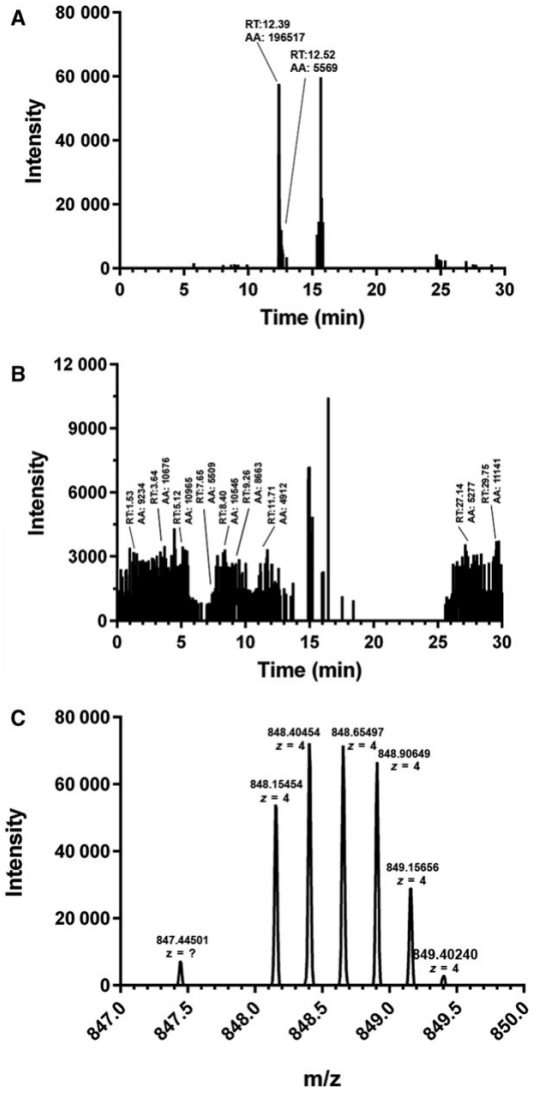


**Fig. 3.** Extracted-ion chromatograms (XIC) of the ions at *m/z* 848.15381 (A) and *m/z* 479.29371 (B) with a 5 p.p.m. mass tolerance. These ions are associated with the N-terminal peptide DAEFRHDSGYEVHHQKLVFFAEDVGSNKGA ($z = 4$) and C-terminal peptide IIGLMVGGVV ($z = 2$), respectively. Panel C shows the acquired mass spectra at 12.40 min retention time for the N-terminal peptide. No meaningful mass spectrometry data was obtained for the C-terminal peptide.

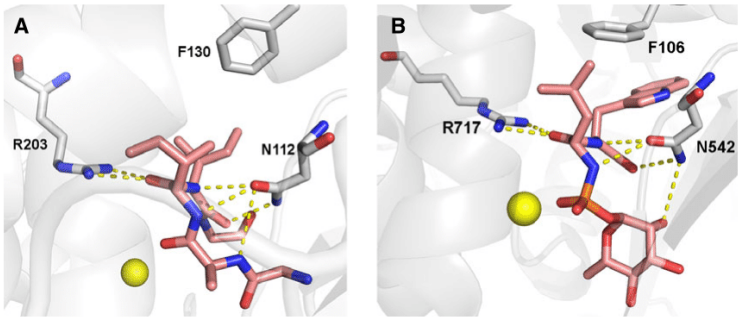


**Fig. 4.** Key structural features for substrate recognition shared by iTLN complexed with $A\beta_{1-40}$ (A) and neprilysin complexed with the inhibitor phosphoramidon (PDB ID 1DMT [57]).

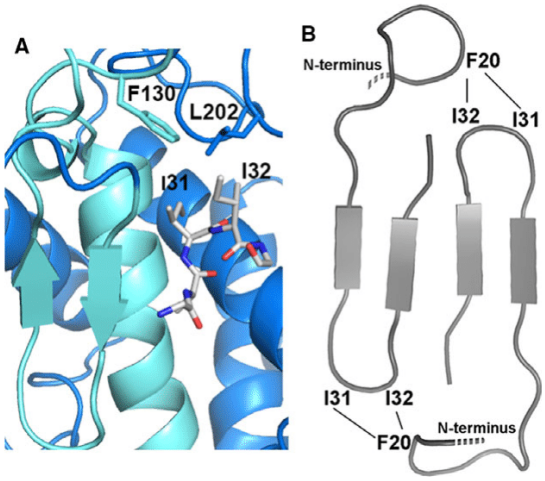


**Fig. 5.** (A) Interaction of the fragment $A\beta_{29-33}$ (gray) with TLN. $TLN_{112-152}$ ββα motif highlighted in light blue. (B) Hypothetical model for $A\beta_{1-40}$ oligomerization, based on the interaction observed in (A).

metalloproteases, the second glutamate may be replaced by an aspartic acid or histidine) [44].

TLN recognizes hydrophobic residues Val, Leu, Ile, and Phe in its S1′ specificity pocket [19]. Surprisingly, the X-ray diffraction analysis presented here shows that the C-terminal product of Ala30-Ile31 proteolysis displays a prolonged residence binding time, inhibiting TLN. In addition, crystal structures of inactive TLN also show Aβ peptides "locked" in place for putative Ala30-Ile31 cleavage. To corroborate our findings, freshly prepared $A\beta_{1-40}$ was incubated with TLN for 7 days prior to analysis with MALDI-TOF MS. Among the fragments generated is the $A\beta_{1-30}$, but not $A\beta_{30-40}$, suggesting that the latter is hardly released from TLN (Fig. 3).

This cleavage site for Aβ has been reported for three AD relevant metalloproteases, namely NEP (identified as one of the preferable cleavage sites), matrix metalloprotease 9 (EC 3.4.24.35, MMP-9) (secondary cleavage site), and mitochondrial peptidase hPreP (secondary cleavage site) [45–49]. NEP, which colocalizes in the brain and peripheral tissues with Aβ, shares a similar active site architecture with TLN. A small ultrastructure difference between the two metallopeptidases results in the ability of TLN to accommodate larger substrates. NEP N-terminal sterically restricts access to the active site of the protein, possibly explaining why TLN can cleave fibrillary Aβ, while NEP degrades mostly monomeric and oligomeric Aβ [19,45,46,50].

The key common features of substrate recognition shared by TLN and NEP can be observed in Fig. 4, in which iTLN:$A\beta_{1-40}$ is shown side to side with NEP complexed with the generic metalloproteinase inhibitor phosphoramidon (PDB ID 1DMT [51]). Both structures show hydrophobic P1′ and P2′ residues of the substrate in a β turn conformation, with both side chains interacting with a Phe residue of each enzyme. Moreover, the backbone of the β turn is stabilized by a hydrogen bond of the C=O of P1′ residue with an Arg and the N-H of P2′ residue with Asn. Therefore, it is tempting to suggest that NEP shares the same Aβ peptide recognition mechanism with TLN and, even more important, that the Ile-Ile repetition, present in Aβ, shares the structural features of endopeptidases inhibitors. Previous studies had correlated the rate-limiting step of dissociation of TLN inhibitors with the strength of interaction with Asn112 [52], which in fact is tightly bound to the peptide in our model (Fig. 4, left).

Furthermore, the structural models iTLN:$A\beta_{1-40}$ and iTLN:$A\beta_{29-40}$ (Fig. 1B,C) evidence that the Aβ fragment is in close contact with the TLN 40 amino acid segment Asn112-Thr152, that encompasses a β-turn-β-α motif, with the β-turn-β followed by a long loop that brings the α-helix over the two β-strands surface and the Aβ fragment (Fig. 5A). $A\beta_{29-33}$ residues

are in a U-turn arrangement nearly coplanar to the above mentioned TLN β-turn-β motif (Fig. 5A). As it is frequently suggested that $A\beta_{1–40}$ fibrils adopt a C-terminus β1-turn-β2 U-shaped motif, with the monomers packed in a two-fold symmetry [53,54], we speculate that the core of the Aβ fibrils share the structural features of the complex $TLN_{112–152}$:Aβ fragment, as described in Fig. 5B. Obviously many additional experiments are necessary to corroborate this model.

In conclusion, we showed that Aβ cleavage site (Ala30-Ile31) is inhibitory for TLN activity due to the slow dissociation of the C-terminal product from the enzyme. Given the discussed similarities between the binding modes of this fragment to TLN and of inhibitors to NEP, our findings suggest that NEP should be more efficient against Aβ polymorphs where this bond is sterically inaccessible. In fact, it was already hypothesized that while IDE mediates much of the degradation of soluble and monomeric Aβ, NEP has little role in degrading soluble Aβ, but can degrade SDS-extractable Aβ associated with membranes [55], producing mostly the fragment $A\beta_{10–37}$ [56].

## Acknowledgements

This work was supported by Norte-01-0145-FEDER-000008—Porto Neurosciences and Neurologic Disease Research Initiative at I3S, supported by Norte Portugal Regional Operational Programme (NORTE2020), under the PORTUGAL 2020 Partnership Agreement; by COMPETE 2020—Operational Programme for Competitiveness and Internationalization (POCI), Portugal 2020, through the European Regional Development Fund (FEDER); and, by Portuguese funds through FCT—Fundação para a Ciência e a Tecnologia/Ministério da Ciência, Tecnologia e Ensino Superior in the framework of the project "Institute for Research and Innovation in Health Sciences" (POCI-01-0145-FEDER-007274). JPL is a FCT fellow (grant SFRH/BD/129921/2017). The mass spectrometry technique was performed at the Proteomics i3S Scientific Platform with the assistance of Hugo Osório and the support of the Portuguese Mass Spectrometry Network (ROTEIRO/0028/2013; LISBOA-01-0145-FEDER-022125). We also thank the ESRF beamline staff for the assistance during data collection, as well as the staff of the SOLEIL (Essonne, France) and ALBA (Barcelona, Spain) synchrotrons for assistance in the collection of preliminary data.

## Author contributions

LG conceived and supervised the study; LG and JPL designed experiments; LG and JPL performed experiments; LG provided reagents. LG and JPL analyzed data; LG and JPL wrote the manuscript.

## References

1 Selkoe DJ and Hardy J (2016) The amyloid hypothesis of Alzheimer's disease at 25 years. *EMBO Mol Med* **8**, 595–608.
2 Chen GF, Xu TH, Yan Y, Zhou YR, Jiang Y, Melcher K and Xu HE (2017) Amyloid beta: structure, biology and structure-based therapeutic development. *Acta Pharmacol Sin* **38**, 1205–1235.
3 Hardy J (2007) Does Abeta 42 have a function related to blood homeostasis? *Neurochem Res* **32**, 833–835.
4 Pearson HA and Peers C (2006) Physiological roles for amyloid beta peptides. *J Physiol* **575**, 5–10.
5 Bailey JA, Maloney B, Ge YW and Lahiri DK (2011) Functional activity of the novel Alzheimer's amyloid beta-peptide interacting domain (AbetaID) in the APP and BACE1 promoter sequences and implications in activating apoptotic genes and in amyloidogenesis. *Gene* **488**, 13–22.
6 Hook V, Hook G and Kindy M (2010) Pharmacogenetic features of cathepsin B inhibitors that improve memory deficit and reduce beta-amyloid related to Alzheimer's disease. *Biol Chem* **391**, 861–872.
7 Mueller-Steiner S, Zhou Y, Arai H, Roberson ED, Sun B, Chen J, Wang X, Yu G, Esposito L, Mucke L *et al.* (2006) Antiamyloidogenic and neuroprotective functions of cathepsin B: implications for Alzheimer's disease. *Neuron* **51**, 703–714.
8 Tucker HM, Kihiko M, Caldwell JN, Wright S, Kawarabayashi T, Price D, Walker D, Scheff S, McGillis JP, Rydel RE *et al.* (2000) The plasmin system is induced by and degrades amyloid-β aggregates. *J Neurosci* **20**, 3937–3946.
9 Barker R, Love S and Kehoe PG (2010) Plasminogen and plasmin in Alzheimer's disease. *Brain Res* **1355**, 7–15.
10 Shen Y, Joachimiak A, Rich Rosner M and Tang WJ (2006) Structures of human insulin-degrading enzyme reveal a new substrate recognition mechanism. *Nature* **443**, 870–874.
11 Larmuth KM, Masuyer G, Douglas RG, Schwager SL, Acharya KR and Sturrock ED (2016) Kinetic and structural characterization of amyloid-beta peptide hydrolysis by human angiotensin-1-converting enzyme. *FEBS J* **283**, 1060–1076.
12 King JV, Liang WG, Scherpelz KP, Schilling AB, Meredith SC and Tang WJ (2014) Molecular basis of substrate recognition and degradation by human presequence protease. *Structure* **22**, 996–1007.
13 Iijima-Ando K, Hearn SA, Granger L, Shenton C, Gatt A, Chiang HC, Hakker I, Zhong Y and Iijima K (2008) Overexpression of neprilysin reduces Alzheimer

amyloid-beta42 (Abeta42)-induced neuron loss and intraneuronal Abeta42 deposits but causes a reduction in cAMP-responsive element-binding protein-mediated transcription, age-dependent axon pathology, and premature death in *Drosophila*. *J Biol Chem* **283**, 19066–19076.

14 Hama E, Shirotani K, Masumoto H, Sekine-Aizawa Y, Aizawa H and Saido TC (2001) Clearance of extracellular and cell-associated amyloid β peptide through viral expression of neprilysin in primary neurons. *J Biochem* **130**, 721–726.

15 Marr RA, Rockenstein E, Mukherjee A, Kindy MS, Hersh LB, Gage FH, Verma IM and Masliah E (2003) Neprilysin gene transfer reduces human amyloid pathology in transgenic mice. *J Neurosci* **23**, 1992–1996.

16 Guan H, Liu Y, Daily A, Police S, Kim MH, Oddo S, LaFerla FM, Pauly JR, Murphy MP and Hersh LB (2009) Peripherally expressed neprilysin reduces brain amyloid burden: a novel approach for treating Alzheimer's disease. *J Neurosci Res* **87**, 1462–1473.

17 Fulcher IS, Matsas R, Turner AJ and Kenny AJ (1982) Kidney neutral endopeptidase and the hydrolysis of enkephalin by synaptic membranes show similar sensitivity to inhibitors O-P-NH-CHCONH-CH-CO2. *Biochem J* **1**, 519–522.

18 Hausrath AC and Matthews BW (2002) Thermolysin in the absence of substrate has an open conformation. *Acta Crystallogr D Biol Crystallogr* **58**, 1002–1007.

19 Zhang R, Hu X, Khant H, Ludtke SJ, Chiu W, Schmid MF, Frieden C and Lee J-M (2009) Interprotofilament interactions between Alzheimer's Abeta1-42 peptides in amyloid fibrils revealed by cryoEM. *Proc Natl Acad Sci USA* **106**, 4653–4658.

20 Holland DR, Hausrath AC, Juers D and Matthews BW (1995) Structural analysis of zinc substitutions in the active site of thermolysin. *Protein Sci* **4**, 1955–1965.

21 Colletier JP, Laganowsky A, Landau M, Zhao M, Soriaga AB, Goldschmidt L, Flot D, Cascio D, Sawaya MR and Eisenberg D (2011) Molecular basis for amyloid-beta polymorphism. *Proc Natl Acad Sci USA* **108**, 16938–16943.

22 Takano K, Endo S, Mukaiyama A, Chon H, Matsumura H, Koga Y and Kanaya S (2006) Structure of amyloid β fragments in aqueous environments. *FEBS J* **273**, 150–158.

23 Streltsov VA, Varghese JN, Masters CL and Nuttall SD (2011) Crystal structure of the amyloid-β p3 fragment provides a model for oligomer formation in Alzheimer's disease. *J Neurosci* **31**, 1419–1426.

24 Nisbet RM, Nuttall SD, Robert R, Caine JM, Dolezal O, Hattarki M, Pearce LA, Davydova N, Masters CL, Varghese JN *et al.* (2013) Structural studies of the tethered N-terminus of the Alzheimer's disease amyloid-beta peptide. *Proteins* **81**, 1748–1758.

25 Cummings J, Lee G, Mortsdorf T, Ritter A and Zhong K (2017) Alzheimer's disease drug development pipeline: 2017. *Alzheimers Dement (N Y)* **3**, 367–384.

26 Gardberg AS, Dice LT, Ou S, Rich RL, Helmbrecht E, Ko J, Wetzel R, Myszka DG, Patterson PH and Dealwis C (2007) Molecular basis for passive immunotherapy of Alzheimer's disease. *Proc Natl Acad Sci USA* **104**, 15659–15664.

27 Miles LA, Wun KS, Crespi GA, Fodero-Tavoletti MT, Galatis D, Bagley CJ, Beyreuther K, Masters CL, Cappai R, McKinstry WJ *et al.* (2008) Amyloid-beta-anti-amyloid-beta complex structure reveals an extended conformation in the immunodominant B-cell epitope. *J Mol Biol* **377**, 181–192.

28 Basi GS, Feinberg H, Oshidari F, Anderson J, Barbour R, Baker J, Comery TA, Diep L, Gill D, Johnson-Wood K *et al.* (2010) Structural correlates of antibodies associated with acute reversal of amyloid beta-related behavioral deficits in a mouse model of Alzheimer disease. *J Biol Chem* **285**, 3417–3427.

29 Bohrmann B, Baumann K, Benz J, Gerber F, Huber W, Knoflach F, Messer J, Oroszlan K, Rauchenberger R, Richter WF *et al.* (2012) Gantenerumab: a novel human anti-Abeta antibody demonstrates sustained cerebral amyloid-beta binding and elicits cell-mediated removal of human amyloid-beta. *J Alzheimers Dis* **28**, 49–69.

30 Miles LA, Crespi GA, Doughty L and Parker MW (2013) Bapineuzumab captures the N-terminus of the Alzheimer's disease amyloid-beta peptide in a helical conformation. *Sci Rep* **3**, 1302.

31 Teplyakov A, Obmolova G and Gilliland GL (2017) A coiled conformation of amyloid-beta recognized by antibody C706. *Alzheimers Res Ther* **9**, 66.

32 Crespi GA, Hermans SJ, Parker MW and Miles LA (2015) Molecular basis for mid-region amyloid-beta capture by leading Alzheimer's disease immunotherapies. *Sci Rep* **5**, 9649.

33 Ultsch M, Li B, Maurer T, Mathieu M, Adolfsson O, Muhs A, Pfeifer A, Pihlgren M, Bainbridge TW, Reichelt M *et al.* (2016) Structure of Crenezumab complex with Abeta shows loss of beta-hairpin. *Sci Rep* **6**, 39374.

34 La Porte SL, Bollini SS, Lanz TA, Abdiche YN, Rusnak AS, Ho WH, Kobayashi D, Harrabi O, Pappas D, Mina EW *et al.* (2012) Structural basis of C-terminal beta-amyloid peptide binding by the antibody ponezumab for the treatment of Alzheimer's disease. *J Mol Biol* **421**, 525–536.

35 Kabsch W (1993) Automatic processing of rotation diffraction data from crystals of initially unknown symmetry and cell constants. *J Appl Crystallogr* **26**, 795–800.

36 Bailey S (1994) The CCP4 suit - programs for protein crystallography. *Acta Crystallogr Sect D: Biol Crystallogr* **58**, 760–763.

37 Brunger AT (1992) Free R value: a novel statistical quantity for assessing the accuracy of crystal structures. *Nature* **355**, 472–475.
38 Matthews BW (1968) Solvent content of protein crystals. *J Mol Biol* **33**, 491–497.
39 McCoy AJ, Grosse-Kunstleve RW, Adams PD, Winn MD, Storoni LC and Read RJ (2007) Phaser crystallographic software. *J Appl Crystallogr* **40**, 658–674.
40 Adams PD, Afonine PV, Bunkoczi G, Chen VB, Davis IW, Echols N, Headd JJ, Hung LW, Kapral GJ, Grosse-Kunstleve RW *et al.* (2010) PHENIX: a comprehensive Python-based system for macromolecular structure solution. *Acta Crystallogr D Biol Crystallogr* **66**, 213–221.
41 Emsley P, Lohkamp B, Scott WG and Cowtan K (2010) Features and development of Coot. *Acta Crystallogr D Biol Crystallogr* **66**, 486–501.
42 Schrodinger, LLC (2015) The PyMOL Molecular Graphics System, Version 1.8. LLC, New York, NY.
43 Toma S, Campagnoli S, Gregoriis ED, Gianna R, Margarit I, Zamai M and Grandi G (1989) Effect of Glu-143 and His-231 substitutions on the catalytic activity and secretion of *Bacillus subtilis* neutral protease. *Protein Eng Des Sel* **2**, 359–364.
44 Khan MTH, Yimingjiang W and Sylte I (2007) Molecular recognition of thermolysin and homologous zinc-metalloproteinases. *Minerva Biotecnol* **19**, 139–150.
45 Howell S, Nalbantoglu J and Crine P (1995) Neutral endopeptidase can hydrolyze beta-amyloid(1-40) but shows no effect on beta-amyloid precursor protein metabolism. *Peptides* **16**, 647–652.
46 Leissring MA, Lu A, Condron MM, Teplow DB, Stein RL, Farris W and Selkoe DJ (2003) Kinetics of amyloid β-protein degradation determined by novel fluorescence- and fluorescence polarization-based assays. *J Biol Chem* **278**, 37314–37320.
47 Backstrom JR, Lim GP, Cullen MJ, Tokes ZA and Tökés ZA (1996) Matrix metalloproteinase-9 (MMP-9) is synthesized in neurons of the human hippocampus and is capable of degrading the amyloid-beta peptide (1-40). *J Neurosci* **16**, 7910–7919.
48 Yan P, Hu X, Song H, Yin K, Bateman RJ, Cirrito JR, Xiao Q, Hsu FF, Turk JW, Xu J *et al.* (2006) Matrix metalloproteinase-9 degrades amyloid-β fibrils in vitro and compact plaques in situ. *J Biol Chem* **281**, 24566–24574.
49 Falkevall A, Alikhani N, Bhushan S, Pavlov PF, Busch K, Johnson KA, Eneqvist T, Tjernberg L, Ankarcrona M and Glaser E (2006) Degradation of the amyloid β-protein by the novel mitochondrial peptidasome, PreP. *J Biol Chem* **281**, 29096–29104.
50 Huang SM, Mouri A, Kokubo H, Nakajima R, Suemoto T, Higuchi M, Staufenbiel M, Noda Y, Yamaguchi H, Nabeshima T *et al.* (2006) Neprilysin-sensitive synapse-associated amyloid-beta peptide oligomers impair neuronal plasticity and cognitive function. *J Biol Chem* **281**, 17941–17951.
51 Oefner C, D'Arcy A, Hennig M, Winkler FK and Dale GE (2000) Structure of human neutral endopeptidase (Neprilysin) complexed with phosphoramidon. *J Mol Biol* **296**, 341–349.
52 Cramer J, Krimmer SG, Fridh V, Wulsdorf T, Karlsson R, Heine A and Klebe G (2017) Elucidating the origin of long residence time binding for inhibitors of the metalloprotease thermolysin. *ACS Chem Biol* **12**, 225–233.
53 Bertini I, Gonnelli L, Luchinat C, Mao J and Nesi A (2011) A new structural model of Aβ40 fibrils. *J Am Chem Soc* **133**, 16013–16022.
54 Petkova AT, Leapman RD, Guo Z, Yau WM, Mattson MP and Tycko R (2005) Self-propagating, molecular-level polymorphism in Alzheimer's β-amyloid fibrils. *Science* **307**, 262–265.
55 Selkoe DJ (2001) Clearing the brain's amyloid cobwebs. *Neuron* **32**, 177–180.
56 Iwata N, Tsubuki S, Takaki Y, Watanabe K, Sekiguchi M, Hosoki E, Kawashima-Morishima M, Lee HJ, Hama E, Sekine-Aizawa Y *et al.* (2000) Identification of the major Aβ1-42-degrading catabolic pathway in brain parenchyma: suppression leads to biochemical and pathological deposition. *Nat Med* **6**, 143–150.
57 Shirotani K, Tsubuki S, Iwata N, Takaki Y, Harigaya W, Maruyama K, Kiryu-Seo S, Kiyama H, Iwata H, Tomita T *et al.* (2001) Neprilysin degrades both amyloid β peptides 1-40 and 1-42 most rapidly and efficiently among thiorphan- and phosphoramidon-sensitive endopeptidases. *J Biol Chem* **276**, 21895–21901.

# 2.3 Paper II: $A\beta_{31-35}$ decreases Neprilysin-mediated Alzheimer's Amyloid-β peptide degradation

Work contributions:

Neprilysin overexpression and purification was performed by Susan B. Fowler and Carl I. Webster (Antibody Discovery & Protein Engineering, R&D, AstraZeneca, Cambridge, UK). Saturation Transfer Difference Nuclear Magnetic Ressonance experiments were performed by Marta Lete, Ana Gimeno and Jesús J. Jiménez-Baŕbero (CIC bioGUNE, Derio, Spain). Molecular dynamics simulation performed by Sérgio F. Sousa and Juliana F. Rocha (UCIBIO/REQUIMTE, BioSIM-Department of Biomedicine, FMUP, Porto, Portugal).

ACS Chemical Neuroscience

pubs.acs.org/chemneuro Research Article

# $A\beta_{31-35}$ Decreases Neprilysin-Mediated Alzheimer's Amyloid-$\beta$ Peptide Degradation

José P. Leite, Marta G. Lete, Susan B. Fowler, Ana Gimeno, Juliana F. Rocha, Sérgio F. Sousa, Carl I. Webster, Jesús J. Jiménez-Barbero, and Luís Gales*

Cite This: ACS Chem. Neurosci. 2021, 12, 3708−3718 Read Online

ACCESS | Metrics & More | Article Recommendations | Supporting Information

**ABSTRACT:** Alzheimer's disease is associated with the deposition of extracellular senile plaques, made primarily of amyloid-$\beta$ (A$\beta$), particularly peptides $A\beta_{1-42}$ and $A\beta_{1-40}$. Neprilysin, or neutral endopeptidase (NEP), catalyzes proteolysis of the amyloid peptides (A$\beta$) and is recognized as one of the major regulators of the levels of these peptides in the brain, preventing A$\beta$ accumulation and plaque formation. Here, we used a combination of techniques to elucidate the mechanism of A$\beta$ binding and cleavage by NEP. Our findings indicate that the $A\beta_{31-X}$ cleavage products remain bound to the neprilysin active site, reducing proteolytic activity. Interestingly, it was already shown that this $A\beta_{31-35}$ sequence is also critical for recognition of A$\beta$ peptides by other targets, such as the serpin-enzyme complex receptor in neuronal cells.

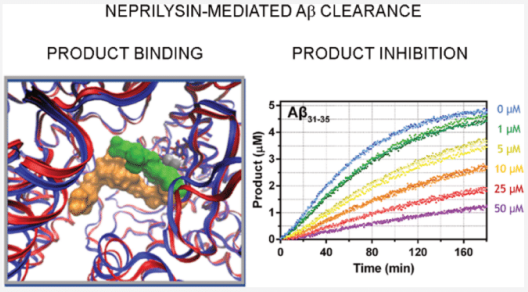


**KEYWORDS:** *Alzheimer's disease, amyloid-$\beta$ peptide, amyloid-degrading enzyme, neprilysin, enzyme kinetics, product inhibition*

## INTRODUCTION

Alzheimer's disease (AD) is the most widespread form of dementia with an estimated 30 million patients worldwide. Clinically, the first striking symptom of the disease is the progressive loss of short-term memory. As disease progresses, more debilitating symptoms appear, such as loss of orientation, language impairment, decision-making hindrance, and lack of judgment.[1] The two defining pathological features of the disease are early onset amyloid-$\beta$ peptide (A$\beta$) deposition followed by accumulation of tangles/neurites containing filaments of wild-type tau.[2−4] A$\beta$ is produced by the cleavage of the amyloid precursor protein (APP). APP is first cleaved by $\beta$-secretase, also known as $\beta$-site APP cleavage enzyme 1, generating a 99 residue C-terminal fragment (CTF$\beta$/C99). The CTF$\beta$/C99 is then cleaved by $\gamma$-secretase at multiple sites yielding different fragments that are, finally, processed within endocytic compartments to yield A$\beta$ isoforms (from 37 to 49 residues), of which the two most commonly occurring are $A\beta_{1-40}$ and $A\beta_{1-42}$, whose abundance varies between cerebrospinal fluid (CSF) and different tissues, in healthy or disease brains. Analysis of cortex tissue of healthy brains and AD brains showed also the presence of the N-terminal truncated $A\beta_{4-42}$.[5]

A$\beta$ deposition occurs in AD, either in familial (i.e., fAD, associated with known mutations of the APP or presenilin genes—presenilin being one of the components of the $\gamma$-secretase complex) or sporadic cases (sAD). A$\beta$ deposition is tightly associated with an overproduction of the peptide in fAD,[6] while late-onset sAD, which accounts for 99% of AD cases, has been strongly linked to a failure of A$\beta$ peptide clearance,[7] which stresses the urgency of completely understanding the clearance mechanisms. A$\beta$ peptides can be eliminated through proteolytic or non-proteolytic (e.g., phagocytosis) pathways. Proteolysis is achieved by the so-called amyloid degrading enzymes (ADEs), which include, for example, serine proteases,[8] cysteine proteases,[9] and zinc-metalloproteases.[10−12] Neprilysin, or neutral endopeptidase (NEP; EC 3.4.24.11), is a 749-amino acid zinc-dependent type II integral membrane protein, a member of the M13 peptidase family, and is classified as an ADE. This enzyme is rather promiscuous, with over 30 identified substrates, such as the natriuretic peptide, substance P or A$\beta$ peptides, conferring it a wide array of roles in the cardio-renal, respiratory, and nervous systems, respectively.[13] In the context of AD, numerous observations place NEP as the most relevant ADE. The enzyme has been shown to degrade both synthetic and cell-secreted $A\beta_{1-40}$ and $A\beta_{1-42}$ *in vitro*,[14] and in addition, it also

Received: June 30, 2021
Published: September 10, 2021

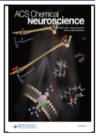





https://doi.org/10.1021/acschemneuro.1c00432
ACS Chem. Neurosci. 2021, 12, 3708−3718

degrades the N-terminal truncated forms of Aβ present in AD patient's brains, $Aβ_{4–40}$ and $Aβ_{4–42}$.[5,15] *In vivo*, Aβ accumulates in the brain of NEP-deficient mice, indicating the rate-limiting role of this enzyme in Aβ catabolism;[16] a similar mechanism may be a trigger for AD in humans as aging and accumulation of oxidative stress damage decrease ADE activity.[17] Accordingly, gene therapy to induce the overexpression of NEP has been pursued as a possible therapeutic option for AD, albeit with somewhat conflicting findings.[18−20] Despite *in vitro* studies indicating that NEP is able to degrade both monomeric and oligomeric forms of $Aβ_{1–40}$ and $Aβ_{1–42}$,[21] the complex *in vivo* environment may hinder its ability to fully catalyze the digestion of Aβ oligomers. Other approaches to lower Aβ have relied on the so-called peripheral sink hypothesis, where it was hypothesized that decreasing peripheric Aβ levels would displace the equilibrium across the blood brain barrier and reduce the brain amyloid burden. However, constant depletion of peripheral Aβ by NEP in mouse and non-human primate models did not alter brain or CSF Aβ levels, even when engineered variants are used, specifically targeting Aβ, such as neprilysin fused to albumin or the G399V/G714K mutant, that showed increased activity and specificity for $Aβ_{1–40}$ over other peptides.[22,23]

Despite the importance of NEP as an ADE, a complete understanding of the interaction between NEP and Aβ peptides is still lacking. NEP hydrolyzes the amino side of hydrophobic residues of peptides up to around 5 kDa. This substrate size specificity is conferred by the occluded cavity (i.e., crypt) where the active site is located, as the enzyme switches between open and closed states, so that the substrate can enter and be recognized, respectively; hence, NEP is dubbed a cryptidase.[24] The catalysis is a zinc-dependent reaction, with two highly conserved motifs, $^{583}$HExxH$^{587}$ and $^{646}$ExxxD$^{650}$, associated with zinc coordination and substrate attack.[25,26] Interestingly, the NEP ectodomain containing the active site is highly similar to the bacterial zinc metallopeptidase thermolysin (TLN), sharing the same zinc-binding consensus motifs, $^{583}$HExxH$^{587}$ and $^{646}$ExxxD$^{650}$.[25,27] Despite having low overall sequence homology, hydrophobic clustering analysis showed structural similarity between NEP C-terminal region (where the active site is located) and TLN.[28] Furthermore, they both have the same catalytic mode (i.e., attacking the N-terminus of hydrophobic residues), are inactivated by the same inhibitors, and share stereochemical dependence.[29] In fact, as it crystallizes more easily, TLN is used as a template for the NEP inhibitor design and a model for kinetic analysis.[27,29,30] In this context, we have previously used TLN as a surrogate structural model to investigate the interaction with Aβ,[31] and showed, using crystal X-ray diffraction and mass spectrometry, that TLN cleaves $Aβ_{1–40}$ between residue 30 and 31 and that the C-terminal product ($Aβ_{31–40}$) stays trapped in the active site.[31] As the same Aβ cleavage site had already been reported for NEP,[32] we decided to investigate, through a combination of enzyme kinetics, saturation-transfer difference nuclear magnetic resonance (STD-NMR), and molecular dynamics (MD) simulations, the interaction of $Aβ_{31–35}$ and NEP, and its consequences on NEP activity, that may affect Aβ clearance, particularly in the context of AD. Pairwise kinetic measurements with two other Aβ fragments ($Aβ_{10–20}$ and $Aβ_{20–29}$) were carried out because it is important to understand if, in the case of product inhibition, it depends on the cleavage site. The fragments were selected on the basis that $Aβ_{9–10}$ and $Aβ_{19–20}$ were identified as two of the major Aβ cleavage sites.[33]

## RESULTS AND DISCUSSION

Recombinant wild-type-soluble NEP ($NEP_{51–749}$) was expressed and purified, and its catalytic activity is confirmed using the substrate Dansyl-$^{D}$AGF(p$NO_2$)G.[34] As expected, NEP degraded Dansyl-$^{D}$AGF(p$NO_2$)G in a concentration-dependent manner, while pre-incubation with inhibitor thiorphan completely inactivated the enzyme (Figure S1). The kinetics of NEP degradation of Abz-VHHQKL-EDDnp were then investigated varying the concentration of the enzyme and the initial concentration of the substrate and following the reaction over time (Figure 1).

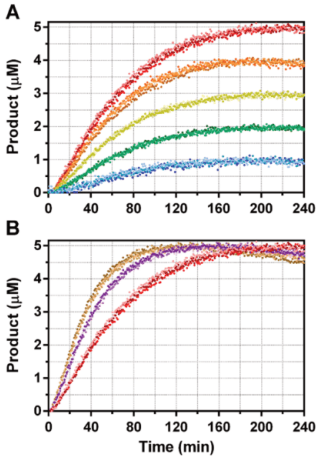


**Figure 1.** Kinetics of hydrolysis of Abz-VHHQKL-EDDnp by NEP at the range of substrate (A) and enzyme (B) concentrations. (A) NEP at 20 nM with initial substrate concentrations of 1 μM (blue), 2 μM (green), 3 μM (yellow), 4 μM (orange), and 5 μM (red). (B) Substrate at 5 μM and NEP at 20 nM (red), 40 nM (purple), and 60 nM (brown). Dots in shades of the same color represent triplicate measurements.

The kinetic parameters were determined and are presented in Table 1. We could not find similar data with this substrate in the literature for comparison. However, $k_{cat}/K_M$ was consistent with the value obtained previously in the degradation of $Aβ_{1–40}$,[22] although the $K_M$ value was ~24-fold lower for Abz-VHHQKL-EDDnp. The inhibition by $Aβ_{10–20}$, $Aβ_{20–29}$, and $Aβ_{31–35}$ was subsequently evaluated using several concen-

**Table 1. Kinetic Parameters of Abz-VHHQKL-EDDnp and $Aβ_{1–40}$ Degradation by NEP**

| | substrate | |
|---|---|---|
| | Abz-VHHQKL-EDDnp | $Aβ_{1–40}$ |
| $K_M$ (μM) | 4.3 ± 0.3 | 20 ± 5 |
| $k_{cat}$ ($s^{-1}$) | 0.040 ± 0.003 | 0.024 ± 0.005 |
| $k_{cat}/K_m$ ($M^{-1}$ $s^{-1}$) | $9.3 \times 10^3$ | $1.2 \times 10^3$ |
| $Aβ_{10–20}$: $K_I$ (μM) | 40 ± 20 | 40 ± 20 |
| $Aβ_{20–29}$: $K_I$ (μM) | 60 ± 10 | 70 ± 40 |
| $Aβ_{31–35}$: $K_I$ (μM) | 7 ± 1 | 12 ± 3 |



https://doi.org/10.1021/acschemneuro.1c00432
ACS Chem. Neurosci. 2021, 12, 3708−3718

trations of the A$\beta$ fragments (Figure 2). A$\beta_{31-35}$ inhibition is noticeably higher (estimated $K_I$ values are listed in Table 1).

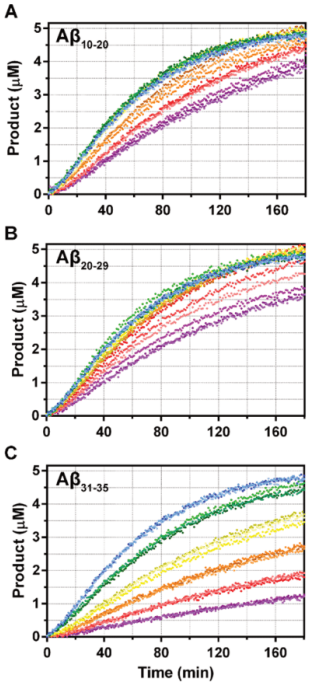


**Figure 2.** Hydrolysis of 5 $\mu$M Abz-VHHQKL-EDDnp by NEP (20 nM), in the presence of increasing concentrations of A$\beta$ fragments, at 0 $\mu$M (blue), 1 $\mu$M (green), 5 $\mu$M (yellow), 10 $\mu$M (orange), 25 $\mu$M (red), and 50 $\mu$M (purple). Dots in shades of the same color represent triplicate measurements.

The $K_I$ of A$\beta_{31-35}$ is in the micromolar range, about 10-fold lower than the ones of the other A$\beta$ fragments, and slightly higher than the $K_M$ of Abz-VHHQKL-EDDnp.

The hydrolysis of A$\beta_{1-40}$ by NEP was also investigated. Enzyme activity was followed taking time point samples that were analyzed by Tris-Tricine SDS PAGE (Figure 3A; remaining gels are presented in Supporting Information, Figures S2, S3, and S4). The SDS PAGE band corresponding to A$\beta_{1-40}$ (MW 4.3 kDa) could be clearly identified, and the expected decrease in the substrate bind intensity over time was observed. We attribute the slightly higher apparent molecular weight to a nonlinear migration in the Tris-Tricine 16.5% gels employed, whose lattice formulation lacks SDS.[35] Reactions were followed with and without pre-incubation with the A$\beta$ fragments; slower A$\beta_{1-40}$ degradation in the presence of A$\beta_{31-35}$ is noticeable, as illustrated in Figure 3A. The SDS PAGE gels were analyzed using an image software (ImageJ) for quantification of band intensities which were converted to A$\beta_{1-40}$ degradation (%)[36] and are presented in Figure 3B.

The reaction curves enabled the estimation of NEP kinetic parameters for A$\beta_{1-40}$ hydrolysis (Table 1). $k_{cat}/K_M$ is about 6.7 times lower than that described in the literature.[22] Despite the lower precision of the experimental method used here to follow the reaction, the main reason for the such discrepancy should be the use of the later stages of the reaction curves for analysis, where the conversion rate approaches a first-order reaction $v = k_{cat}/K_M \times E \times S$ due to the low substrate concentration. Since there are several A$\beta$ cleavage sites, numerous A$\beta$ fragments formed as reaction progresses are substrates that compete with A$\beta_{1-40}$ or may even have an inhibitory effect such as the A$\beta_{31-X}$ products. Therefore, $k_{cat}/K_M$ is underestimated and should be taken as an apparent value. Still, applying the same method with pre-incubation of the A$\beta$ fragments yielded $K_I$ values consistent with the ones obtained with the Abz-VHHQKL-EDDnp substrate (Table 1).

To confirm that A$\beta_{31-35}$ binds to the NEP active site, thus delaying A$\beta_{1-40}$ degradation, STD-NMR was employed. STD-NMR experiments demonstrate that A$\beta_{31-35}$ binds to NEP, as described by the appearance of different $^1$H NMR signals of that pentapeptide in the STD-NMR spectrum (Figure 4). The methyl groups of the isoleucine (I31 and I32) and methionine (M35) residues are clearly visible, as well as most of the side-chain signals. However, not all the H$\alpha$ protons appear in the STD-NMR spectrum. To assess the NEP active site, competition experiments with thiorphan, a well-known potent inhibitor of NEP[37] that tightly binds to the NEP active site, were then carried out. Fittingly, in the presence of only 0.5 equiv of thiorphan, basically all the STD-NMR signals previously observed for A$\beta_{31-35}$ disappeared from the STD-NMR spectrum. The side chain protons, including those for the methyl groups, were abolished, strongly suggesting that thiorphan displaces the peptide from the binding site. The STD-NMR data show in a non-ambiguous manner that this pentapeptide binds NEP at the same site as thiorphan (i.e., the active site), although with less affinity (thiorphan $K_I$ = 0.002 $\mu$M[38]). Indeed, the use of sub-stoichiometric amounts of thiorphan effectively removed the STD-NMR signals of A$\beta_{31-35}$ in the presence of NEP. Thus, the observed slowing effect of A$\beta_{1-40}$ degradation stems from the retaining of A$\beta_{31-X}$ following cleavage, making the active site less available for further catalysis.

Next, MD simulations were performed to corroborate the experimental evidence and assess the binding mode of the A$\beta$ peptides to the NEP active site. Figure 5 presents the dominant conformation adopted by A$\beta_{31-35}$ and A$\beta_{31-40}$ in the NEP binding pocket, together with the most important interactions observed in the MD simulations. In both cases, the peptide fragment keeps the N-terminal amino acid residues near the zinc coordination sphere, although for A$\beta_{31-40}$, the distance is larger than that for A$\beta_{31-35}$. The remaining residues develop through the large central cavity that is enveloped by subdomains 1 and 2 of NEP, displaying a significantly higher flexibility. The A$\beta_{31-35}$ peptide adopts an extended conformation, with an average end-to-end distance of 13.5 Å, while the A$\beta_{31-40}$ peptide adopts $\beta$ turn conformation with an average end-to-end distance of 20.3 Å.

Furthermore, the simulations show that A$\beta$ residues Ile31 to Met35 display lower positional variability associated to a lower root-mean-square fluctuation (RMSF, Figure S6). This agrees with the electron density observed in X-ray crystallographic structures of the complexes of A$\beta$ peptides with TLN.[31] Finally, the individual contribution of the different protein-to-peptide residue interactions to the overall NEP-A$\beta$ binding free energy, as well as the most stable hydrogen bonds formed between each complex, with indication of the percentage of the MD simulation in which these interactions are formed, were computed and are illustrated in Figure 6. The highest energetic contribution to the binding free energy of A$\beta_{31-35}$ to NEP is



https://doi.org/10.1021/acschemneuro.1c00432
ACS Chem. Neurosci. 2021, 12, 3708−3718

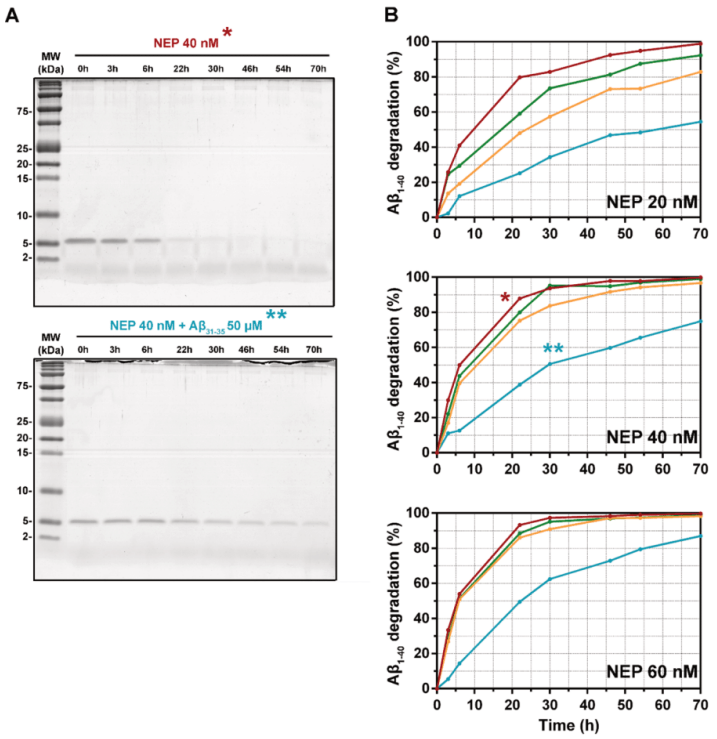


**Figure 3.** (A) Tris-Tricine SDS PAGE analysis of the A$\beta_{31-35}$ effect on NEP-mediated A$\beta_{1-40}$ degradation. A$\beta_{31-35}$ at 50 $\mu$M was incubated with NEP 40 nM overnight at room temperature, followed by the addition of A$\beta_{1-40}$ at 15 $\mu$M. Samples collected at different time points (0, 3, 6, 22, 30, 46, 54, and 70 h). (B) Neprilysin (20, 40, or 60 nM) degradation of A$\beta_{1-40}$ (15 $\mu$M), in the absence (red line) or presence of 50 $\mu$M of the A$\beta$ fragments (A$\beta_{10-20}$, orange line; A$\beta_{20-29}$, green line; and A$\beta_{31-35}$, blue line). A$\beta_{1-40}$ degradation was followed by image analysis of Tris-Tricine SDS-PAGE gels with ImageJ.[36]

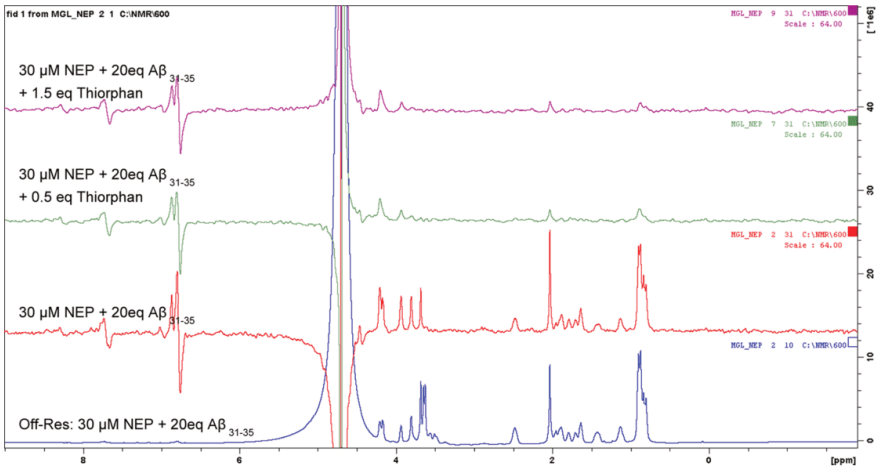


**Figure 4.** (Blue) Bottom. $^1$H NMR reference spectrum (off-resonance frequency set at $\delta$ −25 ppm) obtained for the target sample containing 30 $\mu$M of NEP and 0.6 mM of A$\beta$ peptide at 25 °C (600 MHz). (Red) STD-NMR spectrum (on-resonance frequency $\delta$ 6.77 ppm). Most of the NMR signals obtained for the pentapeptide are clearly visible. (Green) STD-NMR spectrum (on-resonance frequency $\delta$ 6.77 ppm) obtained for the ternary mixture (NEP/A$\beta$:thiorphan; 1:20:0.5 M ratio). The STD-NMR signals for the pentapeptides observed in spectrum B are abolished. (Purple) Top. The same results are obtained when using 1.5 equiv of thiorphan. In cases, the STD-NMR spectrum obtained for NEP alone has been subtracted from that obtained for the complexes (STD spectra).



https://doi.org/10.1021/acschemneuro.1c00432
ACS Chem. Neurosci. 2021, 12, 3708−3718

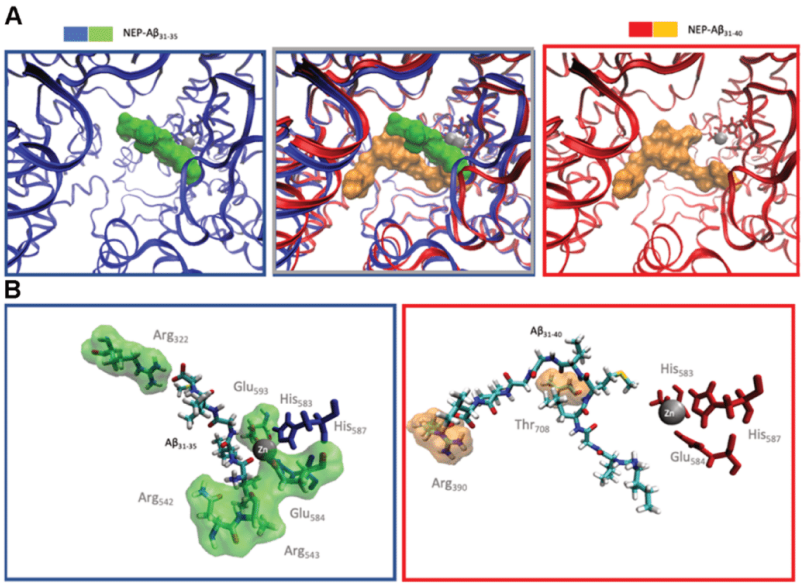


**Figure 5.** Representation of the average structures of the dominant clusters obtained from the last 150 ns of the MD simulations, with indication of the average position occupied by A$\beta_{31-35}$ and A$\beta_{31-40}$, zinc coordination sphere, and most important amino acid residues.

made by Arg222, that establishes two strong hydrogen bonds with Met35. Other important contributions are made by Glu584, Ala543, Glu646, and Asn542. In terms of the peptide fragment, the most important contributions are given by Ile32, Met35, and Ile31. Regarding A$\beta_{31-40}$, the highest energetic contribution to the NEP binding free energy is made by Arg390 and Thr708, which form stable interactions with the C-terminal Val40 residue (in the case of Arg390) and with Met35 and Val36 (in the case of Thr708). Other important contributions are played by Arg222, Pro226, Phe106, and Val710. In terms of the peptide fragment, the most important contributions are played by Ile32, Met35, and Val39.

There is no available structural model of NEP bound to any A$\beta$ fragments. Still, a good approximation can be obtained through the analysis of other crystallographic models. Recently, we determined the structure of inactive thermolysin (iTLN)/A$\beta_{1-40}$.[31] Despite the number of cleavage sites within A$\beta_{1-40}$, only one binding configuration was present in the crystals, with A$\beta$'s Gly29, Ala30, Ile31, Ile32, and Gly33 at *P*2, *P*1, *P*1′, *P*2′, and *P*3′ sites, respectively. The carbonyl group of *P*1′ is stabilized by an arginine (Arg203), while the amide and carbonyl groups of *P*2′ interact with an asparagine (Asn112). The hydrophobic Ile31−Ile32 motif is stabilized in a pocket topped by Phe130, and A$\beta$ exhibits a $\beta$ turn conformation.[31] In the same study, we have also determined the structure of active TLN incubated with A$\beta_{1-40}$ in which A$\beta_{31-X}$ cleavage products could be clearly observed bound in the active site. Protein crystallization is a slow process, and thus, the cleavage products have to remain bound to the active site for a long time to be visible.

Given the structural similarities between NEP and TLN active sites, an analogous trend for the binding of A$\beta$ peptides toward NEP is possible. In agreement to this, there is a crystallographic structure of the complex of inactive human NEP Glu584Asp with peptide substrate C-type natriuretic peptide (CNP).[39] In this case, electron density allowed only to trace the backbone model of four residues (*P*1, *P*1′, *P*2′, and *P*3′) but, interestingly, the CNP peptide exhibits a $\beta$ turn orientation that is similar to the A$\beta$ in complex with iTLN (Figure 7A,C). Moreover, we did obtain experimental evidence, using STD-NMR, that A$\beta_{31-35}$ and the NEP inhibitor thiorphan interact with the same NEP residues, located in the active site. Thiorphan-binding site was disclosed using soluble rabbit NEP, which is virtually identical to the human counterpart, with non-conserved residues located away from the active site. For that reason, it is used as a model to study human NEP-associated diseases.[40] The structure of rabbit NEP in complex with thiorphan shows a similar binding mode to the iTLN/A$\beta_{1-40}$, with Arg718 stabilizing a carbonyl group, Asn543 stabilizing amide, and carbonyl groups and the aromatic ring accommodated in the hydrophobic pocket topped by Phe107 (Figure 7A,B).

In normal and AD brain extracellular fluids, A$\beta$ levels range from picomolar to nanomolar.[42] However, they can reach concentrations several orders of magnitude higher in line with the ones used in this work (i.e., micromolar range) in intracellular compartments,[42] or as a result of phenomena in the extracellular environment, such as interactions with membrane lipid layers,[43] protein complexes,[44] or macromolecular crowding.[45]

A$\beta$ peptides are naturally present in the brains and CSF of normal humans throughout life, but several studies have shown a correlation between the levels of soluble oligomeric species and the extent of synaptic loss and severity of cognitive impairment.[46] Preventing the formation of cytotoxic oligomers through the reduction of the A$\beta$ levels below the critical concentration needed for oligomerization is being pursued in several ways: design of inhibitors of $\beta$- and $\gamma$-secretase that reduce A$\beta$ production; development of small molecules or antibodies that bind A$\beta$ species and foster their clearance; and



https://doi.org/10.1021/acschemneuro.1c00432
ACS Chem. Neurosci. 2021, 12, 3708−3718

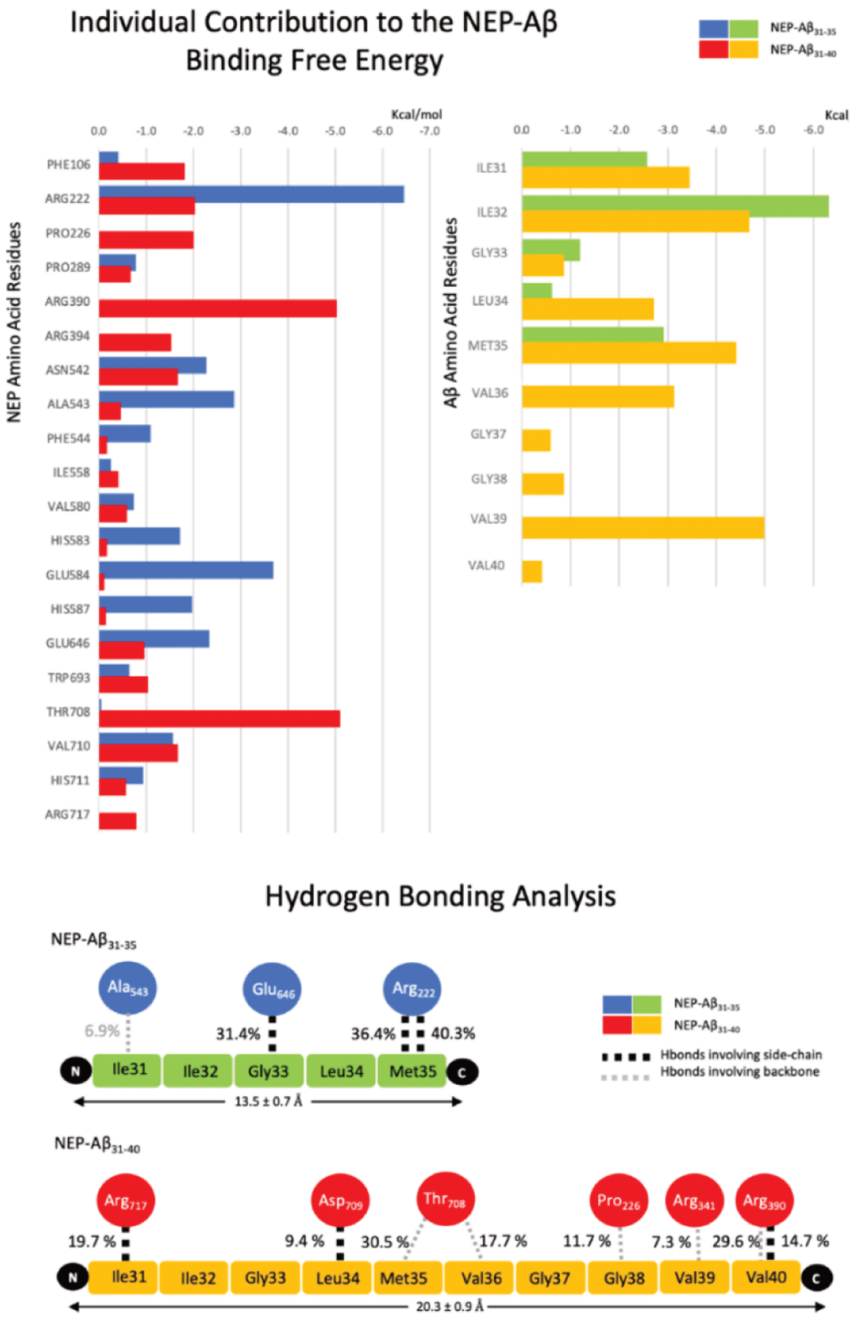


**Figure 6.** Structural and energetic analyses of the interactions formed between A$\beta_{31-35}$ and A$\beta_{31-40}$ and NEP from the MD simulations.

stimulation of proteases that degrade A$\beta$ species. Among the proteases, upregulation of NEP seems particularly appealing since voluntary exercise has been reported to stimulate NEP expression.[46] However, after decades of intensive research, effective therapeutic strategies are yet to be established as our current understanding of the disease process is incomplete. Here, we report new findings that some of the cleavage products of A$\beta$, notably A$\beta_{31-35}$, remain associated with the active site and inhibit the enzyme's activity. This finding has implications for the effectiveness of NEP-mediated clearance of A$\beta$, particularly when local A$\beta$ concentrations are high, and suggest that for NEP to be harnessed as an effective



https://doi.org/10.1021/acschemneuro.1c00432
ACS Chem. Neurosci. 2021, 12, 3708−3718

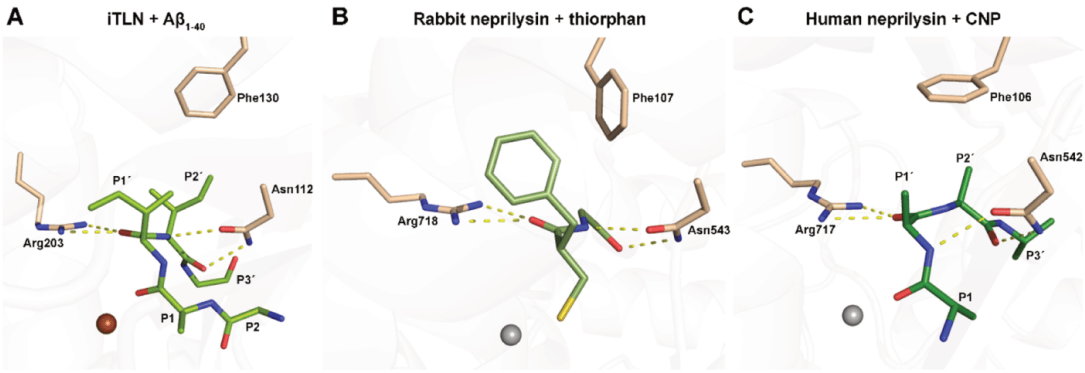


**Figure 7.** Structural comparison of the ligand-binding interactions of iTLN in complex with A$\beta_{1-40}$ (A), rabbit NEP in complex with thiorphan (B), and human NEP Glu584Asp in complex with CNP (C). Carbon atoms from protein side chains in beige, ligand carbon atoms in shades of green, oxygen atoms in red, nitrogen atoms in blue, sulfur atoms in yellow, cadmium as brown sphere, and zinc as gray spheres. Dashed lines indicate close interacting atoms. Figure prepared with PyMol from PDB coordinates 5ONP, 5V48, and 6SH2.[31,39−41]

therapeutic variants of the enzyme, or allosteric modulators, need to be identified that remove, or reduce, this production inhibition. These finding have enhanced our understanding of the mechanism of NEP-mediated A$\beta$ clearance and should be taken into account in the development of new therapeutic strategies.

## ■ CONCLUSIONS

The results presented here show that NEP-mediated catabolism of A$\beta_{1-40}$ is slowed by a C-terminal degradation product encompassing A$\beta_{31-32}$ (i.e., II motif), which has an extended active site residence-binding time. A$\beta_{31-35}$ fragment was supplemented to the *in vitro* reactions, and further studies are necessary to understand the relative abundance of A$\beta_{31-X}$ products generated by NEP-mediated hydrolysis *in vivo*.

Interestingly, A$\beta_{31-35}$ is the shortest of the A$\beta$ fragments that induces cytotoxicity,[47] and it does not form aggregates as longer A$\beta$ fragments and adsorbs to the cell surface, being preferentially internalized by neuronal cells. It was suggested that A$\beta_{31-35}$ peptide could initiate a cascade of events leading to neurotoxicity and cell death within the cells by means of a receptor-mediated mechanism.[48] A$\beta_{31-35}$ pentapeptide sequence was shown to be critical to bind to other proteins, such as the serpin-enzyme complex receptor, present in hepatoma cells and neuronal cells,[49] that plays a protective role by mediating clearance and catabolism of soluble, monomeric amyloid-$\beta$ peptides.[50] In summary, we have reported that A$\beta_{31-35}$ binds in the NEP active site and interferes with the A$\beta$ hydrolysis rate. This finding, taken together with other studies, points to A$\beta_{31-35}$ as being a critical sequence recognized by different target proteins and mediating mechanisms that may be toxic to neurons.

## ■ MATERIALS AND METHODS

**A$\beta$ Peptides.** A$\beta_{1-40}$, A$\beta_{10-20}$, A$\beta_{20-29}$, and A$\beta_{31-35}$ (subscript numbers indicate residue number) were purchased from Bachem (Switzerland), with a sample purity of 93.7, 99.2, 98.9, and 98.5%, respectively, as determined by HPLC in trifluoroacetic acid by the supplier. Amino acid sequences are as follows: DAEFRHDSGYEVHHQKLVFFAEDVGSNKGAIIGLMVGGVV for A$\beta_{1-40}$ (MW 4329.86), YEVHHQKLVFF for A$\beta_{10-20}$ (MW 1446.67), FAEDVGSNKG for A$\beta_{20-29}$ (MW 1023.07), and IIGLM for A$\beta_{31-35}$ (MW 545.74). A$\beta$ samples were prepared based on the reference.[51] Briefly, lyophilized A$\beta$ peptides were equilibrated at room temperature for 30 min to allow complete defrosting and spun before opening the vial, to maximize the sample retrieval, and then dissolved in the fluoroalcohol 1,1,1,3,3,3-hexafluoro-2-propanol (HFIP) and incubated at room temperature for 3 h to disassemble possible pre-existing amyloid aggregates. At this stage, samples should be clear. If a suspension was formed, samples were briefly sonicated in a water bath, and HFIP was removed by overnight evaporation in a fume hood and further dried with a vacuum concentrator for 2.5 h to remove remaining traces. Dried peptide films were thoroughly resuspended in dimethyl sulfoxide (DMSO), and concentrations of the stock solutions were determined using the Pierce BCA Protein Assay Kit (Thermo Fisher Scientific, USA) using bovine serum albumin as standard and multiplied by a 1.51 conversion factor that accounts for the different chromophoric development of albumin and A$\beta$ peptides.[52,53] All other reagents are of analytical grade.

**Expression and Purification of Neprilysin.** NEP was expressed, as previously described.[22] Briefly, the recombinant form of the extracellular soluble domain of human wild-type NEP (amino acids 51-749) was designed with an N-terminal 10× histidine tag, resulting in 10-Hist-wtNEP. Based on amino acid sequence, the construct has a calculated mass of 81200.54 Da and a molar extinction coefficient of 126,920 $M^{-1}$ $cm^{-1}$. This construct was expressed in Chinese hamster ovary cells and purified sequentially using immobilized nickel affinity and size exclusion chromatography. Sample purity was verified by SDS-PAGE analysis, and mass spectrometry confirmed the correct molecular weight. Working protein stock solution was formulated in 25 mM Tris-HCl pH 7.0/150 mM NaCl/2 mM $MgCl_2$, at a concentration of 128 $\mu$M. Protein activity was assessed with the substrate Dansyl-$^{D}$AGF(p$NO_2$)G.[34] Briefly, NEP at three different concentrations (5, 10, and 20 nM) was incubated with 80 $\mu$M Dansyl-$^{D}$AGF(p$NO_2$)G (Bachem, Switzerland) at pH 7.4 and 37 °C, and fluorescence readings (in triplicate) were recorded every minute for 1 h using a Synergy Mx (Biotek, USA), with 342 and 562 nm as excitation and emission wavelengths, respectively. For inhibition tests, 20 $\mu$M thiorphan (Bachem, Switzerland) was incubated with NEP for 1 h at room temperature, before addition of 80 $\mu$M Dansyl-$^{D}$AGF-(p$NO_2$)G and subsequent fluorescence readings. For comparison purposes, arbitrary fluorescence units were normalized by the data with the highest intensity (i.e., NEP at 20 $\mu$M). All the following NEP enzymatic activity assays were performed in 7% DMSO.

**Abz-VHHQKL-EDDnp Degradation Assay.** Abz-VHHQKL-EDDnp (Genscript) is a fluorogenic derivative encompassing A$\beta_{12-17}$. This substrate is an internally quenched fluorescent peptide in which Abz (*ortho*-aminobenzoic acid) is the fluorescent donor and EDDnp [*N*-(ethylenediamine)-2,4-dinitrophenyl amide] is the



https://doi.org/10.1021/acschemneuro.1c00432
ACS Chem. Neurosci. 2021, 12, 3708−3718

fluorescent quencher. Hydrolysis of the fluorogenic substrate, catalyzed by NEP, was monitored by measuring fluorescence every minute using a Synergy Mx (Biotek, USA), with 320 and 420 nm as excitation and emission wavelengths, respectively. Measurements were carried out in triplicate at pH 7.4, 37 °C. The kinetics of the reaction was investigated using different concentrations of NEP (20, 40, and 60 nM) and of the substrate Abz-VHHQKL-EDDnp (1−5 $\mu$M). To determine the inhibitory effect of A$\beta_{10-20}$, A$\beta_{20-29}$, and A$\beta_{31-35}$ on NEP ability to degrade Abz-VHHQKL-EDDnp, the three A$\beta$ fragments (0, 1, 5, 10, 25, and 50 $\mu$M) were pre-incubated overnight with NEP (20 nM) before addition of the substrate (5 $\mu$M). Initial rates of product formation were obtained by linear regression of the linear regions of time courses as a function of the substrate concentration. Michaelis−Menten equation was fitted to the data to obtain $k_{cat}$ and $K_M$. A$\beta$ fragments were considered as competitive inhibitors that bind to the enzyme's active site (as determined by the STD-NMR experiments). The respective inhibition constant $K_I$ of the fragment was calculated by

$$K_M^{app} = K_M\alpha = K_M\left(1 + \frac{I}{K_I}\right)$$

**A$\beta_{1-40}$ Degradation Assay.** NEP (20, 40, and 60 nM) was incubated with A$\beta_{10-20}$, A$\beta_{20-29}$, or A$\beta_{31-35}$ at 50 $\mu$M, overnight at room temperature. Then, A$\beta_{1-40}$ was added at a final concentration of 15 $\mu$M, and the reaction proceeded under quiescent conditions at 37 °C, pH 7.4. Samples were collected at various time points (0−70 h) and stored at −20 °C, after mixing with Tris-Tricine sample buffer. They were then analyzed by Tris-Tricine SDS-PAGE, which allows the electrophoretic analysis of peptides.[35] Collected samples were heated at 95 °C for 10 min before loading into 15% Tris-Tricine gels prepared with 30% acrylamide/bis-acrylamide 29:1 and 3.3% cross-linker (Bio-Rad, USA). Precision Plus Protein Dual Xtra molecular-weight standards (2−250 kDa; Bio-Rad, USA) were used, and gels were run at constant 25 mA per gel. Gels were fixed for 30 min with 5% glutaraldehyde and stained with PageBlue Protein staining solution (Thermo Fisher Scientific, USA). Gel images were acquired with a GS-800 calibrated imaging densitometer (Bio-Rad, USA). Gels were analyzed with the ImageJ software.[36] Band intensity was obtained from the area under the curve of each lane's histogram. For comparison purposes, each area was normalized to the corresponding gel $t_{0h}$ band. Data were plotted using GraphPad Prism ver. 6.0 (GraphPad software, USA). Final stages of the product formation time curve were fitted to a first-order reaction (for low substrate concentrations, the reaction rate varies linearly with the substrate concentration) to obtain $k_{cat}/K_M^{app}$. $K_I$ values are determined by comparison of the progression curves with and without the A$\beta$ fragment. $K_M$ was determined by the linear regression of

$$P/t = V + K_M \ln\left(1 - \frac{P}{S_o}\right)/t$$

where $S_o$ is the initial concentration of the substrate and $P$ is the concentration of the product formed during the reaction.

**STD-NMR: Neprilysin-A$\beta_{31-35}$-Thiorphan.** All spectra were performed at 298 K on a Bruker AVANCE 2 600 MHz spectrometer. The data were analyzed using Bruker Topspin 3.2 software. Ligands were dissolved in deuterated solutions. The protein was buffer exchanged to Tris-d11 (pH 7.0, 2 mM), $MgCl_2$, and 2 mM NaCl. Thiorphan was dried down and resuspended in 100 $\mu$L of DMSO-$d_6$. The A$\beta$ pentapeptide was resuspended in $D_2O$. For STD-NMR experiments, a 30 $\mu$M solution of NEP was incubated with 20 equiv of A$\beta_{31-35}$ for 8 h at RT. Competition STD-NMR experiments were performed by adding 0.5 equiv of Thiorphan with respect to NEP. Additional competition experiments were carried out after adding 1.5 equiv of Thiorphan. Blank STD experiments were also recorded for the protein alone. The on-resonance frequency was set at the aromatic region ($\delta$ 6.77 ppm), while the off-resonance frequency was placed at $\delta$ −25 ppm. To achieve protein saturation, a series of 40 ms PC9 pulses were used with a total saturation time of 2 s. A spin-lock filter (50 ms) was used to minimize the NMR signals of the macromolecule. This experiment was recorded and employed to obtain the final STD data, which results from the subtraction of the blank STD-NMR spectrum (NEP alone) from the STD-NMR spectra obtained for the different mixtures (NEP-A$\beta_{31-35}$ and NEP-A$\beta_{31-35}$-Thiorphan). In this way, the protein background was removed, showing the signals of A$\beta_{31-35}$ alone.

**MD Simulations.** NEP was modeled using the PDB 6GID structure.[54] The A$\beta$ peptides were modeled in the NEP-binding pocket superimposing NEP to the PDB structure of the TLN-A$\beta_{1-40}$ fragment (PDB 5ONR).[55] The two A$\beta$ peptides evaluated were A$\beta_{31-40}$ and A$\beta_{31-35}$. Protonation of all the amino acid residues was predicted using PropKA version 3.0 at pH 7.0.[56] The system was prepared using the AMBER18 software package and Xleap, using the ff14SB[57] and general Amber force field (GAFF).[58] Charges on the NEP-A$\beta$ systems were neutralized through the addition of counter-ions ($Cl^-$), and the system was placed in with TIP3P water boxes with a minimum distance of 12 Å between the protein-surface and the side of the box, using the LEAP module of AMBER. Both systems were submitted to five consecutive minimization stages to remove clashes prior to the MD simulation, followed by heating to 310.15 K and *NVT* equilibration. Finally, molecular dynamic production runs were performed for 300 ns. These were performed with an *NPT* ensemble at constant temperature (310.15 K, Langevin thermostat) and pressure (1 bar, Berendsen barostat), with periodic boundary conditions, with an integration time of 2.0 fs using the SHAKE algorithm to constrain all covalent bonds involving hydrogen atoms. A 10 Å cutoff for nonbonded interactions was used during the entire molecular simulation procedure. Final trajectories were analyzed in terms of root-mean-square deviation, confirming that both systems were well equilibrated after the initial 50 ns (Figure S5). The last 150 ns of the simulation were considered for RMSF, hydrogen bonding analysis, and cluster analysis of the conformations generated. The molecular mechanics/generalized born surface area method[59] was applied to estimate the NEP-A$\beta_{31-40}$ and NEP-A$\beta_{31-35}$ binding free energies (details in the Supporting Information). In addition, the energy decomposition method was employed to estimate the contribution of all the amino acid residues for each of these binding free energies. From each MD trajectory, a total of 300 conformations taken from the last 150 ns of simulation were considered for each MM-GBSA calculation.

## ■ ASSOCIATED CONTENT

### Supporting Information

The Supporting Information is available free of charge at https://pubs.acs.org/doi/10.1021/acschemneuro.1c00432.

Neprilysin activity assays, Tris-Tricine SDS-PAGE gels used to determine neprilysin-mediated degradation of A$\beta_{1-40}$, and MD complementary data of the neprilysin A$\beta_{31-35}$/A$\beta_{31-40}$ interactions (PDF)

## ■ AUTHOR INFORMATION


### Corresponding Author

**Luís Gales** − *i3S—Instituto de Investigação e Inovação em Saúde, Porto 4200-135, Portugal; IBMC—Instituto de Biologia Molecular e Celular, Universidade do Porto, Porto 4200-135, Portugal; ICBAS—Instituto de Ciências Biomédicas Abel Salazar, 4050-313 Porto, Portugal;* orcid.org/0000-0002-8352-6539; Email: lgales@ibmc.up.pt

### Authors

**José P. Leite** − *i3S—Instituto de Investigação e Inovação em Saúde, Porto 4200-135, Portugal; IBMC—Instituto de Biologia Molecular e Celular, Universidade do Porto, Porto 4200-135, Portugal; Programa Doutoral em Biologia Molecular e Celular (MCbiology), ICBAS—Instituto de*




https://doi.org/10.1021/acschemneuro.1c00432
*ACS Chem. Neurosci.* 2021, 12, 3708−3718

*Ciências Biomédicas Abel Salazar, Porto 4050-313, Portugal; ICBAS—Instituto de Ciências Biomédicas Abel Salazar, 4050-313 Porto, Portugal*

**Marta G. Lete** − *CIC bioGUNE, Bizkaia Technology Park, Derio 48170, Spain;* orcid.org/0000-0002-9654-7881

**Susan B. Fowler** − *Antibody Discovery & Protein Engineering R&D, Cambridge CB21 6GH, U.K.*

**Ana Gimeno** − *CIC bioGUNE, Bizkaia Technology Park, Derio 48170, Spain;* orcid.org/0000-0001-9668-2605

**Juliana F. Rocha** − *UCIBIO/REQUIMTE, BioSIM-Department of Biomedicine, Faculty of Medicine, University of Porto, Porto 4200-319, Portugal;* orcid.org/0000-0002-7686-4433

**Sérgio F. Sousa** − *UCIBIO/REQUIMTE, BioSIM-Department of Biomedicine, Faculty of Medicine, University of Porto, Porto 4200-319, Portugal;* orcid.org/0000-0002-6560-5284

**Carl I. Webster** − *Antibody Discovery & Protein Engineering R&D, Cambridge CB21 6GH, U.K.;* orcid.org/0000-0003-2513-2256

**Jesús J. Jiménez-Barbero** − *CIC bioGUNE, Bizkaia Technology Park, Derio 48170, Spain; Ikerbasque, Basque Foundation for Science, Bilbao 48013, Spain; Department of Organic Chemistry II, Faculty of Science and Technology, UPV-EHU, 48940 Leioa, Spain;* orcid.org/0000-0001-5421-8513

Complete contact information is available at: https://pubs.acs.org/10.1021/acschemneuro.1c00432

### Author Contributions

J.P.L.: Data curation (enzyme kinetic assays) and writing—original draft preparation. M.G.L., A.G., and J.J.J.-B.: Conceptualization (NMR), methodology (NMR), and writing—original draft preparation. S.B.F. and C.I.W.: Data curation (enzyme production), contribution to the experimental planning, writing—original draft preparation, reviewing, and editing. J.F.R. and S.F.S.: MD and writing—original draft preparation. L.G.: Conceptualization, methodology, writing—reviewing, and editing.

### Notes

The authors declare the following competing financial interest(s): CIW and SBF were employees of AstraZeneca at the time the work was performed and therefore have a theoretical conflict of interest through being employed by the organisation that part funded the work and may have potential commercial interest in the findings.

## ■ ACKNOWLEDGMENTS

This work was supported by the Norte-01-0145-FEDER-000008-Porto Neurosciences and Neurologic Disease Research Initiative at I3S and the Norte Portugal Regional Operational Programme (NORTE2020), under the PORTUGAL 2020 Partnership Agreement, by COMPETE 2020—Operational Program for Competitiveness and Internationalization (POCI), Portugal 2020, through the European Regional Development Fund (FEDER), and by Portuguese funds through FCT—Fundação para a Ciência e a Tecnologia/Ministério da Ciência, Tecnologia e Ensino Superior in the framework of the project "Institute for Research and Innovation in Health Sciences" (POCI-01-0145-FEDER-007274), PTDC/QUI-QFI/29914/2017 and 2020.01423.CEECIND. Individual grants and scholarships: FCT is gratefully acknowledged for the PhD grant SFRH/BD/129921/2017 (to J.P.L.) and SFRH/BD/136746/2018 (to J.F.R.). Abz-VHHQKL-EDDnp was kindly gifted by Isabel Cardoso, PhD (Molecular Neurobiology group, i3S, Porto, Portugal).

## ■ REFERENCES

(1) Xie, J.; Liang, R.; Wang, Y.; Huang, J.; Cao, X.; Niu, B. Progress in Target Drug Molecules for Alzheimer's Disease. *Curr. Top. Med. Chem.* **2020**, *20*, 4−36.

(2) Wood, J. G.; Mirra, S. S.; Pollock, N. J.; Binder, L. I. Neurofibrillary tangles of Alzheimer disease share antigenic determinants with the axonal microtubule-associated protein $\tau$ ($\tau$). *Proc. Natl. Acad. Sci. U. S. A.* **1986**, *83*, 4040−4043.

(3) Glenner, G. G.; Wong, C. W. Alzheimer's disease: initial report of the purification and characterization of a novel cerebrovascular amyloid protein. *Biochem. Biophys. Res. Commun.* **1984**, *120*, 885−890.

(4) Selkoe, D. J.; Hardy, J. The amyloid hypothesis of Alzheimer's disease at 25 years. *EMBO Mol. Med.* **2016**, *8*, 595−608.

(5) Portelius, E.; Bogdanovic, N.; Gustavsson, M. K.; Volkmann, I.; Brinkmalm, G.; Zetterberg, H.; Winblad, B.; Blennow, K. Mass spectrometric characterization of brain amyloid beta isoform signatures in familial and sporadic Alzheimer's disease. *Acta Neuropathol.* **2010**, *120*, 185−193.

(6) Bateman, R. J.; Munsell, L. Y.; Morris, J. C.; Swarm, R.; Yarasheski, K. E.; Holtzman, D. M. Human amyloid-beta synthesis and clearance rates as measured in cerebrospinal fluid in vivo. *Nat. Med.* **2006**, *12*, 856−861.

(7) Mawuenyega, K. G.; Sigurdson, W.; Ovod, V.; Munsell, L.; Kasten, T.; Morris, J. C.; Yarasheski, K. E.; Bateman, R. J. Decreased clearance of CNS beta-amyloid in Alzheimer's disease. *Science* **2010**, *330*, 1774.

(8) Jacobsen, J. S.; Comery, T. A.; Martone, R. L.; Elokdah, H.; Crandall, D. L.; Oganesian, A.; Aschmies, S.; Kirksey, Y.; Gonzales, C.; Xu, J.; Zhou, H.; Atchison, K.; Wagner, E.; Zaleska, M. M.; Das, I.; Arias, R. L.; Bard, J.; Riddell, D.; Gardell, S. J.; Abou-Gharbia, M.; Robichaud, A.; Magolda, R.; Vlasuk, G. P.; Bjornsson, T.; Reinhart, P. H.; Pangalos, M. N. Enhanced clearance of Abeta in brain by sustaining the plasmin proteolysis cascade. *Proc. Natl. Acad. Sci. U. S. A.* **2008**, *105*, 8754−8759.

(9) Mueller-Steiner, S.; Zhou, Y.; Arai, H.; Roberson, E. D.; Sun, B.; Chen, J.; Wang, X.; Yu, G.; Esposito, L.; Mucke, L.; Gan, L. Antiamyloidogenic and neuroprotective functions of cathepsin B: implications for Alzheimer's disease. *Neuron* **2006**, *51*, 703−714.

(10) Bernstein, K. E.; Koronyo, Y.; Salumbides, B. C.; Sheyn, J.; Pelissier, L.; Lopes, D. H. J.; Shah, K. H.; Bernstein, E. A.; Fuchs, D.-T.; Yu, J. J.-Y.; Pham, M.; Black, K. L.; Shen, X. Z.; Fuchs, S.; Koronyo-Hamaoui, M. Angiotensin-converting enzyme overexpression in myelomonocytes prevents Alzheimer's-like cognitive decline. *J. Clin. Invest.* **2014**, *124*, 1000−1012.

(11) Kilger, E.; Buehler, A.; Woelfing, H.; Kumar, S.; Kaeser, S. A.; Nagarathinam, A.; Walter, J.; Jucker, M.; Coomaraswamy, J. BRI2 protein regulates beta-amyloid degradation by increasing levels of secreted insulin-degrading enzyme (IDE). *J. Biol. Chem.* **2011**, *286*, 37446−37457.

(12) Nisemblat, Y.; Belinson, H.; Dolev, I.; Michaelson, D. M. Activation of the amyloid cascade by intracerebroventricular injection of the protease inhibitor phosphoramidon. *Neurodegener. Dis.* **2008**, *5*, 166−169.

(13) Rawlings, N. D.; Barrett, A. J.; Thomas, P. D.; Huang, X.; Bateman, A.; Finn, R. D. The MEROPS database of proteolytic enzymes, their substrates and inhibitors in 2017 and a comparison with peptidases in the PANTHER database. *Nucleic Acids Res.* **2018**, *46*, D624−D632.

(14) Shirotani, K.; Tsubuki, S.; Iwata, N.; Takaki, Y.; Harigaya, W.; Maruyama, K.; Kiryu-Seo, S.; Kiyama, H.; Iwata, H.; Tomita, T.; Iwatsubo, T.; Saido, T. C. Neprilysin degrades both amyloid beta

peptides 1-40 and 1-42 most rapidly and efficiently among thiorphan- and phosphoramidon-sensitive endopeptidases. *J. Biol. Chem.* **2001**, *276*, 21895−21901.
(15) Hornung, K.; Zampar, S.; Engel, N.; Klafki, H.; Liepold, T.; Bayer, T. A.; Wiltfang, J.; Jahn, O.; Wirths, O. N-Terminal Truncated Abeta4-42 Is a Substrate for Neprilysin Degradation in vitro and in vivo. *J. Alzheimer's Dis.* **2019**, *67*, 849−858.
(16) Iwata, N.; Tsubuki, S.; Takaki, Y.; Shirotani, K.; Lu, B.; Gerard, N. P.; Gerard, C.; Hama, E.; Lee, H. J.; Saido, T. C. Metabolic regulation of brain Abeta by neprilysin. *Science* **2001**, *292*, 1550−1552.
(17) Nalivaeva, N. N.; Turner, A. J. Role of Ageing and Oxidative Stress in Regulation of Amyloid-Degrading Enzymes and Development of Neurodegeneration. *Curr. Aging Sci.* **2017**, *10*, 32−40.
(18) Guan, H.; Liu, Y.; Daily, A.; Police, S.; Kim, M.-H.; Oddo, S.; LaFerla, F. M.; Pauly, J. R.; Murphy, M. P.; Hersh, L. B. Peripherally expressed neprilysin reduces brain amyloid burden: a novel approach for treating Alzheimer's disease. *J. Neurosci. Res.* **2009**, *87*, 1462−1473.
(19) Liu, Y.; Studzinski, C.; Beckett, T.; Guan, H.; Hersh, M. A.; Murphy, M. P.; Klein, R.; Hersh, L. B. Expression of neprilysin in skeletal muscle reduces amyloid burden in a transgenic mouse model of Alzheimer disease. *Mol. Ther.* **2009**, *17*, 1381−1386.
(20) Marr, R. A.; Guan, H.; Rockenstein, E.; Kindy, M.; Gage, F. H.; Verma, I.; Masliah, E.; Hersh, L. B. Neprilysin regulates amyloid Beta peptide levels. *J. Mol. Neurosci.* **2004**, *22*, 5−12.
(21) Kanemitsu, H.; Tomiyama, T.; Mori, H. Human neprilysin is capable of degrading amyloid beta peptide not only in the monomeric form but also the pathological oligomeric form. *Neurosci. Lett.* **2003**, *350*, 113−116.
(22) Webster, C. I.; Burrell, M.; Olsson, L.-L.; Fowler, S. B.; Digby, S.; Sandercock, A.; Snijder, A.; Tebbe, J.; Haupts, U.; Grudzinska, J.; Jermutus, L.; Andersson, C. Engineering neprilysin activity and specificity to create a novel therapeutic for Alzheimer's disease. *PLoS One* **2014**, *9*, No. e104001.
(23) Henderson, S. J.; Andersson, C.; Narwal, R.; Janson, J.; Goldschmidt, T. J.; Appelkvist, P.; Bogstedt, A.; Steffen, A.-C.; Haupts, U.; Tebbe, J.; Freskgård, P. O.; Jermutus, L.; Burrell, M.; Fowler, S. B.; Webster, C. I. Sustained peripheral depletion of amyloid-beta with a novel form of neprilysin does not affect central levels of amyloid-beta. *Brain* **2014**, *137*, 553−564.
(24) Malito, E.; Hulse, R. E.; Tang, W.-J. Amyloid beta-degrading cryptidases: insulin degrading enzyme, presequence peptidase, and neprilysin. *Cell. Mol. Life Sci.* **2008**, *65*, 2574−2585.
(25) Bayes-Genis, A.; Barallat, J.; Richards, A. M. A Test in Context: Neprilysin: Function, Inhibition, and Biomarker. *J. Am. Coll. Cardiol.* **2016**, *68*, 639−653.
(26) Pope, D.; Cascio, M. Chapter 13 - Neprilysin Inhibitors Provide Insight into its Specificity and Therapeutic Potential. In *Drug Design and Discovery in Alzheimer's Disease*; Atta ur, R.; Choudhary, M. I. Eds.; Elsevier, 2014; pp 598−622.
(27) Tiraboschi, G.; Jullian, N.; Thery, V.; Antonczak, S.; Fournie-Zaluski, M.-C.; Roques, B. P. A three-dimensional construction of the active site (region 507−749) of human neutral endopeptidase. *Protein Eng., Des. Sel.* **1999**, *12*, 141−149.
(28) Benchetrit, T.; Bissery, V.; Mornon, J. P.; Devault, A.; Crine, P.; Roques, B. P. Primary structure homologies between two zinc metallopeptidases, the neutral endopeptidase 24 enkephalinase) and thermolysin, through clustering analysis. *Biochemistry* **1988**, *27*, 592−596.
(29) Roques, B. P.; Noble, F.; Daugé, V.; Fournié-Zaluski, M. C.; Beaumont, A. Neutral endopeptidase 24.11: structure, inhibition, and experimental and clinical pharmacology. *Pharmacol. Rev.* **1993**, *45*, 87.
(30) Dion, N.; Le Moual, H.; Fournié-Zaluski, M. C.; Roques, B. P.; Crine, P.; Boileau, G. Evidence that Asn542 of neprilysin (EC 3.4.24.11) is involved in binding of the P2′ residue of substrates and inhibitors. *Biochem. J.* **1995**, *311*, 623−627.
(31) Leite, J. P.; Gales, L. Alzheimer's Abeta1-40 peptide degradation by thermolysin: evidence of inhibition by a C-terminal Abeta product. *FEBS Lett.* **2019**, *593*, 128−137.
(32) Mital, M.; Bal, W.; Frączyk, T.; Drew, S. C. Interplay between Copper, Neprilysin, and N-Truncation of $\beta$-Amyloid. *Inorg. Chem.* **2018**, *57*, 6193−6197.
(33) Grimm, M. O. W.; Mett, J.; Stahlmann, C. P.; Haupenthal, V. J.; Zimmer, V. C.; Hartmann, T. Neprilysin and A$\beta$ Clearance: Impact of the APP Intracellular Domain in NEP Regulation and Implications in Alzheimer's Disease. *Front. Aging Neurosci.* **2013**, *5*, 98.
(34) Florentin, D.; Sassi, A.; Roques, B. P. A highly sensitive fluorometric assay for "enkephalinase," a neutral metalloendopeptidase that releases tyrosine-glycine-glycine from enkephalins. *Anal. Biochem.* **1984**, *141*, 62−69.
(35) Haider, S. R.; Reid, H. J.; Sharp, B. L. Tricine-SDS-PAGE. *Methods Mol. Biol.* **2019**, *1855*, 151−160.
(36) Schneider, C. A.; Rasband, W. S.; Eliceiri, K. W. NIH Image to ImageJ: 25 years of image analysis. *Nat. Methods* **2012**, *9*, 671−675.
(37) Roques, B. P.; Fournié-Zaluski, M. C.; Soroca, E.; Lecomte, J. M.; Malfroy, B.; Llorens, C.; Schwartz, J.-C. The enkephalinase inhibitor thiorphan shows antinociceptive activity in mice. *Nature* **1980**, *288*, 286−288.
(38) Ciapetti, P.; Giethlen, B. Chapter 8 - Molecular Variations Based on Isosteric Replacements. In *The Practice of Medicinal Chemistry*, 4th ed.; Wermuth, C. G.; Aldous, D.; Raboisson, P.; Rognan, D., Eds.; Academic Press: San Diego, 2008; pp 181−241.
(39) Moss, S.; Subramanian, V.; Acharya, K. R. Crystal structure of peptide-bound neprilysin reveals key binding interactions. *FEBS Lett.* **2020**, *594*, 327−336.
(40) Labiuk, S. L.; Sygusch, J.; Grochulski, P. Structures of soluble rabbit neprilysin complexed with phosphoramidon or thiorphan. *Acta Crystallogr., Sect. F: Struct. Biol. Commun.* **2019**, *75*, 405−411.
(41) Schrodinger, L. L. C. *The PyMOL Molecular Graphics System*, version 1.8, 2015.
(42) Hu, X.; Crick, S. L.; Bu, G.; Frieden, C.; Pappu, R. V.; Lee, J.-M. Amyloid seeds formed by cellular uptake, concentration, and aggregation of the amyloid-beta peptide. *Proc. Natl. Acad. Sci.* **2009**, *106*, 20324.
(43) Matsuzaki, K. Physicochemical interactions of amyloid $\beta$-peptide with lipid bilayers. *Biochim. Biophys. Acta, Biomembr.* **2007**, *1768*, 1935−1942.
(44) Cotman, S. L.; Halfter, W.; Cole, G. J. Agrin Binds to $\beta$-Amyloid (A$\beta$), Accelerates A$\beta$ Fibril Formation, and Is Localized to A$\beta$ Deposits in Alzheimer's Disease Brain. *Mol. Cell. Neurosci.* **2000**, *15*, 183−198.
(45) Munishkina, L. A.; Cooper, E. M.; Uversky, V. N.; Fink, A. L. The effect of macromolecular crowding on protein aggregation and amyloid fibril formation. *J. Mol. Recognit.* **2004**, *17*, 456−464.
(46) Walsh, D. M.; Selkoe, D. J. A$\beta$ oligomers - A decade of discovery. *J. Neurochem.* **2007**, *101*, 1172−1184.
(47) Yan, X.-Z.; Qiao, J.-T.; Dou, Y.; Qiao, Z.-D. $\beta$-Amyloid peptide fragment 31-35 induces apoptosis in cultured cortical neurons. *Neuroscience* **1999**, *92*, 177−184.
(48) Misiti, F.; Sampaolese, B.; Pezzotti, M.; Marini, S.; Coletta, M.; Ceccarelli, L.; Giardina, B.; Clementi, M. A$\beta$(31-35) peptide induce apoptosis in PC 12 cells: Contrast with A$\beta$(25-35) peptide and examination of underlying mechanisms. *Neurochem. Int.* **2005**, *46*, 575−583.
(49) Boland, K.; Manias, K.; Perlmutter, D. H. Specificity in recognition of amyloid-$\beta$ peptide by the serpin-enzyme complex receptor in hepatoma cells and neuronal cells. *J. Biol. Chem.* **1995**, *270*, 28022−28028.
(50) Boland, K.; Behrens, M.; Choi, D.; Manias, K.; Perlmutter, D. H. The serpin-enzyme complex receptor recognizes soluble, nontoxic amyloid- $\beta$ peptide but not aggregated, cytotoxic amyloid-$\beta$ peptide. *J. Biol. Chem.* **1996**, *271*, 18032−18044.
(51) Leite, J. P.; Gimeno, A.; Taboada, P.; Jiménez-Barbero, J. J.; Gales, L. Dissection of the key steps of amyloid-$\beta$ peptide 1−40 fibrillogenesis. *Int. J. Biol. Macromol.* **2020**, *164*, 2240−2246.



https://doi.org/10.1021/acschemneuro.1c00432
*ACS Chem. Neurosci.* 2021, 12, 3708−3718

(52) Jan, A.; Hartley, D. M.; Lashuel, H. A. Preparation and characterization of toxic Aβ aggregates for structural and functional studies in Alzheimer's disease research. *Nat. Protoc.* **2010**, *5*, 1186−1209.
(53) Nortley, R.; Korte, N.; Izquierdo, P.; Hirunpattarasilp, C.; Mishra, A.; Jaunmuktane, Z.; Kyrargyri, V.; Pfeiffer, T.; Khennouf, L.; Madry, C.; Gong, H.; Richard-Loendt, A.; Huang, W.; Saito, T.; Saido, T. C.; Brandner, S.; Sethi, H.; Attwell, D. Amyloid β oligomers constrict human capillaries in Alzheimer's disease via signaling to pericytes. *Science* **2019**, *365*, No. eaav9518.
(54) Moss, S.; Subramanian, V.; Acharya, K. R. High resolution crystal structure of substrate-free human neprilysin. *J. Struct. Biol.* **2018**, *204*, 19−25.
(55) Leite, J. P.; Gales, L. Fluorescence properties of the amyloid indicator dye thioflavin T in constrained environments. *Dyes Pigm.* **2019**, *160*, 64−70.
(56) Olsson, M. H. M.; Søndergaard, C. R.; Rostkowski, M.; Jensen, J. H. PROPKA3: Consistent treatment of internal and surface residues in empirical p K a predictions. *J. Chem. Theory Comput.* **2011**, *7*, 525−537.
(57) Maier, J. A.; Martinez, C.; Kasavajhala, K.; Wickstrom, L.; Hauser, K. E.; Simmerling, C. ff14SB: Improving the Accuracy of Protein Side Chain and Backbone Parameters from ff99SB. *J. Chem. Theory Comput.* **2015**, *11*, 3696−3713.
(58) Wang, J.; Wolf, R. M.; Caldwell, J. W.; Kollman, P. A.; Case, D. A. Development and testing of a general Amber force field. *J. Comput. Chem.* **2004**, *25*, 1157−1174.
(59) Miller, B. R.; McGee, T. D.; Swails, J. M.; Homeyer, N.; Gohlke, H.; Roitberg, A. E. MMPBSA.py: An efficient program for end-state free energy calculations. *J. Chem. Theory Comput.* **2012**, *8*, 3314−3321.



https://doi.org/10.1021/acschemneuro.1c00432
*ACS Chem. Neurosci.* 2021, 12, 3708−3718

### 2.3.1. Supporting Information

# Supporting Information

## $A\beta_{31-35}$ decreases Neprilysin-mediated Alzheimer's Amyloid-β peptide degradation

José P. Leite[1,2,3,9], Marta G. Lete[4], Susan B. Fowler[5], Ana Gimeno[4], Juliana F. Rocha[6], Sérgio F. Sousa[6], Carl I. Webster[5], Jesús J. Jiménez-Barbero [4,7,8], Luís Gales[1,2,9*]

[1]i3S – Instituto de Investigação e Inovação em Saúde, Rua Alfredo Allen, 208, 4200-135 Porto, Portugal

[2]IBMC – Instituto de Biologia Molecular e Celular, Universidade do Porto, Rua Alfredo Allen, 208, 4200-135 Porto, Portugal

[3]Programa Doutoral em Biologia Molecular e Celular (MCbiology), ICBAS – Instituto de Ciências Biomédicas Abel Salazar, Rua de Jorge Viterbo Ferreira 228, 4050-313 Porto, Portugal

[4]CIC bioGUNE, Bizkaia Technology Park, Building 801A, 48170 Derio, Spain

[5]Antibody Discovery & Protein Engineering R&D, AstraZeneca, Cambridge, CB21 6GH, UK

[6]UCIBIO/REQUIMTE, BioSIM-Department of Biomedicine, Faculty of Medicine, University of Porto, Alameda Prof. Hernâni Monteiro, Porto, 4200-319, Portugal

[7]Ikerbasque, Basque Foundation for Science, 48013 Bilbao, Spain.

[8]Department of Organic Chemistry II, Faculty of Science and Technology, UPV-EHU, 48940 Leioa, Spain

[9]ICBAS – Instituto de Ciências Biomédicas Abel Salazar, Rua de Jorge Viterbo Ferreira 228, 4050-313 Porto, Portugal

* Corresponding author: Luís Gales, Email: lgales@ibmc.up.pt

## 1. NEP activity measured using the fluorescent substrate Dansyl-$^{D}$AGF(pNO$_2$)G

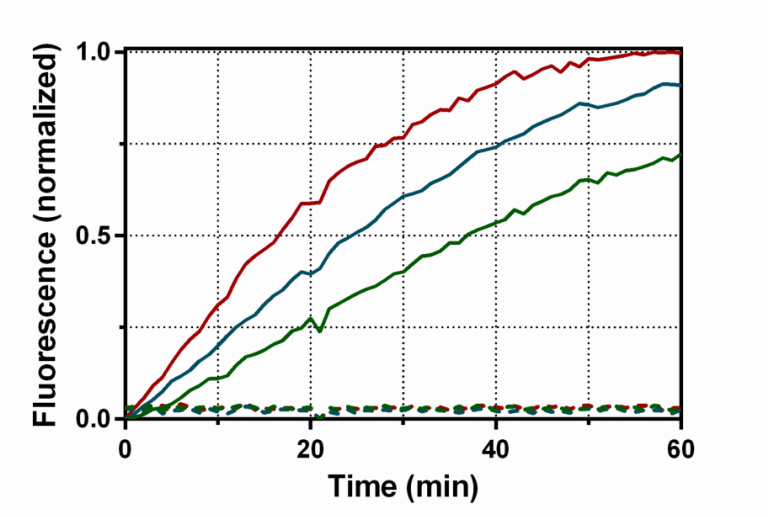


**Figure S1.** Enzymatic activity of recombinant human NEP$_{51-749}$. NEP cleaves substrate Dansyl-$^{D}$AGF(pNO$_2$)G (80 µM), resulting in the unquenching of fluorescence from the dansyl group [1]. Three different concentrations of NEP were tested (5, 10 and 20 nM, as green, blue and red solid lines, respectively). As expected, reaction rate increases with increasing enzyme concentrations. Addition of thiorphan (20 µM; dotted lines) resulted in the complete abolishment of enzyme activity. Thus, the obtained recombinant NEP is suitable for subsequent kinetic analysis.

## 2. Tris-Tricine SDS-PAGE analysis of Aβ fragments effect on NEP mediated $Aβ_{1-40}$ degradation

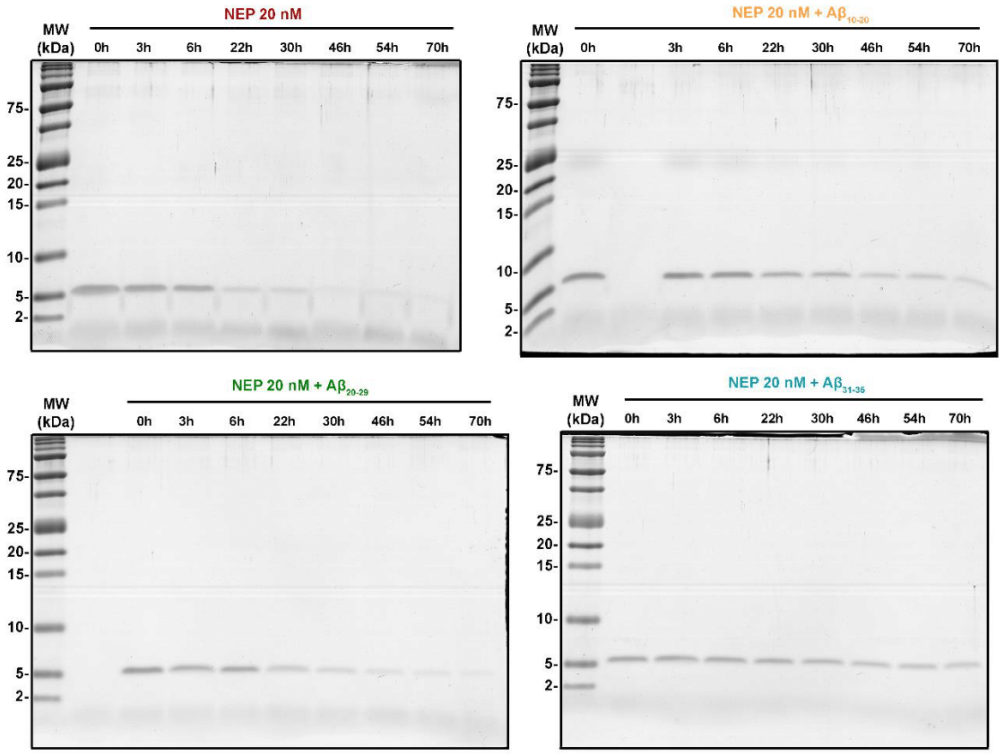


**Figure S2.** Tris-Tricine SDS PAGE analysis of NEP mediated $Aβ_{1-40}$ degradation, in the absence (red) or presence of different Aβ fragments ($Aβ_{10-20}$, orange; $Aβ_{20-29}$, green; $Aβ_{31-35}$, blue). NEP at 20 nM was incubated overnight at room temperature by itself or in the presence of 50 µM of each fragment, followed by addition of $Aβ_{1-40}$ at 15 µM. Samples were collected at different time points (0, 3, 6, 22, 30, 46, 54 and 70h).

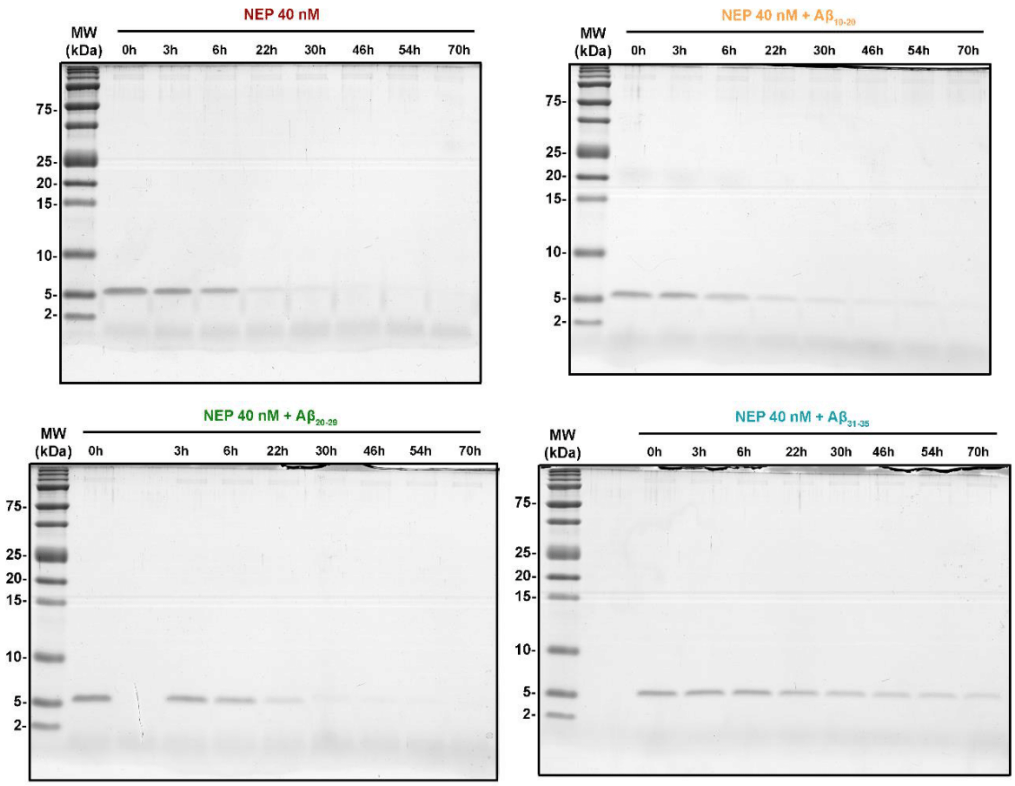


**Figure S3.** Tris-Tricine SDS PAGE analysis of NEP mediated $A\beta_{1-40}$ degradation, in the absence (red) or presence of different Aβ fragments ($A\beta_{10-20}$, orange; $A\beta_{20-29}$, green; $A\beta_{31-35}$, blue). NEP at 40 nM was incubated overnight at room temperature by itself or in the presence of 50 µM of each fragment, followed by addition of $A\beta_{1-40}$ at 15 µM. Samples were collected at different time points (0, 3, 6, 22, 30, 46, 54 and 70h).

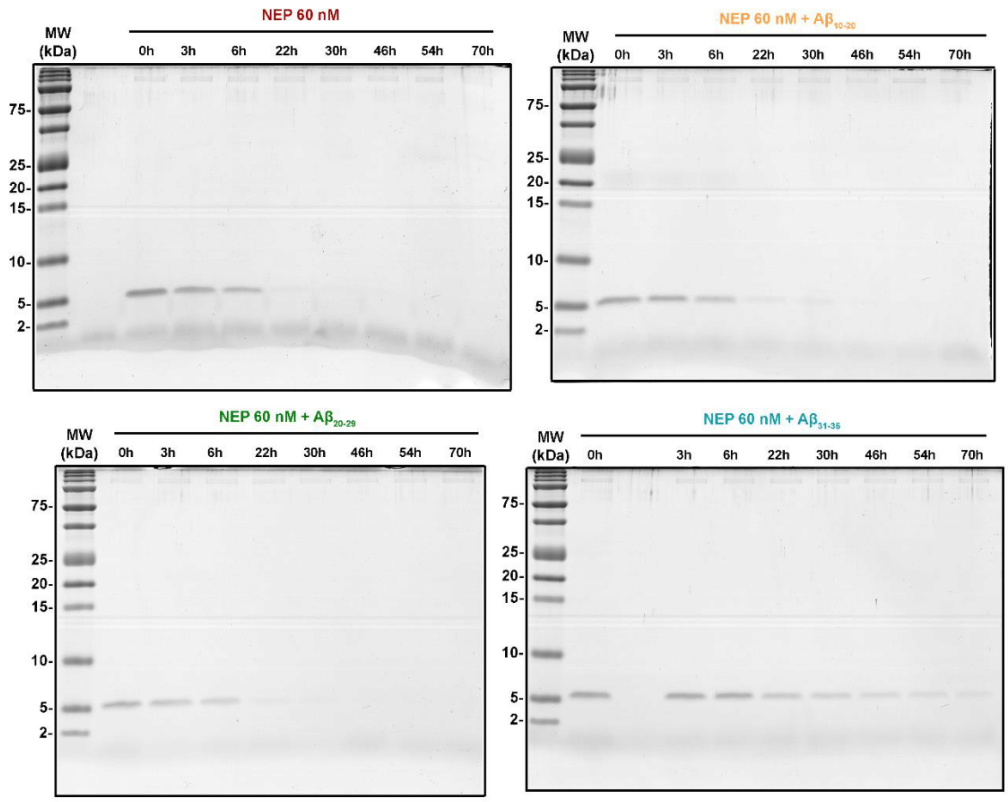


**Figure S4.** Tris-Tricine SDS PAGE analysis of NEP mediated $A\beta_{1-40}$ degradation, in the absence (red) or presence of different Aβ fragments ($A\beta_{10-20}$, orange; $A\beta_{20-29}$, green; $A\beta_{31-35}$, blue). NEP at 60 nM was incubated overnight at room temperature by itself or in the presence of 50 µM of each fragment, followed by addition of $A\beta_{1-40}$ at 15 µM. Samples were collected at different time points (0, 3, 6, 22, 30, 46, 54 and 70h).

## 3. Molecular Dynamics Simulations

### Molecular Mechanics / Generalized Born Surface Area (MM-GBSA)

The MM-GBSA method [2] was applied to estimate the NEP-Aβ 31-40 (IIGLMVGGVV) and NEP-Aβ31-35 (IIGLM) binding free energies. In addition, the energy decomposition method was employed to estimate the contribution of all the amino acid residues for each of these binding free energies. From each MD trajectory, a total of 300 conformations taken from the last 150 ns of simulation were considered for each MM-GBSA calculation. According to the MM-GBSA method, the binding free energy can be decomposed as the sum of different energy terms, defined as:

$$\Delta G_{bind} = G_{complex} - (G_{protein} + G_{ligand})$$

$$\Delta G_{bind} = \Delta H - T\Delta S \approx \Delta E_{gas} + \Delta G_{sol} - T\Delta S$$

Because the structures of the complex, protein, and ligand are extracted from the same trajectory, the internal energy change ($\Delta E_{int}$) is canceled.

$$\Delta E_{gas} = \Delta E_{int} + \Delta E_{ELE} + \Delta E_{VDW}$$

$$\Delta G_{sol} = \Delta G_{GB} + \Delta G_{Surf}$$

The gas-phase interaction energy ($\Delta E_{gas}$) between the components is written as the sum of electrostatic ($\Delta E_{ELE}$) and van der Waals ($\Delta E_{VDW}$) interaction energies. The solvation free energy ($\Delta G_{sol}$) is divided into the polar and non-polar energy terms. The polar solvation energy ($\Delta G_{GB}$) is calculated by using the Generalized-born (GB) model. In this case, the GB model proposed by Onufriev, Bashford and Case was considered [3]. The non-polar contribution is calculated based on the solvent-accessible surface area ($\Delta G_{Surf}$), calculated in the present work with the LCPO method [4]. The calculated binding free energy ($\Delta G_{bind}$) is hence written as the sum of the gas-phase interaction energy and solvation free energy.

NEP binding free energies for Aβ31-35 and Aβ31-40 predicted by the MM-GBSA approach are presented in Table S1. Both peptides remain bound to NEP with good affinity, with Aβ31-40 binding with approximately 2x the affinity of Aβ31-35 (-38.6 vs -19.1 kcal/mol). In both cases, the binding free energy is dominated by the non-polar contribution.

**Table S1.** Estimated NEP binding free energies for $A\beta_{31-35}$ and $A\beta_{31-40}$ predicted by the MM-GBSA approach, with indication of the corresponding components.

| Binding Free Energy | Total (kcal/mol) | VDW (kcal/mol) | EEL (kcal/mol) | EGB (kcal/mol) | ESURF (kcal/mol) | POLAR (kcal/mol) | NON-POLAR (kcal/mol) |
|---|---|---|---|---|---|---|---|
| **$A\beta_{31-35}$ (IIGLM)** | -19.1 ± 0.3 | -29.6 ± 0.3 | -151.1 ± 0.9 | 167.4 ± 0.8 | -5.8 ± 0.0 | 16.2 | -35.4 |
| **$A\beta_{31-40}$ (IIGLMVGGVV)** | -38.6 ± 0.3 | -75.4 ± 0.3 | -186.5 ± 1.4 | 233.5 ± 1.2 | -10.3 ± 0.0 | 47.2 | -85.7 |

VDW, van der Waals; EEL, electrostatic; EGB, polar component to the solvation free energy determined by the generalized Born method; ESURF, non-polar contribution to the solvation free energy; Polar, sum of the EEL and EGB energy terms; NON-POLAR, sum of the VDW and ESURF energy terms

## Root Mean Square Deviation (RMSd)

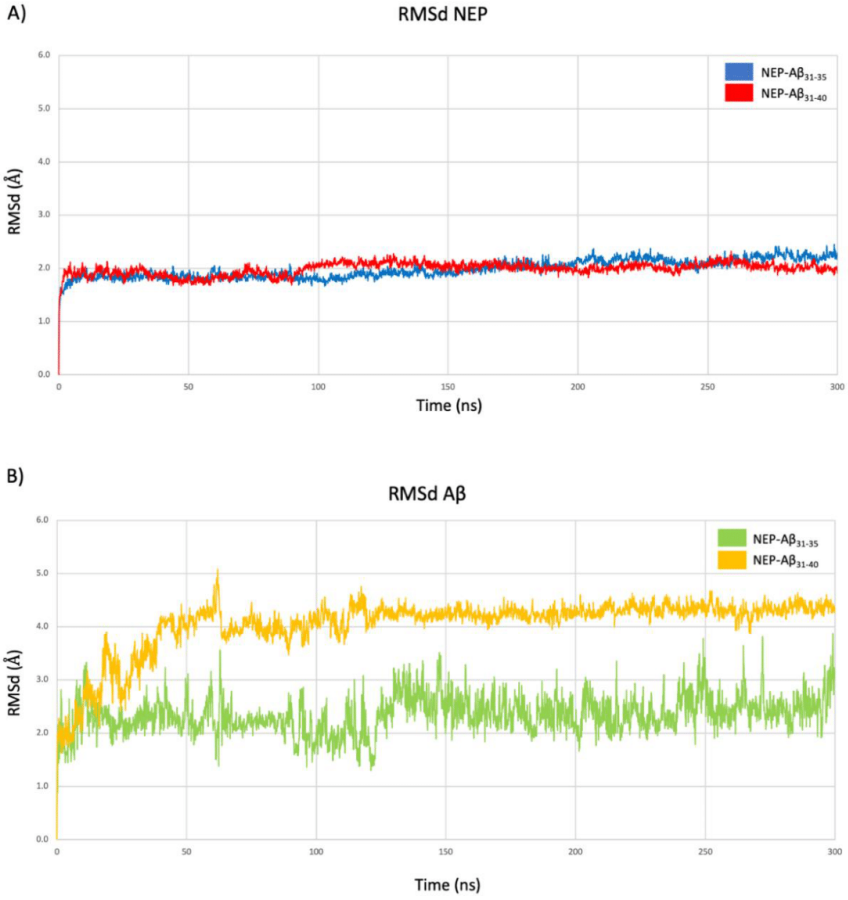


**Figure S5.** Root Mean Square Deviation of the backbone atoms in the NEP-Aβ simulations for a) NEP and b) Aβ peptide fragments along the 300 ns of MD simulation.

### Root-mean-square fluctuation (RMSF)

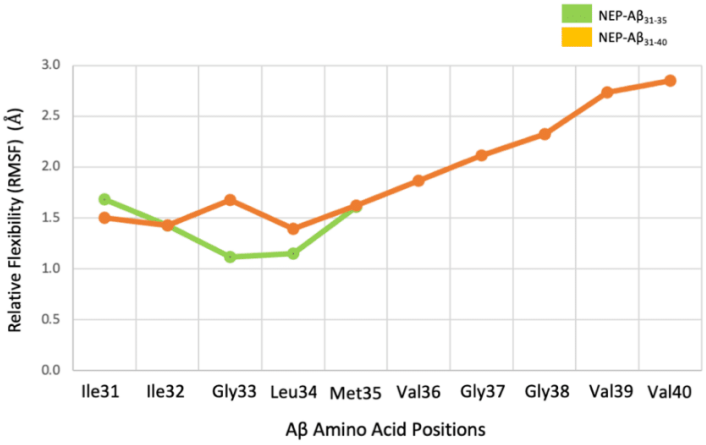


**Figure S6.** Representation of the Relative Flexibility expressed in terms of RMSF of the different amino acid residues that comprise the $A\beta_{31-35}$ and $A\beta_{31-40}$ peptides.

## References

1. Florentin, D., Sassi, A., and Roques, B. P. (1984) A highly sensitive fluorometric assay for "enkephalinase," a neutral metalloendopeptidase that releases tyrosine-glycine-glycine from enkephalins, *Anal Biochem 141*, 62-69.
2. Miller Iii, B. R., McGee, T. D., Swails, J. M., Homeyer, N., Gohlke, H., and Roitberg, A. E. (2012) MMPBSA.py: An efficient program for end-state free energy calculations, *Journal of Chemical Theory and Computation 8*, 3314-3321.
3. Onufriev, A., Bashford, D., and Case, D. A. (2004) Exploring Protein Native States and Large-Scale Conformational Changes with a Modified Generalized Born Model, *Proteins: Structure, Function and Genetics 55*, 383-394.
4. Weiser, J., Shenkin, P. S., and Still, W. C. (1999) Approximate atomic surfaces from linear combinations of pairwise overlaps (LCPO), *Journal of Computational Chemistry 20*, 217-230.

# CHAPTER III. Fusion-protein constructs for the crystallization of the amyloid-β peptide

Work contributions:

*In silico* fusion-protein plasmid design was performed with assistance from Sara Pereira (Bioengineering and Synthetic Microbiology group, i3S, Porto Portugal). I would also like to thank Tatiana Cereija (Structural Biochemistry group, i3S, Porto, Portugal) for the insightful discussions about X-Ray data processing and refinement. Differential scanning fluorimetry kit was kindly gifted by Johnny Lisboa (Fish Immunology & Vaccionology group, i3S, Porto, Portugal).

## 3.1 Introduction

In macromolecular crystal structure determination by X-Ray diffraction, crystallization is widely regarded as the major bottleneck (Holcomb *et al.*, 2017). For this reason, fusion proteins constitute a complex strategy to crystallize a peptide or protein of interest. Fusion-proteins are chimeric constructions from two or more different protein segments linked together and expressed as a single protein. They may be used to aid the crystallization of hard to crystallize proteins or peptides (*e.g.* highly hydrophobic or complexes with weak interactions) (Kobe *et al.*, 2015). In addition, fusion-proteins also help tackle the phase problem in X-Ray diffraction data for newly crystallized targets, avoiding the use of seleno-methionine protein expression or heavy-atom derivatization of pre-formed crystals. T4 Lysozyme (lysozyme from phage T4) is a possible heterologous partner in fusion constructs, since it is a soluble well folded protein and readily crystallizes under many conditions (Kobe *et al.*, 2015). It is mostly used with membrane proteins where polar areas are scarce (Lee *et al.*, 2015; Thorsen *et al.*, 2014; Tuukkanen *et al.*, 2019).

Given its hydrophobic and intrinsically disordered nature, Aβ emerges as a prime candidate for crystallization using a fusion protein approach. However, to date, only three reports are available (Nisbet *et al.*, 2013; Streltsov *et al.*, 2011; Takano *et al.*, 2006). Together, these fusion protein models shed some light on oligomerization of Aβ in a pre-fibrillary state. However, in the big picture of Alzheimer's disease research, they are clearly scarce and, strikingly, none encompasses the full-length peptide. Here, we designed three constructs to try obtaining atomic resolution crystallographic structures of the peptide. First, the peptide was added to the C-terminal end of T4 Lysozyme (used as a heterologous fusion partner), yielding T4 Lysozyme-$A\beta_{1-40}$. Then, a construct encompassing $A\beta_{17-40}$ and also using T4 Lysozyme as heterologous partner was used to investigate possible structural differences by the lack of the N-terminal region, given that it significantly affects the fibril formation rate (Kuhn *et al.*, 2020). Finally, a construct in which $A\beta_{1-40}$ is "intra protein" (*i.e.,* not on the N- or C-terminal sides of the heterologous partner) was designed. Proteasome assembly chaperone 3 (PAC3) was selected for this approach as heterologous fusion partner (Satoh *et al.*, 2019). This protein has a mobile loop region that in the native crystal packing faces a porous network (S51-V61). With our fusion construct (henceforth referred as PAC3-$A\beta_{1-40}$), we aimed at inserting $A\beta_{1-40}$ within this constrained environment.

## 3.2 T4 Lysozyme-Aβ$_{1-40}$

### 3.2.1 Materials and methods

#### 3.2.1.1 Plasmid design

T4Lysozyme-Aβ$_{1-40}$ fusion protein construct was designed *in silico* and ordered from GenScript (USA). Briefly, Aβ$_{1-40}$ nucleotide sequence optimized for expression in *E. coli* was obtained from the literature (Walsh *et al.*, 2009). The nucleotide sequence of a wild-type cysteine-free inactive mutant of T4 lysozyme, named T4 lysozyme wt* T26Q, was obtained by merging and reverse translating PDB entries 3RUN and 1QT4 (Economou *et al.*, 2012; Kuroki *et al.*, 1999; Stothard, 2000). The peptide and the protein were merged to form a sequence starting with T4 lysozyme at the N-terminal side, directly followed by Aβ$_{1-40}$ and added to the pET-15b (Novagen) expression plasmid between restriction sites NdeI and BamHI. The His-tag is located at the N-terminal of the construction, prior to the T4 lysozyme sequence. The fusion protein was named T4Lysozyme-Aβ$_{1-40}$. The final plasmids were codon optimized for *E. coli*, synthesized, and purchased from Genscript (USA). Aminoacid sequence and overall information, computed with Expasy ProtParam (Wilkins *et al.*, 1999), is presented on Table 3.1. Upon arrival, plasmids were transformed into *E. coli* DH5α for plasmid propagation, obtained by using NZYMiniprep kit (NZYTech, Portugal), and sequenced for integrity confirmation (StabVida, Portugal), before proceeding.

**Table 3.1.** Amino acid sequence of T4Lysozyme-Aβ$_{1-40}$ fusion protein construct and general construct information. Legend: His-tag and thrombin cleavage site underlined; T4 Lysozyme wt* T26Q in italic; Aβ$_{1-40}$ in bold.

| HHHHHHSSGLVPRGSH*MNIFEMLRIDEGLRLKIYKDTEGYYQIGIGHLLTKSPSLNAAKSELDKAI GRNTNGVITKDEAEKLFNQDVDAAVRGILRNAKLKPVYDSLDAVRRAALINMVFQMGETGVAGF TNSLRMLQQKRWDEAAVNLAKSRWYNQTPNRAKRVITTFRTGTWDAYKNL***DAEFRHDSGYEV HHQKLVFFAEDVGSNKGAIIGLMVGGVV** | |
|---|---|
| Number of amino acids: | 220 |
| Molecular weight (kDa) | 24.741 |
| Theoretical pI | 9.47 |
| Extinction coefficient ($M^{-1}$ $cm^{-1}$) | 26930 |

#### 3.2.1.2 Over expression and purification

For overexpression, a glycerol stock of T4Lysozyme-Aβ$_{1-40}$ transformed *E. coli* BL21 (DE3) was inoculated in LB media supplemented with ampicillin (100 µg.ml$^{-1}$) and grown overnight at 37°C. The next day, appropriate amount of pre-culture was inoculated in fresh LB/ ampicillin (100 µg.ml$^{-1}$) for an initial $OD_{600}$ of 0.1. Culture was incubated at 37°C until $OD_{600}$ around 0.6, at which point it was subjected to a cold shock at 4°C for 30 minutes (Qing *et al.*, 2004). IPTG at 0.25 mM was then added and cultures incubated at 18°C

overnight. Grown culture was collected by centrifugation (3990 x g, 4ºC, 30 min on a Beckman JLA 8.1000 rotor). Cell pellets were resuspended in lysis buffer (50 mM Tris-HCl pH 7.4, 0.3 M NaCl, 0.2 $mg.ml^{-1}$ lysozyme, 10 $\mu g.ml^{-1}$ DNase, 1 mM $MgCl_2$, 1 mM PMSF and a tablet of Roche cOmplete™ protease inhibitor cocktail) and stored at -20°C. Pellets were thawed and lysed by sonication (macrotip on a Branson Sonifier® 250 200W; Duty 50%, output 5, 3x30 s, with 1 minute interval on ice). The soluble fraction was clarified by centrifugation (35 000 x g, 45 min., 4°C, on a Beckman JA-25.50 rotor) and filtered (0.22 µm filter), imidazole added to a final concentration of 20 mM and finally loaded on a nickel immobilized metal affinity chromatography (IMAC) column (His-Trap™ HP, GE Healthcare, USA), pre-equilibrated with 50 mM Tris-HCl pH 7.4, 0.3 M NaCl, 20 mM imidazole as binding buffer. Elution was performed in a step-mode with elution buffer 50 mM Na-citrate pH 6.0, 0.3 M NaCl, 500 mM imidazole at 6%, 10%, 40%, 60% and 100%. Collected fractions were pooled using 3 kDa Amicon® Ultra-15 centrifugal filter units (Merck, Germany), spun to remove precipitates and loaded onto a Superose 12 10/300 size exclusion chromatography (SEC) column (GE Healthcare, USA), with 50 mM Na-citrate pH 6.0, 0.1 M NaCl as mobile phase. Selected purified fractions were pooled and concentrated with a 3 kDa Amicon® Ultra-4 centrifugal filter unit (Merck, Germany). Concentration was determined by absorbance at 280 nm in a Nanodrop ND-1000 Spectrophotometer (Thermo Fisher Scientific, USA) according to data on Table 3.1. Protein aliquots were flash frozen in liquid nitrogen and stored at -20°C until used.

#### 3.2.1.3 Differential scanning fluorimetry

To evaluate protein stability in a range of pH values and salt concentrations, a thermal shift assay was performed. Conditions are illustrated on Table 3.2. The plate was sealed (BioRad Microseal B Adhesive Sealer) and incubated at room temperature for 30 minutes, followed by addition of SYPRO Orange (Thermo Fisher Scientific, USA) to a final concentration of 2.5x. The plate was then heated from 20 to 80°C in 0.5°C increments on an iCycler iQ5 Multicolor Real-Time PCR Detection System (Bio-Rad, USA). Fluorescence was followed with a Cy3 dye filter and resulting melting curves analyzed with CFX manager software (BioRad, USA). The inflexion point of the melting curve indicates melting temperature.

**Table 3.2.** Conditions tested in differential scanning fluorimetry.

| | pH | | | | | | | | | | | |
|---|---|---|---|---|---|---|---|---|---|---|---|---|
| **Salt** | **4.0** | **4.5** | **5.0** | **5.5** | **6.0** | **6.5** | **7.0** | **7.5** | **8.0** | **8.5** | **9.0** | **9.5** |
| **No Salt** | Na Acetate 200 mM pH 4 | Na Acetate 200 mM pH 4.5 | Na Citrate 200 mM pH 5 | Na Citrate 200 mM pH 5.5 | Na Cacodylate 200 mM pH 6 | Na Cacodylate 200 mM pH 6.5 | Hepes 200 mM pH 7 | Hepes 200 mM pH 7.5 | Tris 200 mM pH 8 | Tris 200 mM pH 8.5 | CHES 200 mM pH 9 | CHES 200 mM pH 9.5 |
| | Acid Citric 200 mM pH 4 | Acid Citric 200 mM pH 4.5 | Acid Citric 200 mM pH 5 | Acid Citric 200 mM pH 5.5 | MES 200 mM pH 6 | Bis-Tris 200 mM pH 6.5 | MOPS 200 mM pH 7 | Bis-Tris Propane 200 mM pH 7.5 | Tricine 200 mM pH 8 | Bicine 200 mM pH 8.5 | Glycine 200 mM pH 9 | CAPSO 200 mM pH 9.5 |
| **200 mM NaCl** | Na Acetate 200 mM pH 4 | Na Acetate 200 mM pH 4.5 | Na Citrate 200 mM pH 5 | Na Citrate 200 mM pH 5.5 | Na Cacodylate 200 mM pH 6 | Na Cacodylate 200 mM pH 6.5 | Hepes 200 mM pH 7 | Hepes 200 mM pH 7.5 | Tris 200 mM pH 8 | Tris 200 mM pH 8.5 | CHES 200 mM pH 9 | CHES 200 mM pH 9.5 |
| | Acid Citric 200 mM pH 4 | Acid Citric 200 mM pH 4.5 | Acid Citric 200 mM pH 5 | Acid Citric 200 mM pH 5.5 | MES 200 mM pH 6 | Bis-Tris 200 mM pH 6.5 | MOPS 200 mM pH 7 | Bis-Tris Propane 200 mM pH 7.5 | Tricine 200 mM pH 8 | Bicine 200 mM pH 8.5 | Glycine 200 mM pH 9 | CAPSO 200 mM pH 9.5 |
| **400 mM NaCl** | Na Acetate 200 mM pH 4 | Na Acetate 200 mM pH 4.5 | Na Citrate 200 mM pH 5 | Na Citrate 200 mM pH 5.5 | Na Cacodylate 200 mM pH 6 | Na Cacodylate 200 mM pH 6.5 | Hepes 200 mM pH 7 | Hepes 200 mM pH 7.5 | Tris 200 mM pH 8 | Tris 200 mM pH 8.5 | CHES 200 mM pH 9 | CHES 200 mM pH 9.5 |
| | Acid Citric 200 mM pH 4 | Acid Citric 200 mM pH 4.5 | Acid Citric 200 mM pH 5 | Acid Citric 200 mM pH 5.5 | MES 200 mM pH 6 | Bis-Tris 200 mM pH 6.5 | MOPS 200 mM pH 7 | Bis-Tris Propane 200 mM pH 7.5 | Tricine 200 mM pH 8 | Bicine 200 mM pH 8.5 | Glycine 200 mM pH 9 | CAPSO 200 mM pH 9.5 |
| **1000 mM NaCl** | Na Acetate 200 mM pH 4 | Na Acetate 200 mM pH 4.5 | Na Citrate 200 mM pH 5 | Na Citrate 200 mM pH 5.5 | Na Cacodylate 200 mM pH 6 | Na Cacodylate 200 mM pH 6.5 | Hepes 200 mM pH 7 | Hepes 200 mM pH 7.5 | Tris 200 mM pH 8 | Tris 200 mM pH 8.5 | CHES 200 mM pH 9 | CHES 200 mM pH 9.5 |
| | Acid Citric 200 mM pH 4 | Acid Citric 200 mM pH 4.5 | Acid Citric 200 mM pH 5 | Acid Citric 200 mM pH 5.5 | MES 200 mM pH 6 | Bis-Tris 200 mM pH 6.5 | MOPS 200 mM pH 7 | Bis-Tris Propane 200 mM pH 7.5 | Tricine 200 mM pH 8 | Bicine 200 mM pH 8.5 | Glycine 200 mM pH 9 | CAPSO 200 mM pH 9.5 |

### 3.2.1.4 Circular dichroism (CD)

CD spectra was recorded in a J-815 spectrometer (Jasco, Japan), at 20°C controlled by a Peltier system. Spectra was recorded using a 1 mm pathlength quartz cell (Hellma Analytics, Germany) from 260 to 190 nm, at 50 nm.min$^{-1}$, D.I.T. of 2 s, data-pitch 0.2 nm and 16 accumulations per measurement. Spectra was smoothed using the Savitzky–Golay algorithm and corrected for the blank sample. CD data was converted to molar ellipticity using:

$$\Theta\ (deg.cm2.dmol-1)\ = \frac{mdeg \times 106}{l\ (mm) \times protein\ (\mu M) \times peptide\ bonds}$$

### 3.2.1.5 Protein crystallization

T4Lysozyme-A$\beta_{1\text{-}40}$ crystallization was extensively screened at 293 K using commercial sparse-matrix crystallization kits. Drops were set up in 96-well plates using an Oryx4 protein crystallization robot (Douglas Instruments, UK) in 1:1 protein to precipitant ratio. Protein concentration was tested from 6 to 35 mg.ml$^{-1}$. Protein crystals were identified in three distinct conditions: SG-1 Screen 2-31 (30% w/v PEG 1500), SG-1 Screen 2-41 (30% w/v PEG 4000) and JCSG-plus 2-8 (1.0 M ammonium phosphate dibasic, 0.1 M sodium acetate pH 4.5). These were refined to obtain improved crystals. Crystals took about a week to form, were cryo-protected in mother liquor supplemented with glycerol (gradient up to 20% for

JCSG-plus 2-8) or by increasing precipitant concentration (for SG-1 Screen 2-31 and SG-1 Screen 2-41) and flash-frozen in liquid nitrogen.

#### 3.2.1.6 X-Ray diffraction data collection, processing and refinement

High-resolution X-Ray diffraction data was collected from cryo-cooled single crystals (100 K) on a PILATUS 6M detector (Dectris, Switzerland) at synchrotron beamline BL13 XALOC (ALBA, Spain)(Juanhuix *et al.*, 2014) and on EIGER X 16/9M detectors (Dectris, Switzerland) at the PROXIMA-1 and PROXIMA-2A beamlines of the French National Synchrotron Source (SOLEIL, France)(Coati *et al.*, 2017). Images were processed using standard software packages (Bailey, 1994; Kabsch, 2010). For data indexed to the $P2_12_12_1$ space group, phases were generated by molecular replacement with Phaser MR using a manually prepared model starting from T4 Lysozyme PDB entry 3RUN (Economou *et al.*, 2012; McCoy *et al.*, 2007). For data indexed to the $P4_32_12$ space group, a combination of the CCP4i online pipeline MoRDa and ARP/wARP was used (Chojnowski *et al.*, 2020; E. Krissinel *et al.*, 2018; Vagin *et al.*, 2015). The final models were obtained after refinement and manual model building with Refmac/PHENIX and Coot, respectively (Adams *et al.*, 2010; Emsley *et al.*, 2010; Murshudov *et al.*, 1997). Protein structure figures were generated with PyMol (Schrodinger, 2015). A summary of T4Lysozyme-A$\beta_{1\text{-}40}$ X-ray diffraction data collection and refinement statistics is presented on Table 3.3.

### 3.2.2 Results and discussion

After iterative expression and purification optimization, the T4 Lysozyme-A$\beta_{1\text{-}40}$ fusion construct was obtained. Before crystallization studies, a brief biophysical characterization was performed. First, circular dichroism spectroscopy disclosed that the sample retains secondary structure conformation in solution (Figure 3.1A). In addition, crystallization likelihood was assayed by differential scanning fluorimetry (Figure 3.1B), testing a range of pH and salt concentrations (see Table 3.2). Accordingly, several of the conditions tested resulted in a melting temperature ($T_m$) above 318K (44.85˚C). This threshold was empirically determined to translate in a crystallization success rate of 49% (Dupeux *et al.*, 2011). Together with the sigmoidal profile of the melting curve (Figure 3.4B, left), these results suggest that the T4 Lysozyme-A$\beta_{1\text{-}40}$ was likely to crystallize (Dupeux *et al.*, 2011).

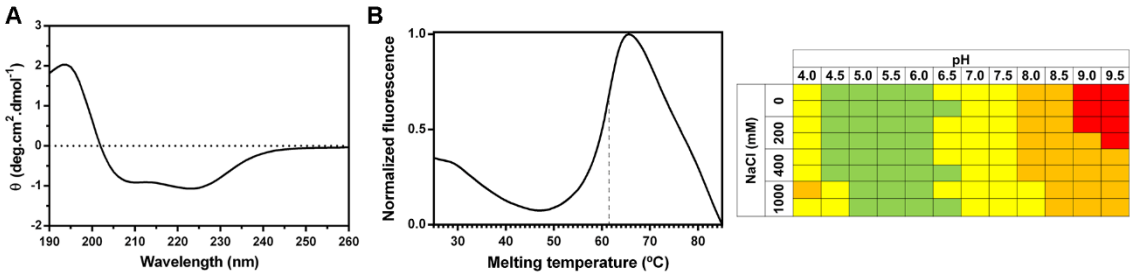


**Figure 3.1.** Biophysical characterization of T4 Lysozyme-Aβ$_{1-40}$. (A) Circular dichroism spectroscopy shows that the fusion construct possesses secondary structure features (*i.e.,* it is not a random, disordered sample). (B) Determination of melting temperature by variation of buffer pH/salt concentration by differential scanning fluorimetry. (left) Representative thermal denaturation curve, with melting temperature calculated at the inflection point indicated by dashed line; (right) color representation of melting temperatures for conditions tested (see Table 3.2): <50 ˚C (red), 50-54˚C (orange), 55-60˚C (yellow) and >60˚C (green).

According to the obtained $T_m$ values, crystallization experiments were made at 293K (Dupeux *et al.*, 2011). After an exhaustive screening, in which several crystals that appeared were later determined by X-Ray diffraction to be salt crystals, good diffracting protein crystals appeared in three conditions: the closely related SG-1 Screen 2-31 and SG-1 Screen 2-41, and JCSG-plus 2-8. These were successfully optimized *in lab*. Out of a total of 72 collected and analyzed T4 Lysozyme-Aβ$_{1-40}$ crystals, diffraction data was collected and processed from 46. Despite the number of tested crystals, only a few showed electron densities attributable to Aβ (data collection, processing and refinement statistics can be found on Table 3.3).

**Table 3.3.** T4 Lysozyme-Aβ$_{1-40}$ X-Ray diffraction data collection, processing and refinement statistics[a].

| **Collection and processing** | | | | | |
|---|---|---|---|---|---|
| Dataset ID | Dataset 1 | Dataset 2 | Dataset 3 | Dataset 4 | Dataset 5 |
| Cryo loop code | B8X3_ba3382 | B8X5_ad9380 | B8X6 ag3340 | B8X8 ag3333 | ag3088 |
| Visible Aβ residues | Aβ$_{1-10}$ | Aβ$_{1-8}$ | Aβ$_{1-5}$ + Aβ$_{1-9}$ | Aβ$_{1-17}$ | Unassigned density only |
| Synchrotron radiation facility | ALBA | ALBA | ALBA | ALBA | SOLEIL |
| Beamline | XALOC | XALOC | XALOC | XALOC | PROXIMA-1 |
| Detector | PILATUS 6M | PILATUS 6M | PILATUS 6M | PILATUS 6M | Dectris Eiger 16M |
| Wavelength (Å) | 0.9793 | 0.9793 | 0.9793 | 0.9793 | 0.9786 |
| Frames | 1800 | 1800 | 1200 | 1400 | 3600 |
| Rotation (°) | 0.1 | 0.1 | 0.2 | 0.15 | 1.0 |
| Space Group | P $2_12_12_1$ | P $2_12_12_1$ | P $2_12_12_1$ | P $2_12_12_1$ | P $4_32_12$ |
| Unit-cell parameters (Å) | | | | | |
| *a* | 38.811 | 38.199 | 38.691 | 37.534 | 83.315 |
| *b* | 55.585 | 56.510 | 55.930 | 55.879 | 83.315 |
| *c* | 167.664 | 160.325 | 168.023 | 158.543 | 107.348 |
| α, β, γ (°) | 90, 90, 90 | 90, 90, 90 | 90, 90, 90 | 90, 90, 90 | 90, 90, 90 |
| Resolution range (Å) | 46.33 - 1.60 (1.657 - 1.60) | 46.19 - 1.55 (1.605 - 1.55) | 42.01 - 1.60 (1.657 - 1.60) | 79.27 - 1.80 (1.864 - 1.80) | 41.66 - 1.90 (1.968 - 1.90) |
| Observed reflections | 299421 (15295) | 301460 (8470) | 395772 (20196) | 235281 (13370) | 809840 (120405) |
| No. of unique reflections | 48372 (2394) | 50420 (2039) | 48033 (2403) | 31916 (1825) | 30506 (4367) |
| Completeness (%) | 98.8 (100) | 97.9 (81.1) | 97.5 (100) | 100 (100) | 100 (100) |
| Multiplicity | 6.2 (6.4) | 6.0 (4.2) | 8.2 (8.4) | 7.4 (7.3) | 26.5 (27.6) |
| <I/σ(I)> | 11.6 (2.2) | 13.6 (1.4) | 12.7 (1.1) | 13.8 (3.4) | 25.5 (4.5) |
| Half-set correlation $CC_{1/2}$ | 0.996 (0.900) | 0.998 (0.557) | 0.998 (0.502) | 0.997 (0.837) | 1.000 (0.973) |
| $R_{merge}$[b] | 0.070 (0.478) | 0.068 (0.714) | 0.080 (1.575) | 0.088 (0.646) | 0.084 (0.777) |
| $R_{meas}$[c] | 0.084 (0.570) | 0.081 (0.886) | 0.092 (1.796) | 0.102 (0.754) | 0.086 (0.792) |
| $R_{p.i.m.}$[d] | 0.045 (0.307) | 0.044 (0.516) | 0.044 (0.853) | 0.050 (0.385) | 0.017 (0.150) |
| **Refinement** | | | | | |
| $R_{work}$(%) | 0.2235 (0.2781) | 0.2061 (0.3131) | 0.2110 (0.3103) | 0.2003 (0.2632) | 0.2269 (0.2960) |
| $R_{free}$(%) | 0.2502 (0.3248) | 0.2231 (0.3275) | 0.2340 (0.3466) | 0.2414 (0.3166) | 0.2532 (0.3836) |
| RMSD for bonds (Å) | 0.006 | 0.007 | 0.008 | 0.007 | 0.007 |
| RMSD for angles (°) | 0.82 | 1.05 | 1.21 | 0.92 | 0.87 |
| Ramachandran plot statistics (%) | | | | | |
| Favoured regions | 96.54 | 96.93 | 97.72 | 97.16 | 98.77 |
| Allowed regions | 3.17 | 2.23 | 2.28 | 2.84 | 1.23 |
| Outliers | 0.29 | 0.84 | 0.00 | 0.00 | 0.00 |
| Rotamer outliers (%) | 0.34 | 0.33 | 0.66 | 0.33 | 0.75 |
| B-factor (Å$^2$) | | | | | |
| Average | 37.47 | 26.24 | 36.77 | 30.97 | 32.66 |
| Macromolecules | 37.49 | 25.60 | 36.61 | 30.72 | 32.05 |
| Solvent | 37.15 | 32.05 | 39.23 | 34.82 | 39.53 |

[a]Statistics for the highest-resolution shell are shown in parentheses

[b]$Rmerge$ = ΣΣ|$Ii(hkl)$ − ⟨$Ihkl$⟩| $i\ hkl$ ΣΣ$Ii(hkl)i\ hkl$⁄, where $Ii(hkl)$ is the observed intensity and ⟨$Ihkl$⟩ is the average intensity of multiple observations of symmetry-related reflections.

[c]$Rmeas$ = Σ √ $n\ n$−1 $hkl$ Σ |$Ii(hkl)$ − ⟨$Ihkl$⟩| $ni$=1 ΣΣ$Ii(hkl)i\ hkl$⁄, where $Ii(hkl)$ is the observed intensity and ⟨$Ihkl$⟩ is the average intensity of multiple observations of symmetry-related reflections.

[d]$Rp.i.m.$ = Σ √ 1 $n$−1 Σ |$Ii(hkl)$ − ⟨$Ihkl$⟩| $ni$=1 $hkl$ ΣΣ$Ii(hkl)i\ hkl$⁄, where $Ii(hkl)$ is the observed intensity and ⟨$Ihkl$⟩ is the average intensity of multiple observations of symmetry-related reflections

Most of the datasets were obtained from condition SG-1 Screen 2-31 (30% w/v PEG 1500). Initial image processing was ambiguous about the space group, indicating orthorhombic P222 and related ones, such as $P222_1$, $P2_12_12$ and $P2_12_12_1$. To tackle this issue, space group was determined using XDS package without biasing unit cell parameters (Kabsch, 2010), settling with $P2_12_12_1$. In addition to the $P2_12_12_1$ data sets, crystals grown with crystallization condition JCSG-plus 2-8 indexed to space group $P4_12_12$. This dataset, initially processed by the SOLEIL automatic processing pipeline (Coati et al., 2017), was solved using the MORDA pipeline (Vagin et al., 2015), and, after addressing enantiomorphic ambiguity, the space group $P4_32_12$ was assigned. Both space groups encompass an asymmetric unit with two molecules (Figure 3.2). Confirming information extracted from the elution profile of the protein in a size-exclusion chromatography (data not shown), PISA analysis indicates that the dimer is a crystallographic occurence (*i.e.* T4 Lysozyme-$A\beta_{1-40}$ does not complexate in solution) (Evgeny Krissinel *et al.*, 2007), with contacts exclusively between lysozyme chains' amino acids. In terms of crystal arrangement, for the $P2_12_12_1$ data, the His-tag/thrombin cleavage site at the N-terminal end (of chain A) and Aβ at the C-terminal end (of chain B) are important to establish the network. Regarding $P4_32_12$ data, no electron density was found for His-tag/thrombin cleavage site or at the C-terminal of the construct beyond T4 Lysozyme residues.

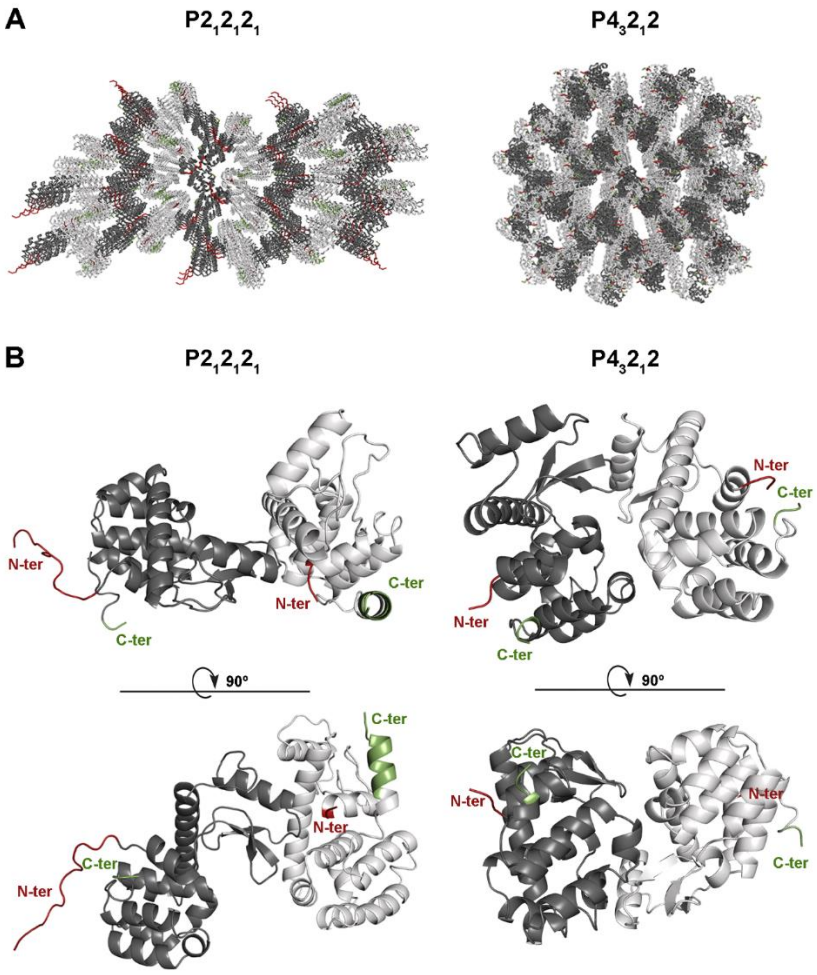


**Figure 3.2.** Crystal packing (A) and three-dimensional structure (B) of T4 Lysozyme-$A\beta_{1-40}$ fusion-protein, obtained in two different crystallization conditions and indexed to two distinct space groups ($P2_12_12_1$ data from Dataset 1 crystallized in 30% w/v PEG 1500 and $P4_32_12$ data from Dataset 5 crystallized in 1.0 M ammonium phosphate dibasic, 0.1 M sodium acetate pH 4.5; see Table 3.3). Legend: crystal packing (A) in ribbon representation; asymmetric unit (B) in cartoon representation; T4 Lysozyme chains in shades of grey; fusion-protein N-terminal end in red and C-terminal end in green.

Aβ residues only appear in $P2_12_12_1$ data and almost entirely on chain B of the asymmetric unit (Figure 3.3A-D), with an exception for Dataset 3, where the first five residues of the peptide are present at the C-terminal of chain A (Figure 3.3C, left). Due to the constrained environment, they adopt a helical conformation. Dataset 4 presents the longest fitted Aβ segment ($A\beta_{1-17}$; Figure 3.3D). Here, both $A\beta_{1-9}$ and $A\beta_{12-17}$ are well fitted to the $2F_oF_c$ map at 1.0 σ. Oddly, density for $A\beta_{9-11}$ could not be found. For this dataset, unit cell dimensions are slightly different when compared to Datasets 1 through 3, with shorter dimensions in *a* and *c* (Table 3.3), which may be explained by a somewhat more rigid arrangement conferred by interactions of the extended Aβ segment (Figure 3.4B). The overall absence of complete or longer Aβ electron densities may be explained by the crystal

arrangement in the $P2_12_12_1$ space group, in which the C-terminal of both chains in the asymmetric unit face relatively loosely packed regions, leading into the pores observed in Figure 3.2A.

Regarding the $P4_32_12$ data, a significant electron density is present (Figure 3.3E). This density was subjected to extensive attempts of manual model building, including the implementation of Phenix map modification tools, such as RESOLVE (Liebschner *et al.*, 2019). Poly-alanine tracing hints that about 12 residues may fit the density. Model building attempts included fitting single Aβ segments (*e.g.* $Aβ_{15-28}$ and $Aβ_{27-40}$) or interpreting the map as two Aβ chains from different molecules (*e.g.* $Aβ_{28-32}$ and $Aβ_{21-28}$). However, side-chain fitting could not be unambiguously performed, with apparent symmetry related residues within the found density. As such, the data could not be solved (Figure 3.3E).

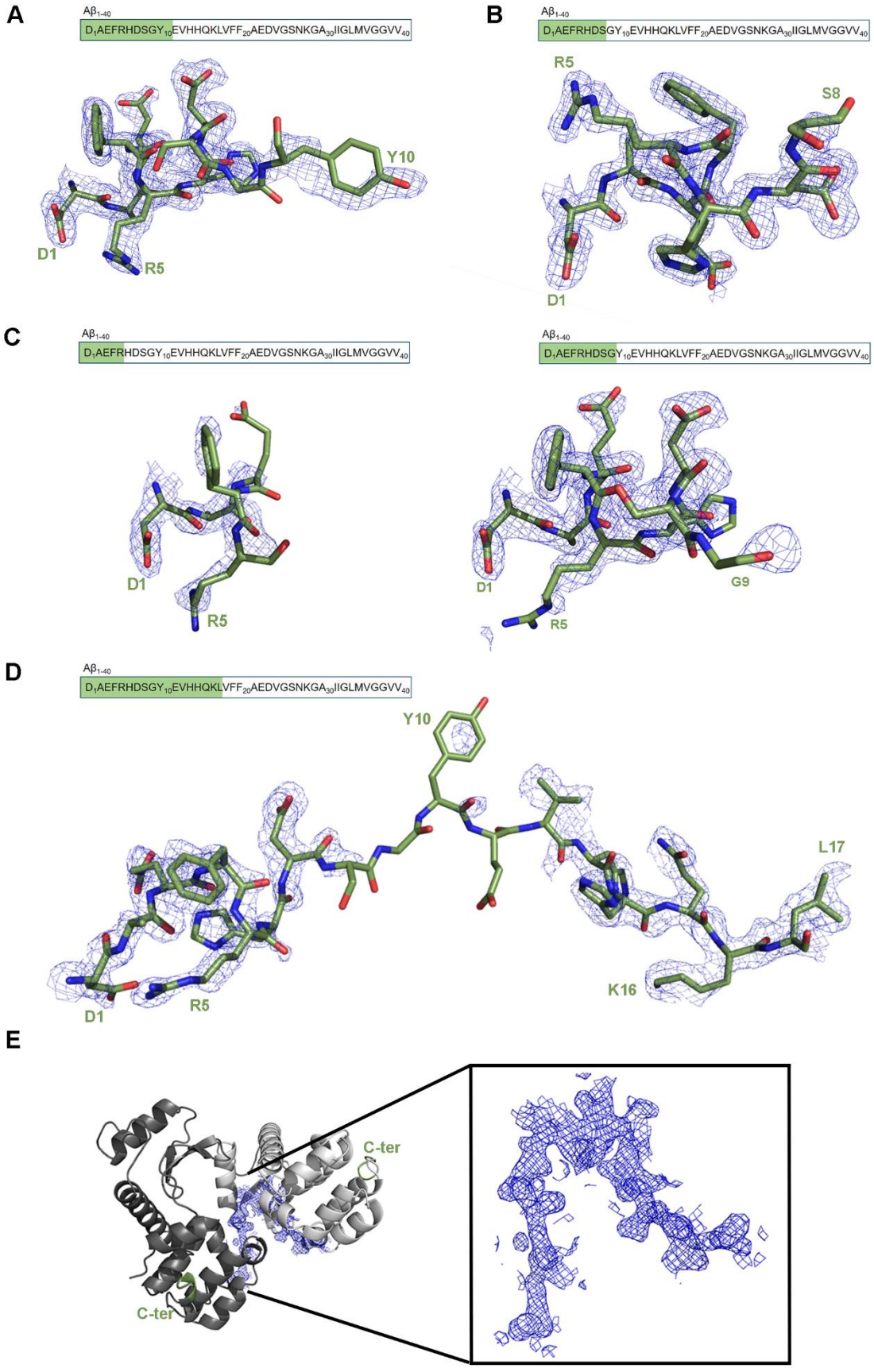


**Figure 3.3.** X-Ray diffraction data of isolated amyloid-β peptide residues from datasets listed on Table 3.3 (contour for $2F_oF_c$ maps at 1.0 σ). For clarity purposes, residue numbering follows $Aβ_{1-40}$

nomenclature instead of the fusion-protein construct numbering and displayed residues are highlighted in green in the full peptide sequence. A – Dataset 1, $A\beta_{1-10}$ (DAEFRHDSGY). B – Dataset 2, $A\beta_{1-8}$ (DAEFRHDS). C – Dataset 3, $A\beta_{1-5}$ (DAEFR, left) and $A\beta_{1-9}$ (DAEFRHDSG, right). D – Dataset 4, $A\beta_{1-17}$ (DAEFRHDSGYEVHHQKL), with $A\beta_{9-11}$ fitted but assigned zero occupancy. E – Dataset 5, a U-shaped electron density corresponding to around twelve residues (as seen by poly-alanine tracing) was found between the two molecules of the asymmetric unit. Despite extensive attempts, no Aβ residues side-chains could be fitted. Legend: Aβ residues in stick representation, with oxygen atoms in red, nitrogen atoms in blue and carbon atoms in green; lysozyme chains in grey cartoon representation, with C-terminal portion highlighted in green.

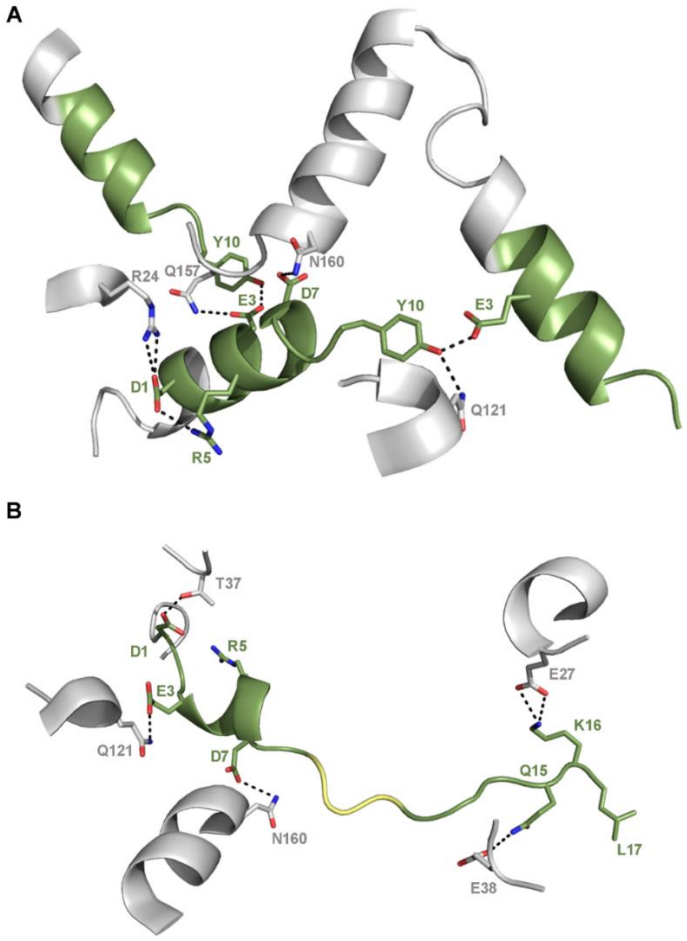


**Figure 3.4.** Close-up view of Aβ residues' interactions, for Dataset 1 $A\beta_{1-10}$ (A) and Dataset 4 ($A\beta_{1-17}$). Lysozyme residues backbone in gray and Aβ residues in green, oxygen atoms in red and nitrogen atoms in blue. Side chains of residues involved in polar bonds (dashed lines) are represented as sticks and labeled (lysozyme residues according to T4 Lysozyme-$A\beta_{1-40}$ numbering and Aβ to $A\beta_{1-40}$ sequence numbering). Residues attributed zero occupancy (B) are displayed in yellow.

## 3.3 T4 Lysozyme-Aβ$_{17-40}$

### 3.3.1 Materials and methods

#### 3.3.1.1 Plasmid design

T4Lysozyme-Aβ$_{17-40}$ fusion protein construct was designed as previously described for T4Lysozyme-Aβ$_{1-40}$. Aminoacid sequence and overall information, computed with Expasy ProtParam (Wilkins *et al.*, 1999), is presented on Table 3.4.

**Table 3.4.** Amino acid sequence of T4Lysozyme-Aβ$_{17-40}$ fusion protein construct and general construct information. Legend: His-tag and thrombin cleavage site underlined; T4 Lysozyme wt* T26Q in italic; Aβ$_{17-40}$ in bold.

| HHHHHHSSGLVPRGSH*MNIFEMLRIDEGLRLKIYKDTEGYYQIGIGHLLTKSPSLNAAKSELDKAI GRNTNGVITKDEAEKLFNQDVDAAVRGILRNAKLKPVYDSLDAVRRAALINMVFQMGETGVAGF TNSLRMLQQKRWDEAAVNLAKSRWYNQTPNRAKRVITTFRTGTWDAYKNL***LVFFAEDVGSNK GAIIGLMVGGVV*** | |
|---|---|
| Number of amino acids | 204 |
| Molecular weight (kDa) | 22.804 |
| Theoretical pI | 9.72 |
| Extinction coefficient ( $M^{-1}$ $cm^{-1}$) | 25440 |

#### 3.3.1.2 Over expression and purification

For overexpression, a glycerol stock of T4Lysozyme-Aβ$_{17-40}$ transformed *E. coli* Nico21 (DE3) was inoculated in LB media supplemented with ampicillin (100 µg.ml$^{-1}$) and 1% glucose and grown overnight at 37°C. The next day, appropriate amount of pre-culture was inoculated in fresh LB/ ampicillin (100 µg.ml$^{-1}$)/ 1% glucose for an initial $OD_{600}$ of 0.1. Culture was incubated at 37°C until $OD_{600}$ around 0.6, at which point it was subjected to a cold shock at 4°C for 30 minutes (Qing *et al.*, 2004), followed by adding absolute ethanol to a final concentration of 2%. Protein expression was induced with IPTG to a final concentration of 0.2 mM, with cultures incubated overnight at 15°C. Grown culture was collected by centrifugation (3990 x g, 4ºC, 30 min on a Beckman JLA 8.1000 rotor). Cell pellets were subjected to an osmotic shock protocol to remove *E. coli* periplasmic fraction and reduce downstream purification contaminants (Magnusdottir *et al.*, 2009) and subsequently resuspended in lysis buffer (50 mM Tris-HCl pH 7.4, 0.5 M NaCl, 0.2 mg.ml$^{-1}$ lysozyme, one cOmplete Protease inhibitor tablet), flash frozen in liquid nitrogen and stored at -20°C. Thawed cells were lysed by sonication (macrotip on a Branson Sonifier® 250 200W; Duty 50%, output 5, 4x20 s, with 1 minute interval on ice). The soluble fraction was clarified by centrifugation (35 000 x g, 45 min., 4°C, on a Beckman JA-25.50 rotor), imidazole added to a final concentration of 40 mM and loaded on a nickel IMAC column (His-Trap$^{TM}$ HP, GE Healthcare, USA), pre-equilibrated with 20 mM Sodium phosphate pH 7.4, 0.5 M NaCl, 40

mM imidazole as binding buffer. Elution was performed in a step-mode with elution buffer 20 mM Sodium phosphate pH 7.4; 0.5 M NaCl, 500 mM imidazole at 16% 32% and 100%. Collected fractions were pooled using 3 kDa Amicon® Ultra-15 centrifugal filter units (Merck, Germany), spun to remove precipitates and loaded onto a Superose 12 10/300 size exclusion chromatography (SEC) column (GE Healthcare, USA), with 50 mM Na phosphate pH 7.4, 150 mM NaCl as mobile phase. Selected purified fractions were pooled and concentrated with a 3 kDa Amicon® Ultra-4 centrifugal filter unit (Merck, Germany). Concentration was determined by absorbance at 280 nm in a Nanodrop ND-1000 Spectrophotometer (Thermo Fisher Scientific, USA) using data from Table 3.4. Protein aliquots were flash frozen in liquid nitrogen and stored at -20°C until further use.

#### 3.3.1.3 Differential scanning fluorimetry

*See 3.2.1.3.*

#### 3.3.1.4 Circular dichroism (CD)

*See 3.2.1.4.*

#### 3.3.1.5 Protein crystallization

T4Lysozyme-A$\beta_{17-40}$ crystallization screening was performed by sitting-drop vapor-diffusion with an Oryx4 protein crystallization robot (Douglas Instruments, UK), using commercial sparse-matrix crystallization kits in 1:1 protein to precipitant ratio, in 96-well plates, at 293 K. A single protein crystal growing condition was identified from SG-1 Screen 1-38 (0.1 M sodium citrate pH 5.5, 20 % w/v PEG 3000). Crystals, which took up to a year to form, were cryo-protected in 0.1 M sodium citrate pH 6.0, 20 % w/v PEG 1000, 20% glycerol and flash-frozen in liquid nitrogen.

#### 3.3.1.6 X-Ray diffraction data collection, processing and refinement

High-resolution X-Ray diffraction data was collected from cryo-cooled single crystals (100 K) on a PILATUS 6M detector (Dectris, Switzerland) at synchrotron beamline BL13 XALOC (ALBA, Spain)(Juanhuix *et al.*, 2014) and on EIGER X 9M detector (Dectris, Switzerland) at the PROXIMA-2A beamline of the French National Synchrotron Source (SOLEIL, France)(Coati *et al.*, 2017). Images were processed using standard software

packages (Bailey, 1994; Kabsch, 2010). For phase generation, molecular replacement, model building and refinement, a combination of the CCP4i online pipeline MoRDa and ARP/wARP was employed (Chojnowski *et al.*, 2020; E. Krissinel *et al.*, 2018; Vagin *et al.*, 2015). The model was manually inspected, and final model was obtained after iterative cycles of refinement and manual model building with Refmac/PHENIX and Coot, respectively (Adams *et al.*, 2010; Emsley *et al.*, 2010; Murshudov *et al.*, 1997). Protein structure figures were generated with PyMol (Schrodinger, 2015). A summary of T4Lysozyme-Aβ$_{17-40}$ X-ray diffraction data collection, processing and refinement statistics is presented on Table 3.5.

### 3.3.2 Results and discussion

T4Lysozyme-Aβ$_{17-40}$ plasmid design and protein expression and purification workflows followed an identical strategy to the previously discussed T4Lysozyme-Aβ$_{1-40}$, albeit with some optimization and minor differences (*e.g.,* buffer compositions) to better suit this protein. Eventually, it was obtained as a homogeneous soluble sample. Circular dichroism spectroscopy confirmed the presence of secondary structure in solution (Figure 3.5). In addition, differential scanning fluorimetry hinted that this fusion-protein retains an empirically tested crystallization success rate of 49%, as several conditions present a melting temperature ($T_m$) above 318K (44.85°C) (Dupeux *et al.*, 2011). Nevertheless, thermal-stability wise, T4Lysozyme-Aβ$_{17-40}$ shows less stability when compared to T4Lysozyme-Aβ$_{1-40}$. One may wonder that the lack of the N-terminus in this construct turns the fusion-protein less stable, as reported for the native p3 peptide when compared to Aβ$_{1-40}$ (Kuhn *et al.*, 2020).

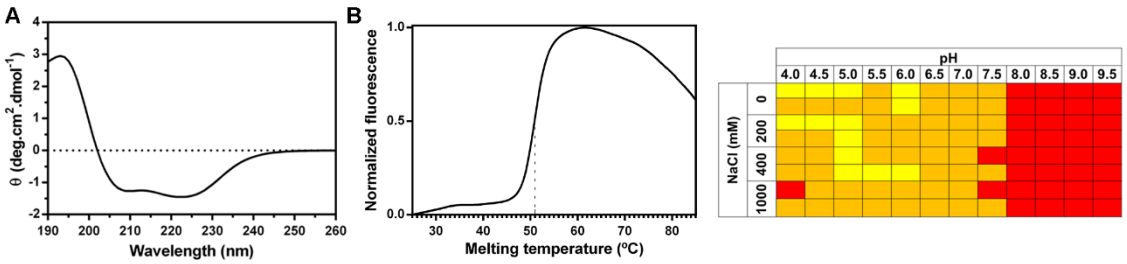


**Figure 3.5.** Biophysical characterization of T4 Lysozyme-Aβ$_{17-40}$. (A) Circular dichroism spectroscopy shows that the fusion construct is correctly folded in solution (*i.e.,* not a random, disordered sample). (B) Determination of melting temperature by variation of buffer pH/salt concentration by differential scanning fluorimetry, with a representative thermal denaturation curve (left; melting temperature calculated at the inflection point indicated by dashed line) and color representation of melting

temperatures for conditions tested (right; see Table 3.2): <50 ˚C (red), 50-54˚C (orange), 55-60˚C (yellow).

Given the DSF results, T4 Lysozyme-$A\beta_{17-40}$ crystallization screening followed the same methodology as the one employed for T4 Lysozyme-$A\beta_{1-40}$. One condition, SG-1 Screen 1-38 (0.1 M sodium citrate pH 5.5, 20 % w/v PEG 3000), indicated a protein X-Ray diffraction electron pattern. Notably, these crystals, took up to a year to form. Data collection, processing and refinement statistics are presented on Table 3.5. It indexed to space group $P3_121$ and the asymmetric unit contains one molecule (Matthews, 1968). Diffraction images were initially processed by the SOLEIL automatic processing pipeline (Coati *et al.*, 2017) and phases were found by molecular replacement using the MORDA pipeline, followed by manual model building and refinement (Adams *et al.*, 2010; Emsley *et al.*, 2010; Vagin *et al.*, 2015). The crystal arrangement shows a porous channel network, to which the C-terminal is facing (Figure 3.6A, B). With this fusion-protein construction, we intended to avoid the flexibility of the N-terminal observed in the T4 Lysozyme-$A\beta_{1-40}$ data. However, there is electron density only assignable to four Aβ residues ($A\beta_{17-20}$, Figure 3.6C). Thus, no relevant peptide structural information could be extracted from this fusion-protein construction.

**Table 3.5.** T4 Lysozyme-Aβ$_{17-40}$ X-Ray diffraction data collection, processing and refinement statistics[a].

| **Collection and processing** | |
|---|---|
| Dataset ID | Dataset 6 |
| Cryo loop code | B2X2 BI1273 |
| Visible Aβ residues | Aβ$_{17-20}$ |
| Synchrotron radiation facility | ALBA |
| Beamline | XALOC |
| Detector | PILATUS 6M |
| Wavelength (Å) | 0.9792 |
| Frames | 1000 |
| Rotation (°) | 0.2 |
| Space Group | $P3_121$ |
| Unit-cell parameters (Å) | |
| *a* | 81.071 |
| *b* | 81.071 |
| *c* | 56.881 |
| α, β, γ (°) | 90, 90, 120 |
| Resolution range (Å) | 44.2 - 2.40 (2.487 - 2.40) |
| Observed reflections | 80308 (9056) |
| No. of unique reflections | 8734 (916) |
| Completeness (%) | 100 (100) |
| Multiplicity | 9.2 (9.9) |
| <I/σ(I)> | 13.1 (4.4) |
| Half-set correlation $CC_{1/2}$ | 0.998 (0.971) |
| $R_{merge}$[b] | 0.110 (0.580) |
| $R_{meas}$[c] | 0.123 (0.646) |
| $R_{p.i.m.}$[d] | 0.055 (0.281) |
| **Refinement** | |
| $R_{work}$(%) | 0.1838 (0.2178) |
| $R_{free}$(%) | 0.2312 (0.3046) |
| RMSD for bonds (Å) | 0.008 |
| RMSD for angles (°) | 0.89 |
| Ramachandran plot statistics (%) | |
| Favoured regions | 96.99 |
| Allowed regions | 3.01 |
| Outliers | 0.00 |
| Rotamer outliers (%) | 1.42 |
| B-factor (Å$^2$) | |
| Average | 48.83 |
| Macromolecules | 48.84 |
| Solvent | 47.87 |

[a]Statistics for the highest-resolution shell are shown in parentheses

[b]$Rmerge$ = ΣΣ|$Ii(hkl)$ − ⟨$Ihkl$⟩| $i\ hkl$ ΣΣ$Ii(hkl)i\ hkl/$, where $Ii(hkl)$ is the observed intensity and ⟨$Ihkl$⟩ is the average intensity of multiple observations of symmetry-related reflections.

[c]$Rmeas$ = Σ √ $n\ n$−1 $hkl$ Σ |$Ii(hkl)$ − ⟨$Ihkl$⟩| $ni$=1 ΣΣ$Ii(hkl)i\ hkl/$, where $Ii(hkl)$ is the observed intensity and ⟨$Ihkl$⟩ is the average intensity of multiple observations of symmetry-related reflections.

[d]$Rp.i.m.$ = Σ √ 1 $n$−1 Σ |$Ii(hkl)$ − ⟨$Ihkl$⟩| $ni$=1 $hkl$ ΣΣ$Ii(hkl)i\ hkl/$, where $Ii(hkl)$ is the observed intensity and ⟨$Ihkl$⟩ is the average intensity of multiple observations of symmetry-related reflections

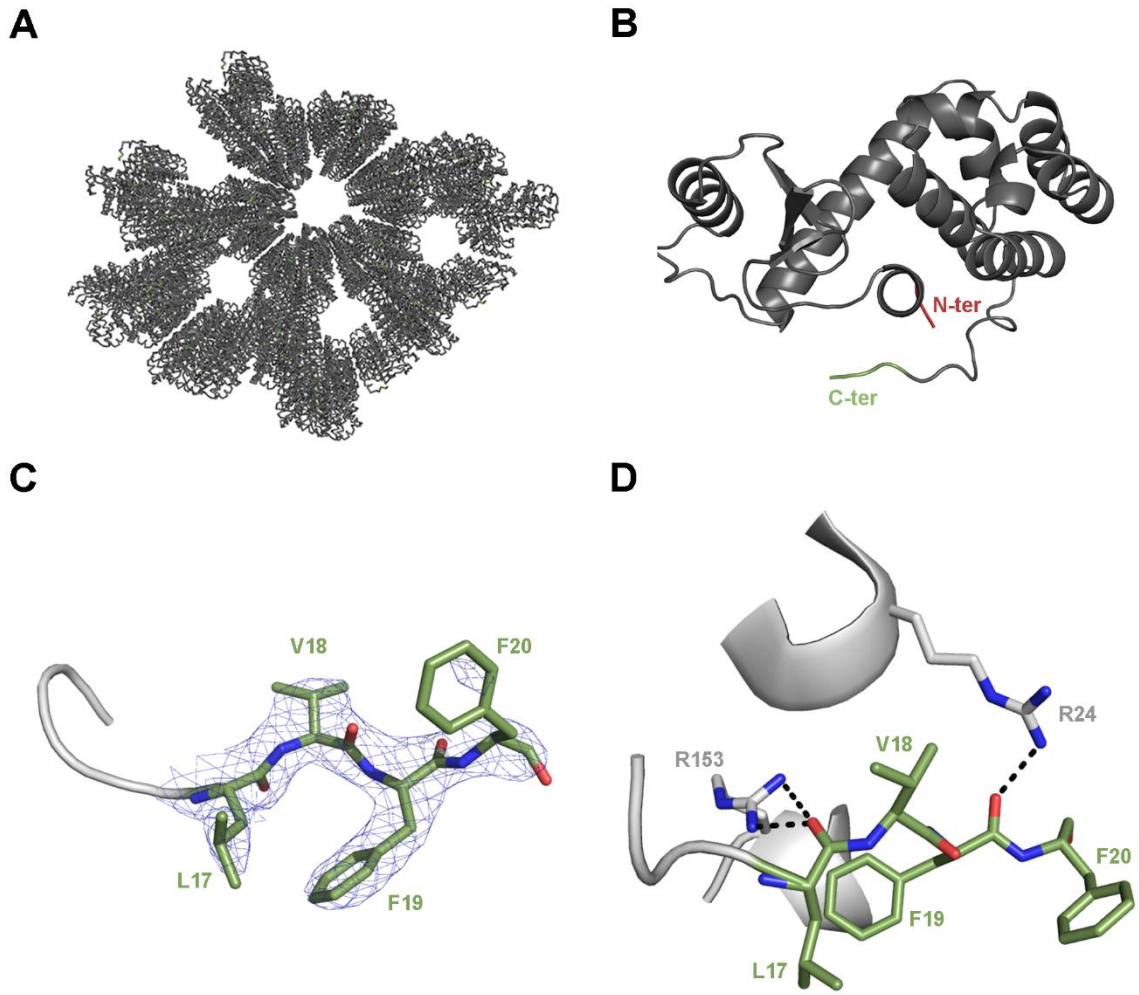


**Figure 3.6.** (A) Crystal packing (grey ribbon representation) of T4 Lysozyme-$A\beta_{17-40}$ fusion-protein crystallized in SG-1 Screen 1-38 (0.1 M sodium citrate pH 5.5, 20 % w/v PEG 3000) and indexed to space group $P3_121$. (B) Three-dimensional structure of T4 Lysozyme-$A\beta_{17-40}$ (cartoon representation in grey, with fusion-protein N-terminal and C-terminal ends highlighted in red and green, respectively). (C) X-Ray diffraction data of isolated amyloid-β peptide residues from dataset 6 (Table 3.5), with contour for $2F_oF_c$ map at 1.0 σ. Residue numbering follows $A\beta_{1-40}$ nomenclature instead of the fusion-protein construct numbering (e.g., L181 from T4 Lysozyme-$A\beta_{17-40}$ corresponds to L17 from $A\beta_{1-40}$). (D) Close-up view of Aβ ($A\beta_{17-20}$) residues' interactions within the crystal packing, for dataset 6 (Table 3.5). Side chains of residues involved in polar contacts (dashed lines) are represented as sticks and labeled (lysozyme residues according to T4 Lysozyme-$A\beta_{1-40}$ numbering and Aβ to $A\beta_{1-40}$ sequence numbering). Legend: Aβ residues in stick representation, with oxygen atoms in red, nitrogen atoms in blue and carbon atoms in green; lysozyme chains in grey cartoon representation, with relevant side-chains as sticks.

## 3.4 PAC3-Aβ$_{1-40}$

### 3.4.1 Materials and methods

#### 3.4.1.1 Plasmid design

PAC3-Aβ$_{1-40}$ fusion protein construct was designed similarly to T4Lysozyme-Aβ$_{1-40}$ and T4Lysozyme-Aβ$_{17-40}$. The nucleotide sequence for proteasome-assembling chaperone 3 (PAC3) was obtained by reverse translation of amino acid sequence from PDB entry 6JPT (Satoh *et al.*, 2019; Stothard, 2000). The final construction, PAC3-Aβ$_{1-40}$, contains, from N to C terminal: histidine-tag, thrombin cleavage site, three alanine spacer, HRV3C cleavage site and PAC3-Aβ$_{1-40}$ chimera. The final plasmid was codon optimized for *E. coli*, synthesized, and purchased from Genscript (USA). Aminoacid sequence and overall information, computed with Expasy ProtParam (Wilkins *et al.*, 1999), is presented on Table 3.6.

**Table 3.6.** Amino acid sequence of PAC3 and PAC3-Aβ$_{1-40}$ fusion protein construct, plus general construct information of the latter. Legend: PAC3 – loop region in bold; removed residues to insert Aβ$_{1-40}$ in underlined bold. PAC3-Aβ$_{1-40}$ fusion protein – His-tag and thrombin cleavage site underlined; triple alanine spacer in italic; HRV3C cleavage site in underlined bold; PAC3 amino acids in regular characters; Aβ$_{1-40}$ in bold.

| **PAC3** | |
|---|---|
| MEDTPLVISKQKTEVVCGVPTQVVCTAFSSHILVVVTQFGKMGTLVSLEP**SSVASD**<u>**VSKP**</u>**V**LTT KVLLGQDEPLIHVFAKNLVAFVSQEAGNRAVLLAVAVKDKSMEGLKALREVIRVCQVW | |
| **PAC3-Aβ$_{1-40}$ fusion protein** | |
| <u>HHHHHHSSGLVPRGSHM</u>*AAA*<u>**LEVLFQGP**</u>EDTPLVISKQKTEVVCGVPTQVVCTAFSSHILVVVT QFGKMGTLVSLEPSSVAS**DAEFRHDSGYEVHHQKLVFFAEDVGSNKGAIIGLMVGGVV**LTTKV LLGQDEPLIHVFAKNLVAFVSQEAGNRAVLLAVAVKDKSMEGLKALREVIRVCQVW | |
| Number of amino acids | 183 |
| Molecular weight (kDa) | 19.688 |
| Theoretical pI | 6.66 |
| Ext. Coefficient ($M^{-1}$ $cm^{-1}$) | 7115 (Cys form cystines)/ 6990 (Cys reduced) |

#### 3.4.1.2 Small-scale protein expression tests

Initial PAC3-Aβ$_{1-40}$ expression tests were performed in small-scale 3-ml cultures of *E. coli* Nico21(DE3) and using the same conditions as reported for T4 Lysozyme-Aβ$_{17-40}$ (see section 3.3.1.2). Then, they were further expanded by searching the total fraction instead of solely the soluble fraction, using *E. coli* strains Rosetta (DE3), BL21(DE3), BL21(DE3) pLysS, Artic Express (DE3) and SoluBL21, in 100 ml cultures. For the Rosetta (DE3) tests, the following variables were tested: IPTG concentration at 0, 0.25 and 0.5 mM; induction temperature of 18 or 30°C; and induction time of 1h, 2h, 3h, 4h or 5h (30°C) or over-night growth (18°C). PAC3-Aβ$_{1-40}$ transformed *E. coli* Rosetta (DE3) glycerol stock was inoculated in LB media supplemented with ampicillin (100 μg.$ml^{-1}$) and grown overnight at 30°C. The

next day, appropriate volume of pre-culture was used to achieve an initial $OD_{600}$ of 0.1. Cultures were grown at 30°C until reaching an $OD_{600}$ around 0.6. Then, IPTG was added to induce expression and temperature was set to testing value. At each endpoint, cells were collected and stored frozen at -20°C. Afterwards, cells were lysed in lysis buffer (50 mM Tris-HCl pH 8.0; 0.3 M NaCl) by sonication (microtip at the following settings: output 3, duty cycle 30% for 2x10 s on a Branson Sonifier® 250 200W). For the BL21(DE3), BL21(DE3) pLysS, Artic Express(DE3) and SoluBL21 tests, the following variables were tested: IPTG concentration at 0 and 0.1 mM; induction temperature of 10°C (Artic Express) or 15 and 30°C (BL21, BL21pLysS and SoluBL21); and induction time of 1h and 2h (30°C) or over-night growth (10°C and 18°C; in these cases, a cold shock step was also included (Qing *et al.*, 2004)). PAC3-$A\beta_{1-40}$ transformed *E. coli* strains glycerol stocks were inoculated in LB media supplemented with ampicillin (100 $\mu g.ml^{-1}$) and glucose (1%, except for BL21(DE3) pLysS) and grown overnight at 30°C. The next day, appropriate volume of pre-culture was used to achieve an initial $OD_{600}$ of 0.1. Cultures were grown at 30°C until reaching an $OD_{600}$ around 0.6. Then, absolute ethanol to a final concentration of 2% was added, followed by IPTG to induce expression, and temperature was set to testing value. At each endpoint, cells were collected and stored frozen at -20°C. Afterwards, cells were lysed in lysis buffer (50 mM Tris-HCl pH 8.0; 0.3 M NaCl; 0.2 $mg.ml^{-1}$ lysozyme) by sonication (microtip at the following settings: output 3, duty cycle 30% for 2x10s on a Branson Sonifier® 250 200W). Results were assessed by combined SDS-PAGE/Western Blot analysis of the total (*i.e.,* soluble and insoluble fraction) and soluble fractions, with the amount loaded per well normalized by each culture's optical density for comparison purposes, according to the formula:

$$Volume\ to\ load\ (\mu l) = \frac{270}{\left(\frac{Volume\ bacterial\ cells}{Volume\ buffer}\right) \times OD600}$$

### 3.4.1.3 Purification from *E. coli* inclusion bodies

To extract PAC3-$A\beta_{1-40}$ from the insoluble fraction, a purification protocol from inclusion bodies was tested, based on "GE Healthcare Handbook Purifying Challenging Proteins Principles and Methods" and application note 18-1134-37 AC "Rapid and efficient purification and refolding of a (histidine)6-tagged recombinant protein produced in E. coli as inclusion bodies" (Cytiva Life Sciences, USA). Thawed cell pellet was resuspended in resuspension buffer (20 mM Tris-HCl pH 8.0) and lysed by sonication (macrotip on a Branson Sonifier® 250 200W; Duty 50%, output 5, 4x10 s, with 1-minute interval on ice). Total lysate was centrifuged at 10 000 x g for 10 min., 4°C, followed by resuspension of the

pellet (insoluble fraction) in cold isolation buffer (20 mM Tris-HCl pH 8.0, 2M Urea, 0.5 M NaCl; 2% Triton-X 100). The resuspension was re-sonicated, centrifuged and pellet resuspended in cold isolation buffer twice. At this point, pellet was resuspended in washing buffer (20 mM Tris-HCl pH 8.0, 0.5 M NaCl, 2% Triton-X 100), centrifuged and flash-frozen in liquid nitrogen for storage. Thawed washed pellet was solubilized by incubating with agitation at room temperature for 1h in binding buffer (20 mM Tris-HCl pH 8.0, 0.5 M NaCl, 6M Urea, 10 mM imidazole, 1 mM β-mercaptoethanol). Extract was loaded on a nickel immobilized metal affinity chromatography column (His-Trap™ HP, GE Healthcare, USA), and refolding performed *on-column* with a gradient against refolding buffer (20 mM Tris-HCl pH 8.0, 0.5 M NaCl, 10 mM imidazole, 1 mM β-mercaptoethanol). Alternatively, refolding was tested by serial dialysis against decreasing concentrations of urea, outside the His-Trap™ HP column. Finally, elution was performed with a gradient of elution buffer (20 mM Tris-HCl pH 8.0, 0.5 M NaCl, 500 mM imidazole, 1 mM β-mercaptoethanol). Throughout different attempts at inclusion body purification, several parameters were tested and varied, such as composition of buffers (*e.g.,* imidazole concentrations; Triton-X 100 concentrations), solubilization time and extract loading time and temperature on His-Trap™ HP column. Fractions of interest were pooled using 3 kDa Amicon® Ultra-15 centrifugal filter units (Merck, Germany) and applied to a Superose 12 10/300 size exclusion chromatography (SEC) column (GE Healthcare, USA), with 50 mM Na-Phosphate pH 7.4; 150 mM NaCl as mobile phase.

#### 3.4.1.4 SDS-PAGE and western blot

SDS-PAGE was performed based on (Laemmli, 1970). NZYColour Protein Marker II (NZYTech, Portugal) was used as molecular weight ladder and gels were stained by using PageBlue™ Protein Staining Solution (Thermo Fisher Scientific, USA). Gel images were acquired with a GS-800 calibrated imaging densitometer (Bio-Rad, USA). For western blot analysis, samples were separated by SDS-PAGE as described above and then transferred to a polyvinylidine difluoride membrane (Amersham Hybond P 0.45; GE Healthcare, USA) in a semi-dry system (primary antibody, in a 1:2000 dilution, Invitrogen Anti-6x-HisTag, eBiosciences; secondary antibody, in a 1:5000 dilution; Sigma Anti-Mouse IgG H+L x-adsorbed HRP SAB3701073).

### 3.4.2 Results and discussion

Small-scale protein expression screens using *E. coli* strain NiCo21(DE3), designed to decrease contamination of IMAC fractions with *E. coli* proteins, led to no protein expression detected in the soluble fraction. Alternatively, other *E. coli* strains were tested, both in the total and soluble fractions. The strains were: ArcticExpress (DE3), with low-growth temperature and chaperonins to promote recombinant protein folding and solubility; BL21(DE3), for high protein expression; Solu21, based on BL21 to improve soluble mammalian protein expression; and, BL21(DE3) pLysS, to increase stability of target protein and eliminate background expression (*i.e.* basal expression without IPTG added and, therefore, no need to add 1% glucose to the growth media). Overall, PAC3-A$\beta_{1-40}$ was found to be expressed into inclusion bodies, as indicated by gel bands in the total fractions and absent in the soluble fractions, whose identity was confirmed by western blot using an antibody against His-tag of the construct (Figure 3.7). Nevertheless, for the case of expression using *E. coli* Arctic Express, a faint degree of expression to the soluble fraction was detected (Figure 3.7).

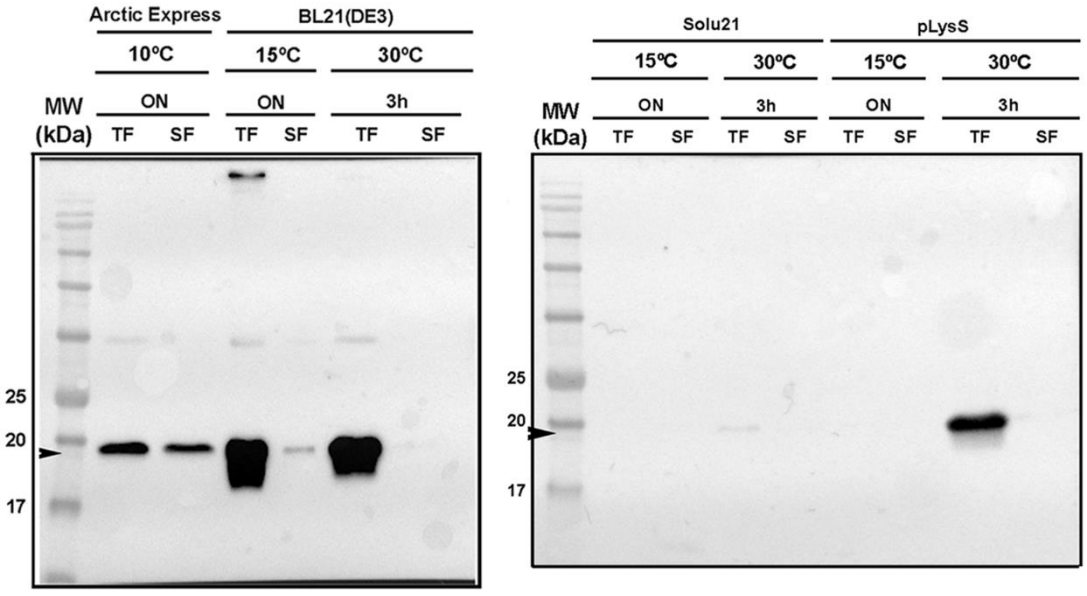


**Figure 3.7.** PAC3-A$\beta_{1-40}$ small-scale protein expression screens, analyzed by western blot. The protein has an expected molecular weight of 19.7 kDa (indicated by black arrow). Western blot analysis of expression in *E. coli* strains ArcticExpress (DE3), BL21 (DE3), Solu21 and BL21 (DE3) pLysS. Legend: MW – molecular weight; TF – total fraction; SF – soluble fraction; ON – overnight.

Scaled-up expression using *E. coli* Arctic Express was performed and iterative attempts made to purify protein from the soluble fraction. However, no soluble protein was obtained. Facing this prospect, purification from inclusion bodies was pursued, with several iterations

of a protocol initially designed from the sources listed in section 3.4.1.3. Inclusion bodies were subjected to two rounds of isolation and washing, prior to solubilization of the target protein. Surprisingly, PAC3-A$\beta_{1-40}$ was found to be solubilized at the first isolation step, as indicated by electrophoretic analysis of the supernatant from this step (Figure 3.8). Here, buffer contained urea and a significant amount of Triton X-100. Because of this, optimization trials were performed to achieve a solubilization protocol compatible with IMAC, as protein refolding was attempted *on-column*. Alternatively, the "classical" inclusion body protein refolding protocol using serial dilutions was also tested. However, IMAC elution of solubilized protein extracts yielded no appreciable protein amounts. To sum up, despite the exhaustive attempts performed, both from an expression and purification point of view, soluble amounts of PAC3-A$\beta_{1-40}$ could not be obtained and, thus, no crystallization could be attempted.

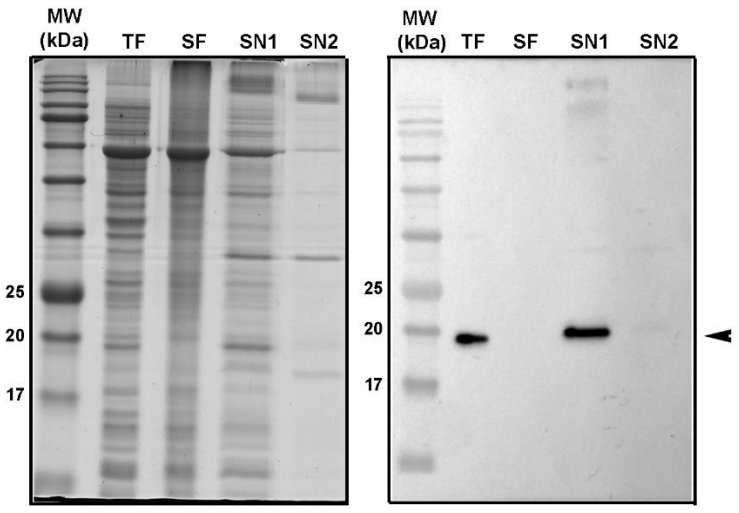


**Figure 3.8.** Combined Page Blue stained SDS-PAGE (left) and western blot (right) analysis of PAC3-A$\beta_{1-40}$, which was expressed to the insoluble fraction of *E. coli* Arctic Express (DE3). PAC3-A$\beta_{1-40}$ has an expected molecular weight of 19.7 kDa (indicated by black arrows). Legend: MW – molecular weight; TF – total fraction; SF – soluble fraction; SN1 – supernatant of first isolation step; SN2 – supernatant of second isolation step.

## 3.5 Conclusion

Despite the recognized theoretical potential of fusion-proteins for crystallization, the number of X-Ray diffraction structures is rather limited when compared to the total number of depositions available at the PDB. For example, as of 2015, from a total of around 102 000 crystallographic structures available, only around 100 were fusion-protein constructs using one of the most used heterologous partners, maltose-binding protein (MBP) (Kobe *et al.*,

2015; Waugh, 2016). These statistics clearly evidence low success rates, which may be explained by the high “trial and error” nature of this technique. Despite the best educated efforts in conjugating target and heterologous partners chemistries, there are no definitive formulas for their selection, as well as critical aspects, such as the type and length of linker to include, if any. For Aβ, only three fusion constructs cases were reported, with none encompassing the full-peptide, and one of which requiring a ternary complex to aid crystallization (Nisbet *et al.*, 2013; Streltsov *et al.*, 2011; Takano *et al.*, 2006).

Here we designed and attempted to crystallize Aβ using three distinct constructs: T4Lysozyme-$Aβ_{1-40}$, T4Lysozyme-$Aβ_{17-40}$ and PAC3-$Aβ_{1-40}$. As the peptide is highly hydrophobic, a feature shared with integral membrane proteins, T4 Lysozyme was initially selected among the most common fusion tags, since this protein has been successfully used to solve the structure of cell receptors, particularly from the G protein-coupled family (Gacasan *et al.*, 2017). T4Lysozyme-$Aβ_{1-40}$ and T4Lysozyme-$Aβ_{17-40}$ were successfully expressed in *E. coli* and single crystal X-Ray diffraction could be performed for both. However, the obtained structures were disappointing given the initial expectations. Only a very limited amount of Aβ residues could be traced to the electron density, and no significant or novel disease-relevant information could be extracted. Regarding PAC3-$Aβ_{1-40}$, the construct proved to be overly hydrophobic, essentially expressing to inclusion bodies and, despite extensive efforts, it was not possible to solubilize and refold it. Thus, no crystallization screening could be set up.

## 3.6 References

Adams, P. D., Afonine, P. V., Bunkoczi, G., Chen, V. B., Davis, I. W., Echols, N., Headd, J. J., Hung, L. W., Kapral, G. J., Grosse-Kunstleve, R. W., McCoy, A. J., Moriarty, N. W., Oeffner, R., Read, R. J., Richardson, D. C., Richardson, J. S., Terwilliger, T. C., & Zwart, P. H. (2010). PHENIX: a comprehensive Python-based system for macromolecular structure solution. *Acta Crystallogr D Biol Crystallogr, 66*(Pt 2), 213-221. doi:10.1107/S0907444909052925

Bailey, S. (1994). The CCP4 suit - programs for protein crystallography. *Acta Crystallographica Section D: Biological Crystallography, 58*, 760-763. doi:10.1107/S0907444994003112

Chojnowski, G., Choudhury, K., Heuser, P., Sobolev, E., Pereira, J., Oezugurel, U., & Lamzin, V. S. (2020). The use of local structural similarity of distant homologues for crystallographic model building from a molecular-replacement solution. *Acta Crystallogr D Struct Biol, 76*(Pt 3), 248-260. doi:10.1107/S2059798320000455

Coati, A., Chavas, L. M. G., Fontaine, P., Foos, N., Guimaraes, B., Gourhant, P., Legrand, P., Itie, J. P., Fertey, P., Shepard, W., Isabet, T., Sirigu, S., Solari, P. L., Thiaudiere, D., & Thompson, A. (2017). Status of the crystallography beamlines at synchrotron SOLEIL⋆. *The European Physical Journal Plus, 132*(4), 174. doi:10.1140/epjp/i2017-11403-3

Dupeux, F., Rower, M., Seroul, G., Blot, D., & Marquez, J. A. (2011). A thermal stability assay can help to estimate the crystallization likelihood of biological samples. *Acta Crystallographica Section D, 67*(11), 915-919. doi:doi:10.1107/S0907444911036225

Economou, N. J., Nahoum, V., Weeks, S. D., Grasty, K. C., Zentner, I. J., Townsend, T. M., Bhuiya, M. W., Cocklin, S., & Loll, P. J. (2012). A carrier protein strategy yields the structure of dalbavancin. *J Am Chem Soc, 134*(10), 4637-4645. doi:10.1021/ja208755j

Emsley, P., Lohkamp, B., Scott, W. G., & Cowtan, K. (2010). Features and development of Coot. *Acta Crystallogr D Biol Crystallogr, 66*(Pt 4), 486-501. doi:10.1107/S0907444910007493

Gacasan, S. B., Baker, D. L., & Parrill, A. L. (2017). G protein-coupled receptors: the evolution of structural insight. *AIMS Biophys, 4*(3), 491-527. doi:10.3934/biophy.2017.3.491

Holcomb, J., Spellmon, N., Zhang, Y., Doughan, M., Li, C., & Yang, Z. (2017). Protein crystallization: Eluding the bottleneck of X-ray crystallography. *AIMS Biophys, 4*(4), 557-575. doi:10.3934/biophy.2017.4.557

Juanhuix, J., Gil-Ortiz, F., Cuni, G., Colldelram, C., Nicolas, J., Lidon, J., Boter, E., Ruget, C., Ferrer, S., & Benach, J. (2014). Developments in optics and performance at BL13-XALOC, the macromolecular crystallography beamline at the Alba Synchrotron. *Journal of Synchrotron Radiation, 21*(4), 679-689. doi:doi:10.1107/S160057751400825X

Kabsch, W. (2010). XDS. *Acta crystallographica. Section D, Biological crystallography, 66*(Pt 2), 125-132. doi:10.1107/S0907444909047337

Kobe, B., Ve, T., & Williams, S. J. (2015). Fusion-protein-assisted protein crystallization. *Acta Crystallogr F Struct Biol Commun, 71*(Pt 7), 861-869. doi:10.1107/S2053230X15011061

Krissinel, E., & Henrick, K. (2007). Inference of Macromolecular Assemblies from Crystalline State. *Journal of Molecular Biology, 372*(3), 774-797. doi:10.1016/j.jmb.2007.05.022

Krissinel, E., Uski, V., Lebedev, A., Winn, M., & Ballard, C. (2018). Distributed computing for macromolecular crystallography. *Acta Crystallogr D Struct Biol, 74*(Pt 2), 143-151. doi:10.1107/S2059798317014565

Kuhn, A. J., Abrams, B. S., Knowlton, S., & Raskatov, J. A. (2020). Alzheimer's Disease "Non-amyloidogenic" p3 Peptide Revisited: A Case for Amyloid-α. *ACS Chemical Neuroscience, 11*(11), 1539-1544. doi:10.1021/acschemneuro.0c00160

Kuroki, R., Weaver, L. H., & Matthews, B. W. (1999). Structural basis of the conversion of T4 lysozyme into a transglycosidase by reengineering the active site. *Proc Natl Acad Sci U S A, 96*(16), 8949-8954. doi:10.1073/pnas.96.16.8949

Laemmli, U. K. (1970). Cleavage of Structural Proteins during the Assembly of the Head of Bacteriophage T4. *Nature, 227*(5259), 680-685. doi:10.1038/227680a0

Lee, Y., Min, C. K., Kim, T. G., Song, H. K., Lim, Y., Kim, D., Shin, K., Kang, M., Kang, J. Y., Youn, H. S., Lee, J. G., An, J. Y., Park, K. R., Lim, J. J., Kim, J. H., Kim, J. H., Park, Z. Y., Kim, Y. S., Wang, J., Kim, D. H., & Eom, S. H. (2015). Structure and function of the N-terminal domain of the human mitochondrial calcium uniporter. *EMBO Rep, 16*(10), 1318-1333. doi:10.15252/embr.201540436

Liebschner, D., Afonine, P. V., Baker, M. L., Bunkoczi, G., Chen, V. B., Croll, T. I., Hintze, B., Hung, L. W., Jain, S., McCoy, A. J., Moriarty, N. W., Oeffner, R. D., Poon, B. K., Prisant, M. G., Read, R. J., Richardson, J. S., Richardson, D. C., Sammito, M. D., Sobolev, O. V., Stockwell, D. H., Terwilliger, T. C., Urzhumtsev, A. G., Videau, L. L., Williams, C. J., & Adams, P. D. (2019). Macromolecular structure determination using X-rays, neutrons and electrons: recent developments in Phenix. *Acta Crystallogr D Struct Biol, 75*(Pt 10), 861-877. doi:10.1107/S2059798319011471

Magnusdottir, A., Johansson, I., Dahlgren, L.-G., Nordlund, P., & Berglund, H. (2009). Enabling IMAC purification of low abundance recombinant proteins from E. coli lysates. *Nature Methods, 6*(7), 477-478. doi:10.1038/nmeth0709-477

Matthews, B. W. (1968). Solvent content of protein crystals. *J Mol Biol, 33*(2), 491-497. doi:10.1016/0022-2836(68)90205-2

McCoy, A. J., Grosse-Kunstleve, R. W., Adams, P. D., Winn, M. D., Storoni, L. C., & Read, R. J. (2007). Phaser crystallographic software. *Journal of Applied Crystallography, 40*(4), 658-674. doi:doi:10.1107/S0021889807021206

Murshudov, G. N., Vagin, A. A., & Dodson, E. J. (1997). Refinement of macromolecular structures by the maximum-likelihood method. *Acta Crystallogr D Biol Crystallogr, 53*(Pt 3), 240-255. doi:10.1107/S0907444996012255

Nisbet, R. M., Nuttall, S. D., Robert, R., Caine, J. M., Dolezal, O., Hattarki, M., Pearce, L. A., Davydova, N., Masters, C. L., Varghese, J. N., & Streltsov, V. A. (2013). Structural studies of the tethered N-terminus of the Alzheimer's disease amyloid-beta peptide. *Proteins, 81*(10), 1748-1758. doi:10.1002/prot.24312

Qing, G., Ma, L. C., Khorchid, A., Swapna, G. V., Mal, T. K., Takayama, M. M., Xia, B., Phadtare, S., Ke, H., Acton, T., Montelione, G. T., Ikura, M., & Inouye, M. (2004). Cold-

shock induced high-yield protein production in Escherichia coli. *Nat Biotechnol, 22*(7), 877-882. doi:10.1038/nbt984

Satoh, T., Yagi-Utsumi, M., Okamoto, K., Kurimoto, E., Tanaka, K., & Kato, K. (2019). Molecular and Structural Basis of the Proteasome alpha Subunit Assembly Mechanism Mediated by the Proteasome-Assembling Chaperone PAC3-PAC4 Heterodimer. *Int J Mol Sci, 20*(9). doi:10.3390/ijms20092231

Schrodinger, LLC. (2015). *The PyMOL Molecular Graphics System, Version 1.8*.

Stothard, P. (2000). The Sequence Manipulation Suite: JavaScript Programs for Analyzing and Formatting Protein and DNA Sequences. *BioTechniques, 28*(6), 1102-1104. doi:10.2144/00286ir01

Streltsov, V. A., Varghese, J. N., Masters, C. L., & Nuttall, S. D. (2011). Crystal structure of the amyloid-β p3 fragment provides a model for oligomer formation in Alzheimer's disease. *Journal of Neuroscience, 31*, 1419-1426. doi:10.1523/JNEUROSCI.4259-10.2011

Takano, K., Endo, S., Mukaiyama, A., Chon, H., Matsumura, H., Koga, Y., & Kanaya, S. (2006). Structure of amyloid β fragments in aqueous environments. *FEBS Journal, 273*, 150-158. doi:10.1111/j.1742-4658.2005.05051.x

Thorsen, T. S., Matt, R., Weis, W. I., & Kobilka, B. K. (2014). Modified T4 Lysozyme Fusion Proteins Facilitate G Protein-Coupled Receptor Crystallogenesis. *Structure, 22*(11), 1657-1664. doi:10.1016/j.str.2014.08.022

Tuukkanen, A. T., Freire, D., Chan, S., Arbing, M. A., Reed, R. W., Evans, T. J., Zenkeviciute, G., Kim, J., Kahng, S., Sawaya, M. R., Chaton, C. T., Wilmanns, M., Eisenberg, D., Parret, A. H. A., & Korotkov, K. V. (2019). Structural Variability of EspG Chaperones from Mycobacterial ESX-1, ESX-3, and ESX-5 Type VII Secretion Systems. *J Mol Biol, 431*(2), 289-307. doi:10.1016/j.jmb.2018.11.003

Vagin, A., & Lebedev, A. (2015). MoRDa, an automatic molecular replacement pipeline. *Acta Crystallographica Section A, 71*(a1), s19. doi:10.1107/S2053273315099672

Walsh, D. M., Thulin, E., Minogue, A. M., Gustavsson, N., Pang, E., Teplow, D. B., & Linse, S. (2009). A facile method for expression and purification of the Alzheimer's disease-associated amyloid beta-peptide. *FEBS J, 276*(5), 1266-1281. doi:10.1111/j.1742-4658.2008.06862.x

Waugh, D. S. (2016). Crystal structures of MBP fusion proteins. *Protein Sci, 25*(3), 559-571. doi:10.1002/pro.2863

Wilkins, M. R., Gasteiger, E., Bairoch, A., Sanchez, J. C., Williams, K. L., Appel, R. D., & Hochstrasser, D. F. (1999). Protein identification and analysis tools in the ExPASy server. *Methods Mol Biol, 112*, 531-552. doi:10.1385/1-59259-584-7:531

# CHAPTER IV. Dissection of the key steps of $A\beta_{1-40}$ fibrillogenesis

Work from this chapter has been published on:

**Leite, J. P.**, Gimeno, A., Taboada, P., Jiménez-Barbero, J. J., & Gales, L. (2020). Dissection of the key steps of amyloid-β peptide 1–40 fibrillogenesis. International Journal of Biological Macromolecules, 164, 2240-2246.

# 4.1. Paper III: Dissection of the key steps of amyloid-β peptide 1-40 fibrillogenesis

Work contributions:

I would like to thank Pablo Taboada (Colloids and Polymers Physics group, Universidade Santiago Compostela, Spain) for hosting me to perform DLS measurements and assistance in data analysis. Nuclear Magnetic Ressonance experiments were performed by Ana Gimeno and Jesús J. Jiménez-Barbero (CIC bioGUNE, Derio, Spain).

International Journal of Biological Macromolecules 164 (2020) 2240–2246

Contents lists available at ScienceDirect

International Journal of Biological Macromolecules

journal homepage: http://www.elsevier.com/locate/ijbiomac

# Dissection of the key steps of amyloid-β peptide 1–40 fibrillogenesis

José P. Leite [a,b,c], Ana Gimeno [d], Pablo Taboada [e], Jesús J. Jiménez-Barbero [d,f,g], Luís Gales [a,b,c,*]

[a] i3S – Instituto de Investigação e Inovação em Saúde, Rua Alfredo Allen, 208, Porto, Portugal
[b] IBMC – Instituto de Biologia Molecular e Celular Universidade do Porto, Rua Alfredo Allen, 208, Porto, Portugal
[c] ICBAS – Instituto de Ciências Biomédicas Abel Salazar, Rua de Jorge Viterbo Ferreira 228, Porto, Portugal
[d] CIC bioGUNE, Bizkaia Technology Park, Building 801A, 48170 Derio, Spain
[e] Colloids and Polymers Physics Group, Particle Physics Department, 15782 Campus Vida, Universidade de Santiago de Compostela, Spain
[f] Ikerbasque, Basque Foundation for Science, Maria Diaz de Haro 13, 48009 Bilbao, Spain
[g] Department of Organic Chemistry II, Faculty of Science & Technology, University of the Basque Country, 48940 Leioa, Bizkaia, Spain

ARTICLE INFO

*Article history:*
Received 9 June 2020
Received in revised form 27 July 2020
Accepted 3 August 2020
Available online 06 August 2020

*Keywords:*
Amyloid
Nucleation
Amyloid-β peptide
Alzheimer's disease
Aggregation kinetics
Amyloid-β peptide oligomers
Aβ1–40

ABSTRACT

The aggregation kinetics of Aβ1–40 peptide was characterized using a synergistic approach by a combination of nuclear magnetic resonance, thioflavin-T fluorescence, transmission electron microscopy and dynamic light scattering. A major finding is the experimental detection of high molecular weight oligomers (HMWO) that converts into fibrils nuclei. Our observations are consistent with a mechanism of Aβ1–40 fibrillogenesis that includes the following key steps: i) slow formation of HMWO (Rh ~ 20 nm); ii) conversion of the HMWO into more compact Rh ~ 10 nm fibrils nuclei; iii) fast formation of additional fibrils nuclei through fibril surface catalysed processes; and iv) growth of fibrils by addition of soluble Aβ species. Moreover, NMR diffusion experiments show that at 37 °C soluble Aβ1–40 remains intrinsically disordered and mostly in monomeric form despite evidences of the presence of dimers and/or other small oligomers. A mathematical model is proposed to simulate the aggregation kinetics of Aβ1–40.



## 1. Introduction

The denaturation and aggregation of proteins and peptides, resulting in the loss of their structural and functional properties and the formation of amyloid-like fibrous deposits, are associated with more than 20 diseases, like Huntington's, Parkinson's or Alzheimer's disease (AD). Intriguingly, the site of deposition and the pathologies associated may diverge significantly due to, for example, a single amino acid mutation. The main component of amyloid aggregates found in the brains of Alzheimer's patients are the β-amyloids peptides. These peptides are produced by the two-step cleavage of the amyloid precursor protein (APP) by β- and γ-secretases [1]. The most prevalent form is Aβ1–40, followed by Aβ1–42, and other less prevalent N-terminal truncated or post-synthetically modified forms, such as Aβ2-x and AβpE3-x.

The amyloidogenic aggregates, independent of the source protein, show common features which enable their distinction from amorphous precipitates by several methods. Congo red staining, thioflavin-T fluorescence, ultra-structural analysis, circular dichroism and X-ray diffraction are among the most used [2]. A major breakthrough was the production of an antibody that specifically recognizes soluble oligomers of many amyloidogenic proteins and peptides [3], which indicates that they definitely share a common structure.

High-resolution techniques used for the determination of the structure of biomolecules, such as X-ray crystallography and nuclear magnetic resonance (NMR), are less suitable for analysis of high molecular weight amyloid arrangements. Thus, the self-assembly mechanism at the molecular level has remained elusive. In this context, the analysis of the kinetics of protein aggregation, which can be followed by a plethora of biophysical and biochemical methods [4], has become a valuable tool in deciphering the mechanistic models. The problem is that typically the progression of protein aggregation follows a sigmoidal curve that can be fitted by many mathematical functions. The topic has been the subject of comprehensive reviews [4,5].

Different approaches have been used to predict the protein polymerization process, ranging from atomistic simulations [6–8] to mesoscopic mass actions equations (for a review see ref. [4]). Thermodynamically, the process has been described at different levels of detail [9–11]. An increase in the model's complexity can lead to over-parametrization and make the simulations too difficult, while oversimplification may weaken the theoretical foundations of the model. Probably, among the most used are the Ferrone model that postulated the presence of secondary events [12,13]; the Finke–Watzky model based on nucleation

* Corresponding author at: i3S – Instituto de Investigação e Inovação em Saúde, Rua Alfredo Allen, 208, Porto, Portugal.
*E-mail address:* lgales@ibmc.up.pt (L. Gales).

https://doi.org/10.1016/j.ijbiomac.2020.08.023
0141-8130/

followed by autocatalytic surface growth [14]; and the Knowles analytical equation of the mechanistic model that combines primary nucleation, secondary nucleation, fibril elongation and fibril fragmentation [15].

Despite the diversity of mathematical models available in the literature, it is believed that proteins polymerize through a common mechanistic model, consisting in a nucleation-dependent polymerization where the formation of nuclei from soluble proteins is slower than the elongation step. However, it was noticed that experimental data were sometimes not correctly predicted by this simple two-step mechanism. Thus, secondary nucleation processes were proposed, in which the two most popular are fibril fragmentation [2,11,15,16], suggested to be involved in β2-microglobulin aggregation and prion propagation, and heterogeneous nucleation which was detected in the polymerization of insulin [17–20] and amyloid-β peptide [21–23], and in the gelation of sickle cell hemoglobin at low concentrations [10].

NMR techniques have been used to identify and characterize the formation of Aβ oligomers in solution and in the presence of lipid membranes [24–26]. Nevertheless, the aggregation of amyloid-β peptides remains particularly elusive. Knowles and colleagues developed a widely accepted model for the aggregation of Aβ1–42 based on the presence of two species, monomers and fibrils [22]. The authors could not fit this model to the kinetic curves of Aβ1–40 without major assumptions regarding the dependence of secondary nucleation events on the concentration of monomers [23]. On the other hand, Lomakin and co-workers [21] and Luchinat and co-workers [27], among others, provided evidences for the conversion of Aβ1–40 oligomers into fibrils nuclei. Very recently, Knowles and colleagues also brought up evidence of the presence of a population of Aβ1–42 oligomers during the initial stages of aggregation [28]. Thus, the mechanism of aggregation of amyloid-β peptides is more complex than previously thought, which prompted us to investigate the aggregation of Aβ1–40 using a combination of complementary experimental techniques that enable us to observe the shape/mass variation of Aβ1–40 species in the early stages.

## 2. Materials and methods

### 2.1. Reagents

Aβ peptides 17–40, 1–40 and 1–42 were purchased from Bachem (Switzerland) with HPLC determined sample purity of 91.6%, 93.7% and 96.7%, respectively. Aβ peptide solutions were prepared based on ref. [29]. Briefly, Aβ peptides were equilibrated at room temperature for 30 min to allow complete defrosting and spun before opening the vial. To each sample, 500 μl of 1,1,1,3,3,3-Hexafluoro-2-propanol (HFIP) were added to complete disassemble pre-existing aggregates. Samples were incubated at room temperature overnight. HFIP was removed under a gentle flow of pure nitrogen gas and further dried with a vacuum concentrator to remove remaining traces. If samples were not clear after a single HFIP passage, the procedure was repeated, adding a brief homogenization step using a sonication bath. Dried peptide films were thoroughly resuspended in pure dimethyl sulfoxide (DMSO) and stored at −20 °C between measurements. All other reagents were of analytical grade.

### 2.2. NMR spectroscopy

All experiments were performed at 37 °C using a Bruker Avance III 600 MHz spectrometer.

*$^1$H NMR experiments.* Samples for the 1D $^1$H NMR experiments were prepared in deuterated buffer (TRIS-d11 50 mM, EDTA-d16 1 mM, pH 7.4) with a peptide concentration of 60 μM. 25 μM of 3-(Trimethylsilyl)propionic-2,2,3,3-d4 acid sodium salt (TSP) was used as internal standard. Samples are prepared at room temperature and maintained at 37 °C. The aggregation process was monitored by following the $^1$H signal intensities of the peptide (relative to the signal intensity of the internal standard TSP) in 1D spectra over time. $^1$H spectra were acquired with 256 transients and 2 s recycle delay. The excitation sculpting scheme was employed to suppress residual $H_2O$ signal [30].

*Diffusion experiments.* Samples for DOSY experiments were prepared similarly as above: deuterated buffer (TRIS-$d_{11}$ 50 mM, EDTA-$d_{16}$ 1 mM, pH 7.4) with a peptide concentration of 60 μM. During the aggregation process DOSY experiments were measured at 37 °C and performed employing an array of 32 spectra for each experiment (128 or 256 transients each, with a 1 s recycle delay), and varying the gradient strength between 2% and 95%. The lengths of and delays between the gradient pulses were optimized for each sample. Data fitting and diffusion coefficients determination were performed with the T1/T2 Relaxation module available in the Bruker TopSpin software.

The radius of gyration ($R_g$) of reference aprotinin was computed with model coordinates PDB 4PTI [31] using the program HYDROPRO [32]. The hydrodynamic radius ($R_h$) of a globular protein such as the reference can be predicted by the relationship $R_g = \sqrt{3/5}R_h$.

Diffusion coefficients are inversely proportional to the hydrodynamic radius as shown by the Stokes-Einstein equation:

$$D = \frac{k_B T}{6\pi\eta R_h} \tag{1}$$

Thus, for Aβ peptides and reference in the same solution,

$$R_h^{A\beta} = \frac{D^{ref}}{D^{A\beta}} R_h^{ref} \tag{2}$$

### 2.3. Dynamic light scattering (DLS)

Aβ1–40 2 mM stock in DMSO was diluted to 50 μM in 10 mM sodium phosphate buffer pH 7.4. Samples were centrifuged for 15 min at 5000 ×g to remove pre-formed aggregates. DLS measurements were performed at 25 °C using an ALV/DLS/ SLS-5000F instrument equipped with a SP-86 goniometer system (ALV-GmbH, Langen, Germany) and a CW diode-pumped Nd:YAG solid-state Compass-DPSS laser with a symmetrizer (Coherent Inc., Santa Clara, CA). The laser operates at 532 nm with an output power of 400 mW. The intensity scale was calibrated against scattering from toluene. Measurements were made at a scattering angle 90° to the incident beam for 5–10 min, for time points 0 h, 2 h, 4 h, 6 h and 8 h. Data were analyzed with ALV Correlator Software (version 3.0).

### 2.4. Thioflavin-T (ThT) amyloid formation kinetics

Amyloid fluorescent dye Thioflavin-T (ThT) was used to follow amyloid kinetics. ThT stock solution was freshly prepared for each set of measurements at a concentration of 3 mM in ultrapure water (concentration was determined spectrophotometrically at 411 nm, $\varepsilon = 2.2 \cdot 10^4\,M^{-1}\,cm^{-1}$) and then diluted to 30 μM for the kinetic assays. Aβ peptides were diluted to the final concentration from the working DMSO stocks in 20 mM sodium phosphate buffer at pH 7.4. Measurements were made at 37 °C at quiescent conditions with a plate fluorimeter FluorDia T70 (Otsuka Electronics, Japan) using ThT excitation and emission filters (440 nm and 480 nm, respectively). Triplicate measurements were performed in 96-well plates (total volume of 300 μl) and averaged. Each well was sealed with 30 μl paraffin oil to avoid evaporation.

### 2.5. Transmission electron microscopy

Aliquots (10 μl) of Aβ1–40 and Aβ17–40 mature fibril solutions were adsorbed onto carbon-coated Formvar 300-mesh nickel grids (Electron Microscope Sciences, USA). The grids were washed and

stained with 2% (w/v) uranyl acetate. The samples were viewed with a TEM JEOL JEM-1400 microscope (JEOL Ltd., Tokyo, Japan) at 120 kV.

## 3. Results and discussion

Hydrodynamic radius of proteins and peptides, namely of amyloid beta fragments, are remarkably well fitted to the molecular mass (or the number of chain residues) by scaling laws [33–35]. Estimation of the scaling factor provides a framework that can be used to analyse the conformational properties [33–35] and/or the oligomerization state [34] of proteins and peptides underscoring the usefulness of analysing more than one amyloid beta fragment. Thus, in addition to Aβ1–40, the biologically relevant Aβ17–40 peptide was investigated by NMR techniques. Aβ17–40, also called P3 peptide, results from the α- and γ-secretase cleavage of the amyloid precursor protein (APP) and is, similarly to the full length peptides, a major constituent of diffuse plaques observed in Alzheimer's disease (AD) brains and pre-amyloid plaques in people affected by Down's syndrome [36].

Aggregation kinetics of Aβ1–40 and Aβ17–40 peptides was followed by NMR. Simple 1D $^1$H NMR experiments were acquired, and a decay in the intensities of the proton signals of the peptides over time was observed. The presence of new peaks was not detected. Although exchange processes could also provide signal broadening [37,38], these observations strongly pointed to the conversion of the peptide monomer or small sized oligomers (NMR visible species) into large sized oligomeric species (species whose NMR signals are broadened beyond detection, i.e. NMR-invisible species). Thus, monitoring the reduction of the proton signal intensity over time can be exploited to measure the aggregation kinetics (Fig. 1).

The aggregation behavior of the two Aβ peptides was remarkably different. Aβ1–40 showed the expected nucleation polymerization behavior, observed by other investigators [23,27], while the concentration of Aβ17–40 soluble species decays exponentially with time, which points to a protective role of the *N*-terminal region against aggregation.

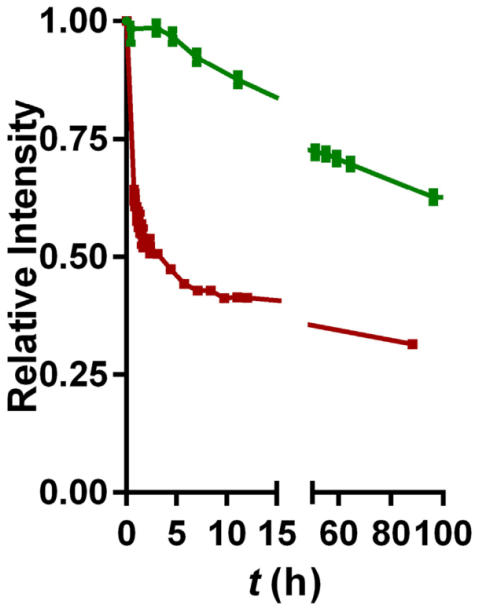


**Fig. 1.** Aggregation of Aβ1–40 (green) and Aβ17–40 (red) followed by NMR. Decay of the relative $^1$H NMR signal intensity of the soluble species (error range estimated from the signal to noise ratio shown).

Moreover, diffusion ordered spectroscopy (DOSY) experiments provided information about the size/shape of the visible species during the time course of the aggregation process. Interestingly, the diffusion coefficients, and thus the average size of these species (hydrodynamic radius calculated using Eq. (2)), remained nearly constant within the experimental uncertainty for both Aβ1–40 and Aβ17–40 peptides (Table 1).

Several researchers have found that hydrodynamic radius of proteins and peptides with $N_R$ residues are well fitted to the scaling law:

$$R_h = R_o N_R^{\nu} \tag{3}$$

The scaling factor $\nu$ was empirically determined to be 0.29 for native folded proteins and 0.57 for highly denatured peptides and proteins by Smith and co-workers [35]; the authors measured hydrodynamic radii by pulse field gradient PFG-NMR techniques. Damaschun et al. reported $\nu = 0.5 \pm 0.02$ obtained from proteins denatured in 6 M guanidine hydrochloride [33]. Danielsson and colleagues studied the hydrodynamic properties of Aβ fragments at 25 °C, also by PFG-NMR, and found $\nu =$ 0.415 [34]. The exponent lies below that for the fully denatured state but above the exponent for the native one. The authors concluded that there is some residual structure in the longer Aβ fragments at 25 °C.

Despite the fact we have only collected data for two Aβ peptides, it is interesting to observe they correlate by a scaling factor $\nu = 0.57$ which strongly suggests that these peptides remain fully disordered at 37 °C. Furthermore, the scaling data for disordered proteins collected by Smith et al. [35] was used to estimate the expected number of residues ($N_R$) of peptides whose hydrodynamic radii matches the ones measured for Aβ1–40 and Aβ17–40 (Table 1). As can be observed in Fig. 2, $R_h =$ 19.9Å is expected for a peptide of 49 residues and $R_h = 14.9$Å for a peptide of 29 residues. The Aβ peptides are shorter than predicted values even assuming that they are fully disordered, which is an indication that there should be some degree of oligomerization at 37 °C.

It is reasonable to assume that monomeric and dimeric peptides give the major contributions to the decay of the resonance intensity in the diffusion experiment of Aβ peptides [34]. If the chemical shifts of the monomer and the dimer are the same, the measured diffusion coefficient is the weighted mean value of the two diffusion coefficients [34] and

$$\frac{1}{(R_h)_{meas}} = f_{mon}\frac{1}{(R_h)_{mon}} + f_{dimer}\frac{1}{(R_h)_{dimer}} \tag{4}$$

Making use of the empirical correlation for unfolded peptides and proteins provided by Smith et al. [35] to estimate the hydrodynamic radius of the pure species yields an approximate mass fraction of monomers of nearly 65%, both for Aβ1–40 and Aβ17–40. Thus, there is a measurable degree of dimerization at physiological temperature (37 °C) in contrast to what was observed at 25 °C [34]. DOSY experiments are not expected to provide multimodal results in a mixture of monomer to tetramer Aβ species, however, dimers and tetramers of Aβ1–40 were already identified as major species in solution using ion mobility coupled with mass spectrometry [39] and photoinduced cross-linking [40].

Transmission electron microscopy (TEM) analysis of Aβ mature samples confirms that Aβ1–40 fibrils are longer and present in a smaller number than Aβ17–40 ones (Fig. 3). Moreover, Aβ17–40 fibrils show a

**Table 1**
Diffusion coefficients and corresponding hydrodynamic radii determined by NMR at 37 °C.

| Compound | Diffusion coefficient (m$^2$/s)[a] | MW (Da) | $R_h$ (Å) |
|---|---|---|---|
| Aprotinin | $(1.88 \pm 0.02)\cdot 10^{-10}$ | 6500 | 15.8 |
| Aβ17–40 | $(1.99 \pm 0.05)\cdot 10^{-10}$ | 2393 | 14.9 |
| Aβ1–40 | $(1.49 \pm 0.05)\cdot 10^{-10}$ | 4330 | 19.9 |

[a] For Aβ peptides averaged values are displayed.

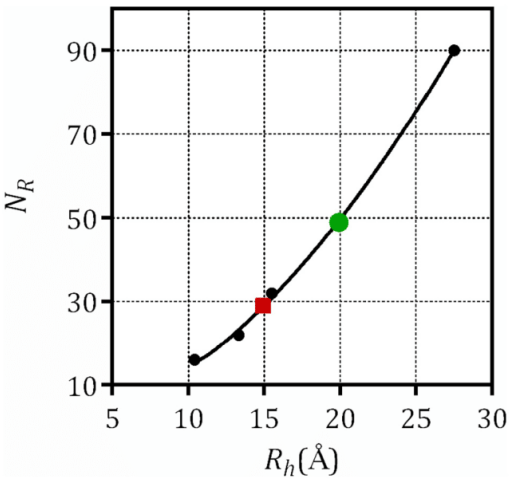


**Fig. 2.** Plot of the number of residues of highly denatured polypeptide chains versus the hydrodynamic radius. Black symbols are values reported by [35], green and red symbols denote the measured hydrodynamic radius of Aβ1–40 (green) and Aβ17–40 (red), respectively.

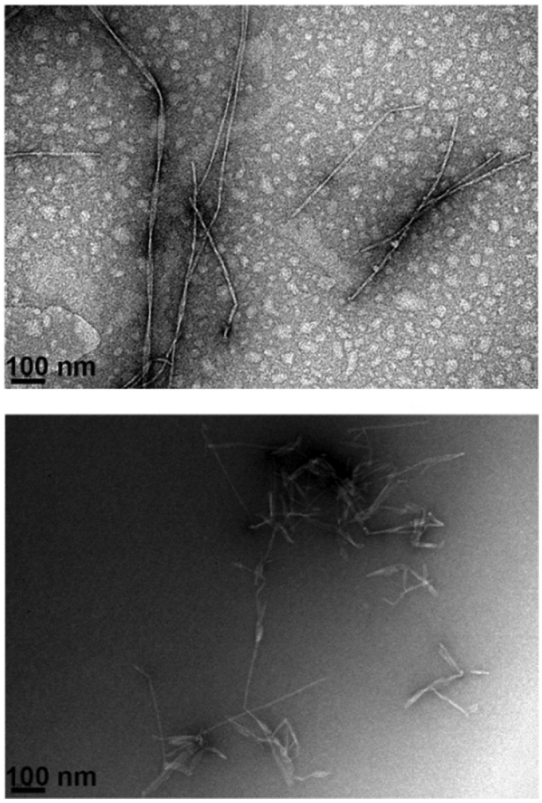


**Fig. 3.** TEM images of mature fibrils of Aβ1–40 (top) and Aβ17–40 (bottom).

propensity for lateral packing, while some Aβ1–40 fibrils exhibit twisting of two protofilaments.

The aggregation of Aβ1–40 was further monitored by dynamic light scattering (DLS), which enables the observation of aggregates (NMR-invisible species) since the scattering intensity is very dependent on the particle mass/size. The evolution of the particle size distribution with time is shown in Fig. 4. These data indicate that soluble Aβ1–40 do not nucleate directly into fibrils but go through a transient oligomeric state. When the oligomers reach a critical oligomeric size (HMWO with Rh ~ 20 nm) they seem to irreversible convert to fibrils nuclei (Rh ~ 10 nm). Fibrils grow by the addition of Aβ1–40 soluble species (which are no longer detected due to the much stronger scattering intensity of the large entities) at a rate of ~1.5 nm/h in the used experimental conditions. As fibrils grow, the concentration of Aβ1–40 soluble species falls and no more HMWO formation occurs, achieving a separation in time between the two processes, HMWO formation and fibril growth. A similar two-step model was already proposed by Luchinat's group [27] based on the analysis of the kinetic curves and not in the direct observation of these transient species. Lomakin and colleagues [21] studied the fibrillogenesis of Aβ1–40 in acidic conditions using quasi-elastic light-scattering spectroscopy and proposed that fibrils nuclei emerge from micelles and that, actually, nuclei are smaller.

The data in Fig. 4 has two additional important features. The formation of the HMWO (Rh ~ 20 nm) is neither spontaneous nor occurs at constant rate (not detected at $t = 2$ h but very visible at $t = 4$ h). Secondly, the fibrils nuclei (Rh ~ 10 nm) outnumbered HMWO since the relative scattering signal of the soluble species disappeared once HMWO starts to convert into first nuclei. The most plausible explanation is that fibril nuclei are also formed by surface processes (secondary) which occur in a much shorter time scale than the primary nucleation events. Fibril surface-catalysed nucleation seems to produce directly compact fibril nuclei as large oligomers (Rh ~ 20 nm) cease to be detected.

The present results are in agreement with the conversion model illustrated in Fig. 5. The first step consists in the formation of HMWO and depends on the concentration of monomers ($m_0$). The second step corresponds to the structural conversion of HMWO into fibrils nuclei, which should not depend on the concentration of the soluble peptide. Then, the number of fibrils nuclei seems to rapidly increase probably due to heterogeneous nucleation.

For high monomer concentrations, the formation of HMWO becomes fast and the characteristic time for the formation of fibrils nuclei ($t^*_{MN}$) approximates the time of conversion of HMWO into nuclei ($t^*_N$), remaining independent of $m_0$ (phase I in Fig. 5).

For low concentrations of $m_0$, the HMWO formation kinetics ($t^*_M$) plays a role in the dynamics of the whole system. It is expected that the formation of HMWO occurs at nearly constant monomer concentration $m \sim m_0$, and most of the monomer is consumed in the fibril growth step. Moreover, if HMWO are formed by a step-wise addition of

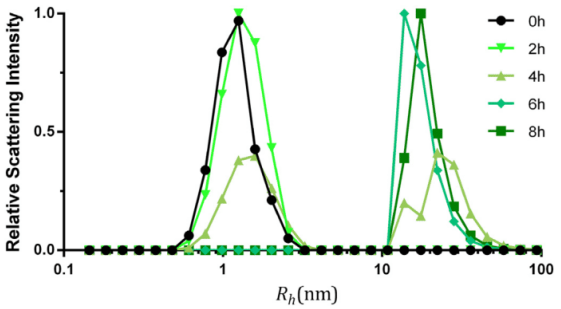


**Fig. 4.** Temporal evolution of Aβ1–40 hydrodynamic radius (Rh), followed by DLS.

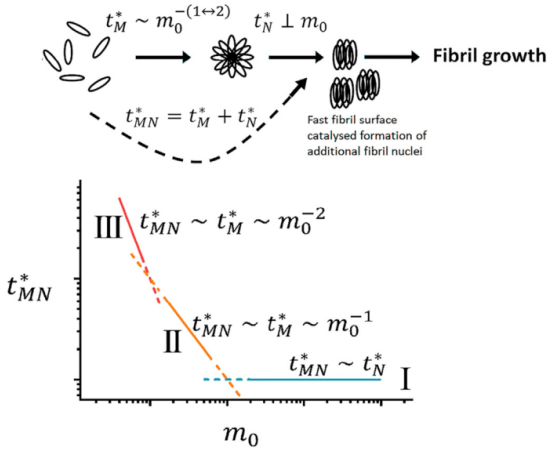


**Fig. 5.** Proposed two-step conversion model for Aβ1–40 aggregation (top) and characteristic fibril nucleation time dependence on the initial concentration of monomer (bottom).

monomers, the average time of HMWO formation is $t_M^* \sim m_0^{-1}$, as it will be discussed later (phase II, in Fig. 5). In the unforeseen case that most of the monomer is consumed in the formation of HMWO, the reaction rate is $\sim m_0^2$ and $t_M^* \sim m_0^{-2}$ (phase III in Fig. 5). If fibril growth is significantly faster than nucleation $t_{1/2}$, the characteristic half-time of reaction (that is, the is the time at which 50% of the protein is found in aggregated form), should maintain the same monomer dependence as $t_{MN}^*$ (Fig. 5). Indeed, it was already observed for Aβ1–40 that this scaling exponent is highly dependent on the concentration, and it varies from $-1.2 \pm 0.2$ at low protein concentrations (ca. 5 μM) to $-0.2 \pm 0.05$ at higher protein concentrations (ca. 60 μM) [23].

If formation of HMWO is represented by a step-wise addition reaction of $N$ monomers and the addition rates are considered constant $Km_0 = k_+ m_0 - k_-$ ($m_0$ being the initial monomer concentration), the concentration of HMWO $M(t)$ can be readily calculated by [41]:

$$\frac{M(t)}{M_\infty} = 1 - \sum_{i=1}^{N} \frac{(Km_0 t)^{i-1} e^{-Kt}}{(i-1)!} \tag{5}$$

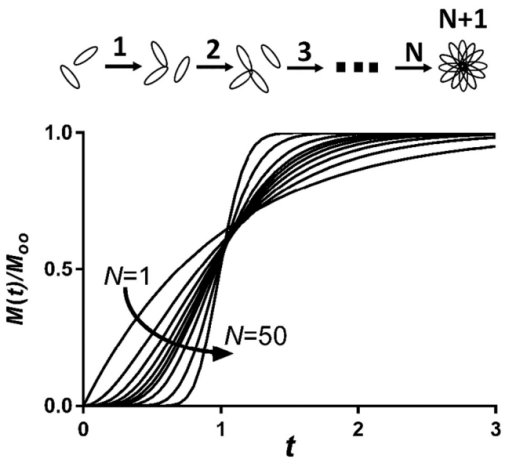


**Fig. 6.** $M(t)/M_\infty$ profiles for increasing number of reactions $N$. Standardized for $E(t) = N/Km_0 = 1$.

The average time of HMWO formation is then $E(t) = N/Km_0$. In Fig. 6, $M(t)/M_\infty$ are presented for different $N$.

The following mathematical treatment is simplified by simulating the profiles in Fig. 6 with $N = 2$ and fitting the time lag of HMWO formation $t_M^*$ and $Km_0$

$$\frac{M(t)}{M_\infty} = 1 - \left[1 + Km_0\left(t - t_M^*\right)\right] e^{-Km_0\left(t - t_M^*\right)} \tag{6}$$

The fibrils nuclei $N(t)$ are formed after a lag time $t_{MN}^*$ that combines $t_M^*$ with the lag time for the conversion HMWO into nuclei. Due to the significant differences on the timescales of formation of fibrils nuclei by primary and secondary processes, it will be considered that secondary nucleation is spontaneous.

$$\frac{N(t)}{N_\infty} = 1 - \left[1 + Km_0\left(t - t_{MN}^*\right)\right] e^{-Km_0\left(t - t_{MN}^*\right)} \tag{7}$$

$N_\infty$ is the total concentration number of fibrils nuclei formed (either by primary or secondary nucleation), $\alpha m_0/(N+1)$, and $\alpha$ and $(1-\alpha)$ are the fractions of the monomer converted to fibrils nuclei and consumed in fibril elongation, respectively. Assuming that the rate of monomer consumption in fibril elongation is $K_f m(t) N(t)$

$$\frac{m_0 - m(t)}{m_0} = \alpha\left[1 - (1 + Km_0\tau_M)\, exp(-Km_0\tau_M)\right] + (1-\alpha)\left[1 - exp\left[\frac{-K_f \alpha}{K(N+1)}\left[Km_0\tau_{MN} - 2 + (Km_0\tau_{MN} + 2)\, exp(-Km_0\tau_{MN})\right]\right]\right] \tag{8}$$

where $\tau_{MN} = t - t_{MN}^*$ and $\tau_M = t - t_M^*$. Eq. (8) is able to simulate the diversity of amyloid kinetic shapes found in the literature (Fig. 7).

Aggregation of Aβ1–40 was also monitored by thioflavin-T (ThT) fluorescence. The fibrillation kinetics of Aβ1–40 has been extensively studied by fluorimetric methods; the overall curves have a sigmoidal shape including a lag phase, a growth phase and a plateau. We have obtained the expected sigmoidal curves for Aβ1–40 that can be well reproduced by our model (Fig. 8, top). Moreover, the role that oligomeric species also play in Aβ1–42 aggregation was very recently stressed [28], and thus we decided to apply the model to Aβ1–42 kinetics too (Fig. 8, bottom).

Despite the very good fitting of the mathematical model to the aggregation kinetics of Aβ1–40 and Aβ1–42, we should stress that we have only investigated the formation of high molecular weight intermediates of Aβ1–40 peptide. Nevertheless, Knowles and colleagues provided evidences that Aβ1–42 mature fibrils must originate from oligomers [28], supporting the application of Eq. (8) to the Aβ1–42 kinetic curves.

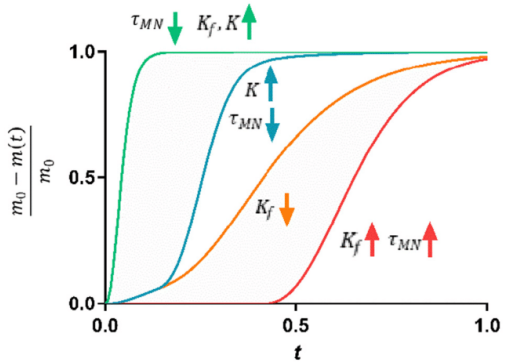


**Fig. 7.** Amyloid kinetic curve shapes that can be obtained by Eq. (8).

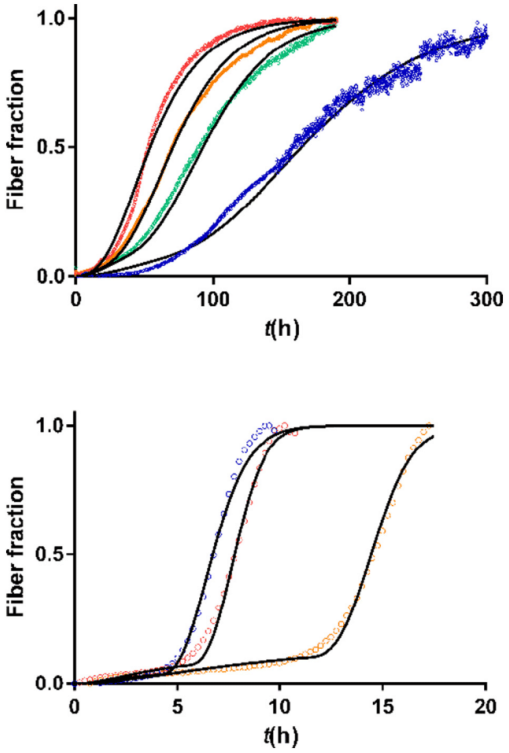


**Fig. 8.** ThT aggregation kinetic assays of Aβ1–40 (top) and Aβ1–42 (bottom). Initial concentrations of soluble Aβ1–40 are 100, 70, 55 and 30 μM and of Aβ1–42 are 20, 15 and 7.4 μM. Lines represent the best fit obtained with Eq. (8); the values of the fitted lag-times for the three replicates are $\tau_{MN} = 6.5 \pm 1.4$ h (100 μM Aβ1–40), $\tau_{MN} = 17.0 \pm 1.1$ h (70 μM Aβ1–40), $\tau_{MN} = 33 \pm 2$ h (55 μM Aβ1–40), $\tau_{MN} = 55 \pm 3$ h (30 μM Aβ1–40), and $\tau_{MN} = 4.7 \pm 0.4$ h (20 μM Aβ1–42), $\tau_{MN} = 5.2 \pm 0.4$ h (15 μM Aβ1–42), $\tau_{MN} = 10.3 \pm 0.9$ h (7.4 μM Aβ1–42).

In conclusion, our findings reveal the role of oligomeric intermediates in the formation of Aβ1–40 amyloid fibrils. Clearly a more systematic investigation is mandatory to fully understand the underlying molecular mechanisms of Aβ1–40 fibrillogenesis but the experimental data displayed here point to the slow formation of high molecular weight oligomers (HMWO) that reorganise structurally into more compact species (nuclei formation) that subsequently proceeds to fibril growth through the addition of soluble Aβ1–40 species. Fibrils nuclei seem to outnumber HMWO which points to a parallel mechanism of nuclei formation, probably heterogeneous nucleation. In addition, the NMR diffusion measurements of Aβ1–40 and Aβ17–40 are consistent with the minority presence of dimers or other small oligomers in solution at the physiological temperature of 37 °C.

## CRediT authorship contribution statement

José Leite: Data curation, Writing- Original draft preparation.

Ana Gimeno: Data curation (NMR), Methodology (NMR), Writing-Original draft preparation (NMR).

Pablo Taboada: Conceptualization (DLS), Methodology (DLS), Writing- Reviewing.

Jesús J. Jiménez-Barbero: Conceptualization (NMR), Methodology (NMR), Writing- Reviewing.

Luís Gales: Conceptualization, Methodology, Writing- Reviewing and Editing.

## Acknowledgements

This work was supported by Norte-01-0145-FEDER-000008- Porto Neurosciences and Neurologic Disease Research Initiative at I3S, supported by Norte Portugal Regional Opera-tional Programme (NORTE2020), under the PORTUGAL 2020 Partnership Agreement, by COMPETE 2020—Operacional Programme for Competitiveness and Internationalisation (POCI), Portugal 2020, through the European Regional Development Fund (FEDER), and by Portuguese funds through FCT—Fundação para a Ciência e a Tecnologia/Ministério da Ciência, Tecnologia e Ensino Superior in the framework of the project "Institute for Research and Innovation in Health Sciences" (POCI-01-0145-FEDER-007274) and PhD grant SFRH/BD/129921/2017 (José P. Leite). We also thank Fundació la Marató de TV3 (neurodegenerative diseases call, project reference: 20140330-31-32-33-34). Pablo Taboada thanks the Agencia Estatal de Investigación (AEI) by project MAT2016-80266-R, and Xunta de Galicia for additional funding (Grupo de Referencia Competitiva ED431C 2018/26 and Agrupación Estratégica en Materiales-AEMAT ED431E 2018/08). ERDF funds are also greatly acknowledged. Ana Gimeno thanks MINECO (Spain) for a Juan de la Cierva contract.

## References

[1] T. Mohamed, A. Shakeri, P.P. Rao, Eur. J. Med. Chem. 113 (2016) 258–272.
[2] S.R. Collins, A. Douglass, R.D. Vale, J.S. Weissman, PLoS Biol. 2 (2004) 1582–1590.
[3] R. Kayed, E. Head, J.L. Thompson, T.M. McIntire, S.C. Milton, C.W. Cotman, C.G. Glabe, Science 300 (2003) 486–489.
[4] A.M. Morris, M.A. Watzky, R.G. Finke, BBA-Proteins Proteomics 1794 (2009) 375–397.
[5] C.J. Roberts, Biotechnol. Bioeng. 98 (2007) 927–938.
[6] F. Baftizadeh, X. Biarnes, F. Pietrucci, F. Affinito, A. Laio, J. Am. Chem. Soc. 134 (2012) 3886–3894.
[7] F. Baftizadeh, F. Pietrucci, X. Biarnes, A. Laio, Phys. Rev. Lett. 110 (2013).
[8] R. Cabriolu, D. Kashchiev, S. Auer, J. Chem. Phys. 133 (2010).
[9] R. Crespo, F.A. Rocha, A.M. Damas, P.M. Martins, J. Biol. Chem. 287 (2012) 30585–30594.
[10] F.A. Ferrone, J. Hofrichter, H.R. Sunshine, W.A. Eaton, Biophys. J. 32 (1980) 361–380.
[11] W.F. Xue, S.W. Homans, S.E. Radford, Proc. Natl. Acad. Sci. U. S. A. 105 (2008) 8926–8931.
[12] F. Ferrone, Methods Enzymol. 309 (1999) 256–274.
[13] F.A. Ferrone, J. Hofrichter, W.A. Eaton, J. Mol. Biol. 183 (1985) 611–631.
[14] A.M. Morris, M.A. Watzky, J.N. Agar, R.G. Finke, Biochemistry 47 (2008) 2413–2427.
[15] T.P.J. Knowles, C.A. Waudby, G.L. Devlin, S.I.A. Cohen, A. Aguzzi, M. Vendruscolo, E.M. Terentjev, M.E. Welland, C.M. Dobson, Science 326 (2009) 1533–1537.
[16] M. Tanaka, S.R. Collins, B.H. Toyama, J.S. Weissman, Nature 442 (2006) 585–589.
[17] V. Fodera, S. Cataldo, F. Librizzi, B. Pignataro, P. Spiccia, M. Leone, J. Phys. Chem. B 113 (2009) 10830–10837.
[18] R. Jansen, W. Dzwolak, R. Winter, Biophys. J. 88 (2005) 1344–1353.
[19] F. Librizzi, C. Rischel, Protein Sci. 14 (2005) 3129–3134.
[20] V. Fodera, M. van de Weert, B. Vestergaard, Soft Matter 6 (2010) 4413–4419.
[21] A. Lomakin, D.S. Chung, G.B. Benedek, D.A. Kirschner, D.B. Teplow, Proc. Natl. Acad. Sci. U. S. A. 93 (1996) 1125–1129.
[22] S.I.A. Cohen, S. Linse, L.M. Luheshi, E. Hellstrand, D.A. White, L. Rajah, D.E. Otzen, M. Vendruscolo, C.M. Dobson, T.P.J. Knowles, Proc. Natl. Acad. Sci. U. S. A. 110 (2013) 9758–9763.
[23] G. Meisl, X. Yang, E. Hellstrand, B. Frohm, J.B. Kirkegaard, S.I.A. Cohen, C.M. Dobson, S. Linse, T.P.J. Knowles, Proc. Natl. Acad. Sci. U. S. A. 111 (2014) 9384–9389.
[24] B.R. Sahoo, S.J. Cox, A. Ramamoorthy, Chem. Commun. 56 (2020) 4627–4639.
[25] J.R. Brender, A. Ghosh, S.A. Kotler, J. Krishnamoorthy, S. Bera, V. Morris, T.B. Sil, K. Garai, B. Reif, A. Bhunia, A. Ramamoorthy, Chem. Commun. 55 (2019) 4483–4486.
[26] S.A. Kotler, P. Walsh, J.R. Brender, A. Ramamoorthy, Chem. Soc. Rev. 43 (2014) 6692–6700.
[27] G. Bellomo, S. Bologna, L. Gonnelli, E. Ravera, M. Fragai, M. Lelli, C. Luchinat, Chem. Commun. 54 (2018) 7601–7604.
[28] T.C.T. Michaels, A. Šarić, S. Curk, K. Bernfur, P. Arosio, G. Meisl, A.J. Dear, S.I.A. Cohen, C.M. Dobson, M. Vendruscolo, S. Linse, T.P.J. Knowles, Nat. Chem. 12 (2020) 445–451.
[29] K. Broersen, W. Jonckheere, J. Rozenski, A. Vandersteen, K. Pauwels, A. Pastore, F. Rousseau, J. Schymkowitz, Protein Eng. Des. Sel. 24 (2011) 743–750.
[30] S.B. Stefan Berger, Experiment 11.17, in: Wiley-VCH (Ed.), 200 and More NMR Experiments: A Practical Course, Weinheim 2004, pp. 509–511.
[31] M. Marquart, J. Walter, J. Deisenhofer, W. Bode, R. Huber, Acta Crystallographica Section B 39 (1983) 480–490.
[32] A. Ortega, D. Amorós, J. García De La Torre, Biophys. J. 101 (2011) 892–898.
[33] G. Damaschun, H. Damaschun, K. Gast, D. Zirwer, Biochem. Mosc. 63 (1998) 259–275.
[34] J. Danielsson, J. Jarvet, P. Damberg, A. Gräslund, Magn. Reson. Chem. 40 (2002) S89–S97.

[35] D.K. Wilkins, S.B. Grimshaw, V. Receveur, C.M. Dobson, J.A. Jones, L.J. Smith, Biochemistry 38 (1999) 16424–16431.
[36] M. Lalowski, A. Golabek, C.A. Lemere, D.J. Selkoe, H.M. Wisniewski, R.C. Beavis, B. Frangione, T. Wisniewski, J. Biol. Chem. 271 (1996) 33623–33631.
[37] N.L. Fawzi, D.S. Libich, J. Ying, V. Tugarinov, G.M. Clore, Angew. Chem. Int. Ed. Eng. 53 (2014) 10345–10349.
[38] N.L. Fawzi, J. Ying, R. Ghirlando, D.A. Torchia, G.M. Clore, Nature 480 (2011) 268–272.
[39] S.L. Bernstein, N.F. Dupuis, N.D. Lazo, T. Wyttenbach, M.M. Condron, G. Bitan, D.B. Teplow, J.E. Shea, B.T. Ruotolo, C.V. Robinson, M.T. Bowers, Nat. Chem. 1 (2009) 326–331.
[40] G. Bitan, M.D. Kirkitadze, A. Lomakin, S.S. Vollers, G.B. Benedek, D.B. Teplow, Proc. Natl. Acad. Sci. U. S. A. 100 (2003) 330–335.
[41] R.C. Bailey, G.S. Eadie, F.H. Schmidt, Biometrics 30 (1974) 67–75.

# CHAPTER V. Metal-Organic Frameworks and amyloids

Work from this chapter has been published on:

**Leite, J. P.**, & Gales, L. (2019). Fluorescence properties of the amyloid indicator dye thioflavin T in constrained environments. Dyes and Pigments, 160, 64-70. doi:10.1016/j.dyepig.2018.07.049

**Leite, J. P.**, Rodrigues, D., Ferreira, S., Figueira, F., Almeida Paz, F. A., & Gales, L. (2019). Mesoporous Metal–Organic Frameworks as Effective Nucleating Agents in Protein Crystallography. Crystal Growth & Design, 19(3), 1610-1615. doi:10.1021/acs.cgd.8b01444

## 5.1 Introduction

Excerpt adapted from: *Mendes, R. F., Figueira, F.,* ***Leite, J. P.****, Gales, L., & Almeida Paz, F. A. (2020). Metal–organic frameworks: a future toolbox for biomedicine? Chemical Society Reviews, 49(24), 9121-9153. doi:10.1039/D0CS00883D*

Metal-Organic Frameworks (MOFs), and Coordination Polymers (CPs) in general, stand now as a well-established emerging class of materials which rose as serious contestants in a myriad of consumer and industrial applications in modern society (Czaja *et al.*, 2009; Silva *et al.*, 2015). Their structural versatility, stability and ability to be tailored into different crystallite sizes (ranging from bulk micrometric materials down to the nanometer size) paved the way for their use in many applications (Firmino *et al.*, 2017; Li *et al.*, 2016; Liang *et al.*, 2017; Mendes *et al.*, 2016; Mendes *et al.*, 2015; Pereira *et al.*, 2018; Ramaswamy *et al.*, 2014; Ren *et al.*, 2013; Zhu *et al.*, 2017).

Particularly interesting is the potential usefulness of these compounds in biomedical/bioengineering applications (Della Rocca *et al.*, 2011; Gimenez-Marques *et al.*, 2016; Keskin *et al.*, 2011; Sun *et al.*, 2013). In the past decade, we have witnessed a tremendous increase of research in various areas of biomedicine, which was vastly promoted by our better understanding of the various biological mechanisms governing the human body. A few areas of research, particularly those focused on anticancer and antitumoural studies, still face great challenges, mainly because of:

i) stability of the designed and prepared organic molecules under specific conditions;
ii) efficiency of delivery to the intended target and
iii) continuous and controlled biodistribution.

This class of hybrid materials shows real promising abilities for their use in biomedicine, particularly the ability of the co-existence in the same material of bioactive organic linkers and biologically relevant metal centres, sometimes with networks very stable in aqueous medium. MOFs can also truly sustain exceptional pore volume, thus opening the window towards bio-applications based on the encapsulation and protection of bioactive molecules (accomplished by trapping molecules in the framework and allowing their release over time with controllable kinetics) (Baeza *et al.*, 2017; Chowdhury, 2017b; Wang *et al.*, 2018). The literature is rich with studies of MOFs used in imaging (Chowdhury, 2017a; Shah *et al.*, 2018; Zhang *et al.*, 2019), as API (active pharmaceutical ingredient) delivery agents and phototherapy studies (Lan *et al.*, 2019; Liu *et al.*, 2016). Most reports lack, however, a transposition into real-life applications, those which may really interest pharmaceutical

industry. Figure 5.1 shows potential uses of MOF materials in biomedicine. In this chapter, the use of MOFs with amyloids will be explored.

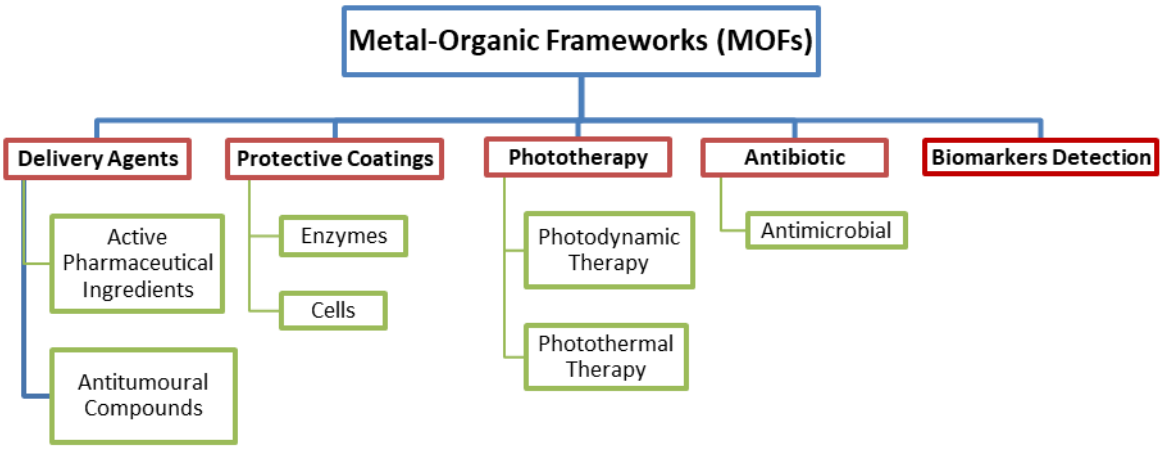


**Figure 5.1.** Possible applications of MOFs in biomedicine.

### 5.1.1 References

Baeza, A., Ruiz-Molina, D., & Vallet-Regi, M. (2017). Recent advances in porous nanoparticles for drug delivery in antitumoral applications: inorganic nanoparticles and nanoscale metal-organic frameworks. *Expert Opin. Drug Deliv., 14*(6), 783-796. doi:10.1080/17425247.2016.1229298

Chowdhury, M. A. (2017a). Metal-Organic-Frameworks as Contrast Agents in Magnetic Resonance Imaging. *Chembioeng Reviews, 4*(4), 225-239. doi:10.1002/cben.201600027

Chowdhury, M. A. (2017b). Metal-organic-frameworks for biomedical applications in drug delivery, and as MRI contrast agents. *J. Biomed. Mater. Res. Part A, 105*(4), 1184-1194. doi:10.1002/jbm.a.35995

Czaja, A. U., Trukhan, N., & Muller, U. (2009). Industrial applications of metal-organic frameworks. *Chemical Society Reviews, 38*(5), 1284-1293. doi:10.1039/b804680h

Della Rocca, J., Liu, D. M., & Lin, W. B. (2011). Nanoscale Metal-Organic Frameworks for Biomedical Imaging and Drug Delivery. *Acc. Chem. Res., 44*(10), 957-968. doi:10.1021/ar200028a

Firmino, A. D. G., Mendes, R. F., Antunes, M. M., Barbosa, P. C., Vilela, S. M. F., Valente, A. A., Figueiredo, F. M. L., Tomé, J. P. C., & Paz, F. A. A. (2017). Robust Multifunctional Yttrium-Based Metal Organic Frameworks with Breathing Effect. *Inorganic Chemistry, 56*(3), 1193-1208. doi:10.1021/acs.inorgchem.6b02199

Gimenez-Marques, M., Hidalgo, T., Serre, C., & Horcajada, P. (2016). Nanostructured metal-organic frameworks and their bio-related applications. *Coordination Chemistry Reviews, 307*, 342-360. doi:10.1016/j.ccr.2015.08.008

Keskin, S., & Kizilel, S. (2011). Biomedical Applications of Metal Organic Frameworks. *Industrial & Engineering Chemistry Research, 50*(4), 1799-1812. doi:10.1021/ie101312k

Lan, G., Ni, K., & Lin, W. (2019). Nanoscale metal–organic frameworks for phototherapy of cancer. *Coordination Chemistry Reviews, 379*, 65-81. doi:10.1016/j.ccr.2017.09.007

Li, L., Zhu, Y. L., Zhou, X. H., Brites, C. D. S., Ananias, D., Lin, Z., Paz, F. A. A., Rocha, J., Huang, W., & Carlos, L. D. (2016). Visible-Light Excited Luminescent Thermometer Based on Single Lanthanide Organic Frameworks. *Advanced Functional Materials, 26*(47), 8677-8684. doi:10.1002/adfm.201603179

Liang, J., Liang, Z. B., Zou, R. Q., & Zhao, Y. L. (2017). Heterogeneous Catalysis in Zeolites, Mesoporous Silica, and Metal-Organic Frameworks. *Advanced Materials, 29*(30), 1701139 doi:10.1002/adma.201701139

Liu, J. J., Yang, Y., Zhu, W. W., Yi, X., Dong, Z. L., Xu, X. N., Chen, M. W., Yang, K., Lu, G., Jiang, L. X., & Liu, Z. (2016). Nanoscale metal-organic frameworks for combined photodynamic & radiation therapy in cancer treatment. *Biomaterials, 97*, 1-9. doi:10.1016/j.biomaterials.2016.04.034

Mendes, R. F., Antunes, M. M., Silva, P., Barbosa, P., Figueiredo, F., Linden, A., Rocha, J., Valente, A. A., & Paz, F. A. A. (2016). A Lamellar Coordination Polymer with Remarkable Catalytic Activity. *Chem. Eur. J., 22*(37), 13136-13146. doi:10.1002/chem.201602157

Mendes, R. F., & Paz, F. A. A. (2015). Transforming metal-organic frameworks into functional materials. *Inorganic Chemistry Frontiers, 2*(6), 495-509. doi:10.1039/c4qi00222a

Pereira, C. F., Figueira, F., Mendes, R. F., Rocha, J., Hupp, J. T., Farha, O. K., Simões, M. M. Q., Tomé, J. P. C., & Paz, F. A. A. (2018). Bifunctional Porphyrin-Based Nano-Metal-Organic Frameworks: Catalytic and Chemosensing Studies. *Inorganic Chemistry, 57*(7), 3855-3864. doi:10.1021/acs.inorgchem.7b03214

Ramaswamy, P., Wong, N. E., & Shimizu, G. K. H. (2014). MOFs as proton conductors - challenges and opportunities. *Chemical Society Reviews, 43*(16), 5913-5932. doi:10.1039/c4cs00093e

Ren, Y. Q., Chia, G. H., & Gao, Z. Q. (2013). Metal-organic frameworks in fuel cell technologies. *Nano Today, 8*(6), 577-597. doi:10.1016/j.nantod.2013.11.004

Shah, S. S. A., Najam, T., Cheng, D., Hafeez, A., Lu, Y., & Waseem, A. (2018). Nano-metal Organic Frame Work an Excellent Tool for Biomedical Imaging. *Current Medical Imaging, 14*(5), 669-674. doi:10.2174/1573405613666170919151454

Silva, P., Vilela, S. M. F., Tomé, J. P. C., & Paz, F. A. A. (2015). Multifunctional metal-organic frameworks: from academia to industrial applications. *Chemical Society Reviews, 44*(19), 6774-6803. doi:10.1039/c5cs00307e

Sun, C. Y., Qin, C., Wang, X. L., & Su, Z. M. (2013). Metal-organic frameworks as potential drug delivery systems. *Expert Opin. Drug Deliv., 10*(1), 89-101. doi:10.1517/17425247.2013.741583

Wang, L., Zheng, M., & Xie, Z. G. (2018). Nanoscale metal-organic frameworks for drug delivery: a conventional platform with new promise. *J. Mater. Chem. B, 6*(5), 707-717. doi:10.1039/c7tb02970e

Zhang, Z., Sang, W., Xie, L. S., & Dai, Y. L. (2019). Metal-organic frameworks for multimodal bioimaging and synergistic cancer chemotherapy. *Coordination Chemistry Reviews, 399*, 213022. doi:10.1016/j.ccr.2019.213022

Zhu, L., Liu, X. Q., Jiang, H. L., & Sun, L. B. (2017). Metal-Organic Frameworks for Heterogeneous Basic Catalysis. *Chemical Reviews, 117*(12), 8129-8176. doi:10.1021/acs.chemrev.7b00091

## 5.2. Paper IV: Fluorescence properties of the amyloid indicator dye thioflavin-T in constrained environments

Work contributions:

ThT:salicylate complex was first synthesized by Ricardo Amorim. TGA and fluorescent microscopy measurements made with assistance from Seyedali Emani and Adélio Mendes (FEUP, Porto, Portugal) and Paula Sampaio (i3S, Porto, Portugal), respectively.

Dyes and Pigments 160 (2019) 64–70

Contents lists available at ScienceDirect

Dyes and Pigments

journal homepage: www.elsevier.com/locate/dyepig

# Fluorescence properties of the amyloid indicator dye thioflavin T in constrained environments

José P. Leite[a,b,c], Luís Gales[a,b,c,*]

[a] i3S – Instituto de Investigação e Inovação em Saúde, Rua Alfredo Allen, 208, Porto, Portugal
[b] IBMC – Instituto de Biologia Molecular e Celular Universidade do Porto, Rua Alfredo Allen, 208, Porto, Portugal
[c] ICBAS – Instituto de Ciências Biomédicas Abel Salazar, Rua de Jorge Viterbo Ferreira 228, Porto, Portugal

ARTICLE INFO

*Keywords:*
Thioflavin T
Amyloid
Fluorescent marker
Photophysical properties
MOF
Metal-organic framework

ABSTRACT

Proteins and peptides may lose their structural and functional properties and form amyloid-like fibrous deposits that are associated with more than 20 diseases. Several biophysical methods are used to classify a protein aggregate as amyloid; among them, thioflavin T (ThT) fluorescence is certainly the most used *in vitro*. Nevertheless, the molecular basis of ThT binding to amyloid fibrils and its implications in the changes of the photophysical properties of ThT are poorly understood. Here, we investigated the ThT fluorescence behaviour in four crystalline frameworks in which the ThT molecules are (i) packed in a rigid dimeric conformation or (ii) disordered in porous crystals with different cage dimensions. Our results show that ThT fluorescence is enhanced when this fluorophore is adsorbed in the flat surfaces of large pores. ThT molecules trapped in a rigid conformation in small crystal cages show very weak ThT fluorescence.

## 1. Introduction

Amyloids are aggregates of proteins folded in β-rich structures forming linear fibrils that are linked to the development of several diseases [1]. Thioflavin–T (ThT) and Congo Red are the most used molecular probes for amyloid fibril detection [2]. ThT is used as the chloride salt of a cation ($ThT^+$) that consists of an N-methylated benzothiazole linked to a dimethylaniline ring (Scheme 1).

The binding mode of ThT to amyloid fibres is difficult to investigate by high-resolution techniques, such as X-ray crystallography or Nuclear Magnetic Resonance, due to the insolubility and heterogeneity of the amyloid samples. Co-crystallization studies of ThT with short peptides that presumably resemble the amyloid fibril core structure [3] are scarce. The structure of the complex of ThT with an engineered protein that mimics a segment of β-rich peptide self-assembly was obtained [4], showing that ThT binds perpendicular to the β-strands. Moreover, co-crystal structures of ThT with two other proteins, β-2 microglobulin [5] and the peripheral site of *Torpedo californica* acetylcholinesterase [6], were determined. The influence of the protein state, monomeric or oligomeric, in ThT fluorescence was investigated in the case of β-2 microglobulin, a protein involved in dialysis-associated amyloidosis [5], while in the case of the *Torpedo californica* acetylcholinesterase: ThT complex, the influence of additional ligands that form ternary complexes and change ThT fluorescence was discussed [6]. The lack of more high-resolution models leads to the proposal of several conflicting models in the literature for binding mode of ThT towards amyloid fibrils.

In fact, monomeric [7–9], dimeric [10] and, more rarely, micellar forms [11] of ThT have been proposed to be involved in amyloid binding. The monomeric hypothesis assumes that ThT behaves as a molecular rotor [12,13], where adhesion to amyloid fibers blocks rotation, which suppresses quenching and a high quantum yield of fluorescence [8,14]. The observed fluorescence enhancement of ThT in viscous solvents supports this hypothesis [8]. On the other hand, the dimeric hypothesis assumes that the characteristic ThT fluorescence is due to an excited-state dimer (excimer) that induces the observed red shift due to the formation of an increased conjugated system [15].

Amyloid fibres are large protein aggregates with highly ordered β-sheet arrangements. Single crystal X-ray diffraction of an engineered β-rich protein [4] and confocal microscopy studies of bovine insulin and bovine β-lactoglobulin spherulites containing radially arranged amyloid fibrils [7] suggest that ThT binds with its long axis parallel to the amyloid fiber axis. Moreover, X-ray insulin fibre diffraction studies revealed structural alterations in the equatorial direction upon ThT binding [16]. Molecular dynamics simulations suggest that ThT binds perpendicular to the β-strands [17,18] despite the propensity to bind parallel to the β-strands at the end of β-sheets [17].

A proper binding environment for ThT to induce fluorescence due to

* Corresponding author. i3S – Instituto de Investigação e Inovação em Saúde, Rua Alfredo Allen, 208, Porto, Portugal.
*E-mail address:* lgales@ibmc.up.pt (L. Gales).

https://doi.org/10.1016/j.dyepig.2018.07.049
Received 12 January 2018; Received in revised form 27 June 2018; Accepted 27 July 2018
Available online 29 July 2018
0143-7208/ 

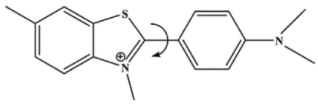

**Scheme 1.** Thioflavin-T cation.

the block of free internal rotation may be provided by cavities, channels, or grooves that may exist in amyloid fibrils [2]. Cavities of 8-9Å, long enough to incorporate the entire ThT molecule, were shown to induce ThT fluorescence [10,19]. It is conceivable that cavities with such dimensions are present in amyloid protofilaments or that are formed during the assembly of protofilaments into a mature fibril. However, ThT monomer has most often been proposed to bind in narrow grooves formed between the side chains of the residues of the β-strands forming the β-sheet [7,18,20].

ThT fluorescence assay is used to study amyloid formation with many peptides and proteins. Thus, it is likely that the fluorescence enhancement arises from physical restrains to the fluorophore configuration rather than to interaction with specific protein residues. Here we investigate the photophysical properties of ThT in physically restrained environments.

## 2. Experimental

### 2.1. Reagents

Unless stated otherwise, all reagents were of analytical grade, purchased from Sigma-Aldrich (USA) and used without further purification.

### 2.2. Crystal synthesis

#### 2.2.1. ThT: salicylate complex

Suitable crystals were obtained by dissolving 0.032 g of sodium salicylate and 0.032 g of ThT in 1 ml of methanol and allowing the mixture to react for 24 h at 80 °C in a sealed scintillation vial. The mixture was slowly cooled down for 10 h until room temperature was reached. Suitable crystals for X-ray diffraction were mounted on Hampton Research CryoLoops using paratone oil (Hampton Research, USA). The structure of the complex was determined by single crystal X-ray diffraction. Data was collected at room temperature with a Gemini PX Ultra equipped with Cu$K_\alpha$ radiation ($\lambda$ = 1.54184 Å). The structure was solved by direct methods using SHELXS-97 and refined with SHELXL-97 [21]. One of the three salycilate molecules of the asymmetric unit was refined isotropically, all other carbon, nitrogen, sulphur and oxygen atoms were refined anisotropically. Hydrogen atoms were placed at their idealized positions using appropriate HFIX instructions in SHELXL and included in subsequent refinement cycles. Full details of the data collection and refinement and tables of atomic coordinates, bond lengths and angles, and torsion angles have been deposited with the Cambridge Crystallographic Data Centre (CCDC, 1816441).

#### 2.2.2. Metal-organic frameworks (MOFs) synthesis and ThT soaking

MOF-5, MOF-177 and UMCM-1 were synthesized based on [22–24]. Briefly, for MOF-5, zinc nitrate hexahydrate ($1.76 \times 10^{-3}$ mol) was dissolved in 15 ml of N,N-Diethylformamide (DEF), followed by the addition of benzene-1,4-dicarboxylic acid ($H_2BDC$; $5.93 \times 10^{-4}$ mol). For MOF-177, zinc nitrate hexahydrate ($1.18 \times 10^{-3}$ mol) and 1,3,5-Tris(4-carboxyphenyl)benzene ($H_3BTB$; $1.5 \times 10^{-4}$ mol) were dissolved in DEF (10 ml). Finally, for UMCM-1, zinc nitrate hexahydrate ($6.5 \times 10^{-4}$ mol), $H_2BDC$ ($1.63 \times 10^{-4}$ mol) and $H_3BTB$ ($1.46 \times 10^{-4}$ mol) were dissolved in DEF (6 ml). All three mixtures were sonicated in a water bath for 30 min and then placed in sealed vials at 85 °C for 72 h. Afterwards, DEF was removed and crystals were washed with N,N-Dimethylformamide (DMF). For dye soaking, ThT was dissolved at 3 mM in DMF and crystals were immersed for 5 days, with periodic solvent removal and fresh ThT added, prior to thermogravimetric analysis and fluorescence microscopy observations.

### 2.3. Thermogravimetric analysis (TGA)

TGA experiments were performed in a NETZSCH TG 209 F1 thermal analysis system (NETZSCH, Germany) under nitrogen atmosphere, with a heating rate of 5 °C/min from 30 to 600 °C.

### 2.4. $A\beta_{1\text{-}42}$ fibril preparation and fluorescence imaging

Amyloid-$\beta_{1\text{-}42}$ was purchased from Bachem (Switzerland). Lyophilized peptide (1 mg) was suspended in 1,1,1,3,3,3-Hexafluoro-2-propanol and incubated overnight at room temperature. Solvent was then removed with $N_2$ stream. The resulting peptide film was suspended in DMSO and stored at −20 °C. To grow amyloid fibrils, $A\beta_{1\text{-}42}$ was diluted to 50 μM in 50 mM Tris-HCl pH7.4, 1 mM EDTA buffer and incubated for 7 days at 37 °C. ThT was added to a final concentration of 150 μM and samples were placed in closed chamber to avoid evaporation during fluorescence microscopy analysis. Fibril-free ThT was used as a control. Fluorescence signal integrated across a 258 μm × 128 μm area.

### 2.5. Fluorescence microscopy imaging of MOF crystals

MOF crystals (soaked and non-soaked with ThT) were imaged using a Leica TCS SP5 II laser scanning confocal system. Samples were excited with an Ar 458 nm laser, and fluorescence was collected through a Leica DMI6000-CS inverted microscope, with a 470–745 nm filter (Leica Microsystems, Germany). All data was collected with identical settings (*e.g* lamp power, gain, signal integrated area and exposure) as well as the same excitation laser, so that a quantitative analysis is possible. Fluorescence intensity was normalized to the ThT ⊂ UMCM-1 crystal sample. Image data was analysed in LAS X software (Leica Microsystems, Germany).

## 3. Results and discussions

ThT has been widely used to stain amyloid aggregates. We started this work by confirming the characteristic fluorescent behaviour of ThT with fibers of amyloid β peptide (section 3.1). To further investigated the photophysical behaviour of ThT, we report the co-crystal structure of ThT: salicylate and its fluorescence properties (section 3.2). To our knowledge, there are only four crystallographic studies with this dye: the structure of free ThT [18] and structures of ThT in complex with proteins β-2 microglobulin and the peripheral site of *Torpedo californica* acetylcholinesterase [5,6] and with an engineered β-rich protein [17].

ThT: salicylate, as will be shown in sections 3.2, forms a compact non-porous crystal in which ThT molecules movement or rotation is nearly impossible. In the third section, we soaked three porous crystalline frameworks with ThT. The pore dimensions of the crystals were different which allowed us to access its influence on the fluorescence behaviour of the dye. It is important to mention that the selected crystals (MOF-5, MOF-177 and UMCM-1) are highly porous solids, containing a high density of channels which accommodate small molecule dye, such as ThT. ThT molecules can travel into these solvent channels and colour the crystals.

### 3.1. ThT fluorescence of amyloid β fibrils

Aβ peptides are 36–43 residues in length, constituting the main component of amyloid aggregates found in the brains of Alzheimer's patients, with $A\beta_{1\text{-}40}$ and $A\beta_{1\text{-}42}$ being the two most common and studied forms. The peptides derive from the amyloid precursor protein (APP), which is present in neurons, oligodendrocytes and at neuronal

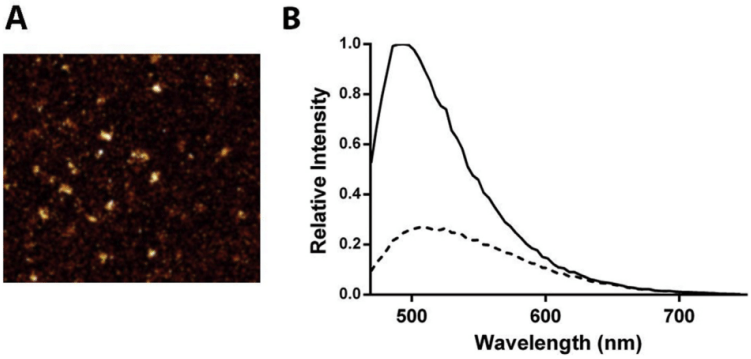


**Fig. 1.** (A) ThT fluorescence images of $A\beta_{1-42}$ fibrils collected at 506 nm (150 μm × 128 μm area). (B) Emission spectra of $A\beta_{1-42}$ fibrils (solid line) and the control, ThT without fibrils (dotted line), when excited at 458 nm. Signal integrated across a 258 μm × 128 μm area.

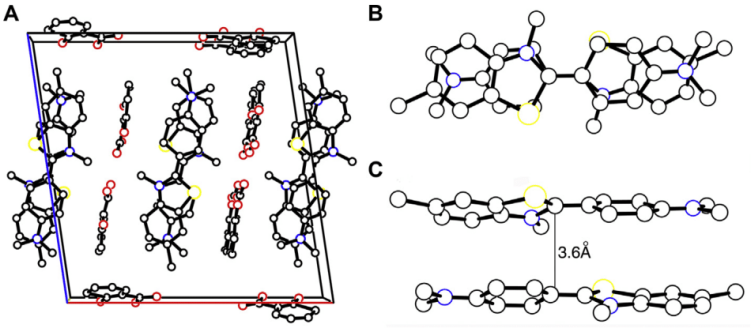


**Fig. 2.** Crystal structure of ThT: salycilate complex. View of the unit cell along the *b* axis (A) and two orthogonal views of the ThT dimers (B and C).

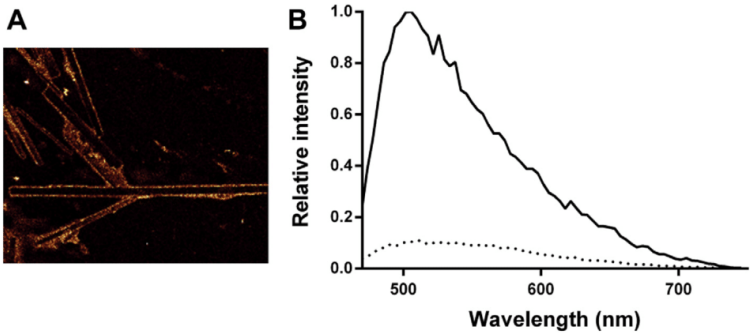


**Fig. 3.** (A) Fluorescence images of THT:salycilate crystals collected at 506 nm. (B) Emission spectra of the crystals at the border (solid line) and in the bulk (dotted line), when excited at 458 nm.

synapses.

$A\beta_{1-42}$ fibrils were grown for seven days. ThT was added prior to excitation at 458 nm and fluorescence was collected through a inverted microscope. The characteristic ThT fluorescence spectrum is observed although with underestimated fluorescence enhancement (Fig. 1) because the microscope does not have sufficient resolution to measure the fluorescence of the amyloid fibers directly; the signal is integrated over an area of 258 μm × 128 μm which includes the background (ThT in solution) as can be observed in Fig. 1.

The fluorescence of the non-conventional ThT samples that will be described in the next sections will be investigated using this same procedure used with the $A\beta_{1-42}$ amyloid samples. Importantly, unlike amyloid samples, the size of the crystals will enable directly measurement of ThT fluorescence.

### 3.2. *ThT: salicylate crystal*

The crystal structure is shown in Fig. 2. ThT forms dimers, with the molecules stacked in a head-to-tail disposition, 3.6 Å apart. The dimers are packed in columns along the *b* crystallographic axis and the columns are intercalated by the salicylate molecules. The dihedral angle between the two planar benzothiazole and dimethylaniline moieties are

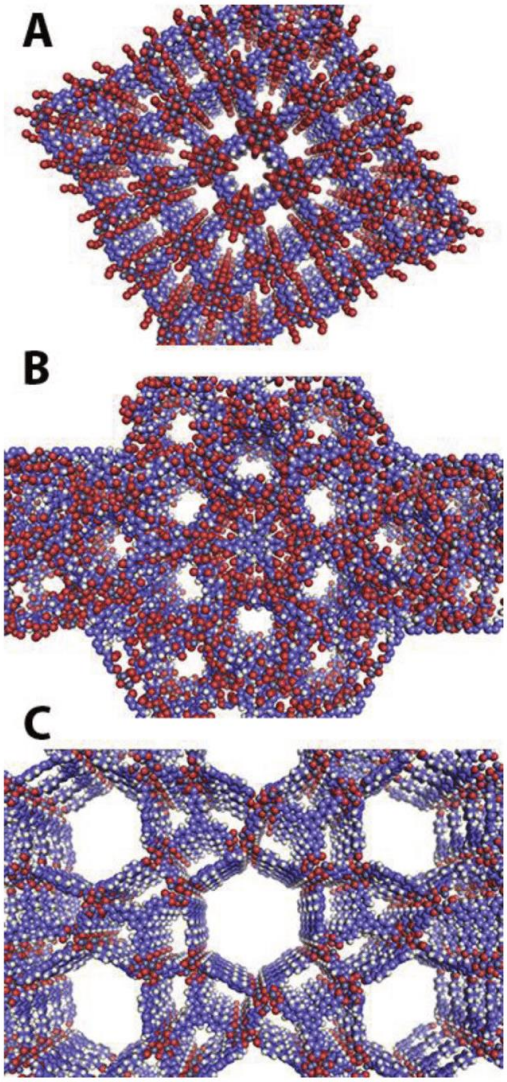


**Fig. 4.** Pore topologies of the crystals incubated with ThT: MOF-5 (A), MOF-177(B) and UMCM-1(C).

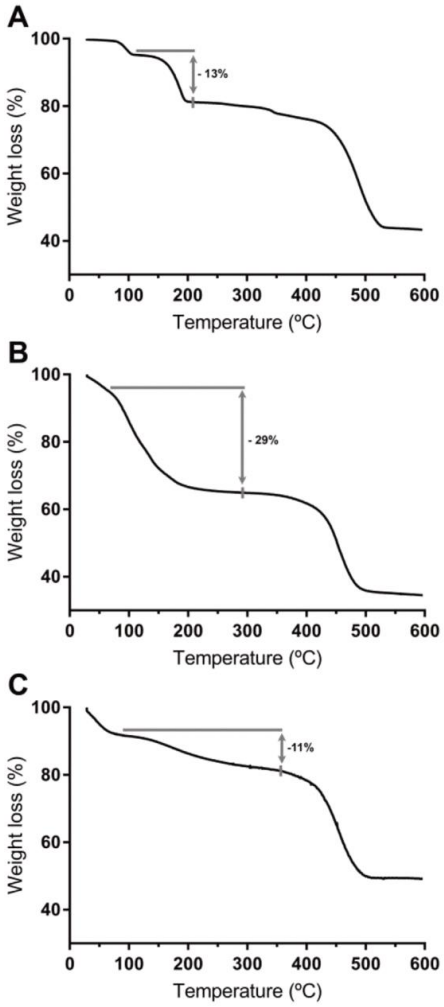


**Fig. 5.** Thermogravimetric analysis of MOF-5 (A), MOF-177(B) and UMCM-1 (C) pre-incubated with ThT. The estimated ThT mass percentages are displayed in the figure.

26° and 32° in the two molecules of the asymmetric unit. The head-to-tail arrangement was also observed in the other published structure of the free ThT [18] and maximizes the distance between the neighbouring $N^+$ cations. The dihedral angles of ThT in our crystal structure are slightly bigger than that previously obtained (24° and 20°) [18] and smaller than the computed for the ground state (37°) [5].

Fluorescence microscopy images of the crystals were taken (Fig. 3). The crystals exhibit very low fluorescence except near the surface, presumably due to ThT molecules that adsorb at the crystals faces. The packed ThT dimers are usually associated either with the presence of an excimer [6] or, alternatively, results in auto-quenching [5]. In our crystals, most likely the dimers are quenched. The same photophysical behaviour of ThT dimers was observed in the crystal structure of ThT with β-2 microglobulin.

Next, we investigated the photophysical properties of ThT molecules absorbed in crystals displaying diverse pore geometries.

### 3.3. ThT inclusion in MOF-5, MOF-177 and UMCM-1

Three metal-organic frameworks were used: MOF-5, MOF-177 and UMCM-1. These crystals are built with organic linkers possessing aryl carboxylic acid coordinating groups and zinc centres. Thus, the interactions of ThT molecules with the framework should be similar for the three crystals and any difference in the fluorescence properties of ThT is most likely related with the pore dimensions of the crystals.

MOF-5 has 1D channels with pore diameters along the channel varying from 7.8 to 15.0 Å with a total pore volume of 1.55 $cm^3/g$ (Fig. 4). It was already shown that several organic dyes, such as Pyronin Y, Pyronin B, Thionin, Toluidine Blue O, Azure A, Brilliant Green, and Methyl Yellow can diffuse through the MOF-5 framework, while Congo red and Coomassie Blue cannot penetrate [22]. MOF-177 displays a large pore volume (1.89 $cm^3/g$) and a uniform micropore size distribution with a median pore diameter of 12.7 Å. It can accommodate

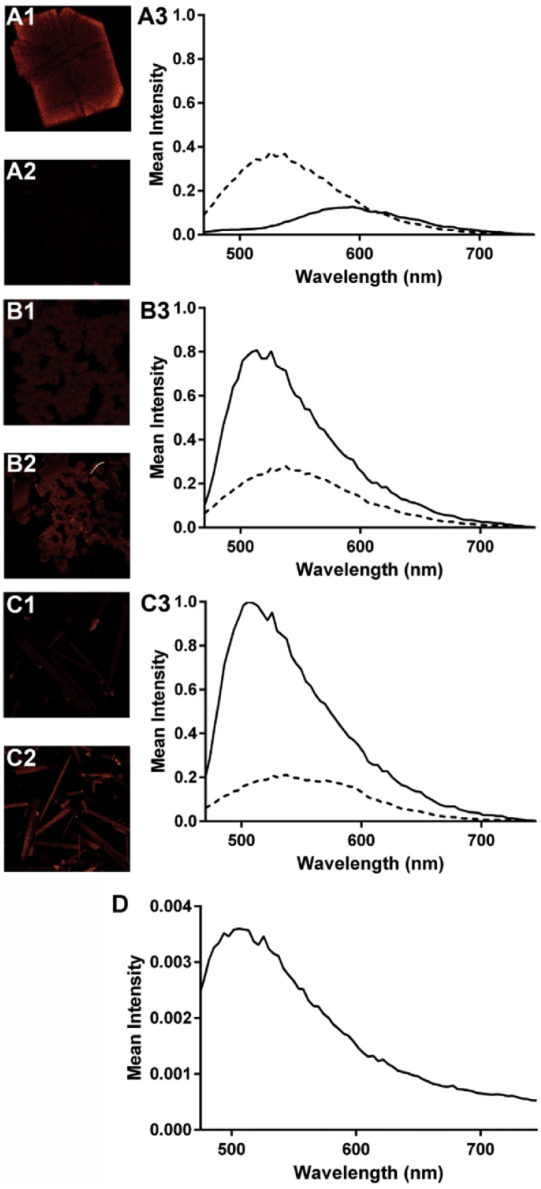


**Fig. 6.** Fluorescence images of the crystals (MOF-5(A), MOF-177(B) and UMCM-1(C)) unloaded (1) and loaded with ThT (2), collected using blue light (458 nm) excitation. Emission spectra of ThT loaded crystals (continuous line) and unloaded (dashed line), when excited at 458 nm, are shown in A3, B3 and C3. ThT fluorescence in solution in negligible with respect to that in the crystals (D). (For interpretation of the references to colour in this figure legend, the reader is referred to the Web version of this article.)

spheres of diameter 11.8 and 10.8 Å respectively without touching any framework atoms [24]. UMCM-1 displays a bimodal distribution of micropores, in cage-like structures, centred in 1.4 nm and 3.2 nm [23] pore volume (2.14 $cm^3/g$).

Single crystal X-ray diffraction analysis of the three MOFs incubated with ThT revealed that the guests are disordered, despite the marked colour change of crystals observed due to absorption of ThT molecules. Thermogravimetric analysis was used to estimate the amount of ThT incorporated in the crystals (Fig. 5). MOF-177 accommodates ThT more efficiently than the two other MOFs (guest ThT represents about 29% of the MOF177 crystal mass and around 11–13% of the MOF5 and of the UMCM-1 mass).

The fluorescent properties of ThT molecules trapped in the MOFs crystals cages were investigated (Fig. 6). The emission spectra of the pure crystals were also collected. MOF-5 in particular exhibits high luminescence at 535 nm upon excitation at 458 nm, which was previously assigned to ZnO impurities [25]. ThT inclusion resulted in a significant fluorescence enhancement in MOF-177 and UMCM-1 crystals. In contrast, ThT ⊂ MOF-5 crystals displayed very modest intensity. ThT fluorescence in solution is negligible when compared to ThT molecules that enter the MOF crystals.

To understand the photophysical behaviour of ThT trapped in the crystals, we used the compact ThT: salycilate crystal structure to estimate the minimum dimensions of a cage that could incorporate a ThT molecule (Fig. 7). Accordingly, a cage with a cross-section diameter above 9.3 Å allows free rotation between the two planar benzothiazole and dimethylaniline moieties. Our results are summarized in Fig. 7, together with the ones of a previous work that investigated the ThT fluorescence properties when bound to cyclodextrins [10]. The pore dimensions (atom to atom distances), measured in crystal structures deposited in the Cambridge Crystallographic Database, are also presented in Fig. 7. It should be noticed, however that porous crystals as well as cyclodextrins, most likely display flexible structures.

β-cyclodextrin displays an inner diameter smaller than the minimum requested for ThT inclusion. Thus, most likely there is an alteration in the structure of β-cyclodextrin induced by ThT binding. ThT probably remains tightly bound and the rotation between the two ring systems is very restricted. MOF-5 displays square like cages of 7.7 × 7.7 Å. The distance between opposite corners of these cages is 10.1 Å. Similarly, the rotation of the ThT aromatic rings should be very limited inside MOF-5 crystals. Thus, a fix angle between the two conjugated rings of ThT seems to be associated with a weak fluorescence signal.

On the other hand, γ-cyclodextrin, MOF-177 and UMCM-1 cages should not present steric limitation to the rotation of ThT rings. ThT molecules trapped inside these cages all exhibit fluorescence. ThT ⊂ UMCM-1 crystals exhibit the highest ThT fluorescence despite the lowest ThT mass content (11%). UMCM-1 displays large channels, with hexagonal shape (3.2 nm between opposite corners) and flat surfaces decorated by aromatic rings (Fig. 4C). Each of pores' flat surfaces is 1.8 nm wide; ThT molecules may attach along these flat surfaces without contact with the other pore walls.

Our findings point to an absence of ThT fluorescence in systems where the rotation between the two cyclic moieties of ThT molecules is blocked (ThT: salicylate crystal) or severely restricted (ThT ⊂ MOF-5). Cavities with minimum diameter around 10.8 Å (ThT ⊂ MOF-177) induced ThT fluorescence, as was already observed [10]. However, ThT fluorescence is stronger in larger channels (ThT ⊂ UMCM-1) in which ThT molecules interact with just one of the flat sides of the channel.

Amyloid fibers are β-sheet rich linear polymers. Conflicting structural models of amyloid are found in the literature. While some suggest that Aβ peptides [26,27], the plasma protein transthyretin [28], polyglutamines [29], the SH3 domain of phosphatidylinositol-3′-kinase [30], and pathogenic SOD1 mutant proteins [31], form water-filled nanotubes many others propose non-tubular structures for amyloid. In our opinion, ThT fluorescence enhancement most likely arises from the adsorption of ThT molecules to β-sheets at the fibril surface because they are more accessible than existing channels or cavities. We showed in this work that ThT fluorescence enhancement in large channels (3.2 nm) is not compatible with most of the amyloid nanotubular models proposed (around 1 nm).

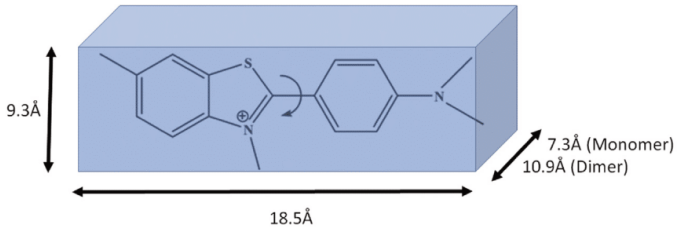


| Framework /pore size (Å) | ThT fluorescence | Reference |
|---|---|---|
| β-cyclodextrin / 8.7 | No | [10] |
| MOF-5 / 7.7 (min) x10.1(max) | No | This work |
| γ-cyclodextrin / 10.7 | Yes | [10] |
| MOF-177 / 10.8 | Yes | This work |
| UMCM-1 / 12.8 and 32.0 | Yes | This work |

**Fig. 7.** Top: Minimum cage dimensions that allow the inclusion of ThT molecules. Bottom: Summary of ThT fluorescence properties when incorporated in molecular and crystal cages.

## 4. Conclusion

In conclusion, our observations point to ThT fluorescence being enhanced when intrinsic rotation of ThT molecules is hampered, but not barred by extend adsorption on surfaces. Molecules or assembly of molecules that trap ThT in a rigid conformation should not induce ThT fluorescence. Most probably, ThT fluorescence in presence of amyloid aggregates arises from ThT binding to flat amyloid β-sheets.

## Acknowledgments

This work was supported by Norte-01-0145-FEDER-000008- Porto Neurosciences and Neurologic Disease Research Initiative at I3S, supported by Norte Portugal Regional Opera-tional Programme (NORTE2020), under the PORTUGAL 2020 Partnership Agreement, by COMPETE 2020—Operacional Programme for Competitiveness and Internationalisation (POCI), Portugal 2020, through the European Regional Development Fund (FEDER), and by Portuguese funds through FCT—Fundação para a Ciência e a Tecnologia/Ministério da Ciência, Tecnologia e Ensino Superior in the framework of the project "Institute for Research and Innovation in Health Sciences" (POCI-01-0145-FEDER-007274) and grant SFRH/BD/129921/2017. We would like to thank Paula Sampaio for their technical assistance in fluorescence microscopy and Seyedali Emami and Adélio Mendes in thermogravimetric analysis.

## References

[1] Knowles TPJ, Vendruscolo M, Dobson CM. The amyloid state and its association with protein misfolding diseases. Nat Rev Mol Cell Biol 2014;15(6):384–96.
[2] Groenning M. Binding mode of Thioflavin T and other molecular probes in the context of amyloid fibrils-current status. J Chem Biol 2010;3(1):1–18.
[3] Nelson R, Sawaya MR, Balbirnie M, Madsen AØ, Riekel C, Grothe R, et al. Structure of the cross-β spine of amyloid-like fibrils. Nature 2005;435(7043):773–8.
[4] Biancalana M, Makabe K, Koide A, Koide S. Molecular mechanism of thioflavin-T binding to the surface of β-rich peptide self-assemblies. J Mol Biol 2009;385(4):1052–63.
[5] Wolfe LS, Calabrese MF, Nath A, Blaho DV, Miranker AD, Xiong Y. Protein-induced photophysical changes to the amyloid indicator dye thioflavin T. Proc Natl Acad Sci USA 2010;107(39):16863–8.
[6] Harel M, Sonoda LK, Silman I, Sussman JL, Rosenberry TL. Crystal structure of thioflavin T bound to the peripheral site of Torpedo californica acetylcholinesterase reveals how thioflavin T acts as a sensitive fluorescent reporter of ligand binding to the acylation site. J Am Chem Soc 2008;130(25):7856–61.
[7] Krebs MRH, Bromley EHC, Donald AM. The binding of thioflavin-T to amyloid fibrils: localisation and implications. J Struct Biol 2005;149(1):30–7.
[8] Stsiapura VI, Maskevich AA, Kuzmitsky VA, Uversky VN, Kuznetsova IM, Turoverov KK. Thioflavin T as a molecular rotor: fluorescent properties of thioflavin T in solvents with different viscosity. J Phys Chem B 2008;112(49):15893–902.
[9] Friedhoff P, Schneider A, Mandelkow EM, Mandelkow E. Rapid assembly of Alzheimer-like paired helical filaments from microtubule-associated protein tau monitored by fluorescence in solution. Biochemistry 1998;37(28):10223–30.
[10] Groenning M, Olsen L, van de Weert M, Flink JM, Frokjaer S, Jørgensen FS. Study on the binding of Thioflavin T to β-sheet-rich and non-β-sheet cavities. J Struct Biol 2007;158(3):358–69.
[11] Khurana R, Coleman C, Ionescu-Zanetti C, Carter SA, Krishna V, Grover RK, et al. Mechanism of thioflavin T binding to amyloid fibrils. J Struct Biol 2005;151(3):229–38.
[12] Freire S, De Araujo MH, Al-Soufi W, Novo M. Photophysical study of Thioflavin T as fluorescence marker of amyloid fibrils. Dyes Pigments 2014;110:97–105.
[13] Amdursky N, Erez Y, Huppert D. Molecular rotors: what lies behind the high sensitivity of the thioflavin-T fluorescent marker. Accounts Chem Res 2012;45(9):1548–57.
[14] Stsiapura VI, Maskevich AA, Kuzmitsky VA, Turoverov KK, Kuznetsova IM. Computational study of thioflavin T torsional relaxation in the excited state. J Phys Chem 2007;111(22):4829–35.
[15] Ilanchelian M, Ramaraj R. Emission of thioflavin T and its control in the presence of DNA. J Photochem Photobiol Chem 2004;162(1):129–37.
[16] Groenning M, Norrman M, Flink JM, van de Weert M, Bukrinsky JT, Schluckebier G, et al. Binding mode of Thioflavin T in insulin amyloid fibrils. J Struct Biol 2007;159(3):483–97.
[17] Wu C, Wang Z, Lei H, Duan Y, Bowers MT, Shea J-E. The binding of Thioflavin-T and its neutral analog BTA-1 to protofibrils of the Alzheimer Aβ(16-22) peptide probed by molecular dynamics simulations. JMB (J Mol Biol) 2008;384(3):718–29.
[18] Rodríguez-Rodríguez C, Rimola A, Rodríguez-Santiago L, Ugliengo P, Álvarez-Larena A, Gutiérrez-De-Terán H, et al. Crystal structure of thioflavin-T and its binding to amyloid fibrils: insights at the molecular level. Chem Commun 2010;46(7):1156–8.
[19] Retna Raj C, Ramaraj R. Influence of cyclodextrin complexation on the emission of thioflavin T and its off-on control. J Photochem Photobiol Chem 1999;122(1):39–46.
[20] Wu C, Wang Z, Lei H, Zhang W, Duan Y. Dual binding modes of Congo red to amyloid protofibril surface observed in molecular dynamics simulations. J Am Chem Soc 2007;129(5):1225–32.
[21] Sheldrick GM. Crystal structure refinement with SHELXL. Acta Crystallogr C: Struct Chem 2015;71:3–8.
[22] Han S, Wei Y, Valente C, Lagzi I, Gassensmith JJ, Coskun A, et al. Chromatography in a single metal-organic framework (MOF) crystal. J Am Chem Soc 2010;132(46):16358–61.
[23] Koh K, Wong-Foy AG, Matzger AJ. A crystalline mesoporous coordination copolymer with high microporosity. Angew Chem Int Ed Engl 2008;47(4):677–80.
[24] Chae HK, Siberio-Perez DY, Kim J, Go Y, Eddaoudi M, Matzger AJ, et al. A route to

high surface area, porosity and inclusion of large molecules in crystals. Nature 2004;427(6974):523–7.
[25] Feng PL, Perry Iv JJ, Nikodemski S, Jacobs BW, Meek ST, Allendorf MD. Assessing the purity of metal-organic frameworks using photoluminescence: MOF-5, ZnO quantum dots, and framework decomposition. J Am Chem Soc 2010;132(44):15487–9.
[26] Serpell LC, Smith JM. Direct visualisation of the β-sheet structure of synthetic Alzheimer's amyloid. J Mol Biol 2000;299(1):225–31.
[27] Malinchik SB, Inouye H, Szumowski KE, Kirschner DA. Structural analysis of Alzheimer's β(1-40) amyloid: protofilament assembly of tubular fibrils. Biophys J 1998;74(1):537–45.
[28] Blake C, Serpell L. Synchrotron X-ray studies suggest that the core of the transthyretin amyloid fibril is a continuous β-sheet helix. Structure 1996;4(8):989–98.
[29] Perutz MF, Finch JT, Berriman J, Lesk A. Amyloid fibers are water-filled nanotubes. Proc Natl Acad Sci USA 2002;99(8):5591–5.
[30] Jiménez JL, Guijarro JI, Orlova E, Zurdo J, Dobson CM, Sunde M, et al. Cryo-electron microscopy structure of an SH3 amyloid fibril and model of the molecular packing. EMBO J 1999;18(4):815–21.
[31] Elam JS, Taylor AB, Strange R, Antonyuk S, Doucette PA, Rodriguez JA, et al. Amyloid-like filaments and water-filled nanotubes formed by SOD1 mutant proteins linked to familial ALS. Nat Struct Biol 2003;10(6):461–7.

## 5.3. Paper V: Mesoporous Metal−Organic Frameworks as Effective Nucleating Agents in Protein Crystallography

Work contributions:

Organic linker synthesis was performed by Flávio Figueira and Filipe Paz (CICECO, Aveiro, Portugal). TGA measurements made with assistance from Seyedali Emani and Adélio Mendes (FEUP, Porto, Portugal).

CRYSTAL GROWTH & DESIGN

Article

Cite This: *Cryst. Growth Des.* 2019, 19, 1610−1615

pubs.acs.org/crystal

# Mesoporous Metal−Organic Frameworks as Effective Nucleating Agents in Protein Crystallography

José P. Leite,[†,‡,§] Diogo Rodrigues,[†,‡] Susana Ferreira,[†,‡] Flávio Figueira,[∥] Filipe A. Almeida Paz,[∥] and Luís Gales*[,†,‡,§]

[†]i3S − Instituto de Investigação e Inovação em Saúde, Rua Alfredo Allen, 208, Porto, Portugal

[‡]IBMC − Instituto de Biologia Molecular e Celular Universidade do Porto, Rua Alfredo Allen, 208, Porto, Portugal

[§]ICBAS − Instituto de Ciências Biomédicas Abel Salazar, Rua de Jorge Viterbo Ferreira 228, Porto, Portugal

[∥]Department of Chemistry, University of Aveiro, CICECO - Aveiro Institute of Materials, Campus Universitário de Santiago, Aveiro, Portugal

*Supporting Information*

**ABSTRACT:** Mesoporous metal−organic frameworks (mesoMOFs) have gained some attention as protein immobilization agents. Herein, and for the first time, three model proteins (lysozyme, trypsin, and albumin) were used to show that crystallization is effectively induced when the protein is immobilized inside the mesoMOF, with this occurring for lysozyme, while trypsin and albumin were size-excluded. It is shown that heterogeneous nucleation is truly remarkable in the case of lysozyme with a strong adhesion to the mesoMOF surface. These findings suggest that the ability to fix the target protein with a molecular-scale periodicity constitutes a significant advantage of mesoMOFs over other nucleating agents.

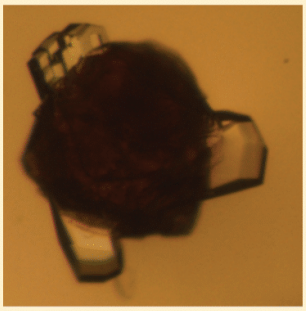

## 1. INTRODUCTION

Most of the organic or hybrid metal−organic crystalline materials are either microporous or nonporous. Microporous crystals can absorb small molecules and may find application in, among other things, adsorption/separation of gases.[1−4] Bigger guest molecules require larger pore cavities, and, indeed, the diversity of mesoporous crystals, particularly those within the realm of metal−organic frameworks (MOFs), has been continuously growing.[5] Some of these materials show good stability in several solvents and can be soaked in solutions of macromolecules. Proteins are one example of guests able to diffuse through meso-MOFs crystals. The process is not limited, interestingly, to proteins that are smaller than the pore constrictions,[6] but it can also be observed with others that, as is the case of cytochrome *c*, must undergo a significant conformational change during translocation into the interior of the MOF usually known as a Tb-mesoMOF, a framework containing cages of about 39 and 47 Å in diameter interconnected through five- and six-membered-ring pores, which, on the basis of the van der Waals radii, have free diameters of about 13 and 17 Å, respectively.[7] The saturation loading of cytochrome *c* was reached within 2 days.[8]

Incorporation of enzymes into mesoMOFs is useful to enhance protein stability, particularly in rather aggressive environments, such as, for example, in the lysosomes of human cells,[9] as well as to facilitate separation and recovery.[10] Moreover, mesoMOFs with bimodal pore distribution may be used to couple two enzymes[11,12] or to ensure that substrate and products may diffuse through the smaller channels while the enzymes remain confined to the large cages.[13] In contrast to soft polymeric gels,[14−16] the regular, molecular-sized, pore geometry of MOFs allow proteins to be retained inside the crystals for longer periods of time without leaching.[17]

Crystal growth remains a bottleneck of X-ray protein crystallography, one of the main techniques used to determine the structure of proteins, together with nuclear magnetic resonance and, more recently, with cryoelectron microscopy. The use of porous materials with pore dimensions large enough to incorporate protein molecules as nucleating agents has been pursued for a few years with some significant results.[18] Chayen and colleagues showed the advantage of using porous silicon in the crystallization of five of the six tested proteins (catalase, lysozyme, a phycobiliprotein, thaumatin, and trypsin; they were not successful with concanavalin A).[19] Later, a new material, bioglass, stable in a large range of pH conditions, was developed by the same group and shown to be an effective nucleant of several proteins.[20] Meanwhile, a commercial porous glass was also found to induce nucleation of lysozyme, thaumatin, and apoferritin.[21] Other types of materials, such as gold or carbon, were also tested. Nanoporous gold particles[22] and solid gold

**Received:** September 25, 2018
**Revised:** January 18, 2019
**Published:** January 30, 2019





DOI: 10.1021/acs.cgd.8b01444
*Cryst. Growth Des.* 2019, 19, 1610−1615

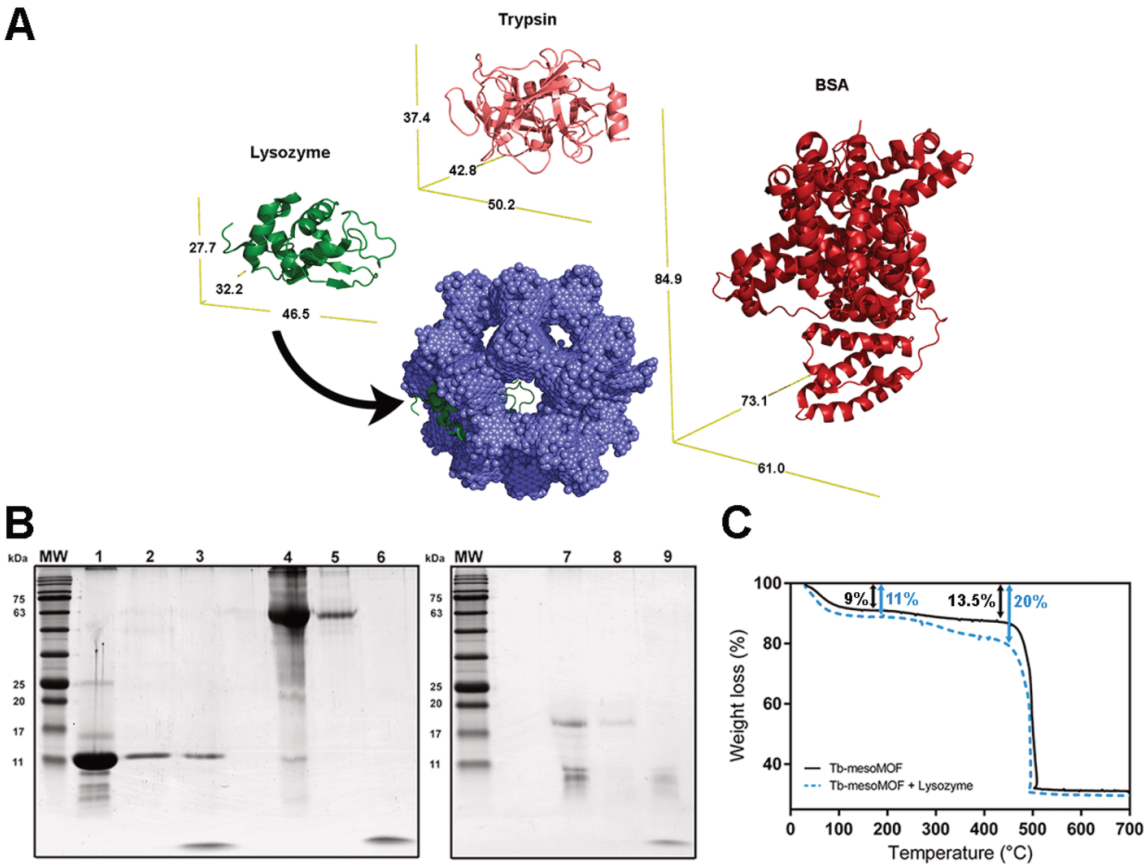


**Figure 1.** (A) Approximate dimensions in Å of the three model proteins used in this study. Only lysozyme can enter the interior of Tb-mesoMOF crystals as shown through gel electrophoresis. (B) SDS-PageBlue stained 15% (w/v) polyacrylamide of 1 – lysozyme in the MOF incubation solution after 60 h; 2 – lysozyme in the MOF washing solution (i.e., adsorbed to crystal surface); 3 – lysozyme in the MOF dissolution sample (i.e., in the interior of the MOF); 4 – albumin in the MOF incubation solution after 60 h; 5 – albumin in the MOF washing solution (i.e., adsorbed to crystal surface); 6 – albumin in the MOF dissolution sample (i.e., in the interior of the MOF, not detected); 7 – trypsin in the MOF incubation solution after 60 h; 8 – trypsin in the crystal washing solution (i.e., adsorbed to crystal surface); 9 – trypsin in the MOF dissolution sample (i.e., in the interior of the MOF, not detected). (C) Thermogravimetric data of the Tb-mesoMOF crystals preincubated with lysozyme and of the parent crystals (estimated loading 3.3 $\mu$mol/g of crystal).

nanoparticles with different sizes and shapes[23] were able to induce crystallization of model proteins. Finally, nanostructured carbon-based nucleants were shown to induce crystallization of model proteins[24,25] and of, at least, two medically relevant ones.[24]

The rationale behind the use of nanoporous materials is that the cavities would entrap the protein molecules in a regular and oriented fashion, thereby promoting nucleation and crystal formation. In this context, mesoMOFs immediately emerge as a superior class of materials, given the possibility to trap protein molecules with molecular-scale periodicity. However, as we will show, the higher pore uniformity of these materials when compared to other nucleating agents reduces its range of application to proteins that are not size-excluded and can be accommodated in the pores of the MOF crystals.

To the best of our knowledge, the study reported in this communication is unprecedented among MOFs materials. In the context of small molecule X-ray crystallography, MOFs have been used to immobilize and orient organic molecules allowing suitable X-ray analysis. With this method, coined the sponge crystalline method, the structures of guests and of the host are determined together.[26,27]

## 2. EXPERIMENTAL SECTION

**2.1. Reagents.** Lysozyme from hen egg white, trypsin from porcine pancreas, and bovine serum albumin, as highly pure lyophilized powders, were purchased from Sigma-Aldrich (UK). Terbium nitrate pentahydrate was also obtained from Sigma-Aldrich (UK) and 4,4′,4″-s-triazine-2,4,6-triyl-tribenzoic acid (H3TATB) was either purchased from Sigma-Aldrich (UK) or synthesized in our laboratory (details in the Supporting Information). All other reagents were of analytical grade.

**2.2. Synthesis of Tb-mesoMOF.** Tb-mesoMOF crystals synthesis was slightly adapted from ref 7. Terbium nitrate ($1.38 \times 10^{-4}$ mol) and 4,4′,4″-s-triazine-2,4,6-triyl-tribenzoic acid ($4.54 \times 10^{-4}$ mol) were dissolved in a mixture of dimethylacetamide/methanol/water (4.0/0.8/0.2 mL, respectively). The solution was heated to 378 K for 48 h in a scintillation vial and then slowly cooled to ambient temperature, at which point colorless truncated octahedral crystals were clearly visible by the naked eye. Crystals were washed with the buffer solutions of the



DOI: 10.1021/acs.cgd.8b01444
Cryst. Growth Des. 2019, 19, 1610–1615

proteins tested and used as grown, or reduced to macroseeds by centrifugation with Hampton seed beads, in the crystallization trials.

**2.3. SDS-PAGE Analysis of Tb-mesoMOF Crystals Soaked with Proteins.** Tb-mesoMOF crystals were equilibrated for 6 h with the respective protein buffer (lysozyme, albumin, and trypsin) to allow the removal of solvent used in the synthesis. Ten milligrams of Tb-mesoMOF crystals were then incubated for 60 h at ambient temperature with 100 $\mu$L of each protein (200 $\mu$M) in the respective crystallization buffer. Crystals were then washed to remove superficially adsorbed protein, dissolved, and analyzed in 15% (w/v) polyacrylamide gels by SDS-PAGE. NZYColour Protein Marker II (NZYtech) was used as a molecular weight marker.

**2.4. Thermogravimetric Analysis (TGA) of the Crystals.** TGA experiments were performed in a NETZSCH TG 209 F1 thermal analysis system (NETZSCH, Germany) in air, with a heating rate of 5 °C/min from 30 to 700 °C.

**2.5. Crystallization Trials.** Three model proteins (lysozyme, trypsin, and albumin) were used in the vapor-diffusion crystallization trials. Lysozyme was prepared in 0.1 M sodium acetate pH 4.5 at 40 mg·mL$^{-1}$. Trypsin was prepared in 10 mg·mL$^{-1}$ benzamidine hydrochloride, 0.01 M calcium chloride, 0.02 M HEPES pH 7.0 at 100 mg·mL$^{-1}$. Albumin was prepared in 0.1 M NaCl and 0.01 M Tris buffer at 7.4 pH, with a final concentration of 60 mg·mL$^{-1}$. Crystallization conditions were based on refs 25 and 28 (details in the Supporting Information): 0.5−1.5 M NaCl, 0.1 M sodium acetate pH 4.5 (lysozyme); 5−30% PEG 8000, 0.2 M ammonium sulfate, 0.1 M cacodylate pH 6.5 (trypsin), and 0.15−0.3 M $NH_4Cl$, 0.1 M MES buffer at pH 6.5 and 20−24% PEG 5000 (albumin).

**2.6. X-ray Image Collection and Processing.** Tb-mesoMOF: lysozyme crystal was gently fractured, and a slice fragment from the interface region was mounted on a cryoloop using Paratone and flash-frozen. X-ray data were measured at 100 K in microfocus beamline (15 $\mu$m beam diameter) ID30A-3 of the European Synchrotron Radiation Facility (Grenoble, France) operating at 12.81 keV. Four diffraction images at 0, 90, 180, and 270° with an oscillation width of 1° were collected at different centered points along the crystal and processed with iMosflm.[29]

## 3. RESULTS AND DISCUSSION

**3.1. Protein Incorporation in the Tb-mesoMOF Framework.** Three models proteins, with significant different sizes and shapes, were tested. Hen egg-white lysozyme is a monomeric protein with 129 residues and 14.3 kDa with orthogonal dimensions of about 45 Å × 30 Å × 23 Å. Trypsin is a 24 kDa protein with a more spherical shape 49 Å × 40 Å × 30 Å and bovine serum albumin is around 66 kDa with approximate dimensions of 85 Å × 80 Å × 78 Å (Figure 1A). As mentioned above, proteins are flexible molecules, and their putative penetration to the interior of a given porous MOF cannot be confidently predict based on their crystal structures. Proteins may undergo important conformational changes, enabling them to eventually squeeze through porous constrictions. Thus, we determined the degree of penetration of the three proteins experimentally, by denaturing polyacrylamide gel electrophoresis (SDS-PAGE) and thermogravimetric analysis of the soaked MOFs. Tb-mesoMOF crystals were incubated with the proteins, then they were washed to remove any adsorbed protein, and finally crystals were dissolved in the SDS buffer (10 min at 363 K). SDS-PAGE was carried with the incubation solution, the washing solution, and the Tb-mesoMOF dissolved solution for each of the tested proteins (Figure 1B). The three proteins were detected in the washing solutions, meaning that they adsorb at the external surface of Tb-mesoMOF crystals, but only lysozyme was found in the MOF dissolution samples. Thermogravimetric analysis of the Tb-mesoMOF crystals preincubated with lysozyme and of the parent crystals allowed

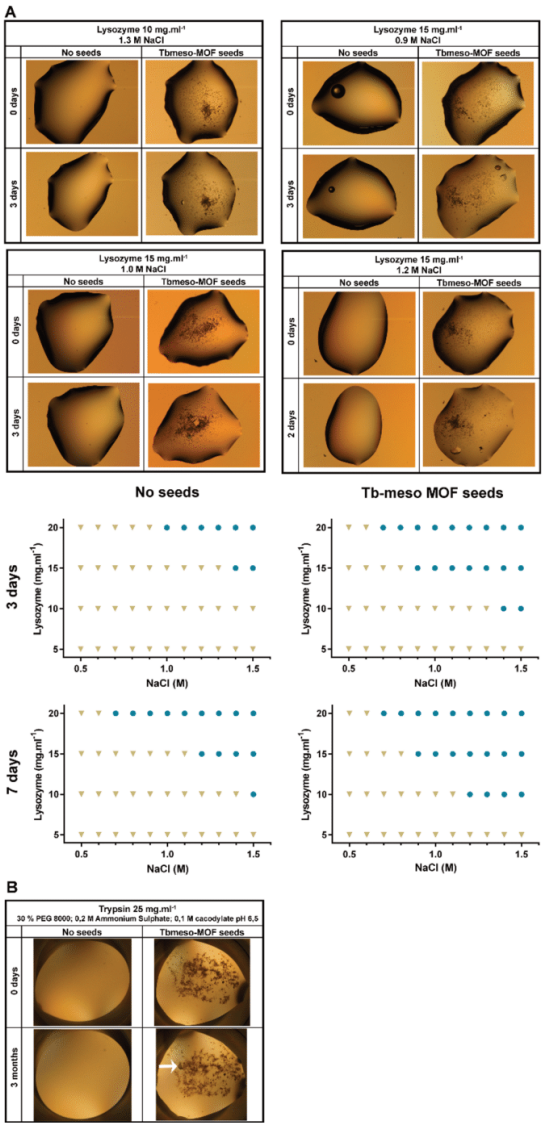


**Figure 2.** Lysozyme (A) and trypsin (B) crystal growing in the presence of Tb-mesoMOFs seeds. (A) Top: The nucleating effect of Tb-mesoMOFs seeds was repeatedly observed in drops with varying concentrations of precipitant. Bottom: Lysozyme crystallization phase diagrams in the absence (left) or presence (right) of Tb-mesoMOF seeds (3 and 7 days incubation). Circles and triangles indicate the presence and absence of crystals, respectively. (B) Small trypsin crystals (pointed in the bottom right panel) appear in some crystallization drops alongside Tb-mesoMOFs seeds after several weeks. No crystals were observed in the controls (without seeds).

us to estimate a loading of 3.3 $\mu$mol/g of crystal. This about one-third of the saturated loading determined for cytochrome c,[8] which is a more compact molecule (~26 Å × 32 Å × 33 Å).

**3.2. Crystallization Promoted by Macroseeds.** Tb-mesoMOF was selected to be tested as a nucleating agent because of its stability in several solvents, particularly water.[7] All



DOI: 10.1021/acs.cgd.8b01444
Cryst. Growth Des. 2019, 19, 1610−1615

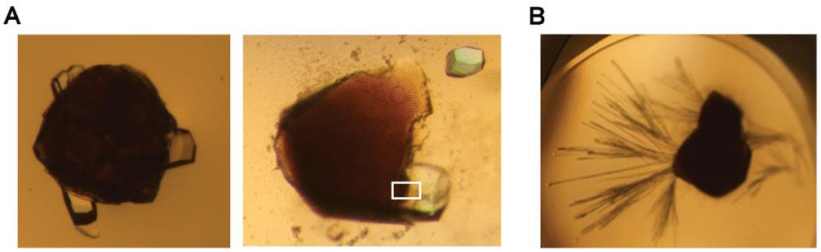


**Figure 3.** (A) Lysozyme crystals grow abundantly at the surface of millimeter-size Tb-mesoMOF crystals. (B) Needle-shaped albumin crystals grown in the presence of Tb-mesoMOF crystals. The white rectangle in (A) indicates the approximate position of the fragment used for X-ray data collection (Figure 4).

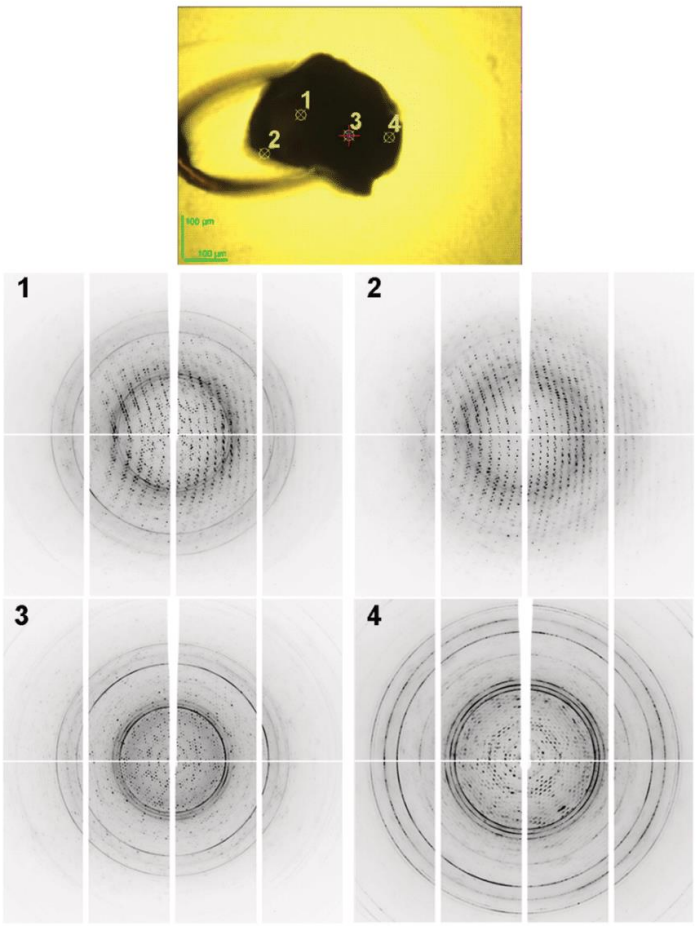


**Figure 4.** X-ray diffraction patterns from a small crystal fragment picked from the interface of a Tb-mesoMOF: lysozyme crystal. The fragment was centered in four positions (top) and is shown in the same orientation as the one highlighted in the rectangle of Figure 3A, with the parent Tb-mesoMOF on the left side and the lysozyme crystal on the right side. Patterns collected at positions 1 and 2 were indexed to the tetragonal lysozyme cell, at 3 could be simultaneously indexed both of the lattices (overlay of the patterns) and at 4 was indexed to the Tb-mesoMOF cell.

trials were carried out at metastable conditions, in which crystals do not nucleate but sustained growth is possible.

Lysozyme crystallization trials were followed over a period of 7 days. Variations in the concentration of the protein or of the precipitant agent always revealed the same trend with a significant positive effect in the addition of the Tb-mesoMOF seeds. Examples of illustrative crystallization drops are shown in Figure 2A, and a collection of crystallization results, after 3 and 7 days, is presented in Figure 2B. Macroseeds clearly induced the growth of crystals that did not appear in the controls (same crystallization conditions without seeds) or appear later (Figure 2B). The effect of the seeds in the crystallization of trypsin was



DOI: 10.1021/acs.cgd.8b01444
*Cryst. Growth Des.* 2019, 19, 1610−1615

much less impressive. Crystals did not appear in the controls within 3 months. At this stage small protein crystals were markedly visible in some of the Tb-mesoMOFs drops (Figure 2B). Albumin did not crystallize in any experimental conditions, control or with macroseeds.

**3.3. Nucleation Promoted by Single Crystals.** An identical set of crystallization experiments was performed using as-prepared Tb-mesoMOF crystals (i.e., millimeter-size) instead of macroseeds. Lysozyme revealed a remarkable propensity to grow at the MOF surface (Figure 3A). In the case of albumin, needle-like crystals were formed in the presence of the Tb-mesoMOFs crystals (Figure 3B). Trypsin did not nucleate at the surface of the MOFs in any of the crystallization trials.

The interaction between the Tb-mesoMOF crystal and the protein crystal was noticeably different for lysozyme and albumin. On the one hand, albumin crystals could be easily separated using manipulation tools, despite being in contact with Tb-mesoMOFs. In the case of Tb-mesoMOF: lysozyme crystals, it was clear from optical microscopy images that there was no clear interface between the Tb-mesoMOF crystal and the lysozyme crystal.

We next proceeded to investigate the interaction between the Tb-mesoMOF and the lysozyme crystal. A Tb-mesoMOF: lysozyme crystal was carefully fractured and a sliced intermediate fragment (approximate position shown in Figure 3) was analyzed by X-ray diffraction, with microfocus beam (15 $\mu$m in diameter) starting at the core of the lysozyme crystal and moving toward the Tb-mesoMOF (Figure 4). X-ray patterns collected at different centered points along the crystal, which looked as a single crystal in the loop (Figure 4), were either characteristic of lysozyme crystals (unit cell: 79.5 Å; 79.5 Å; 37.6 Å; $\alpha = \beta = \gamma = 90°$), or of Tb-mesoMOF (122.86 Å; 126.36 Å; 125.01 Å; $\alpha = \beta = \gamma = 90°$), or exhibit an overlap of the two X-ray diffraction patterns. Thus, we can observe that the parent crystal did not break at the interface, and the lysozyme crystals firmly adhere to the Tb-mesoMOF surface.

## 4. CONCLUSIONS

In summary, this report shows that mesoMOFs can be used as effective promoting agents of the nucleation of proteins, particularly when these biomolecules can effectively enter the mesoMOF crystals. The regular trapping of protein molecules inside mesoMOF cavities/channels seems to induce a slow nucleation with a strong adhesion to the surface of the mesoMOF crystal. The present study also shows that mesoMOFs can be used as size discriminators for proteins since, as expected, the selected framework clearly incorporated the smaller protein (lysozyme) with crystallization occurring from the inside of the channels toward the mother solution. As the number of mesoMOFs studies is continuously growing in the literature, as well as the number of studies of protein incorporation in this class of materials, we hope to have called the attention of the scientific community for this new potential application of MOFs which may help to solve several problems related to protein crystallization. In addition, we also envisage that this crystallization procedure can be used to promote crystallization of other difficult bioinspired or bioactive molecules such as drugs.

## ■ ASSOCIATED CONTENT

### Supporting Information

The Supporting Information is available free of charge on the ACS Publications website at DOI: 10.1021/acs.cgd.8b01444.

Synthesis of the organic linker of the Tb-mesoMOF, preparation of the seeds, crystallization conditions (PDF)

## ■ AUTHOR INFORMATION


### Corresponding Author

*E-mail: lgales@ibmc.up.pt Tel: +351 220 408 800.

### ORCID

Filipe A. Almeida Paz: 0000-0003-2051-5645

Luís Gales: 0000-0002-8352-6539



### Funding

This work was financed by Norte-01-0145-FEDER-000008-Porto Neurosciences and Neurologic Disease Research Initiative at I3S, supported by Norte Portugal Regional Operational Programme (NORTE2020), under the PORTUGAL 2020 Partnership Agreement, by COMPETE 2020 - Operacional Programme for Competitiveness and Internationalisation (POCI), Portugal 2020, through the European Regional Development Fund (FEDER), and by Portuguese funds through FCT - Fundação para a Ciência e a Tecnologia/Ministério da Ciência, Tecnologia e Ensino Superior in the framework of the project "Institute for Research and Innovation in Health Sciences" (POCI-01−0145-FEDER-007274) and Grant SFRH/BD/129921/2017. This work was also developed within the scope of the project CICECO-Aveiro Institute of Materials, POCI-01-0145-FEDER-007679 (FCT ref. UID/CTM/50011/2013), financed by national funds through the FCT/MEC and when appropriate cofinanced by FEDER under the PT2020 Partnership Agreement.


### Notes

The authors declare no competing financial interest.

## ■ ACKNOWLEDGMENTS

We would like to thank the ESRF beamline (Grenoble, France) staff for the assistance during X-ray data collection, and to Seyedali Emami and Adélio Mendes for their help in thermogravimetric data collection.

## ■ REFERENCES


(1) Kitagawa, S.; Kitaura, R.; Noro, S. I. Functional porous coordination polymers. *Angew. Chem., Int. Ed.* **2004**, *43* (18), 2334−2375.

(2) Li, J. R.; Sculley, J.; Zhou, H. C. Metal-organic frameworks for separations. *Chem. Rev.* **2012**, *112* (2), 869−932.

(3) Afonso, R.; Mendes, A.; Gales, L. Peptide-based solids: Porosity and zeolitic behavior. *J. Mater. Chem.* **2012**, *22* (5), 1709−1723.

(4) Afonso, R. V.; Durão, J.; Mendes, A.; Damas, A. M.; Gales, L. Dipeptide crystals as excellent permselective materials: Sequential exclusion of argon, nitrogen, and oxygen. *Angew. Chem., Int. Ed.* **2010**, *49* (17), 3034−3036.

(5) Xuan, W.; Zhu, C.; Liu, Y.; Cui, Y. Mesoporous metal-organic framework materials. *Chem. Soc. Rev.* **2012**, *41* (5), 1677−1695.

(6) Lykourinou, V.; Chen, Y.; Wang, X. S.; Meng, L.; Hoang, T.; Ming, L. J.; Musselman, R. L.; Ma, S. Immobilization of MP-11 into a mesoporous metal-organic framework, MP-11@mesoMOF: A new platform for enzymatic catalysis. *J. Am. Chem. Soc.* **2011**, *133* (27), 10382−10385.

(7) Park, Y. K.; Choi, S. B.; Kim, H.; Kim, K.; Won, B. H.; Choi, K.; Choi, J. S.; Ahn, W. S.; Won, N.; Kim, S.; Jung, D. H.; Choi, S. H.; Kim, G. H.; Cha, S. S.; Jhon, Y. H.; Yang, J. K.; Kim, J. Crystal structure and




DOI: 10.1021/acs.cgd.8b01444
*Cryst. Growth Des.* 2019, 19, 1610−1615

guest uptake of a mesoporous metal-organic framework containing cages of 3.9 and 4.7 nm in diameter. *Angew. Chem., Int. Ed.* **2007**, *46* (43), 8230−8233.
(8) Chen, Y.; Lykourinou, V.; Vetromile, C.; Hoang, T.; Ming, L. J.; Larsen, R. W.; Ma, S. How can proteins enter the interior of a MOF? investigation of cytochrome c translocation into a MOF consisting of mesoporous cages with microporous windows. *J. Am. Chem. Soc.* **2012**, *134* (32), 13188−13191.
(9) Lian, X.; Erazo-Oliveras, A.; Pellois, J. P.; Zhou, H. C., High efficiency and long-term intracellular activity of an enzymatic nanofactory based on metal-organic frameworks. *Nat. Commun.* **2017**, *8*, (1). DOI: 10.1038/s41467-017-02103-0
(10) Mehta, J.; Bhardwaj, N.; Bhardwaj, S. K.; Kim, K. H.; Deep, A. Recent advances in enzyme immobilization techniques: Metal-organic frameworks as novel substrates. *Coord. Chem. Rev.* **2016**, *322*, 30−40.
(11) Kim, Y.; Yang, T.; Yun, G.; Ghasemian, M. B.; Koo, J.; Lee, E.; Cho, S. J.; Kim, K. Hydrolytic Transformation of Microporous Metal-Organic Frameworks to Hierarchical Micro- and Mesoporous MOFs. *Angew. Chem., Int. Ed.* **2015**, *54* (45), 13273−13278.
(12) Lian, X.; Chen, Y. P.; Liu, T. F.; Zhou, H. C. Coupling two enzymes into a tandem nanoreactor utilizing a hierarchically structured MOF. *Chemical Science* **2016**, *7* (12), 6969−6973.
(13) Li, P.; Modica, J. A.; Howarth, A. J.; Vargas, E. L.; Moghadam, P. Z.; Snurr, R. Q.; Mrksich, M.; Hupp, J. T.; Farha, O. K. Toward Design Rules for Enzyme Immobilization in Hierarchical Mesoporous Metal-Organic Frameworks. *Chem.* **2016**, *1* (1), 154−169.
(14) Appel, E. A.; Loh, X. J.; Jones, S. T.; Dreiss, C. A.; Scherman, O. A. Sustained release of proteins from high water content supramolecular polymer hydrogels. *Biomaterials* **2012**, *33* (18), 4646−4652.
(15) Leite, J. P.; Mota, R.; Durao, J.; Neves, S. C.; Barrias, C. C.; Tamagnini, P.; Gales, L., Cyanobacterium-Derived Extracellular Carbohydrate Polymer for the Controlled Delivery of Functional Proteins. *Macromol. Biosci.* **2017**, *17*, (2).1600206
(16) Nagai, Y.; Unsworth, L. D.; Koutsopoulos, S.; Zhang, S. Slow release of molecules in self-assembling peptide nanofiber scaffold. *J. Controlled Release* **2006**, *115* (1), 18−25.
(17) Chen, Y.; Han, S.; Li, X.; Zhang, Z.; Ma, S. Why does enzyme not leach from metal-organic frameworks (MOFs)? Unveiling the interactions between an enzyme molecule and a MOF. *Inorg. Chem.* **2014**, *53* (19), 10006−10008.
(18) Khurshid, S.; Saridakis, E.; Govada, L.; Chayen, N. E. Porous nucleating agents for protein crystallization. *Nat. Protoc.* **2014**, *9* (7), 1621−1633.
(19) Chayen, N. E.; Saridakis, E.; El-Bahar, R.; Nemirovsky, Y. Porous silicon: An effective nucleation-inducing material for protein crystallization. *J. Mol. Biol.* **2001**, *312* (4), 591−595.
(20) Chayen, N. E.; Saridakis, E.; Sear, R. P. Experiment and theory for heterogeneous nucleation of protein crystals in a porous medium. *Proc. Natl. Acad. Sci. U. S. A.* **2006**, *103* (3), 597−601.
(21) Rong, L.; Komatsu, H.; Yoshizaki, I.; Kadowaki, A.; Yoda, S. Protein crystallization by using porous glass substrate. *J. Synchrotron Radiat.* **2004**, *11* (1), 27−29.
(22) Kertis, F.; Khurshid, S.; Okman, O.; Kysar, J. W.; Govada, L.; Chayen, N.; Erlebacher, J. Heterogeneous nucleation of protein crystals using nanoporous gold nucleants. *J. Mater. Chem.* **2012**, *22* (41), 21928−21934.
(23) Ko, S.; Kim, H. Y.; Choi, I.; Choe, J. Gold nanoparticles as nucleation-inducing reagents for protein crystallization. *Cryst. Growth Des.* **2017**, *17* (2), 497−503.
(24) Asanithi, P.; Saridakis, E.; Govada, L.; Jurewicz, I.; Brunner, E. W.; Ponnusamy, R.; Cleaver, J. A. S.; Dalton, A. B.; Chayen, N. E.; Sear, R. P. Carbon-nanotube-based materials for protein crystallization. *ACS Appl. Mater. Interfaces* **2009**, *1* (6), 1203−1210.
(25) Leese, H. S.; Govada, L.; Saridakis, E.; Khurshid, S.; Menzel, R.; Morishita, T.; Clancy, A. J.; White, E. R.; Chayen, N. E.; Shaffer, M. S. P. Reductively PEGylated carbon nanomaterials and their use to nucleate 3D protein crystals: A comparison of dimensionality. *Chemical Science* **2016**, *7* (4), 2916−2923.
(26) Hoshino, M.; Khutia, A.; Xing, H.; Inokuma, Y.; Fujita, M. The crystalline sponge method updated. *IUCrJ* **2016**, *3*, 139−151.
(27) Inokuma, Y.; Yoshioka, S.; Ariyoshi, J.; Arai, T.; Hitora, Y.; Takada, K.; Matsunaga, S.; Rissanen, K.; Fujita, M. X-ray analysis on the nanogram to microgram scale using porous complexes. *Nature* **2013**, *495* (7442), 461−466.
(28) Bujacz, A.; Zielinski, K.; Sekula, B. Structural studies of bovine, equine, and leporine serum albumin complexes with naproxen. *Proteins: Struct., Funct., Genet.* **2014**, *82* (9), 2199−2208.
(29) Battye, T. G. G.; Kontogiannis, L.; Johnson, O.; Powell, H. R.; Leslie, A. G. W. iMOSFLM: A new graphical interface for diffraction-image processing with MOSFLM. *Acta Crystallogr., Sect. D: Biol. Crystallogr.* **2011**, *67* (4), 271−281.



DOI: 10.1021/acs.cgd.8b01444
*Cryst. Growth Des.* 2019, 19, 1610−1615

## 5.3.1. Supporting Information

### Mesoporous metal-organic frameworks as effective nucleating agents in protein crystallography

*José P. Leite[abc], Diogo Rodrigues[ab], Susana Ferreira[ab], Flávio Figueira[d], Filipe A. Almeida Paz[d] and Luís Gales[abc]**

[a] i3S – Instituto de Investigação e Inovação em Saúde, Rua Alfredo Allen, 208, Porto, Portugal.

[b] IBMC – Instituto de Biologia Molecular e Celular Universidade do Porto, Rua Alfredo Allen, 208, Porto, Portugal.

[c] ICBAS – Instituto de Ciências Biomédicas Abel Salazar, Rua de Jorge Viterbo Ferreira 228, Porto, Portugal.

[d] Department of Chemistry, University of Aveiro, CICECO - Aveiro Institute of Materials, Campus Universitário de Santiago, Aveiro, Portugal

**Synthesis of the organic linker**

**2,4,6-Tris(4-methylphenyl)-1,3,5-triazine**

4-Methylbenzonitrile (1.5 g, 12.8 mmol) was slowly added to trifluoromethanesulfonic acid (3.0 mL, 33,9 mmol). After stirring at room temperature for 24 h, the yellow reaction mixture was poured on ice and neutralized with aqueous ammonia solution (2 M). The white precipitate was filtered by filtration and washed with water and acetone. Recrystallization from hot toluene gave 1.2 g (3.4 mmol, yield: 85%) of 2,4,6-tris(4-methylphenyl)-1,3,5-triazine in the form of white crystals. This synthesis was performed following a literature procedure and the characterization is in accordance with published data [1-3].

$^1$H NMR (300 MHz, Chloroform-*d*) $\delta$ 8.64 (d, J = 8.0 Hz, 6H), 7.35 (d, J = 8.0 Hz, 6H), 2.47 (s, 9H).

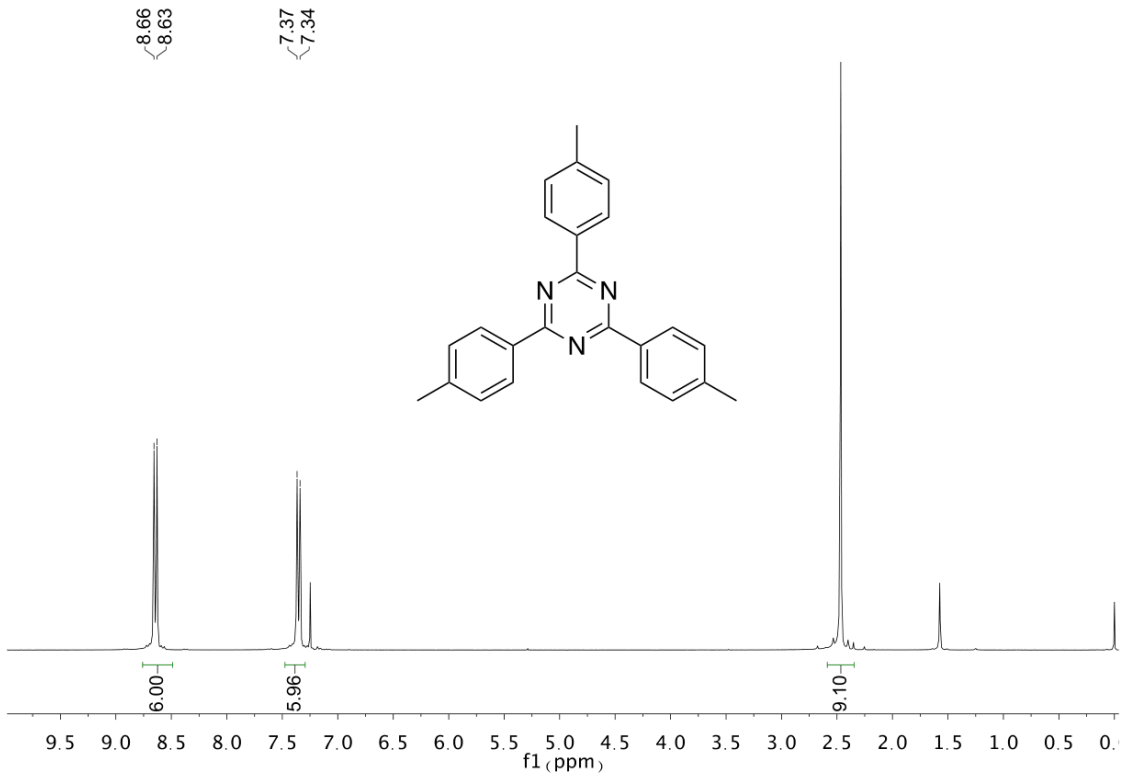


Figure 1: $^{1}$H NMR spectra of 2,4,6-Tris(4-methylphenyl)-1,3,5-triazine.

**4,4',4''-(1,3,5-Triazine-2,4,6-triyl)-tribenzoic acid**

A solution of 2,4,6-tris(4-methylphenyl)-1,3,5-triazine (1.0 g, 2,8 mmol), acetic acid (60 mL, 1.0 mol) and sulfuric acid (2,0 mL, 37,5 mmol) was stirred, while chromium (VI)-oxide (2.62 g, 26.2 mmol) and acetic anhydride (6.6 mL, 70.5 mmol) were added with stirring while keeping the temperature below 50 ºC. The resulting green-brown slurry was stirred overnight, poured into 100 mL of cold water, and the resulting solution was mixed well and filtered. The collected solid was washed with water and dissolved in 200 mL of a 2 N NaOH solution. After the unreacted starting material was removed by filtration, the solution was acidified with HCl to give the crude product. Recrystallization from DMF gave pure product as a white solid (0.65 g, 1.47 mmol, Yield: 52.5 %) This synthesis was also performed following a literature procedure and the characterization is in accordance with the published data [3, 4].

$^{1}$H NMR (300 MHz, DMSO-*d6*) $\delta$ 13.32 (s, 2H), 8.76 (d, J = 8.5 Hz, 6H), 8.15 (d, J = 8.5 Hz, 6H).

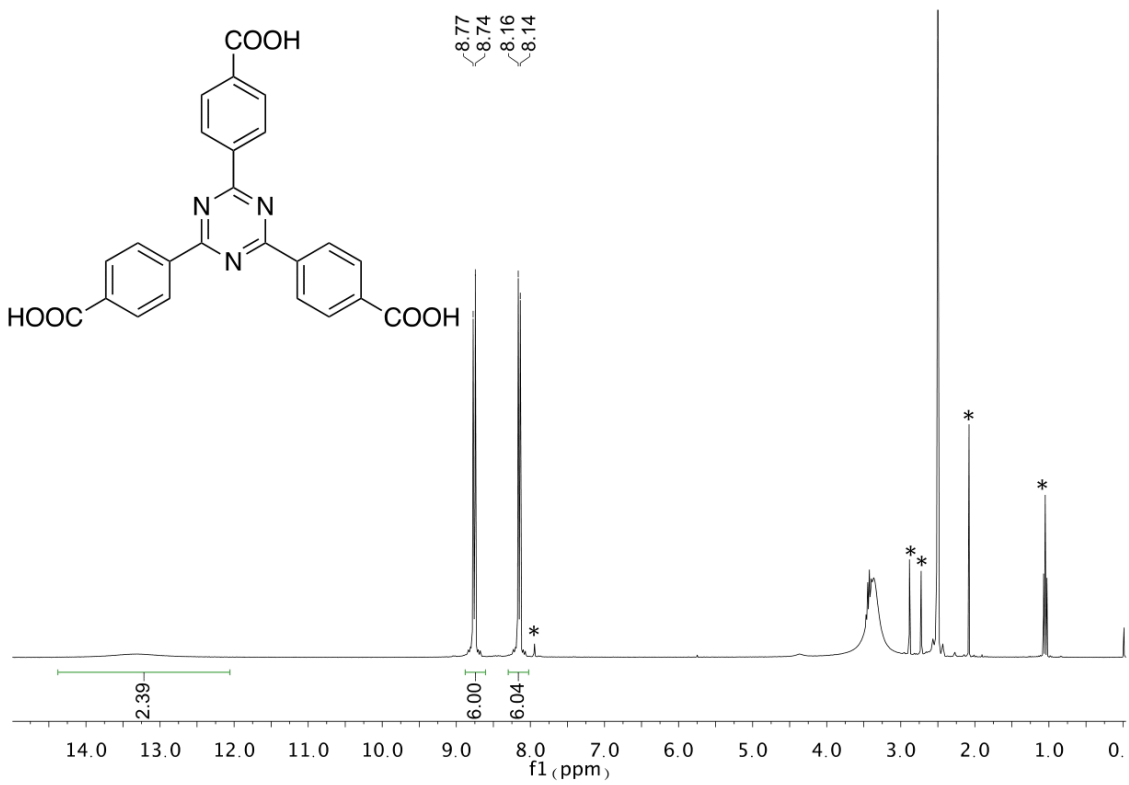


Figure 2: $^{1}$H NMR spectra of 4,4',4''-(1,3,5-Triazine-2,4,6-triyl)-tribenzoic acid (* solvent impurities).

**Preparation of the seeds of Tb-mesoMOF**

Tb-mesoMOF crystals were washed with each of the protein buffers to remove synthesis solvent (both adsorbed and within the channels), as follows: 0.1 M sodium acetate pH 4.5 (lysozyme); 10 mg.ml$^{-1}$ benzamidine hydrochloride, 0.01 M calcium chloride, 0.02 M HEPES pH 7.0 (trypsin); 0.01 M Tris at 7.4 pH (albumin). For microseeding, washed Tb-mesoMOF crystals were placed in a micro-tube with a Seed Bead (HR2-320, Hampton Research, USA) and vortexed until a homogenous seed stock was obtained. For lysozyme macroseeding experiments, Tb-mesoMOF crystals were incubated in 0.25 M NaCl, 0.2 M sodium acetate pH 4.7, 25 mg.ml$^{-1}$ lysozyme solution at room temperature for 48 to 72 h to allow incorporation of the protein within the MOF structure and, subsequently, a single crystal was transferred per vapor diffusion crystallization plate drop.

**Crystallization conditions**

Crystallization solutions were freshly prepared and kept at room temperature (salt and buffer stock solutions) or at 4°C (Polyethylene glycol 5000 and 8000) for the duration of the experiments. Protein crystal nucleation experiments were performed by the vapour diffusion technique at 20°C. For each reservoir, 500 µl of precipitant solution were dispensed and each drop had a final volume of 4 µl, with different protein/reservoir ratios to allow multiple final protein concentrations. For micro seeding, seed stocks were homogenized immediately before adding to each drop and constitute 12.5% of the final volume of the drop. Lysozyme was prepared in 0.1 M sodium acetate pH 4.5 at 40 $mg.ml^{-1}$; trypsin was prepared in 10 $mg.ml^{-1}$ benzamidine hydrochloride, 0.01 M calcium chloride, 0.02 M HEPES pH 7.0 at 100 $mg.ml^{-1}$; finally, albumin was prepared in 0.1 M NaCl and 0.01 M Tris Buffer at 7.4 pH, with a final concentration of 60$mg.ml^{-1}$. Crystallization conditions were 0.5-1.5 M NaCl, 0.1 M sodium acetate pH 4.5 (lysozyme); 5-30 % PEG 8000, 0.2 M ammonium sulphate, 0.1 M cacodylate pH 6,5 (trypsin) and 0.15-0.3 M $NH_4Cl$, 0.1 M MES Buffer at pH 6.5 and 20-24% PEG 5000 (albumin).

[1] Park, Y.K.; Choi, S.B.; Kim, H.; Kim, K.; Won, B.-H.; Choi, K.; Choi, J.-S.; Ahn, W.-S.; Won, N.; Kim, S.; et al. Crystal Structure and Guest Uptake of a Mesoporous Metal–Organic Framework Containing Cages of 3.9 and 4.7 nm in Diameter. *Angew. Chem. Int. Ed.* **2007**, *46*, 8230–8233.

[2] Sun, D.; Ma, S.; Ke, Y.; Collins, D.J.; Zhou, H.-C. An Interweaving MOF with High Hydrogen Uptake*. J. Am. Chem. Soc.* **2006**, *128*, 3896–3897.

[3] Iwami, H.; Nakanishi, R.; Horii, Y.; Katoh, K.; Breedlove, B.K.; Yamashita, M. Metal-Organic Framework of Lanthanoid Dinuclear Clusters Undergoes Slow Magnetic Relaxation. *Materials,* **2017***, 10,* 81.

[4] Mühlbauer, E.; Klinkebiel, A.; Beyer, O.; Auras, F.; Wuttke, S.; Lüning, U.; Beina, T. Functionalized PCN 6 metal organic frameworks. *Microporous Mesoporous Mater.*, **2015**, *216*, 51–55.

# CHAPTER VI. Final Remarks

## 6.1 Final Remarks

Following the first report of Alzheimer's disease (AD) in 1907 (Alzheimer *et al.*, 1995), extensive research has been devoted to AD, particularly since the main components of its two most striking features have been identified: tau protein intracellular neurofibrillary tangles and Aβ peptide extracellular senile plaques (Glenner *et al.*, 1984; Wood *et al.*, 1986). Currently, no definitive or unique cause for the disease is known. Three main hypotheses have been proposed over the years (*i.e.* cholinergic dysfunction, tau protein hyperphosphorylation or Aβ amyloid cascade), but none has single-handedly accounted for AD (Goedert *et al.*, 1991; Hardy *et al.*, 1992; Perry, 1986).

In this thesis, we focused on *in vitro* studies of Aβ peptides, with the aim of expanding the overall knowledge of Aβ and its interactions and oligomeric states, crucial to completely understand normal and pathological functions of this puzzling peptide.

Chapter II – Amyloid-β peptide interaction with proteins

Given their intrinsically disordered nature, Aβ peptides are known to interact with a wide array of peptides and proteins, including circulating proteins in the blood and cerebrospinal fluid, intracellular proteins (within the cytoplasm or organelles, namely mitochondria) and multiple membrane receptors (as reviewed by (Han *et al.*, 2016)). A sub-set of Aβ interactors are amyloid-degrading enzymes (ADEs), responsible for the enzymatic clearance of the peptide, such as serine protease plasmin (Jacobsen *et al.*, 2008), cysteine protease cathepsin B (Mueller-Steiner *et al.*, 2006) and zinc-metalloproteases angiotensin-converting enzyme, insulin-degrading enzyme or neprilysin (Bernstein *et al.*, 2014; Kilger *et al.*, 2011; Nisemblat *et al.*, 2008). Furthermore, carrier protein transthyretin (TTR) has also been linked to Aβ proteolytic clearance (C. S. Silva *et al.*, 2017). Interestingly, a failure in clearance mechanisms has been linked more strongly to AD when compared to disruption in production rates (Mawuenyega *et al.*, 2010). In this context, understanding the molecular mechanisms of Aβ clearance may help elucidate novel therapeutic avenues. Here, we aimed at characterizing Aβ interaction with transthyretin and neprilysin.

Transthyretin

The human TTR structure is well known, with first reports dating from the 1970s and hundreds of structures since describing several mutations and interactions with small molecules (Blake *et al.*, 1971; Palaninathan, 2012). Despite the mounting evidence linking TTR and Aβ, the exact oligomeric states, as well as interaction mechanism are elusive. Recent studies suggest that TTR inhibits fibril formation by binding to Aβ oligomers

(Ghadami *et al.*, 2020; Nilsson *et al.*, 2018). NMR interaction studies also suggested that tetrameric TTR-monomeric Aβ interaction is possible, disclosing $Aβ_{18-21}$ as the core segment of the interaction. However, one study indicates that the Aβ monomer binds the thyroxine pocket, while the other suggests that the core interaction occurs on the surface of the TTR tetramer (Gimeno *et al.*, 2017; Li *et al.*, 2013).

Here, we extensively attempted to co-crystallize or perform TTR crystal soaking with Aβ. Although we routinely obtained good diffracting crystals of wtTTR or TTR55, we were never able to attribute density to Aβ. An indication that the TTR-Aβ complex failed to form was given during X-Ray diffraction data collection by the fact that unit cell dimensions and space group assigned to wtTTR or TTR55 never differed from the apo protein structures. To the best of my knowledge, to date, only one report mentioning TTR-Aβ crystallography is available (Ciccone *et al.*, 2018). Ciccone and co-workers studied the influence of divalent metals, particularly copper, on TTR-Aβ interaction (Ciccone *et al.*, 2018). However, and similarly to our results, they were also unable to obtain electron density attributable to Aβ. These results may stem from the fact that tetrameric TTR-monomeric Aβ is a weak or very transient interaction. Claims that TTR can proteolytic degrade Aβ are scarce and still lack enzyme kinetic analysis. Regarding our experiment parameters, protein buffer pH was 7.5 and reservoir solution pH was either between 5.2 to 5.6 or 7.5. Taking $Aβ_{1-40}$ and $Aβ_{1-42}$ as reference, their critical aggregation concentration (CAC) is in the nanomolar range ($94 \pm 37$ nM for $Aβ_{1-40}$ and $28 \pm 4$ nM for $Aβ_{1-42}$, at pH 7.4)(Iljina *et al.*, 2016). Moreover, the CAC lowers with a decrease in pH (Brännström *et al.*, 2014). Together, the weak TTR-monomeric Aβ interaction, the CAC, pH values and crystallographic time scale may explain the absence of the crystallographic complex. Alternatively, given the metallopeptidase nature of TTR, a TTR-Aβ crystal complex may only be obtained if an inactive mutant of the protein is tested, although only about 7% of wtTTR fraction is proteolytically active (Liz *et al.*, 2012). The inactive TTR-Aβ complex could potentially be obtained by size-exclusion chromatography prior to crystallization (King *et al.*, 2014; Shen *et al.*, 2006). Finally, we took advantage of the established TTR crystallization pipeline and studied its interaction with two small-molecule chaperones, with both binding to the thyroxine binding pocket. This strategy envisions to contribute to the AD drug development pipeline by repurposing already approved drugs capable of enhancing Aβ clearance by TTR. The fact that the drug pipeline directly targeting Aβ has consistently offered less than optimal results indicates that a direct strategy to eliminate Aβ may be an oversimplification of this issue. Despite aducanumab ending a near two decade long hiatus in AD drug approval - although not without controversy (Lowe, 2021)) - most of AD drug candidates fail within or before phase III trials (Amanatkar *et al.*, 2017). Thus, the use of naturally occurring Aβ clearance pathways may be beneficial.

Neprilysin

Neprilysin (NEP) is regarded as the major ADE, with numerous accounts linking it to Alzheimer's disease (Hellstrom-Lindahl *et al.*, 2008; Maruyama *et al.*, 2005). Given the relevance of the NEP-Aβ interaction, we aimed at further elucidating its mechanism, starting by structural studies with thermolysin (TLN). TLN is a bacterial protein, originally from *Bacillus thermoproteolyticus* Rokko, that is used as a kinetic and structural surrogate model for NEP (Dion *et al.*, 1995; Roques *et al.*, 1993; Tiraboschi *et al.*, 1999). They share the same catalytic motifs (*i.e.* HExxH and ExxxD) (Bayes-Genis *et al.*, 2016; Tiraboschi *et al.*, 1999); are structurally similar (Benchetrit *et al.*, 1988), have the same catalytic mode (*i.e.,* attack on the N-terminus of hydrophobic residues), are inactivated by the same inhibitors and share stereochemical dependence (Roques *et al.*, 1993). Plus, TLN crystallizes easily, is commercially available and can be effectively inactivated by a simple metal change (from zinc to cadmium)(Holland *et al.*, 1995), instead of requiring the process of generating single-residue inactive mutants. Following confirmation that TLN also cleaves Aβ (Zhang *et al.*, 2009), we performed crystallographic assays with active and inactive TLN (aTLN and iTLN, respectively), in complex with several Aβ fragments ($Aβ_{1-40}$, $Aβ_{29-40}$, $Aβ_{1-16}$, $Aβ_{20-29}$ and $Aβ_{31-35}$). From these experiments, we concluded that TLN cleavage of Aβ between residues 30 and 31 generates a C-terminal product that presents a prolonged residence binding time to the enzyme, possibly delaying or inhibiting further catalysis.

Motivated by these results, and by the fact that cleavage at $Aβ_{30-31}$ has also been reported for NEP (Mital *et al.*, 2018), we set out to assess if this striking effect translated to this ADE. Currently, the majority of available NEP structures at the PDB disclose interaction with small molecule inhibitors, with only one account of interaction with a substrate (Moss *et al.*, 2020). Initially, we attempted NEP crystallization, based on reservoir conditions reported on the PDB, as well as sparse matrix screening, with the goal of co-crystallizing or performing crystal soaking with Aβ fragments. However, no crystals could be obtained. To assess the kinetic effect of Aβ C-terminal fragments on NEP, we performed a combination of enzyme kinetics, saturation-transfer difference nuclear magnetic resonance (STD-NMR) and molecular dynamics simulations. Our results showed that NEP mediated catabolism of $Aβ_{1-40}$ is slowed by a C-terminal degradation product containing $Aβ_{31-32}$ (*i.e.* II motif), as we predicted with the TLN-Aβ structures. In fact, using two substrates (fluorescent fragment Abz-VHHQKL-EDDnp and $Aβ_{1-40}$), we found that $Aβ_{31-35}$ shows a $K_I$ value around ten times lower than fragments $Aβ_{10-20}$ and $Aβ_{20-29}$.

This effect should now be assessed *in vivo*. Here, we used 750:1 (substrate) or 2500:1 (inhibitor) Aβ to NEP molar ratios. Similar proportions are within known physiological levels of Aβ and NEP. In normal and AD conditions, Aβ levels were determined to range from pico to nanomolar in brain extracellular fluids, possibly reaching micromolar concentrations in

intracellular compartments (Hu *et al.*, 2009) or in the extracellular environment, as a consequence of interacting with cholesterol in ganglioside clusters (Matsuzaki, 2007) or macromolecular crowding events (Munishkina *et al.*, 2004). On the other hand, neprilysin, localizing in pre and post neuronal synapses, has levels in the picomolar range, as determined in *post-mortem* midfrontal cortex (Miners *et al.*, 2009). In conclusion, further studies are essential to understand if this *in* vitro observation translates to *in vivo*, starting by detecting $A\beta_{31\text{-}X}$ fragments in cells and tissues. Depending on the microenvironment features, persistence of such fragments may impact NEP activity on Aβ clearance.

Chapter III – Fusion-protein constructs for the crystallization of the amyloid-β peptide

A complete X-Ray diffraction model of Aβ is yet to be determined. Currently, there are three reports of the application of fusion-protein technology to study Aβ structure (Nisbet *et al.*, 2013; Streltsov *et al.*, 2011; Takano *et al.*, 2006). Nevertheless, this technology offers great potential for hard to crystallize targets (Kobe *et al.*, 2015). In this chapter, we aimed at using a fusion-protein approach to obtain a full $A\beta_{1\text{-}40}$ model, plus a construct to study the P3 peptide (also dubbed amyloid-α peptide).

Three fusion-protein constructs were tested: T4Lysozyme-$A\beta_{1\text{-}40}$, T4Lysozyme-$A\beta_{17\text{-}40}$ and PAC3-$A\beta_{1\text{-}40}$. In short, only T4Lysozyme-$A\beta_{1\text{-}40}$ and T4Lysozyme-$A\beta_{17\text{-}40}$ were successfully expressed and purified from *E. coli* after several iterative rounds of optimization, followed by crystallization and X-Ray diffraction data collection, processing and refinement. However, crystal data was almost limited to T4 Lysozyme residues, with very few Aβ residues to which electron density could be assigned and no significant or novel pathophysiological relevant conformations observed. On the other hand, the PAC3-$A\beta_{1\text{-}40}$ construct could never be successfully expressed and purified in soluble form for crystallization trials.

Despite its advantages (Kobe *et al.*, 2015), fusion-protein crystallography is very depending on trial and error in finding the best suitable construct. Variables to optimize include overexpression host, expression vector, heterologous partner, purification tag and linker. A few alternative follow-ups based on the results here presented will be discussed next:

- Expression host and vector: expression was performed in *E. coli* with a pET system plasmid, which together constitute the most commonly used for easy, soluble, non-toxic protein expression in bacteria (Jia *et al.*, 2016). Ideally, changes to these parameters should only be considered if the final construction presents specific requirements. For example, insect cells can be used if disulphide bond formation is important, or mammalian cells if modifications like glycosylation are critical

(Sharifi - Sirch *et al.*, 2016). In the case of the constructs here presented, optimization should focus elsewhere (see next);

- Carrier protein: T4 Lysozyme was selected as the main heterologous partner, because of its successful use to assist in the crystallization of both soluble and membrane-bound proteins, which, like Aβ, are highly hydrophobic (Gacasan *et al.*, 2017; Kubitza *et al.*, 2018). Furthermore, lysozyme variants have proved to be successful for the structure determination of small peptides (Donahue *et al.*, 1994). On the other hand, PAC3 was selected with the rationale of exploring its native crystal packing by inserting Aβ intra-protein. While using T4 Lysozyme as a carrier protein could be improved, for example, by employing a modified form of the protein ("minimal T4 Lysozyme") or by placing Aβ within its third intracellular loop (Thorsen *et al.*, 2014), PAC3 should be replaced altogether. Alternative carrier protein options include thioredoxin (Corsini *et al.*, 2008), glutathione S-transferase (GST) (Zhan *et al.*, 2001), barnase (Niemann *et al.*, 2006), green fluorescent protein (Suzuki *et al.*, 2010) and the most widely used one, maltose-binding protein (MBP) (Waugh, 2016). Whichever the choice, the carrier protein should be kept on the N-terminal of the construction to maximize protein folding and expression yield (Moon *et al.*, 2010);
- Purification tag: here, a His-tag was used. This tag was selected because of its ease of use, low cost and possibility to detect using an anti-His antibody (Jia *et al.*, 2016). Given the purification of truncated forms, as was the case for T4Lysozyme-$A\beta_{1-40}$, the first logical step would be to move the tag to the C-terminal of the construct. However, it was reported that purification tags can have a drastic effect on protein crystallization and crystal contact formation and quality, an effect mostly influenced by amino acid composition rather than size (Bucher *et al.*, 2002). Thus, a screening of purification tags should ideally be performed. Some alternatives for small-sized, structure-less tags include the Strep-tag/Strep-tag II (biologically inert and does not interfere with protein folding) (T. G. M. Schmidt *et al.*, 2007), FLAG (presents internal enterokinase cleavage site, but requires very expensive resins) (P. M. Schmidt *et al.*, 2012) or Fh8 (enhances protein solubility and purification) (Costa *et al.*, 2014). In addition, larger tags can be used, such as GST or MBP (Kosobokova *et al.*, 2016). These can have the dual role of being simultaneously a purification tag and a carrier protein.
- Linker between carrier protein and target: for the T4Lysozyme-$A\beta_{1-40}$ and T4Lysozyme-$A\beta_{17-40}$ constructs no linker sequence between carrier and target was introduced, while for PAC3-$A\beta_{1-40}$ a three-alanine spacer between the pET15b-native thrombin cleavage site and the HRV3C cleavage site was included. In

fusion-protein crystallography, a rigid assembly between fusion components is preferable, to avoid conformational heterogeneity that may hinder crystal contact formation (Kobe *et al.*, 2015). However, there are no rigorous criteria in choosing a suitable linker. Despite the three-alanine sequence being reported several times in successful fusion-protein crystallization (Moon *et al.*, 2010), there are no systematic studies, with possible options including natural occurring intra domain linkers (rich in threonine, serine, glycine and alanine or proline, arginine, phenylalanine, threonine, glutamate and glutamine residues), as well as rigid proline-rich linkers (Kobe *et al.*, 2015). The exact composition of the linker is greatly subjected to the carrier/target combination and constitutes yet another key point of optimization, similarly to the work performed by Jin and co-workers (Jin *et al.*, 2017).

To sum up, our fusion-protein constructs did not result in novel nor complete Aβ structural models. However, the margin for improvement and testing is exponential. Following a comprehensive design of fusion-constructs, the “trial and error” expression, purification and crystallization workflows would benefit immensely from the application of automated high throughput screening systems. As an example, for protein expression and purification, we have the systems developed by the Berkeley Structural Genomics Center (Nguyen *et al.*, 2004) or the Piccolo robot (Wollerton *et al.*, 2006). Using robotic liquid handlers, expression is performed in small-scale, followed by protein solubility tests (*i.e.* soluble fraction and inclusion bodies screening) and purification in 96-well plates; detection is performed by dot blot using His-tag targeting antibodies, with positive hits further analyzed by SDS-PAGE (Nguyen *et al.*, 2004). The Piccolo system allows to circumvent the iterative and resource/time-consuming process of optimizing protein expression by simultaneously testing several variables (*e.g.* induction time, induction temperature, etc.), in a total of 1152 expression conditions per week (Wollerton *et al.*, 2006). With these systems, an optimized protocol can be found quicker and allow the preparation of large amounts of protein for crystallographic studies. These, in turn, can also be streamlined by automation. In our case, we had access to an Oryx4 protein crystallization robot (Douglas Instruments, UK), which was crucial to allow the test of crystallization in 96-well plates and generate reproducible nanodroplets. However, that only constitutes the second of three steps that make up the crystallization workflow. The pre-filling of reservoir with crystallization solutions and the evaluation and optimization of potential hits to generate good diffracting quality crystals are also very time-consuming. In this regard, automated pipelines for crystallization, crystal growth monitoring (through combination of imaging and machine learning), crystal optimization and X-Ray data collection are very valuable, such

as the pipelines at Institut Pasteur and the MASSIF (Massively Automated Sample Selection Integrated Facility) synchrotron beamlines of the ESRF (Bowler *et al.*, 2015; Weber *et al.*, 2019).

Chapter IV - Dissection of the key steps of Aβ1-40 fibrillogenesis

In this chapter, we employed a set of biophysical techniques to study the aggregation of $A\beta_{1\text{-}40}$. Combining 1D proton nuclear magnetic resonance, thioflavin-T fluorescence, transmission electron microscopy and dynamic light scattering, we disclosed the formation of high molecular weight oligomers (HMWO) and proposed a model for aggregation. Briefly, under the conditions tested, $A\beta_{1\text{-}40}$ monomers slowly convert to HMWO, which in turn reorganize to compact nuclei. Finally, fibril growth occurs through monomer addition. Thus, we highlighted the identification of on-pathway HMWO as a key step in Aβ aggregation.

The shift from the amyloid plaque to the amyloid dysfunction hypothesis, particularly the “oligomer hypothesis”, illustrates the increasingly important role attributed to oligomeric species in cell toxicity and neurodegeneration (Cline *et al.*, 2018). Following our kinetic model, a study of the detected HMWO would be suitable. Oligomers have a metastable nature when compared with soluble monomeric species or mature fibrils and are less abundant than both these species. In fact, we observed that HMWO are outnumbered by fibril nuclei. For *in* vitro study, amyloid oligomers can be isolated by lyophilization (Chen *et al.*, 2015), by preparation in membrane-mimicking environments (Serra-Batiste *et al.*, 2016) or by induced formation through the action of small-molecules (Ehrnhoefer *et al.*, 2008). Alternatively, oligomers can be generated *in vitro* (Ryan *et al.*, 2010). Because of their nature, oligomer study at the molecular level cannot be achieved by crystallization. Thus, a range of biophysical techniques can help elucidate their properties (Bemporad *et al.*, 2012). For example, secondary structure content can be assessed by circular dichroism, Fourier-transform infrared spectroscopy or H/D exchange coupled to mass spectrometry; oligomeric state can be determined by ultracentrifugation, size-exclusion chromatography, photo-induced crosslinking of unmodified proteins or dynamic light scattering; amyloid dyes ThT or Congo red can inform about structural order; fluorescent probes, such as acrylodan, help identify intermolecular interactions (*e.g.* solvent exposure of hydrophobic clusters); finally, morphology and size can be studied by small angle X-ray scattering or transmission electron/atomic force microscopy (Bemporad *et al.*, 2012). Nevertheless, oligomer properties make them difficult to study by these bulk techniques, since these may alter the native/physiological conformations of the oligomers, leading to misleading conclusions. Plus, some don’t allow a real time observation (for example, if prior isolation by lyophilization was performed). Thus, the developments in single molecule techniques based on

fluorescence microscopy offer new avenues for oligomer study *in vitro* (Yang *et al.*, 2021). For example, single-molecule Förster resonance energy transfer (smFRET), fluorescence correlation spectroscopy (FCS) and probe enhancement FRET (PE-FRET) allow to study fast monomer association, detect diffusion coefficients and hydrodynamic radius of high molecular weight species in a inhomogeneous sample (*e.g.* mixture of monomers, oligomers and fibrils) or monitor aggregation of non-labeled or modified monomers (Yang *et al.*, 2021). Combinations thereof allow, for example, to detect only oligomers in a mixture, such as $A\beta_{1-42}$ oligomers detected by FRET-FCS in physiological conditions (Wennmalm *et al.*, 2015). In conclusion, single-molecule techniques applied to amyloid oligomers (including the ~20 nm HMWO we detected) can help elucidate their biophysical properties, with potential implications in AD (Cline *et al.*, 2018; Yang *et al.*, 2021).

Chapter V - Metal-Organic Frameworks and amyloids

Since the inception of Metal-Organic Framework (MOF) research in the late 1990s, these highly porous materials have been applied to numerous fields, including gas storage, catalysis and environmental remediation (P. Silva *et al.*, 2015). Their defining features, namely permanent porosity, high surface area and pore geometries, make them also very appealing for biomedical applications (*e.g.* drug delivery, protective coatings or phototherapy applications)(Mendes *et al.*, 2020).

Here, we envisioned to adapt the crystalline sponge method to Aβ peptides. Briefly, this method consists on taking advantage of MOF properties to incorporate small organic compounds with the aim of solving their structure by X-Ray diffraction (Hoshino *et al.*, 2016). However, these efforts were unsuccessful (data not shown). Nevertheless, a recent report showed that MOFs can adsorb and release Aβ, with varying retention strengths, hinting that these materials can possibly assist in future structural studies (Mensinger *et al.*, 2020). We therefore employed a group of MOFs to tackle two different issues. First, we indirectly applied them to the amyloid field to further elucidate the mechanism of the dye Thioflavin-T when in contact with amyloid structures, showing that fluorescence is enhanced when the dye adsorbs to flat surfaces and not when in rigid conformation. Secondly, we employed a mesoporous MOF to tackle the bottleneck of protein crystallography: crystal growth (Holcomb *et al.*, 2017). Crystal seeding is a recurring technique, either by using seeds of the same protein, of a different protein or an exogenous material, such as porous materials (Khurshid *et al.*, 2014). Here, we added MOFs as potential seeding agents, by disclosing that trapping proteins inside MOF cavities can act as a nucleation inducing element for crystal growth. Overall, despite being in its infancy, MOF show great promise in amyloid related applications.

## 6.2 References

Alzheimer, A., Stelzmann, R. A., Schnitzlein, H. N., & Murtagh, F. R. (1995). An English translation of Alzheimer's 1907 paper, "Uber eine eigenartige Erkankung der Hirnrinde". *Clin Anat, 8*(6), 429-431. doi:10.1002/ca.980080612

Amanatkar, H. R., Papagiannopoulos, B., & Grossberg, G. T. (2017). Analysis of recent failures of disease modifying therapies in Alzheimer's disease suggesting a new methodology for future studies. *Expert Review of Neurotherapeutics, 17*(1), 7-16. doi:10.1080/14737175.2016.1194203

Bayes-Genis, A., Barallat, J., & Richards, A. M. (2016). A Test in Context: Neprilysin: Function, Inhibition, and Biomarker. *J Am Coll Cardiol, 68*(6), 639-653. doi:10.1016/j.jacc.2016.04.060

Bemporad, F., & Chiti, F. (2012). Protein Misfolded Oligomers: Experimental Approaches, Mechanism of Formation, and Structure-Toxicity Relationships. *Chemistry & Biology, 19*(3), 315-327. doi:10.1016/j.chembiol.2012.02.003

Benchetrit, T., Bissery, V., Mornon, J. P., Devault, A., Crine, P., & Roques, B. P. (1988). Primary structure homologies between two zinc metallopeptidases, the neutral endopeptidase 24.11 ("enkephalinase") and thermolysin, through clustering analysis. *Biochemistry, 27*(2), 592-596. doi:10.1021/bi00402a014

Bernstein, K. E., Koronyo, Y., Salumbides, B. C., Sheyn, J., Pelissier, L., Lopes, D. H., Shah, K. H., Bernstein, E. A., Fuchs, D. T., Yu, J. J., Pham, M., Black, K. L., Shen, X. Z., Fuchs, S., & Koronyo-Hamaoui, M. (2014). Angiotensin-converting enzyme overexpression in myelomonocytes prevents Alzheimer's-like cognitive decline. *J Clin Invest, 124*(3), 1000-1012. doi:10.1172/JCI66541

Blake, C. C. F., Swan, I. D. A., Rerat, C., Berthou, J., Laurent, A., & Rerat, B. (1971). An X-ray study of the subunit structure of prealbumin. *Journal of Molecular Biology, 61*(1), 217-224. doi:10.1016/0022-2836(71)90218-X

Bowler, M. W., Nurizzo, D., Barrett, R., Beteva, A., Bodin, M., Caserotto, H., Delageniere, S., Dobias, F., Flot, D., Giraud, T., Guichard, N., Guijarro, M., Lentini, M., Leonard, G. A., McSweeney, S., Oskarsson, M., Schmidt, W., Snigirev, A., von Stetten, D., Surr, J., Svensson, O., Theveneau, P., & Mueller-Dieckmann, C. (2015). MASSIF-1: a beamline dedicated to the fully automatic characterization and data collection from crystals of biological macromolecules. *Journal of Synchrotron Radiation, 22*(6), 1540-1547. doi:doi:10.1107/S1600577515016604

Brännström, K., Öhman, A., Nilsson, L., Pihl, M., Sandblad, L., & Olofsson, A. (2014). The N-terminal Region of Amyloid β Controls the Aggregation Rate and Fibril Stability at Low pH Through a Gain of Function Mechanism. *Journal of the American Chemical Society, 136*(31), 10956-10964. doi:10.1021/ja503535m

Bucher, M. H., Evdokimov, A. G., & Waugh, D. S. (2002). Differential effects of short affinity tags on the crystallization of Pyrococcus furiosus maltodextrin-binding protein. *Acta Crystallographica Section D-Biological Crystallography, 58*, 392-397. doi:10.1107/s0907444901021187

Chen, S. W., Drakulic, S., Deas, E., Ouberai, M., Aprile, F. A., Arranz, R., Ness, S., Roodveldt, C., Guilliams, T., De-Genst, E. J., Klenerman, D., Wood, N. W., Knowles, T. P.

J., Alfonso, C., Rivas, G., Abramov, A. Y., Valpuesta, J. M., Dobson, C. M., & Cremades, N. (2015). Structural characterization of toxic oligomers that are kinetically trapped during α-synuclein fibril formation. *Proceedings of the National Academy of Sciences, 112*(16), E1994. doi:10.1073/pnas.1421204112

Ciccone, L., Fruchart-Gaillard, C., Mourier, G., Savko, M., Nencetti, S., Orlandini, E., Servent, D., Stura, E. A., & Shepard, W. (2018). Copper mediated amyloid-β binding to Transthyretin. *Scientific Reports, 8*(1), 13744. doi:10.1038/s41598-018-31808-5

Cline, E. N., Bicca, M. A., Viola, K. L., & Klein, W. L. (2018). The Amyloid-β Oligomer Hypothesis: Beginning of the Third Decade. *Journal of Alzheimer's Disease, 64*, S567-S610. doi:10.3233/JAD-179941

Corsini, L., Hothorn, M., Scheffzek, K., Sattler, M., & Stier, G. (2008). Thioredoxin as a fusion tag for carrier-driven crystallization. *Protein science : a publication of the Protein Society, 17*(12), 2070-2079. doi:10.1110/ps.037564.108

Costa, S., Almeida, A., Castro, A., & Domingues, L. (2014). Fusion tags for protein solubility, purification and immunogenicity in Escherichia coli: the novel Fh8 system. *Frontiers in Microbiology, 5*(63). doi:10.3389/fmicb.2014.00063

Dion, N., Le Moual, H., Fournié-Zaluski, M. C., Roques, B. P., Crine, P., & Boileau, G. (1995). Evidence that Asn542 of neprilysin (EC 3.4.24.11) is involved in binding of the P2′ residue of substrates and inhibitors. *Biochemical Journal, 311*(2), 623-627. doi:10.1042/bj3110623

Donahue, J. P., Patel, H., Anderson, W. F., & Hawiger, J. (1994). Three-dimensional structure of the platelet integrin recognition segment of the fibrinogen gamma chain obtained by carrier protein-driven crystallization. *Proc Natl Acad Sci U S A, 91*(25), 12178-12182. doi:10.1073/pnas.91.25.12178

Ehrnhoefer, D. E., Bieschke, J., Boeddrich, A., Herbst, M., Masino, L., Lurz, R., Engemann, S., Pastore, A., & Wanker, E. E. (2008). EGCG redirects amyloidogenic polypeptides into unstructured, off-pathway oligomers. *Nature structural & molecular biology, 15*(6), 558-566. doi:10.1038/nsmb.1437

Gacasan, S. B., Baker, D. L., & Parrill, A. L. (2017). G protein-coupled receptors: the evolution of structural insight. *AIMS Biophys, 4*(3), 491-527. doi:10.3934/biophy.2017.3.491

Ghadami, S. A., Chia, S., Ruggeri, F. S., Meisl, G., Bemporad, F., Habchi, J., Cascella, R., Dobson, C. M., Vendruscolo, M., Knowles, T. P. J., & Chiti, F. (2020). Transthyretin Inhibits Primary and Secondary Nucleations of Amyloid-β Peptide Aggregation and Reduces the Toxicity of Its Oligomers. *Biomacromolecules, 21*(3), 1112-1125. doi:10.1021/acs.biomac.9b01475

Gimeno, A., Santos, L. M., Alemi, M., Rivas, J., Blasi, D., Cotrina, E. Y., Llop, J., Valencia, G., Cardoso, I., Quintana, J., Arsequell, G., & Jiménez-Barbero, J. (2017). Insights on the Interaction between Transthyretin and Aβ in Solution. A Saturation Transfer Difference (STD) NMR Analysis of the Role of Iododiflunisal. *Journal of Medicinal Chemistry, 60*(13), 5749-5758. doi:10.1021/acs.jmedchem.7b00428

Glenner, G. G., & Wong, C. W. (1984). Alzheimer's disease: initial report of the purification and characterization of a novel cerebrovascular amyloid protein. *Biochem Biophys Res Commun, 120*(3), 885-890. doi:10.1016/s0006-291x(84)80190-4

Goedert, M., Spillantini, M. G., & Crowther, R. A. (1991). Tau proteins and neurofibrillary degeneration. *Brain Pathol, 1*(4), 279-286. doi:10.1111/j.1750-3639.1991.tb00671.x

Han, S.-H., Park, J.-C., & Mook-Jung, I. (2016). Amyloid β-interacting partners in Alzheimer's disease: From accomplices to possible therapeutic targets. *Progress in Neurobiology, 137*, 17-38. doi:10.1016/j.pneurobio.2015.12.004

Hardy, J. A., & Higgins, G. A. (1992). Alzheimer's disease: the amyloid cascade hypothesis. *Science, 256*(5054), 184. doi:10.1126/science.1566067

Hellstrom-Lindahl, E., Ravid, R., & Nordberg, A. (2008). Age-dependent decline of neprilysin in Alzheimer's disease and normal brain: inverse correlation with A beta levels. *Neurobiol Aging, 29*(2), 210-221. doi:10.1016/j.neurobiolaging.2006.10.010

Holcomb, J., Spellmon, N., Zhang, Y., Doughan, M., Li, C., & Yang, Z. (2017). Protein crystallization: Eluding the bottleneck of X-ray crystallography. *AIMS Biophys, 4*(4), 557-575. doi:10.3934/biophy.2017.4.557

Holland, D. R., Hausrath, A. C., Juers, D., & Matthews, B. W. (1995). Structural analysis of zinc substitutions in the active site of thermolysin. *Protein Science, 4*(10), 1955-1965. doi:10.1002/pro.5560041001

Hoshino, M., Khutia, A., Xing, H., Inokuma, Y., & Fujita, M. (2016). The crystalline sponge method updated. *IUCrJ, 3*(2), 139-151. doi:10.1107/S2052252515024379

Hu, X., Crick, S. L., Bu, G., Frieden, C., Pappu, R. V., & Lee, J.-M. (2009). Amyloid seeds formed by cellular uptake, concentration, and aggregation of the amyloid-beta peptide. *Proceedings of the National Academy of Sciences, 106*(48), 20324. doi:10.1073/pnas.0911281106

Iljina, M., Garcia, G. A., Dear, A. J., Flint, J., Narayan, P., Michaels, T. C. T., Dobson, C. M., Frenkel, D., Knowles, T. P. J., & Klenerman, D. (2016). Quantitative analysis of co-oligomer formation by amyloid-beta peptide isoforms. *Scientific Reports, 6*(1), 28658. doi:10.1038/srep28658

Jacobsen, J. S., Comery, T. A., Martone, R. L., Elokdah, H., Crandall, D. L., Oganesian, A., Aschmies, S., Kirksey, Y., Gonzales, C., Xu, J., Zhou, H., Atchison, K., Wagner, E., Zaleska, M. M., Das, I., Arias, R. L., Bard, J., Riddell, D., Gardell, S. J., Abou-Gharbia, M., Robichaud, A., Magolda, R., Vlasuk, G. P., Bjornsson, T., Reinhart, P. H., & Pangalos, M. N. (2008). Enhanced clearance of Abeta in brain by sustaining the plasmin proteolysis cascade. *Proc Natl Acad Sci U S A, 105*(25), 8754-8759. doi:10.1073/pnas.0710823105

Jia, B., & Jeon, C. O. (2016). High-throughput recombinant protein expression in Escherichia coli: current status and future perspectives. *Open biology, 6*(8), 160196. doi:10.1098/rsob.160196

Jin, T., Chuenchor, W., Jiang, J., Cheng, J., Li, Y., Fang, K., Huang, M., Smith, P., & Xiao, T. S. (2017). Design of an expression system to enhance MBP-mediated crystallization. *Scientific Reports, 7*, 40991-40991. doi:10.1038/srep40991

Khurshid, S., Saridakis, E., Govada, L., & Chayen, N. E. (2014). Porous nucleating agents for protein crystallization. *Nature Protocols, 9*(7), 1621-1633. doi:10.1038/nprot.2014.109

Kilger, E., Buehler, A., Woelfing, H., Kumar, S., Kaeser, S. A., Nagarathinam, A., Walter, J., Jucker, M., & Coomaraswamy, J. (2011). BRI2 protein regulates beta-amyloid degradation

by increasing levels of secreted insulin-degrading enzyme (IDE). *J Biol Chem, 286*(43), 37446-37457. doi:10.1074/jbc.M111.288373

King, J. V., Liang, W. G., Scherpelz, K. P., Schilling, A. B., & Meredith, S. C. (2014). Molecular Basis of Substrate Recognition and Degradation by Human Presequence Protease. *Structure/Folding and Design, 22*, 996-1007. doi:10.1016/j.str.2014.05.003

Kobe, B., Ve, T., & Williams, S. J. (2015). Fusion-protein-assisted protein crystallization. *Acta Crystallogr F Struct Biol Commun, 71*(Pt 7), 861-869. doi:10.1107/S2053230X15011061

Kosobokova, E. N., Skrypnik, K. A., & Kosorukov, V. S. (2016). Overview of fusion tags for recombinant proteins. *Biochemistry (Moscow), 81*(3), 187-200. doi:10.1134/S0006297916030019

Kubitza, C., Ginsel, C., Bittner, F., Havemeyer, A., Clement, B., & Scheidig, A. J. (2018). T4 lysozyme-facilitated crystallization of the human molybdenum cofactor-dependent enzyme mARC. *Acta crystallographica. Section F, Structural biology communications, 74*(Pt 6), 337-344. doi:10.1107/S2053230X18006921

Li, X., Zhang, X., Ladiwala, A. R. A., Du, D., Yadav, J. K., Tessier, P. M., Wright, P. E., Kelly, J. W., & Buxbaum, J. N. (2013). Mechanisms of transthyretin inhibition of β-amyloid aggregation in vitro *The Journal of Neuroscience, 33*(50), 19423. doi:10.1523/JNEUROSCI.2561-13.2013

Liz, Márcia A., Leite, Sérgio C., Juliano, L., Saraiva, Maria J., Damas, Ana M., Bur, D., & Sousa, Mónica M. (2012). Transthyretin is a metallopeptidase with an inducible active site. *Biochemical Journal, 443*(3), 769-778. doi:10.1042/BJ20111690

Lowe, D. (2021). The Aducanumab Approval. Retrieved from https://blogs.sciencemag.org/pipeline/archives/2021/06/08/the-aducanumab-approval

Maruyama, M., Higuchi, M., Takaki, Y., Matsuba, Y., Tanji, H., Nemoto, M., Tomita, N., Matsui, T., Iwata, N., Mizukami, H., Muramatsu, S., Ozawa, K., Saido, T. C., Arai, H., & Sasaki, H. (2005). Cerebrospinal fluid neprilysin is reduced in prodromal Alzheimer's disease. *Ann Neurol, 57*(6), 832-842. doi:10.1002/ana.20494

Matsuzaki, K. (2007). Physicochemical interactions of amyloid β-peptide with lipid bilayers. *Biochimica et Biophysica Acta (BBA) - Biomembranes, 1768*(8), 1935-1942. doi:10.1016/j.bbamem.2007.02.009

Mawuenyega, K. G., Sigurdson, W., Ovod, V., Munsell, L., Kasten, T., Morris, J. C., Yarasheski, K. E., & Bateman, R. J. (2010). Decreased clearance of CNS beta-amyloid in Alzheimer's disease. *Science, 330*(6012), 1774. doi:10.1126/science.1197623

Mendes, R. F., Figueira, F., Leite, J. P., Gales, L., & Almeida Paz, F. A. (2020). Metal–organic frameworks: a future toolbox for biomedicine? *Chemical Society Reviews, 49*(24), 9121-9153. doi:10.1039/D0CS00883D

Mensinger, Z. L., Cook, B. L., & Wilson, E. L. (2020). Adsorption of Amyloid Beta Peptide by Metal–Organic Frameworks. *ACS Omega, 5*(51), 32969-32974. doi:10.1021/acsomega.0c04019

Miners, J. S., Baig, S., Tayler, H., Kehoe, P. G., & Love, S. (2009). Neprilysin and insulin-degrading enzyme levels are increased in Alzheimer disease in relation to disease severity. *J Neuropathol Exp Neurol, 68*(8), 902-914. doi:10.1097/NEN.0b013e3181afe475

Mital, M., Bal, W., Frączyk, T., & Drew, S. C. (2018). Interplay between Copper, Neprilysin, and N-Truncation of β-Amyloid. *Inorganic Chemistry, 57*(11), 6193-6197. doi:10.1021/acs.inorgchem.8b00391

Moon, A. F., Mueller, G. A., Zhong, X., & Pedersen, L. C. (2010). A synergistic approach to protein crystallization: combination of a fixed-arm carrier with surface entropy reduction. *Protein science : a publication of the Protein Society, 19*(5), 901-913. doi:10.1002/pro.368

Moss, S., Subramanian, V., & Acharya, K. R. (2020). Crystal structure of peptide-bound neprilysin reveals key binding interactions. *FEBS Letters, 594*(2), 327-336. doi:10.1002/1873-3468.13602

Mueller-Steiner, S., Zhou, Y., Arai, H., Roberson, E. D., Sun, B., Chen, J., Wang, X., Yu, G., Esposito, L., Mucke, L., & Gan, L. (2006). Antiamyloidogenic and neuroprotective functions of cathepsin B: implications for Alzheimer's disease. *Neuron, 51*(6), 703-714. doi:10.1016/j.neuron.2006.07.027

Munishkina, L. A., Cooper, E. M., Uversky, V. N., & Fink, A. L. (2004). The effect of macromolecular crowding on protein aggregation and amyloid fibril formation. *Journal of Molecular Recognition, 17*(5), 456-464. doi:10.1002/jmr.699

Nguyen, H., Martinez, B., Oganesyan, N., & Kim, R. (2004). An automated small-scale protein expression and purification screening provides beneficial information for protein production. *Journal of Structural and Functional Genomics, 5*(1), 23-27. doi:10.1023/B:JSFG.0000029195.73810.86

Niemann, H. H., Schmoldt, H.-U., Wentzel, A., Kolmar, H., & Heinz, D. W. (2006). Barnase Fusion as a Tool to Determine the Crystal Structure of the Small Disulfide-rich Protein McoEeTI. *Journal of Molecular Biology, 356*(1), 1-8. doi:10.1016/j.jmb.2005.11.005

Nilsson, L., Pamrén, A., Islam, T., Brännström, K., Golchin, S. A., Pettersson, N., Iakovleva, I., Sandblad, L., Gharibyan, A. L., & Olofsson, A. (2018). Transthyretin Interferes with Aβ Amyloid Formation by Redirecting Oligomeric Nuclei into Non-Amyloid Aggregates. *Journal of Molecular Biology, 430*(17), 2722-2733. doi:10.1016/j.jmb.2018.06.005

Nisbet, R. M., Nuttall, S. D., Robert, R., Caine, J. M., Dolezal, O., Hattarki, M., Pearce, L. A., Davydova, N., Masters, C. L., Varghese, J. N., & Streltsov, V. A. (2013). Structural studies of the tethered N-terminus of the Alzheimer's disease amyloid-beta peptide. *Proteins, 81*(10), 1748-1758. doi:10.1002/prot.24312

Nisemblat, Y., Belinson, H., Dolev, I., & Michaelson, D. M. (2008). Activation of the amyloid cascade by intracerebroventricular injection of the protease inhibitor phosphoramidon. *Neurodegener Dis, 5*(3-4), 166-169. doi:10.1159/000113692

Palaninathan, S. K. (2012). Nearly 200 X-Ray Crystal Structures of Transthyretin: What Do They Tell Us About This Protein and the Design of Drugs for TTR Amyloidoses? *Current Medicinal Chemistry, 19*(15), 2324-2342. doi:10.2174/092986712800269335

Perry, E. K. (1986). The cholinergic hypothesis--ten years on. *Br Med Bull, 42*(1), 63-69. doi:10.1093/oxfordjournals.bmb.a072100

Roques, B. P., Noble, F., Daugé, V., Fournié-Zaluski, M. C., & Beaumont, A. (1993). Neutral endopeptidase 24.11: structure, inhibition, and experimental and clinical pharmacology. *Pharmacological Reviews, 45*(1), 87.

Ryan, D. A., Narrow, W. C., Federoff, H. J., & Bowers, W. J. (2010). An improved method for generating consistent soluble amyloid-beta oligomer preparations for in vitro neurotoxicity studies. *Journal of Neuroscience Methods, 190*(2), 171-179. doi:10.1016/j.jneumeth.2010.05.001

Schmidt, P. M., Sparrow, L. G., Attwood, R. M., Xiao, X., Adams, T. E., & McKimm-Breschkin, J. L. (2012). Taking down the FLAG! How Insect Cell Expression Challenges an Established Tag-System. *PLoS One, 7*(6), e37779. doi:10.1371/journal.pone.0037779

Schmidt, T. G. M., & Skerra, A. (2007). The Strep-tag system for one-step purification and high-affinity detection or capturing of proteins. *Nature Protocols, 2*(6), 1528-1535. doi:10.1038/nprot.2007.209

Serra-Batiste, M., Ninot-Pedrosa, M., Bayoumi, M., Gairí, M., Maglia, G., & Carulla, N. (2016). Aβ42 assembles into specific β-barrel pore-forming oligomers in membrane-mimicking environments. *Proceedings of the National Academy of Sciences, 113*(39), 10866. doi:10.1073/pnas.1605104113

Sharifi - Sirch, G. R., & Jalali - Javaran, M. (2016). Selecting appropriate hosts for recombinant proteins production: Review article. *Hormozgan medical journal, 20*(3), -.

Shen, Y., Joachimiak, A., Rich Rosner, M., & Tang, W. J. (2006). Structures of human insulin-degrading enzyme reveal a new substrate recognition mechanism. *Nature, 443*, 870-874. doi:10.1038/nature05143

Silva, C. S., Eira, J., Ribeiro, C. A., Oliveira, Â., Sousa, M. M., Cardoso, I., & Liz, M. A. (2017). Transthyretin neuroprotection in Alzheimer's disease is dependent on proteolysis. *Neurobiology of Aging, 59*, 10-14. doi:10.1016/j.neurobiolaging.2017.07.002

Silva, P., Vilela, S. M. F., Tomé, J. P. C., & Paz, F. A. A. (2015). Multifunctional metal-organic frameworks: from academia to industrial applications. *Chemical Society Reviews, 44*(19), 6774-6803. doi:10.1039/c5cs00307e

Streltsov, V. A., Varghese, J. N., Masters, C. L., & Nuttall, S. D. (2011). Crystal structure of the amyloid-β p3 fragment provides a model for oligomer formation in Alzheimer's disease. *Journal of Neuroscience, 31*, 1419-1426. doi:10.1523/JNEUROSCI.4259-10.2011

Suzuki, N., Hiraki, M., Yamada, Y., Matsugaki, N., Igarashi, N., Kato, R., Dikic, I., Drew, D., Iwata, S., Wakatsuki, S., & Kawasaki, M. (2010). Crystallization of small proteins assisted by green fluorescent protein. *Acta Crystallographica Section D, 66*(10), 1059-1066. doi:doi:10.1107/S0907444910032944

Takano, K., Endo, S., Mukaiyama, A., Chon, H., Matsumura, H., Koga, Y., & Kanaya, S. (2006). Structure of amyloid β fragments in aqueous environments. *FEBS Journal, 273*, 150-158. doi:10.1111/j.1742-4658.2005.05051.x

Thorsen, T. S., Matt, R., Weis, W. I., & Kobilka, B. K. (2014). Modified T4 Lysozyme Fusion Proteins Facilitate G Protein-Coupled Receptor Crystallogenesis. *Structure, 22*(11), 1657-1664. doi:10.1016/j.str.2014.08.022

Tiraboschi, G., Jullian, N., Thery, V., Antonczak, S., Fournie-Zaluski, M.-C., & Roques, B. P. (1999). A three-dimensional construction of the active site (region 507–749) of human neutral endopeptidase (EC.3.4.24.11). *Protein Engineering, Design and Selection, 12*(2), 141-149. doi:10.1093/protein/12.2.141

Waugh, D. S. (2016). Crystal structures of MBP fusion proteins. *Protein Sci, 25*(3), 559-571. doi:10.1002/pro.2863

Weber, P., Pissis, C., Navaza, R., Mechaly, A. E., Saul, F., Alzari, P. M., & Haouz, A. (2019). High-Throughput Crystallization Pipeline at the Crystallography Core Facility of the Institut Pasteur. *Molecules, 24*(24). doi:10.3390/molecules24244451

Wennmalm, S., Chmyrov, V., Widengren, J., & Tjernberg, L. (2015). Highly Sensitive FRET-FCS Detects Amyloid β-Peptide Oligomers in Solution at Physiological Concentrations. *Analytical Chemistry, 87*(23), 11700-11705. doi:10.1021/acs.analchem.5b02630

Wollerton, M. C., Wales, R., Bullock, J. A., Hudson, I. R., & Beggs, M. (2006). Automation and Optimization of Protein Expression and Purification on a Novel Robotic Platform. *JALA: Journal of the Association for Laboratory Automation, 11*(5), 291-303. doi:10.1016/j.jala.2006.08.002

Wood, J. G., Mirra, S. S., Pollock, N. J., & Binder, L. I. (1986). Neurofibrillary tangles of Alzheimer disease share antigenic determinants with the axonal microtubule-associated protein tau (tau). *Proc Natl Acad Sci U S A, 83*(11), 4040-4043. doi:10.1073/pnas.83.11.4040

Yang, J., Perrett, S., & Wu, S. (2021). Single Molecule Characterization of Amyloid Oligomers. *Molecules, 26*(4). doi:10.3390/molecules26040948

Zhan, Y., Song, X., & Zhou, G. W. (2001). Structural analysis of regulatory protein domains using GST-fusion proteins. *Gene, 281*(1), 1-9. doi:10.1016/S0378-1119(01)00797-1

Zhang, R., Hu, X., Khant, H., Ludtke, S. J., Chiu, W., Schmid, M. F., Frieden, C., & Lee, J.-M. (2009). Interprotofilament interactions between Alzheimer's Abeta1-42 peptides in amyloid fibrils revealed by cryoEM. *Proceedings of the National Academy of Sciences of the United States of America, 106*, 4653-4658. doi:10.1073/pnas.0901085106